Magnetic deflagration in Mn_{12}-ac and Nd_5Ge_3: new techniques and phenomena

Diego Villuendas Pellicero

UNIVERSITAT DE BARCELONA

Departament de Física Fonamental

DOCTORAT EN NANOCIÈNCIES

Magnetic deflagrations in Mn_{12}-ac and Nd_5Ge_3

New techniques and phenomena

Doctoral Dissertation of:
Diego Villuendas Pellicero

Advisor and tutor:
Dr. Joan Manel Hernàndez Ferràs

Supervisors of the Doctoral Program:
Prof. Martí Pi, **Prof. Manuel Varela**, **Prof. Blas Garrido**

October 2015

Magnetic deflagrations in Mn_{12}-ac and Nd_5Ge_3

New techniques and phenomena

by

Diego Villuendas Pellicero

Universitat de Barcelona

Cover image is a derivative of:

🅭🅯 — Domino by Jeff Pioquinto, SJ, Taken: October 11, 2014. Retrieved from https://flic.kr/p/pA9ftS on November 1, 2015.

Some styles are adapted from:

🅭🅯🄎 — Sergi Lendinez Escudero — 2015

A mis inmejorables padres Juan José y Esperanza,
a mis queridos hermanos pequeños Darío y Flor,
a mi amada, paciente y divertida ex-novia Laura,
a nuestro fiel amigo Sawyer,
y sobre todo a nuestro delicioso, increíble y adorable hijo Júpiter.

Contents

Acknowledgments

Honestly, I would need an entire chapter to thank properly to those who have helped me in this long journey. Some did it unconsciously, some did it on purpose. To the former, thank you. To the latter, you are the best; I have reserved a place for you in the following paragraphs.

Since this thesis is written in English and some of the people to whom I am grateful do not understand it, I will have to thank twice some people; no problem, gratefulness is free. Prof. Javier Tejada, you are the first to whom I want to thank. You opened to me the doors of your group, and that changed my life, for good. I will be always grateful to you for giving me the opportunity of becoming a professional scientist in a major league laboratory. Thank you as well for bringing Dr. Joan Manel Hernàndez to my life. I had the best advisor ever. And he is also an extraordinary scientist. I have learned from him every single day. And also improved my knowledge on physics. Thank you Joan Manel, for all the good moments, for your extreme patience, for your passion for science, and specially for your support in the tough times. I want to thank Dr. Saül Vélez for giving me the opportunity to start the study of the magnetic deflagrations on the intermetallic compound Nd_5Ge_3, and to Prof. Takanori Tsutaoka for providing the single crystals during the last three years. Thank you Dr. Paulo Santos for the time spent in his group in Berlin. Thank you Tanya and Ruslan Prozorov for inviting me to Ames, and for the collaboration. That time did not work out. Next time will. Many thanks to Enrique del Barco for giving me the chance of spend three months working in his group in Orlando. You give me more than you probably believe. Thank you. I want to thank all the members of the Grup of Magnetisme, we have been a family, and this is forever. Thanks to my family for all the support and patience and love, and for all the love and patience and support. Thank you all. I love you more every day.

Una vez enterados en el extranjero, quiero agradecer ahora en lengua castellana. No voy a ser breve. Quiero agradecer al Prof. Javier Tejada, que pasó de ser mi profesor de Ampliación de Estado Sólido a mi Jefe de Grupo. Gracias por abrirme las puertas del laboratorio, gracias por permitirme formarme en tu grupo, por dejarme ser un científico a sueldo. Gracias. Gracias Javier por conseguir que el

Dr. Joan Manel Hernàndez supervisara un trabajo de la carrera. Gracias porque lo que empezó con una tutoría de un trabajo pequeño ha terminado con la dirección de una tesis doctoral. En Joan Manel he tenido el mejor director de tesis que pudiera pedir. Siempre ha estado ahí cuando lo he necesitado, en los buenos momentos y sobre todo en los malos. He disfrutado de tus ganas voraces de hacer experimentos, de probar cosas, de aprender, de preguntar y de discutir. He aprendido mucho de ti Joan Manel. Y también mucha física. Empecé teniendo un director y ahora además me llevo un buen amigo. Has puesto música en mi vida, literalmente. Gracias de corazón.

El Grup de Magnetisme es una familia. En todos estos años han pasado muchas cosas, y ha pasado mucha gente. Alguna de esa gente me ha visto crecer, y no sólo a mí, ha visto formarse a mi familia, ha visto nacer a mi hijo. Querido Dr. Antoni Garcia, sepa usted que me marcharé de este grupo habiéndole visto renacer, habiéndole incordiado, habiéndole disfrutado y habiéndole suministrado material de primera. Gracias por tu meticulosidad. Quedan pendientes muchos acordes por tocar. Gracias Ferran, por tus comentarios positivos, por tu diligencia, por tu deportividad y por ayudarme en los inicios de la tesis. Gracias. Gracias Alberto, por tu buen humor y por toda la ayuda que me diste cuando empezaba. Gracias. A mis compañeros de despacho y laboratorio qué les puedo decir. Para ser justos debería aparecerme en sus casas soltando fajos de agradecimientos "a lo Mayweather". He disfrutado y he aprendido lo indescriptible junto a vosotros. Gracias Ricardo, por todos estos años de amistad, por compartir los gustos musicales, por todos los ánimos y todos los números que hemos hecho juntos; gracias por preocuparte por mí. Gracias Saül por los buenos momentos en el laboratorio, estuviera éste en Barcelona, en Berlín o donde fuera. Tengo una gran deuda contigo con esta tesis, sin los materiales y sin tu ayuda nunca hubiera conseguido algo así. Debajo de esa coraza (chiquitica) que tienes hay un corazón como un piano de cola. Gracias. Gracias a Víctor, por dejar convertirme en su censurador, su Srta. Rottenmeier, su compañero de horas de escritura y su amigo. Nunca un tío con tan poca gracia ha sido tan gracioso. Te lo agradezco. Gracias al inminente Dr. Lendínez, por esa curiosidad tan profunda que tienes, por el mimo en los detalles, por sacarme a correr, por tantas horas de laboratorio, tantas transferencias y tantos buenos sustos. Ha sido un placer acabar la tesis juntos. Gracias. A ti Gianluca 5, gracias. Por tu hipocondría que nos mantiene alerta, por tu enorme corazón y por tus tantas voces. Eres muy buen científico, nunca lo dudes. Gracias por preocuparte por mí. Gracias Cris, por la simpatía y serenidad que aportabas al grupo, y por el suministro esporádico de magdalenas caseras. Gracias. Gracias Jesús y Antonio, por las charlas entorno a la cafetera. Tendríais que haber estado en la cuarta planta. Gracias a los nuevos, y a los recién partidos. Gracias a Nahuel por ser bárbaro. Tenés una personalidad macanuda; lástima que no te soporte.

Seguro que tendré el placer de tener que aguantarte en el futuro. Gracias a Martí, a Raimon, a Marc y a Jaume por los buenos ratos, suerte en vuestros proyectos, sois buena gente. Gracias Vegard, por traer siempre el fresco. Espero que aprendas el castellano suficiente como para que puedas leer que siento no haber tenido más tiempo para acompañaros en excursiones.

Gracias a Enrique del Barco por la hospitalidad que me brindó en mi estancia en Orlando, y por ofrecerme un puesto de post-doc. Siento mucho que no funcionara. Sinceramente espero volver a cruzarnos en algún camino y poder rehogar una charla muy larga con unas buenas cervezas. Gracias también a su grupo, que me hicieron sentirme uno más desde el primer minuto. Gracias.

Gracias a Alberto Hernando, a Dani Puigdomènech y a Roger Mor por todos estos años. Nos conocimos en la carrera y desde entonces hemos pasado grandísimos momentos juntos. A los que ya os doctorasteis, ¡os pillé! A Roger, ¡disfruta del doctorado, y empieza ya a escribir! A otros amigos de carrera, master y doctorado, Carles Panadés, Ferran Barroso, Adrián Macía, Adrián Hernando, David Mateo, Marta Abad, Guillem Abril, Francesco Aprile, Ana Alemany... Gracias por la compañía durante el trayecto. Viajaría encantado con vosotros de nuevo a muchos otros sitios.

Gracias a mi abuela, a mis tíos, a todos mis cuñados y a mis suegros, por creeros que estaba haciendo algo de provecho. Espero poder contaros de qué va esta tesis algún día. Gracias a mi fiel perro Sawyer. No sabe leer, pero sí sabe que le quiero. Perdona por no haberte podido dedicar más tiempo. Gracias por la alegría que regalas a diario.

Mil una veces gracias a mi ex-novia, Laura, por que nadie más que ella ha sufrido los daños colaterales de este trabajo, los fines de semana sin salir, las noches sin volver a casa, los congresos, los bajones, los subidones... Gracias por casarte conmigo. Gracias por hacerme reír cuando he querido ver el mundo arder. Gracias por compartir mis sueños y hacerme partícipe de los tuyos. Y sobre todo, por encima de todo lo demás, gracias, mil dos veces gracias por formar junto a mí una familia. Júpiter es el mayor y mejor regalo que jamás hubiera soñado. Tengo un tesoro, y lo tengo gracias a ti. Mil tres veces gracias.

Gracias a mis hermanos pequeños Darío y Flor, por todo lo bueno de ser el hermano mayor sin tener la sensación haber pasado por nada de lo malo. Os quiero mucho, aunque penséis que estudio griego clásico. Y para acabar, un número siempre insuficientemente grande de agradecimientos a mis padres Juan José y Esperanza, que desde que tengo uso de razón me han inculcado el amor por el conocimiento, el respeto a los demás y la honestidad. Os quiero, y si no os lo he dicho nunca os lo digo ahora, os admiro y os estaré siempre agradecido por todos los esfuerzos que habéis hecho por mí y por mis hermanos. Si alguien es el responsable último de que haya llegado hasta aquí sois vosotros. Gracias.

Resumen en castellano

Este trabajo que el lector tiene en sus manos es la culminación de dos de los proyectos que he llevado a cabo en el Grup de Magnetisme de la Universitat de Barcelona. El material que aquí se incluye es un fragmento de todo el trabajo realizado en estos años, una recopilación de aquellos proyectos que han llegado a buen puerto. A lo largo de esta disertación expongo mi contribución al campo de la física del estado sólido y del nanomagnetismo, centrada en el estudio del fenómeno de las deflagraciones magnéticas. El objetivo que persigue esta tesis es impulsar el estudio de dichas deflagraciones magnéticas gracias, por una parte al descubrimiento del fenómeno en un sistema nuevo y prometedor como es el compuesto intermetálico $\mathrm{Nd}_5\mathrm{Ge}_3$, y por otra a la presentación de un método nuevo de medición de las dependencias espacio-temporales de las mismas utilizando técnicas magneto-ópticas.

Manteniendo el hilo conductor del fenómeno de las deflagraciones magnéticas, esta tesis doctoral se divide en dos partes. En la primera parte presento mis investigaciones en un sistema bien conocido como es el $\mathrm{Mn}_{12}-$ac. El estudio de las deflagraciones magnéticas en ese sistema empezó unos diez años atrás, y el Grup de Magnetisme de la Universitat de Barcelona ha sido uno de los mayores impulsores en su estudio, bien por experimentos propios, bien por colaboraciones con otros grupos. Hasta la fecha de los experimentos presentados en esta memoria, el estudio de la evolución espacio-temporal de las deflagraciones magnéticas era llevado a cabo utilizando dos opciones experimentales: agrupaciones equidistantes de sondas Hall, o conjuntos de bobinas colectoras. Sin embargo, ninguno de esos métodos es capaz de obtener información detallada de la forma y dinámica del frente de deflagración. Para alcanzar una resolución espacial suficiente se decidió estudiar el fenómeno mediante técnicas magneto-ópticas. Los experimentos se llevaron a cabo en la Vrije Universiteit Amsterdam, en colaboración con el Prof. Wijngaarden. Mi contribución en estos experimentos consistió en el tratamiento y análisis de todos los videos obtenidos. A partir de los videos tratados (consiguiendo duplicar la resolución temporal de los mismos con una pérdida pequeña de resolución espacial), seleccioné las regiones que consideré que podían aportar información sobre la evolución de las deflagraciones y estudié cómo los niveles de grises variaban entre los consecutivos fotogramas. Los resultados confirmaron la presencia de deflagraciones magnéticas. Sin embargo, al analizar los datos en detalle se hicieron patentes ciertas deficiencias en el procedimiento de medición que afectaron a la resolución temporal del experimento. Debido a estas deficiencias, las evoluciones obtenidas, y por consiguiente las velocidades, se mantenían aproximadamente constantes, independientemente del campo magnético aplicado en el momento de la ignición de las deflagraciones. A raíz de todos los experimentos previos sobre deflagraciones es sabida la fuerte dependencia de la velocidad con el campo magnético externo. Lo que sucedió es que se midió sin tener el cuenta que el equipo de medida actuaba como un filtro pasa-bajos, limitando la resolución temporal "efectiva" a unos 60 μs. Sin embargo, como se explica en el capítulo, creemos que es posible resolver dichas deficiencias, por ejemplo, modificando el proceso de medida para no tener en cuenta el signo del campo. Corrigiendo ese factor, la velocidad de captura podría multiplicarse por tres. Esa pérdida de la información de la dirección del campo no sería crucial en nuestro caso ya que lo que se busca es la propagación de la inversión de magnetización, por lo que si existiera un frente en movimiento siempre se vería, fuera cual fuera su signo (es decir, empezando la inversión en un extremo de la muestra o en el otro).

La segunda y más extensa parte de la tesis está dedicada al segundo material en el que se estudian deflagraciones magnéticas, el compuesto intermetálico Nd_5Ge_3. Motivados por el descubrimiento del fenómeno de la deflagración magnética en la transición meta-magnética entre los estados antiferromagnético y ferromagnético del compuesto intermetálico Gd_5Ge_4, encontramos en Nd_5Ge_3 el candidato perfecto para extender de forma definitiva el estudio de las deflagraciones magnéticas más allá de los imanes moleculares. Dos propiedades remarcables del comportamiento magnético del Nd_5Ge_3 son las que nos hicieron centrar nuestra atención en el material. Primero, se trata de uno de los pocos sistemas en los que mediante un campo magnético externo se induce espontáneamente un estado ferromagnético (FM) con gran irreversibilidad proviniendo de un estado antiferromagnético (AFM), y segundo, que los cambios magnéticos que experimenta el sistema, tanto dicha transición AFM→FM como la inversión de la magnetización en el estado FM, ocurren de forma muy abrupta, siendo también uno de los escasos sistemas que presenta esta propiedad.

Antes de estudiar en detalle las deflagraciones en Nd_5Ge_3, y debido a la poca literatura existente sobre medidas en monocristales de este material, dedico tres capítulos al estudio de sus propiedades magnéticas, térmicas y eléctricas, tanto estáticas como dinámicas. La intención no es únicamente extender y/o reproducir las medidas ya realizadas en policristales, sino obtener toda la información posible del sistema y así poder explicar la propiedades de las deflagraciones magnéticas. En esas medidas encuentro una variedad de fenómenos interesantes, desde generación espontánea de voltaje durante las deflagraciones magnéticas, hasta la aparición de saltos espontáneos de la magnetización con el tiempo (manteniendo la temperatura y el campo magnético constantes), pasando por la obtención de términos de origen antiferromagnético en la dependencia térmica de la capacidad calorífica del estado ferromagnético saturado, o una magnetorresistencia gigante entre ambos estados, entre otros.

Como veremos en el quinto capítulo, las medidas experimentales confirman la existencia del fenómeno de la deflagración magnética en ambas fases, AFM y FM, siendo de esta forma la primera vez que este fenómeno es observado en dos distintas fases de un mismo sistema, y más importante, siendo la primera vez que se da en un ferromagneto. La inversión de magnetización en los ferromagnetos suele estar regida por la creación y el desplazamiento a altas velocidades de paredes de dominio, con velocidades directamente proporcionales a la magnitud del campo aplicado. Sin embargo, las "bajas" velocidades encontradas, junto con la dependencia altamente no-lineal de éstas con el campo aplicado descartan la posibilidad de estar ante la presencia de dominios en movimiento. La velocidad de propagación del frente obtenida en la teoría de deflagraciones, aunque siendo ésta desarrollada para los sistemas como el $\mathrm{Mn_{12}}-$ac, se ajusta bien a los datos experimentales. De dicho ajuste somos capaces de obtener la difusividad térmica del $\mathrm{Nd_5Ge_3}$ entorno a los $\sim$ 15 K, obteniendo valores comparables con los de otros compuestos intermetálicos. Utilizando la bondad del ajuste, extrapolamos la velocidad teórica hacia campos magnéticos elevados y encontramos la posibilidad de que ésta iguale o supere la velocidad del sonido en el material. Es decir, la posibilidad de pasar de deflagraciones magnéticas a detonaciones magnéticas. Lo más remarcable es que esta posible transición se observa en la extrapolación para campos menores de 50 kOe. Esto quiere decir que, en principio, reduciendo la temperatura a decenas de milikelvin (evitando así deflagraciones espontáneas antes de llegar a los campos elevados), podríamos ser capaces de obtener medidas de dicha transición. Sin embargo, tal como se muestra en el desarrollo del último capítulo de la tesis, el estudio de las deflagraciones espontáneas en función de la temperatura llevado a cabo en un criostato de dilución, en el que se alcanzan temperaturas de hasta $\sim$ 30 mK, resultó un claro ejemplo de serendipia. En vez de alcanzar velocidades supersónicas, lo que encontré fueron unas discontinuidades de salto en los campos de deflagración espontánea no predichas. Por lo tanto, el capitulo pasa a enfocarse en su estudio, concluyendo que su origen está relacionado con propiedades intrínsecas del $\mathrm{Nd_5Ge_3}$, más concretamente propongo que están directamente relacionadas con una gran anisotropía en las propiedades de transporte de la muestra.

Para terminar, en las conclusiones generales de esta tesis menciono qué creo que debería seguir investigándose en este material (no solo en lo referente a deflagraciones) y propongo una lista de materiales en los que creo que podrían encontrarse también deflagraciones magnéticas. Espero que esta tesis abra el camino para el estudio exhaustivo de las deflagraciones magnéticas en una amplia familia de materiales ferromagnéticos, y espero que dichos estudios puedan llevarse a cabo utilizando avanzadas técnicas magneto-ópticas.

CHAPTER 1

Introduction

The goal pursued in this thesis is to study the magnetic deflagration phenomenon in two very different magnetic systems, using two very different experimental techniques.

In the first section of this introductory chapter I present the general concept of deflagration in a magnetic system, setting the theoretical framework, and present the state of the art of the field. The second and last section of the chapter is devoted to the description of the structure of the thesis, highlighting the motivations, and the consequences of the results obtained, in each part.

1.1 The magnetic deflagration

The propagation of a combustion front at subsonic speeds driven by the transfer of heat is what is known as deflagration. One associates combustion with fire because it is in our daily live, but fire is only a type of combustion, a fast, glowing and high-temperature one. As combustion is defined as a reaction between a fuel and an oxidant that produces heat (exothermic) and a conversion of chemical species, one should expect as well the existence of slow and low-temperature combustion processes [1]. This is the case of the combustion of solid materials which can be sustained without a flame, as it happens in coal among many solids. It is possible to have a combustion without involving chemical reactions? The answer is yes. Imagine a process where a system (fuel) is in a metastable state (oxidable) and receives enough energy to relax to its stable state (oxidized) with the consequent release of energy. This is nothing but a general definition of the combustion process where many systems can fit.

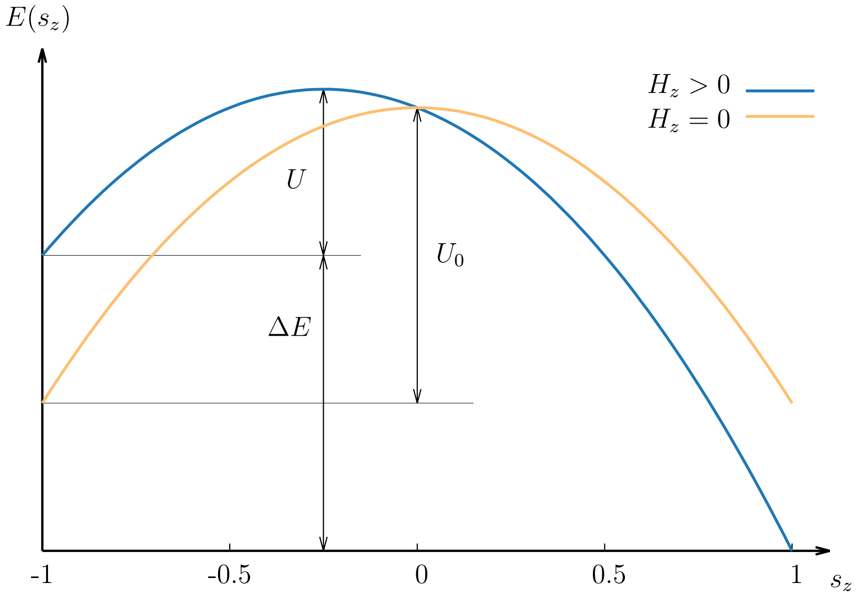

Figure 1.1: Energy profiles of a magnetic system defined by a classical spin $\vec{s} = \vec{S}/S$ in the presence of a magnetic field H_z. The terms U, ΔE and U_0 represent, respectively, the energy barrier to overcome for a system with $s_z = -1$, the energy released of a system going from $s_z = -1$ to $s_z = +1$, and the energy barrier without an external magnetic field.

But combustion does not imply deflagration. The two main words in the definition of the deflagration process are *propagation* and *front*. Imagine again the system in the metastable state, surrounded by copies of the same system, all in the same metastable state. Imagine the system "pushed" towards the equilibrium state and the energy released in this process. Let us assume that the systems are in perfect thermal contact, and that the energy released is enough to make its first neighbors relax to the equilibrium. Now start again and you'll have all the ingredients of a deflagration: propagation of a combustion front driven by the transfer of heat.

1.1.1 Theoretical framework

Let us stop imaging abstract systems. Consider a magnetic system defined by a classic magnetic moment, $\vec{m} = g\mu_B\vec{S}$, and an uniaxial anisotropy, in the presence of a magnetic field parallel to the easy direction of magnetization H_z, governed by the Hamiltonian

$$\mathcal{H} = -DS_z^2 - g\mu_B H_z S_z, \tag{1.1}$$

where $D > 0$ is the axial anisotropy constant, g is the Landé factor and μ_B is the Bohr magneton, and S_z is the projection of $\vec{S}$ in the direction z. The second term in this Hamiltonian is due to the Zeeman effect, which breaks the degeneracy of the $\pm S$ states. The energy of this system follows

$$E = -(s_z^2 + 2hs_z)U_0, \tag{1.2}$$

with

$$U_0 = DS^2 \tag{1.3}$$

being the energy barrier without an external magnetic field, with

$$h = \frac{g\mu_B H_z}{2DS} \tag{1.4}$$

the reduced field bias, and $s_z = S_z/S$.

Studying the evolution of the minima at $s_z = \pm 1$ as a function of h, we can see the barrier that a system in the $s_z = -1$ state under a magnetic field $h > 0$ has to overcome (see Fig. 1.1) is

$$U = U_0(1-h)^2, \tag{1.5}$$

and the energy difference between the two minima is

$$\Delta E = 4hU_0, \tag{1.6}$$

which can also be represented as

$$\Delta E = g\mu_B H \Delta S_z. \tag{1.7}$$

It is easy to see that an applied magnetic field $H_a = \frac{2DS}{g\mu_B}$ brings the barrier U to 0. This field is called anisotropy field, H_a.

What is the role of temperature in the dynamics of this system? We can understand temperature as positive energy, so we find another way to effectively "destroy" the barrier U and promote the system to the lowest energy state ($s_z = +1$), even in the case of $0 \lesssim H < H_\mathrm{a}$. It is the ratio U/k_BT (being k_B the Boltzmann constant) what determines if the system reaches the thermodynamic equilibrium faster or slowly. In the high temperature case $U/k_BT \approx 0$ the system will "jump" to the thermal equilibrium state making $s_z = +1$, while in the low temperature case $U/k_BT \gg 1$ the system will be out of thermal equilibrium and the state will remain $s_z = -1$ for a long time.

The dependence of the transition rate between the two minima in energy with the temperature follows the well known classical Arrhenius' equation

$$\Gamma = \Gamma_{s_z=-1} + \Gamma_{s_z=+1} = \Gamma_0 \exp\left[-\frac{U(H)}{k_BT}\right] + \Gamma_0 \exp\left[-\frac{U(H)+\Delta E(H)}{k_BT}\right], \tag{1.8}$$

which accounts for the two different energy barriers due to the bias field, with Γ_0 being the called attempt frequency, that depends on microscopic properties like the gyromagnetic ratio and the damping constant [2], and is usually considered constant with field and temperature with values between 10^7–10^{11} Hz depending on the material.

In the case where $\Delta E \gg k_B T$, the system can not return to the original state ($s_z = -1$) once jumped over U barrier. We will call this scenario, when the system has crossed its Rubicon, the "burned state", in the sense that no more net energy can be released by this system, like the wood ashes in a campfire.

Now consider an ensemble of n copies of this system in the presence of a magnetic field parallel to the easy axis of the system. Let us suppose they form a crystal in three dimensions, and remain magnetically independent, so the equations presented before apply to the hole new system. When the n_i system makes a transition from the metastable $s_{i,z} = -1$ to the absolute energy minimum $s_{i,z} = +1$ the energy ΔE_i is released. The crystal, due its finite heat capacity, will thermalize this energy by raising its temperature following the relation

$$\Delta E = \int_{T_i}^{T_f} C_p(T) \mathrm{d}T. \tag{1.9}$$

If $U/k_B T \gg 1$, at a precise moment only a very small number of the n copies will release heat (due to the negative exponential dependence in $U/k_B T$), and the crystal will be able to accommodate that heat creating a smooth temperature profile, with the highest temperature at the center of the sample and the temperature equal to the bath at the surface, as it happens in any system with a internal heat production immersed in a thermal bath. But if the crystal can not dissipate the heat released by the increasing relaxation rate, then the smooth and steady temperature profile becomes unstable and a narrow high-temperature burning front appears and propagates across the crystal. The magnetic deflagration is started.

It is obvious that the conditions of a deflagration spontaneously ignited will depend on the next factors: the bath temperature, the crystal size and shape, its thermal properties and how far the system is from the equilibrium. Thus there are two rates involved in the condition of deflagration: how fast the heat is generated, and how fast is diffused. The rate of heat diffusion Γ_d is proportional to the thermal diffusivity κ and inversely proportional to the lateral surface of the heat front of width δ, i. e.,

$$\Gamma_\mathrm{d} \sim \kappa/\delta^2, \tag{1.10}$$

while the heat generation rate Γ_g is given in the equation (1.8), in this case with $\Delta E/k_B T \gg 1$ (we will consider this case from now on). Once the deflagration front is formed and propagating, both rates can be considered equal, and therefore the width of the deflagration front (flame) will be

$$\delta \simeq \sqrt{\frac{\kappa}{\Gamma_{\mathrm{g}}}}. \tag{1.11}$$

We can define a speed of the deflagration front considering that the front "burns" a crystal "slice" of width δ during a time Γ_{g}^{-1}, and then moves to the next unburned slice and so on. The speed of the deflagration front is then

$$v_{\mathrm{d}} \equiv \frac{\delta}{\Gamma_{\mathrm{g}}^{-1}} \simeq \sqrt{\kappa \Gamma_{\mathrm{g}}}. \tag{1.12}$$

As we have seen (Eq. (1.8)) the rate of relaxation Γ_{g} is essentially a function of H and T. In the case of the relaxation of a magnetic system located inside the front of deflagration we should use the right temperature in the expression of the relaxation rate, let us name the temperature of the front (or the temperature of the flame) as T_{f}, which is another of the characteristic parameters of the deflagration front. So then, one should expect that the speed of the deflagration front on a crystal made of identical magnetic systems governed by the Hamiltonian shown in Eq. (1.1) follows the relation:

$$v \simeq \sqrt{\kappa \Gamma_0} \exp\left[-\frac{U_0(1-h)^2}{2k_B T_{\mathrm{f}}}\right]. \tag{1.13}$$

A more rigorous derivation of the expression of the speed will come in the following chapter, where a detailed study of the deflagration threshold and the temperature of the flame will be presented. But for the purpose of this section this straight derivation is sufficient.

We have focused on a magnetic system to obtain the expressions involved in the deflagration process, but the functional dependence is still valid for any deflagration process, magnetic or chemical. As a matter of fact, the analogy of magnetic deflagration with burning of a flammable substance has been confirmed by the study of the dependence of the flame speed on the energy barrier. Comparing both scenarios, chemical and magnetic, is easy to one to realize the great advantages of studying the properties of deflagrations in magnetic systems rather than in chemical, because, opposite to the later, in the former the barrier can be tuned and the process is of a reversible nature.

1.1.2 State of the art of the field

Deflagration phenomena in the reversal of magnetization has been reported in molecular magnets, Mn_{12}−ac and Fe_8 (Ref. [3] and references therein, and Ref. [4], respectively). This phenomenon is also found in systems with abrupt magnetic phase transitions. Deflagration in metamagnetic transitions has been observed first in manganites [5–7], and later in the intermetallic compound Gd_5Ge_4 (Ref. [8, 9]), where the metamagnetic transition is induced by a change in the crystallographic structure.

As magnetic deflagrations can appear spontaneously when one of the experimental parameters under control is changed (namely temperature, magnetic field, pressure, etc.) the experimental investigation of the laws of the spontaneous deflagration phenomenon is rather limited. However, different techniques have been developed to trigger the occurrence of magnetic deflagrations under desirable conditions, leading to the precise test of the theoretical laws. These triggers consist basically in sending controlled heat pulses to the sample. Those heat pulses act as a spark that ignites the deflagration process. Attached resistors [10–12], electrical contacts made on the sample [8], or surface acoustic waves (SAW) [5, 13] are examples of sources that can be used for this purpose.

Simultaneously to the occurrence of the deflagration phenomenon, other effects related to the magnetic and crystallographic properties of those materials have been also observed. Quantum properties of the deflagration phenomenon were observed in the dynamics of the process in Mn_{12}−ac [10, 13, 14] and in Fe_8 [4]. Either the speed, the ignition time or the ignition threshold exhibit signatures related to the resonant quantum tunneling of the magnetic moment. In pulsed magnetic field experiments, a deflagration-to-detonation transition was suggested to occur [15]. In manganese based oxides, the AFM→FM phase transition is accompanied by very fast colossal changes in the magnetoresistance (at times of the order of tens of microseconds) and with percolation effects even with no avalanche. This is because the AFM phase is charge ordered and insulating, whereas the FM one is metallic charge-delocalized. Finally, in Gd_5Ge_4, the AFM→FM phase transition is accompanied by a change in the crystallographic structure. Whereas the AFM state crystallizes in the O(I) low volume orthorhombic polymorph form, the FM one crystallizes in the O(II) high-volume form [16]. Nevertheless up to the date where the results shown in this thesis were presented, no experimental evidence had been observed of deflagration phenomena within a FM state, nor in both AFM and FM phases of a single system.

1.2 The structure of this thesis

Since every chapter begins with a short introduction, in this section I will just highlight the main aspects of the thesis.

In the second chapter of this thesis I will present the study of magnetic deflagration in single crystals of the prototypical single molecule magnet Mn_{12}−ac, using the magneto-optical imaging method, never done before. Theses measurements were performed in collaboration with Dr. Wijngaarden, from the Vrije Universiteit Amsterdam. In the chapter the reader will find out that, effectively, the deflagration process can be explored using this technique. However, by the end of the chapter I will show how some of the experiments revealed hidden experimental limitations, which should be solved in order to extend the experiments in detail. It is worth to mention that my contribution to this experiment required the use of new tools, like scriptable image and video processing software.

The second part of the thesis include the other five chapters. Such a difference in length between both parts is due two factors. The first factor is that the Mn_{12}−ac is a very well known system, with few new experiments to study (I know, one never should say this); while on the contrary, the Nd_5Ge_3 intermetallic compound has been barely studied in its single crystalline form, and therefore there are many experiments to conduct to understand its dynamics. The second factor that explains the difference in length is the rich phenomena that this intermetallic compound presents directly related with the abrupt magnetic changes that possesses. As the reader will see, in this system sudden changes occur in every studied physical property when the magnetization changes in a stepped manner. Motivated by the magnetic deflagration phenomena reported in the metamagnetic antiferromagnetic to ferromagnetic (AFM→FM) transition of the intermetallic compound Gd_5Ge_4, we found in Nd_5Ge_3 the perfect candidate to extend definitively the study of magnetic deflagrations beyond the realm of the single molecule magnets. Two fundamental properties of the magnetic dynamics of the Nd_5Ge_3 system make it so remarkable. First, it is one of few systems with a large irreversible AFM→FM transition induced by the magnetic field, and second, the magnetic changes during its magnetization processes occur in a stepped manner. Therefore, the motivation to investigate the possibility of finding for the first time magnetic deflagration phenomena in a ferromagnet, and also for the first time in two different magnetic phases of a given material, was very high.

In the first two chapters dedicated to the Nd_5Ge_3 I explore the magnetic properties, the heat capacity and the electric resistivity. Some of the measurements were not previously reported in a single crystal. In the fourth chapter I explore explicitly the spontaneous field-induced avalanches in magnetism, heat capacity and resistivity. The reason of this three chapters is to have as much ingredients as possible to be able to answer the questions that the possible magnetic deflagrations would raise. I say possible because it is not until the fifth chapter of this thesis when we get the experimental confirmation that the field-induced spontaneous avalanches that the compound present correspond to magnetic deflagration phenomena. In this chapter the magnetic deflagrations were studied in detail in the AFM→FM transition and in the FM reversal, as a function of the magnetic field and the temperature. Using a dedicated setup of pick-up coils and resistors the spontaneous and induced deflagrations are explored, obtaining good estimations of the propagation speed and the temperature of the deflagration flame. Using the theoretical framework of the magnetic deflagrations we fit the speed propagation of the front to the experimental data using only one parameter, the heat diffusivity of the material; obtaining a value within the range of heat diffusivities found in other intermetallic compounds.

In the last chapter, extrapolating the results obtained in the induced deflagrations at 2 K, I tried to reach a supersonic propagation regime lowering the temperature of the system to tens of millikelvins. The experiments were performed in a $^3\mathrm{He}-^4\mathrm{He}$ dilution refrigerator. Nevertheless, while the theoretical curve pointed the possibility of the occurrence of magnetic detonations, I found a totally unexpected behaviour. As the temperature was lowered, different reproducible jump discontinuities appear in the spontaneous magnetic field. In the chapter different explanations are considered, but the fact that the discontinuities appeared as well measuring in a very different cryostat, took me to interpret them as an intrinsic property of the Nd_5Ge_3. That would imply some hallmarks in the voltage signals induced in the surrounding coils. Effectively, the whole set of spontaneous deflagrations was scrutinized, resulting in the hypothesis that the system possess very anisotropic heat transport properties, which derive in highly anisotropic magnetic deflagration fronts.

As the reader will see through this dissertation I investigate moved by the pressing need of understanding every little detail of an experiment. I do not find any other reason to do this job. I know that I will not have all the answers but I never surrender. I love to learn, I love to discover, I love to understand. I wish to be able to transmit this feelings to the reader.

CHAPTER 2

Magneto-optical imaging of magnetic deflagration

In this chapter I present the first experimental study of magnetic deflagrations using the magneto-optical technique. I will first introduce the magnetic properties and the concepts of magnetic deflagration of the single molecule magnet $Mn_{12}-$acetate. After the introductory part I will present the state of the art of the magnetic deflagrations in this compound, right before describing the theoretical and experimental framework of the magneto-optical measurements. The last part of the chapter is devoted to the analysis and discussion of the results that I obtained in the experiments.

2.1 The Mn_{12}-ac single-molecule magnet and its dynamics

In this section we will present one of the most known and studied molecular magnets, and the subject on the first part of this thesis, the Mn_{12}-acetate. Its magnetic structure and dynamics will be introduced focusing on the properties relevant to the study of magnetic deflagrations.

While it was first synthesized in 1980 by T. Lis [17], who already pointed that this molecule should have interesting magnetic properties, it was more than ten years later, in early 90s, when some of this interesting properties start to be revealed, like the giant molecular spin of $S = 10$ [18] and its magnetic bistability [19]. In the next few years a great interest was devoted on this system, becoming the seed of a completely new discipline in magnetism, the single-molecule magnets (SMMs), where the entire magnet can be understood basically from the properties

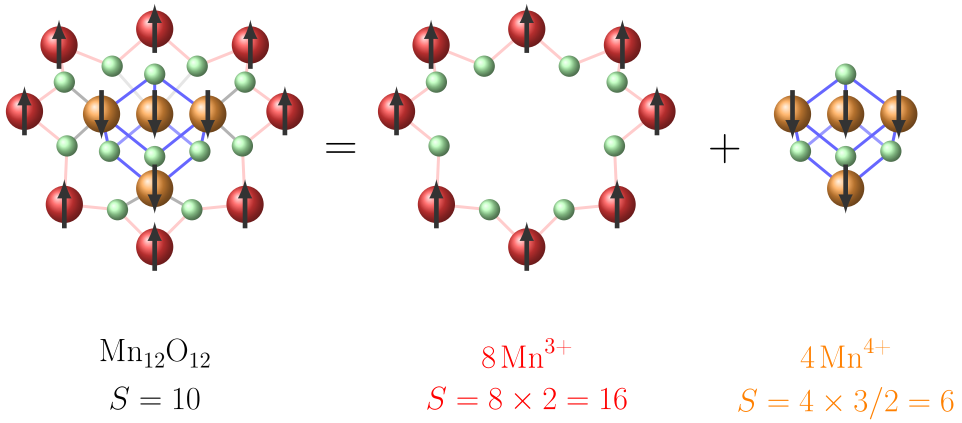

Figure 2.1: The $Mn_{12}O_{12}$ core (on the left), comprised of an inner $[Mn_4^{4+}O_4]^{8+}$ cubane (on the right) that is surrounded by a ring of eight Mn^{3+} ions held together by eight O^{2-} ions (on the center). Manganese atoms Mn^{3+} and Mn^{4+} are represented in red and orange, respectively; oxygen atoms are represented in green color. The spins in both substructures are coupled parallel, while between substructures the spins are coupled antiparallel.

of one molecule, providing the possibility to observe macroscopic quantum effects without needing new types of experiments nor technologies, e. g., the steps at regular intervals of applied field in the hysteresis loops of Mn_{12} [20–24]. Some of the relevant work on this SMM was performed by our group, including the first experimental evidences of the macroscopic tunneling of the magnetization.

2.1.1 The Mn_{12}-ac molecule

The Mn_{12}-acetate, or Mn_{12}-ac, or simply abbreviated Mn_{12}, is a complex metalorganic compound with the chemical formula $(Mn_{12}O_{12}(CH_3COO)_{16}(H_2O)_4)$. The core of a molecule of Mn_{12}-ac is comprised of an inner $[Mn_4^{4+}O_4]^{8+}$ cubane, surrounded by a ring of eight Mn^{3+} ions held together by eight O^{2-} ions (see Fig. 2.1). The residual free sites of the manganese ions are occupied with eight axial and eight equatorial acetate ligands and four water molecules.

The intramolecular coupling of magnetic ions is mediated by indirect exchange through oxygens. The eight spins of the Mn^{3+} ($S = 2$) are ferromagnetically coupled giving a spin of $S = 8 \times 2 = 16$; the four Mn^{4+} ions are also ferromagnetically coupled with an spin $S = 3/2$ per ion, resulting $S = 6$; nevertheless, the coupling between ions of different substructures is antiferromagnetic. Therefore, the total spin of the Mn_{12}-ac is $S = 10$. The magnetic coupling between ions was determined by X-ray magnetic circular dichroism (XMCD) [25] and the total spin was proven by means of electron paramagnetic resonance (EPR) [18]. This magnetic structure corresponds to the ground state and remains up to temperatures above 50 K, meaning that for lower temperatures the interactions between manganese ions can be ignored and the molecule can be treated as a unique rigid entity with spin $S = 10$.

The Mn_{12}-ac crystallizes in a tetragonal lattice as it has been determined by X-ray characterization with lattice parameters $a = b = 1.732$ nm and $c = 1.239$ nm. As the cluster is surrounded by a considerably large shell of acetates and water molecules, the magnetic cores fall apart between each other in the crystalline structure leading a negligible intermolecular magnetic interaction. The crystallization aligns the easy axes (c) of the molecules (Fig. 2.2) along the growing axes of the crystal —this fact will be very convenient as we will see later on. Due to the symmetry of the lattice and the symmetry of the Mn_{12}-ac molecule the resulting magnet posses a large anisotropy. This is one of the key properties that have made this SMM so important, because it has one of the larger, if not the largest, anisotropy barrier. The experimental measurements show that the anisotropy field is $\mu_0 H_\mathrm{a} \approx 10$ T. From this one can calculate the energy barrier at zero-bias and the anisotropy constant (Eq. (1.2)–(1.4)):

$$H_\mathrm{a} = \frac{2DS}{g\mu_B} \Longrightarrow \begin{cases} D \simeq 0.6 \text{ K} \\ U_0 = DS^2 \simeq 60 \text{ K} \end{cases} , \tag{2.1}$$

where the value of the gyromagnetic factor used g is 1.9, based on EPR experiments [18].

2.1.2 Magnetic properties of Mn_{12}-ac

The magnetic properties of the Mn_{12}-ac relay basically on the magnetic properties of the $Mn_{12}O_{12}$ core, and the effects of the ligands on the magnetism of the system can be ignored in a first approximation. Nevertheless, in order to completely understand its magnetic properties one has to take into account the effects that the ligands can have on the magnetic core properties like symmetry properties, oxidation levels etc. Taking this effects into account is crucial when comparing molecules with the same core ($Mn_{12}O_{12}$) but different ligands, like, for instance, other carboxylic acids instead of acetate.

As we have seen in the previous section, the $Mn_{12}O_{12}$ spin is the sum of the spins of the 4 manganese ions of the inner cubane and the spins of the 8 manganese ions of outer ring. The spin of the core is the result of the addition of the ferromagnetic coupling between ions belonging to the same substructure and the antiferromagnetic coupling between ions of different substructures. Another

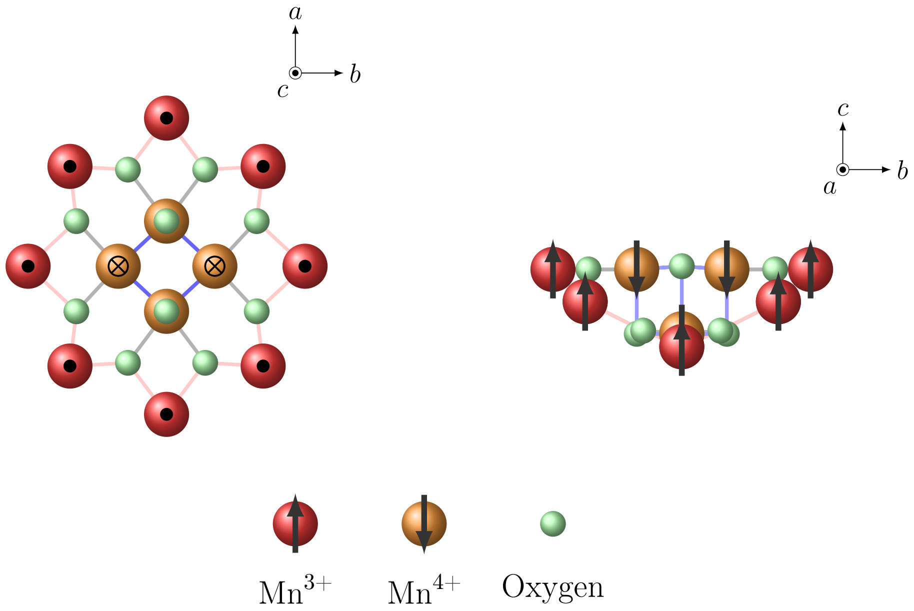

Figure 2.2: Projections of the $Mn_{12}O_{12}$ core. On the left the core is viewed along the easy axis c; on the right is viewed perpendicular to the easy axis.

remarkable property of this molecule is the presence of a strong Jahn-Teller distortion in the of Mn^{3+} ions [17] which results in a large uniaxial anisotropy in the molecule. The first approximation, therefore, is to describe the system with the Hamiltonian of one spin S in an uniaxial anisotropy lattice

$$\mathcal{H} = -DS_z^2 - g\mu_B \vec{S} \cdot \vec{H}, \tag{2.2}$$

where the term $g\mu_B \vec{S} \cdot \vec{H}$ is the Zeeman term (this equation is a generalization of Eq. 1.1). Higher order anisotropy terms as the dipolar and hyperfine terms are omitted in this first approximation. Considering only the longitudinal term (parallel to the easy axis c oriented along z), the Hamiltonian commutes with S_z and we can choose $|m\rangle$ eigenstates of the S_z operator as a basis. Therefore the energy levels of this system follow the relation

$$E_m = -Dm^2 - g\mu_B H_z m, \tag{2.3}$$

with m being the discrete projection of the magnetization defined by $-S \leq m \leq S$. Thus, the number of possible magnetization states is $21 = (2 \times 10 + 1)$. The energy profile is two-wells with energy levels stacking decreasing the absolute value of m, as the $m = \pm S$ levels are the lowest energy levels. In the figure 2.3 we can see the energy levels and its dependence on the longitudinal applied field. In the absence

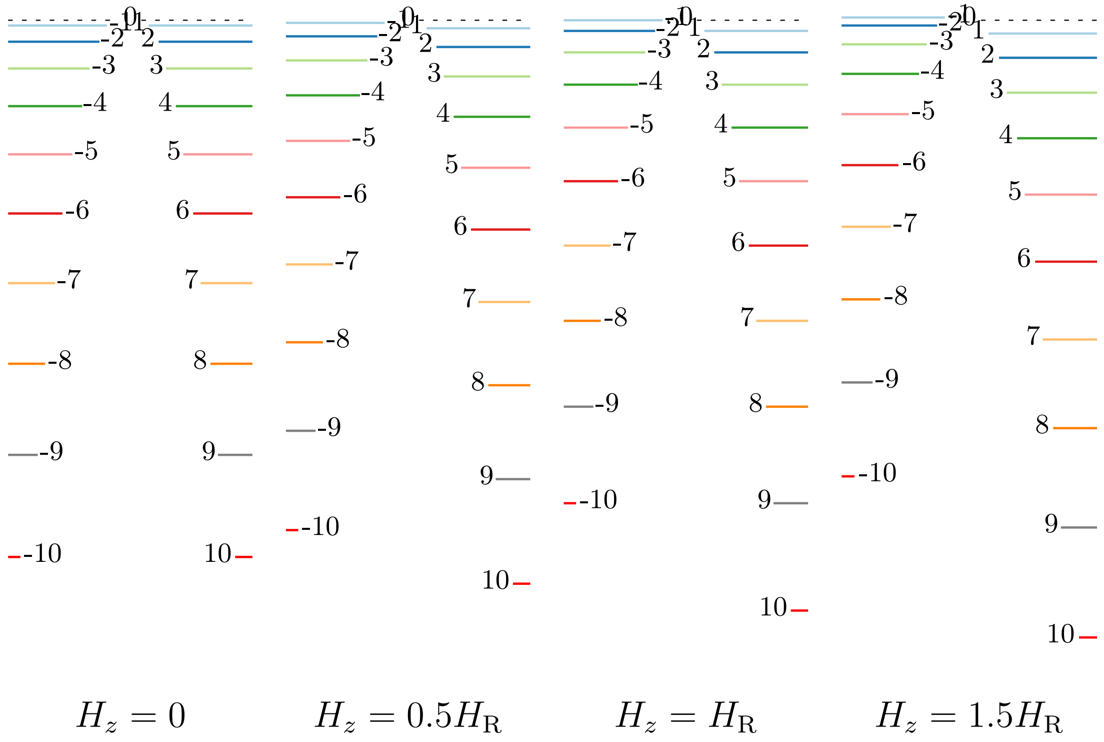

Figure 2.3: Spin energy levels of the Mn$_{12}$ molecule (defined with Eq. (2.2)). Different realizations are shown as a function of a positive longitudinal external field, increasing field from left to right. When the relation of the external field and the resonant field is an integer n the system is resonance and the levels m & $m' = -m - n$ will be degenerated.

of external field the energy levels are degenerated as $E_m = E_{-m}$, so the energy levels are in resonance.

The effect of the longitudinal applied field is the rupture of the degeneracy, but for specific values of H_z the degeneracy appears again so $E_m = E_{-m-n}$ (Fig. 2.3, 3rd from the left). The values of H_z for that to happen are

$$H_{z,n} = nH_\mathrm{R} = n\frac{D}{g\mu_B}, \tag{2.4}$$

being n a integer number. Is important to remark that $H_{z,n}$ does neither depend on m nor on m', which implies the degeneracy of all the “degenerable” levels at the same time, as can be seen in the figure mentioned above.

Now we can consider the case where a perpendicular magnetic field is present:

$$\mathcal{H} = -DS_z^2 - g\mu_B(H_zS_z + H_xS_x). \tag{2.5}$$

The main consequence is that, due to the new x term, S_z does not commute with the Hamiltonian, so m is no longer a conserved quantum number. As a perturbation, this term mixes the degenerated states $|m\rangle$, which can now tunnel under the barrier to states of the same energy. Thus, taking into account this term, the degeneracy is removed due to the mixing of states and the system can change its spin m to m' on the other side of the energy barrier without the needing of overcome it energetically. This is one of the most important features of the system and will be explored along this chapter.

The splitting of the levels due to the mixing term was calculated by D. Garanin in 1991 [26]. His formula for the energetic splitting between symmetric and antisymmetric m states at the nth resonance $(m, -m+n)$ is:

$$\Delta_m^n = \frac{2D}{[(2m-n-1)!]^2} \left(\frac{(S+m-n)!(S+m)!}{(S-m)!(S-m+n)!} \right)^{1/2} \left(\frac{g\mu_B H_x}{2D} \right)^{2m-n} . \tag{2.6}$$

This quantum tunneling behavior has been observed in experiments even at zero external magnetic field —when crossing the $\vec{H}=0$ in a hysteresis loop a enhancement of the relaxation rate. This is now obvious looking the equation above. Imposing $H_z = 0$ $(n = 0)$, we can easily obtain the splitting of the energy levels at zero longitudinal field

$$\Delta_m^0 = \frac{2D}{[(2m-1)!]^2} \frac{(S+m)!}{(S-m)!} \left(\frac{g\mu_B H_x}{2D} \right)^{2m} , \tag{2.7}$$

that we can write in terms of the anisotropy field H_a

$$\Delta_m^0 = \frac{2D}{[(2m-1)!]^2} \frac{(S+m)!}{(S-m)!} \left(S\frac{H_x}{H_\mathrm{a}} \right)^{2m} . \tag{2.8}$$

It is easy to see how that, due to $SH_x/H_\mathrm{a} \ll 1$, the splitting between levels m and $-m$ grows as decreasing the value of m. This feature can be seen in figure 2.4 at zero longitudinal field. As we just said, the change in magnetization at zero field was found not to be zero in experiments at very low temperature (where the possibility of overcoming the barrier thermally is forbidden), meaning that there are some internal fields that actually break the degeneracy: the dipolar and hyperfine. In the case of Mn_{12} both fields are of the same order ($\sim 10^2$ Oe) [27].

In the figure 2.4 one can also see how at zero field (left hand side of the figure) the splitting is not large enough to, in the time of a typical experiment, allow the real mixing of states, and then the population of the $S=-10$ level remains. Obviously this situation is not stable and the system must be prepared in order to be in this state.

The role of temperature on the dynamics of the magnetization of a SMM, with discrete spin energy levels and in the presence of a splitting term, is represented in

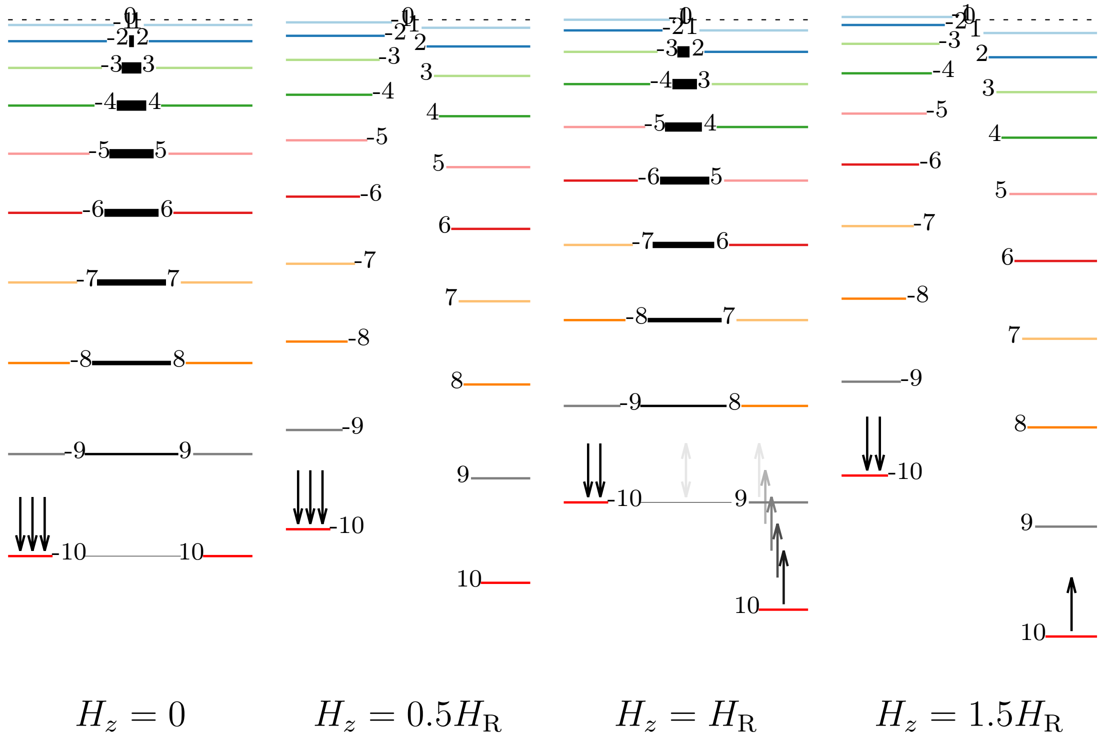

Figure 2.4: At zero temperature, with the SMM prepared in the $S = -10$ state, in the presence of a perturbative field in the perpendicular direction, the energy profile and the population of levels are presented as a function of an external positive longitudinal field. The black lines connecting energy levels on both sides of the barrier represent the energy splitting due to the perpendicular field; and width reflects the amplitude, increasing as levels with lower m are mixed. From left to right, the system is prepared with all the molecules with $S = -10$, the field is raised up to the first resonant field (third sketch) where some molecules tunnel its magnetic moment which relax to the equilibrium state via spin-phonon interaction, and the field is increased out of the resonant condition.

the figure 2.5. Actually, this figure is only representative of the case where $T \ll T_B$, where T_B is known as the blocking temperature, that defines the temperature where in the measurement time the system has been able to overcome thermally the energy barrier, as follows from the Arrhenius law (1.8). It worths to mention that, obviously, for shorter measurement times the blocking temperature will be higher, e. g., if we were able to measure the spin state of a system with a barrier U in a infinitely small time, the blocking temperature associated would be infinite, i. e., we will see the spin blocked in one state. When the measurements are

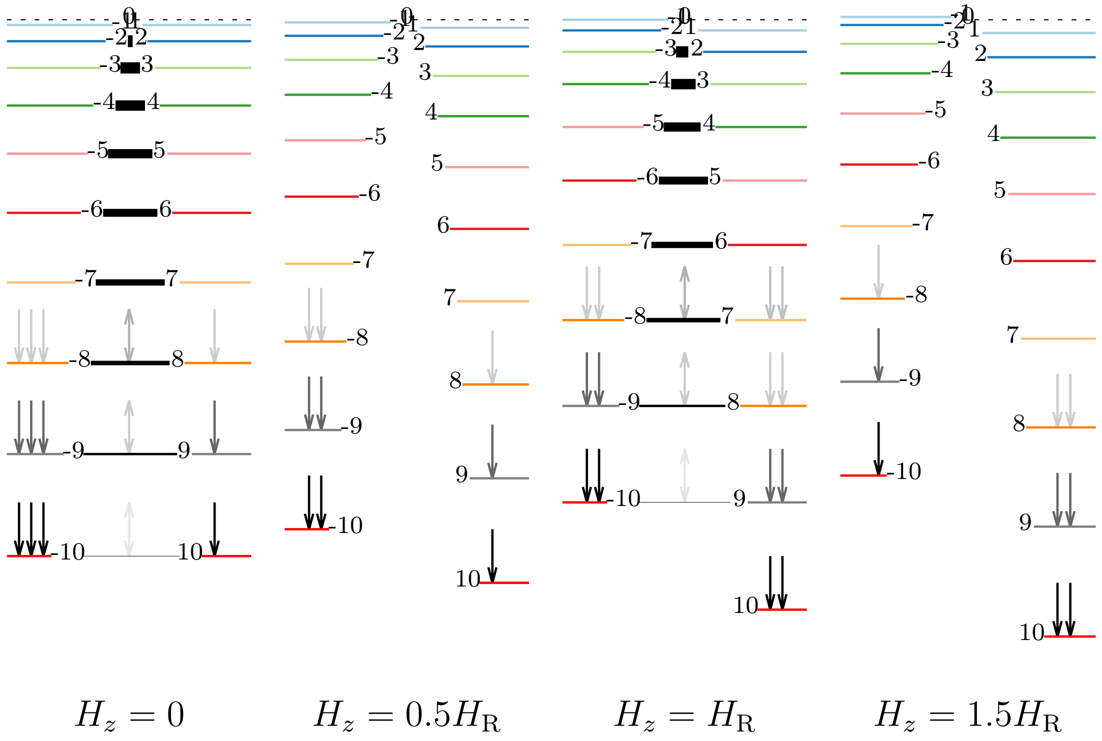

Figure 2.5: At $0 < T \ll T_B$ the evolution of the population of the levels of a system prepared in the $S = -10$ state as a function of an applied external magnetic field is showed. From left to right the applied magnetic field is raised. The darkness of an arrow representing the state of a molecule of Mn_{12} accounts for the Boltzmann probability of occupancy (given by the Arrhenius law) and for the splitting amplitude.

carried out on a comercial magnetometer the measurement times are of the range $\sim 10 - 10^2$ s, and when people talk about blocking temperature, it refers to this type of measurements. We can define the blocking temperature:

$$T_B = \frac{U}{\ln\left(t_\mathrm{meas}\Gamma_0\right)}, \tag{2.9}$$

where t_meas is the measuring time. One way to determine the blocking temperature of a system is to measure the magnetization dependence on temperature via zero-field-cooled field-cooled (ZFC-FC) processes. The ZFC process consists in cooling down the system at zero-field to the lowest possible temperature T_i, then apply a magnetic field and measure the magnetization as the temperature is raised to T_f. The FC process can be performed in two ways: without turning off the magnetic

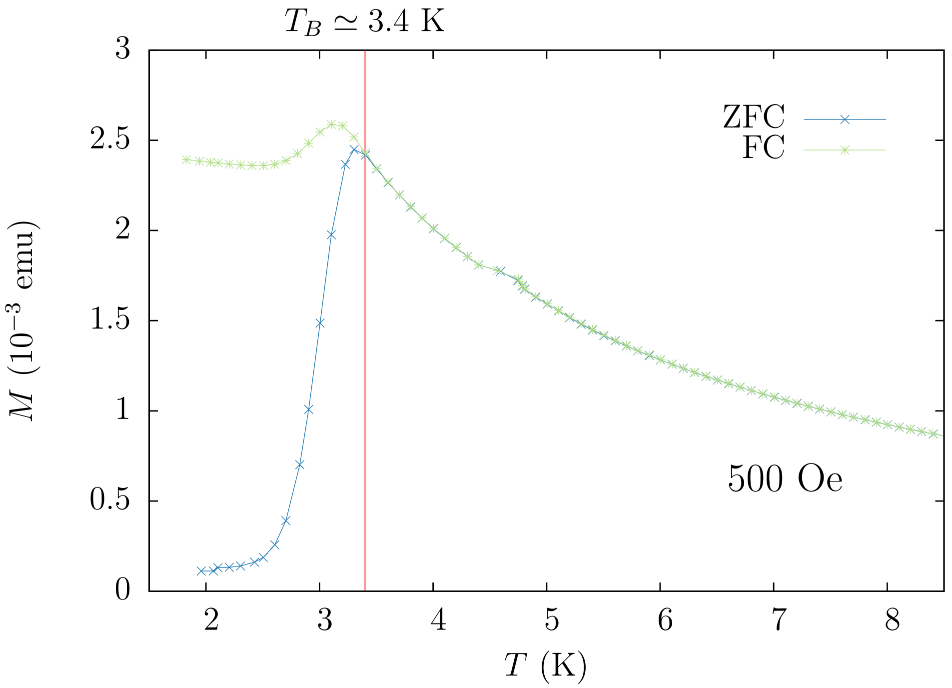

Figure 2.6: ZFC-FC measurement in a single crystal of Mn_{12}-ac. The blocking temperature T_B is defined in this kind of systems (a collection of identical energy barriers, with no interaction between them) as the temperature above which the system presents no hysteresis, i. e., where the ZFC and FC curves coincide; in this case $T_B \simeq 3.4$ K.

field the temperature is lowered to T_i and the magnetization is measured increasing the temperature, which is known as field-cooled warming process (FCW); or, measuring the magnetization as the temperature is decreased from T_f to T_i, which is known as field-cooled cooling process (FCC). Unless stated otherwise, the common ZFC-FC is a ZFC-FCC. In the figure 2.6 a ZFC-FC measure of a single crystal Mn_{12}-ac is shown. The blocking temperature of Mn_{12} is determined to be $\simeq 3.4$ K.

We have seen in Eq. (2.6) how the splitting amplitude grows rapidly as m states with lower values are considered. But while in the time of measurement of a typical hysteresis loop the tunneling probability between the ground levels ($S = \pm 10$) at 0 field can be considered zero, the experimental hysteresis loops at $T < T_B$ do show some relaxation when crossing the zero field (see Fig. 2.7); so there must be another contribution that helps the system to relax without "jumping" the barrier. This contribution comes from the temperature. The role of the temperature thus is to promote a population of levels with lower m where the tunneling probability is high enough to, in the time of measurement, cross the barrier. There is a balance

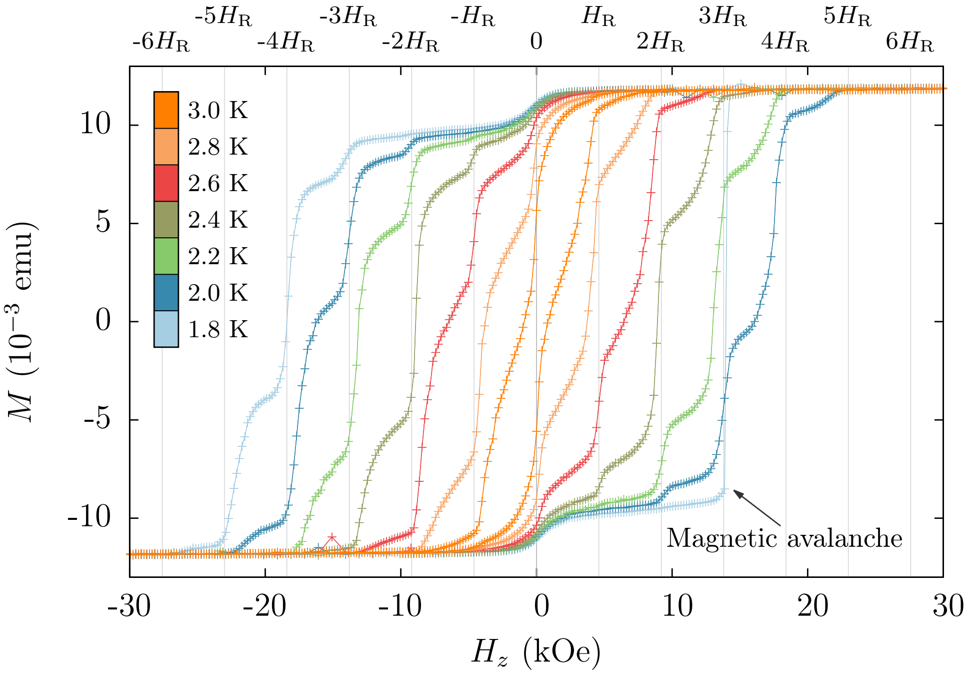

Figure 2.7: Hysteresis loops of a single crystal of Mn_{12}-ac. This behavior corresponds to the description of the figure 2.5, where the relaxation is governed by the balance between Boltzmann populations and the splitting amplitude between levels. Its important to remark the abrupt change in magnetization at 1.8 K around the 3rd resonant field: a magnetic avalanche. Measurements performed in a SQUID magnetometer (MPMS QuantumDesign) under the same field sweep rate.

between the splitting amplitude and the Boltzmann population of the levels. This phenomena is know as *thermally assisted quantum tunneling of the magnetization* (TAQTM).

Below the blocking temperature T_B the relaxation rate that we can infer from the hysteresis loops (Fig. 2.7) depends on the sweeping rate of the applied magnetic field. It is obvious that the longer one remains in resonant conditions, the larger the amount of magnetic relaxation will be. On the one hand, in a case of infinitely slow sweeping rate, the magnetization of the system would evolve to the equilibrium value determined by temperature and field conditions. On the other hand, in an scenario of a infinitely fast sweeping rate, the magnetization will be frozen at the metastable state and would only be able to evolve to the equilibrium once the barrier has disappeared, i. e., once $H_z > H_a$. In the real world of the laboratory the measurements can not be neither infinitely slow, nor infinitely fast, and that is the reason why in the hysteresis loops one can see a situation in between, where the magnetization tends to its equilibrium ($M \rightarrow M_s$) in a enhanced fashion around the resonant fields, but, as the sweeping rate is not zero, some has no time to tunnel the barrier and stays "frozen" waiting its opportunity on the next resonant field. The probability per time unit of one molecule of Mn_{12} to tunnel the barrier being at level m in the nth resonant condition is $\Gamma_{\text{tunnel}} \propto \Delta_m^n/\hbar$ ($\hbar$ is the Planck constant), but there is no information there about the case where the field H_z is being swept. The known as Landau-Zener probability takes this into account. Its theory establishes the probability of a system of two states with mixing term (Δ) to remain in the original state when a parameter that controls the equilibrium probability is swept. In our case, the probability to remain in a state m crossing the level m', under a sweeping energy rate $\nu = g\mu_B|m - m'|\frac{\mathrm{d}H_z}{\mathrm{d}t}$ (rate of variation of energy between states involved) is

$$P = \exp\left(-\frac{\pi\Delta^2}{2\hbar\nu}\right), \tag{2.10}$$

and $1 - P$ is the complementary probability of being in m' after crossing m [28: section 1.7]. Obviously this probability only accounts for a case where $T = 0$; otherwise the probability of being in m' after crossing m is strongly affected by the TAQTM.

2.1.3 Magnetic deflagration theory in molecular magnets

The transition between the metastable and the stable magnetic states, in our case from $-M_{\text{sat}}$ to M_{sat}, sometimes is found to be abrupt as we can see in the case of the positive field sweep branch at 1.8 K in the figure 2.7. This process is known as magnetic avalanche and it was first observed in Mn_{12} in 1994 by Paulsen and Park [29] while sweeping the amplitude of the magnetic field. Such avalanches reversed the magnetization of the sample within a few milliseconds and were accompanied by simultaneous spikes in the temperature measurements of the cryostat. That suggested that the avalanches were driven by the release of the Zeeman energy stored in the system and they linked this process to the propagation of a fire in a three dimensional forest.

At some point, the stochastic avalanches, considered a nuisance that used to ruin the measurement of spin tunneling, start becoming of interest. Several groups began to measure systematically magnetic avalanches in Mn_{12}-ac (our group among them), looking for their spatial and temporal properties, the quantum dependences of the phenomenon or the possibility to observe super-radiance emission (coherent collective photo-emission) (for the later take a look to, for example, the PhD thesis of Hernández-Mínguez [30]).

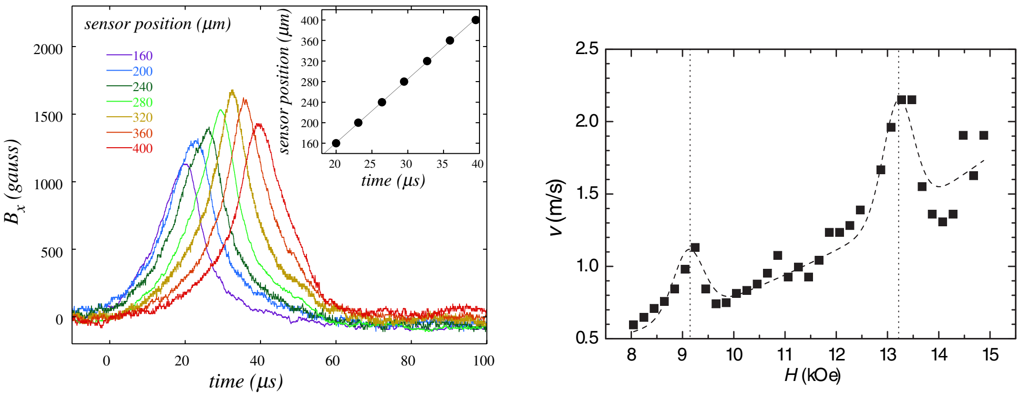

(a) Propagation of a front.

(b) Quantum imprint.

Figure 2.8: Some of the first systematic studies on the magnetic avalanches in Mn_{12}-ac. 2.8(a): Signals recorded by seven equally spaced Hall sensors during an avalanche at 4 T and 250 mK. The inset shows peak amplitude per sensor vs. time, a straight line fits to a constant propagation speed of 12 m/s (Figure extracted from [31]). 2.8(b): Magnetic deflagration speed as a function of the magnetic field. The dashed line represents the fit by Eq. (1.13). Vertical lines show the positions of 2nd and 3rd resonant fields H_R (Figure extracted from [13]).

From the studies of spatial and temporal properties performed by Suzuki et al. in 2005 [31] it was determined that the avalanche actually was like a fire propagating in a forest, with a front that moves from one starting point trough the sample (Fig. 2.8(a)), burning all the combustible material, in this case the metastable local moments. They coined the term magnetic deflagration to name the process. The stochastic nature, subsonic speed range, and dependence of the speed with the field at which the spontaneous deflagration took place were also analyzed in the same paper. On the same year, in our group, Hernández-Mínguez et al. [13] showed the quantum imprint in the deflagration speed due the thermally assisted quantum tunneling of the magnetization. This quantum behavior is observed in an enhancement of the propagation speed due to the effective reduction of the barrier because of the tunnel effect (see Fig. 2.8(b)).

To study the dependence of magnetic deflagrations with the external variables it is sometime required to avoid the randomness of the spontaneous avalanches. Therefore, one desire to be able to trigger the avalanche, to ignite the deflagration. The procedure is always the same: bring the system to a metastable state and then supply energy. Different technologic approaches to supply energy to the system have been used until now in molecular magnets: surface acoustic waves (SAWs)

[13, 32, 33] and heat pulses using attached resistors [10, 11, 29, 34, 35].

These results from spontaneous and induced avalanches led to the development in 2007 of the first theory of magnetic deflagration in single crystals of molecular magnets by Garanin and Chudnovsky [36]. Early in this chapter we have been introduced to the deflagration phenomenon in a generic magnetic system (see page 2) and now an extension to molecular magnets is presented.

In molecular magnets we will have to take into account the discrete levels of energy and the tunneling of magnetization in the study of the magnetic deflagration process. Because of the occurrence of resonant fields, the spins of the molecules in the crystal have to be thermally activated all the way up from the bottom of the metastable state[1] to the top of the barrier when the applied field is not a multiple of the resonant field H_{R}. However, when the applied field is nH_{R} a molecule only needs to be thermally activated up to the the level where the splitting is large enough to, in the time of the measurement, take its spin state to the other side of the barrier (Fig. 2.9(a)). From the experiments of Hernàndez et al. [22] and del Barco et al. [37], the effective barrier has been determined in Ref. [38] to be

$$U_{\text{eff}}(H_z) = U_0\left(1-\frac{H_z}{H_{\mathrm{a}}}\right)^2 - b\left[1-\left|\sin\left(\pi\frac{g\mu_B H_z}{D}\right)\right|\right]^2, \tag{2.11}$$

which fits the data showed in the figure 2.9(b). Actually this figure was obtained from an ensemble of oriented Mn_{12}-ac micrometrical single crystals so the values of b and H_{a} in the fit are a bit different from the values corresponding to the case of a single crystal. In this case $b \simeq 6$ (wider peaks) and the barrier is slightly harder to modify because the (small) misalignment between the easy axes of the micrometrical single crystals and the longitudinal field direction; the later translates into a less pronounced descent of the effective barrier with the applied magnetic field.

We can see in the figure 2.9(a) that due to the splitting Δ_m^n, the temperature T and the applied field H_z, how the value U represent the maximum energy barrier that a system prepared in $S=-10$ has to overcome, while the energy released ΔE is always the difference in energy between the $S=\pm 10$ states. Therefore, as the effective barrier has dips at the resonant fields we will have to study in detail the consequences on the propagation of the deflagration front.

A first requirement for having a deflagration, magnetic, chemical, or of any other kind, is to have enough fuel. In the case of magnetic deflagration the fuel is the metastable magnetization of the system. This implies that the temperature of the system before starting the deflagration must be lower enough than the blocking temperature, because otherwise the magnetization would evolve towards

---

[1] Unless stated otherwise we will consider that the system is always prepared in the $S=-10$ state and then a positive external field is applied.

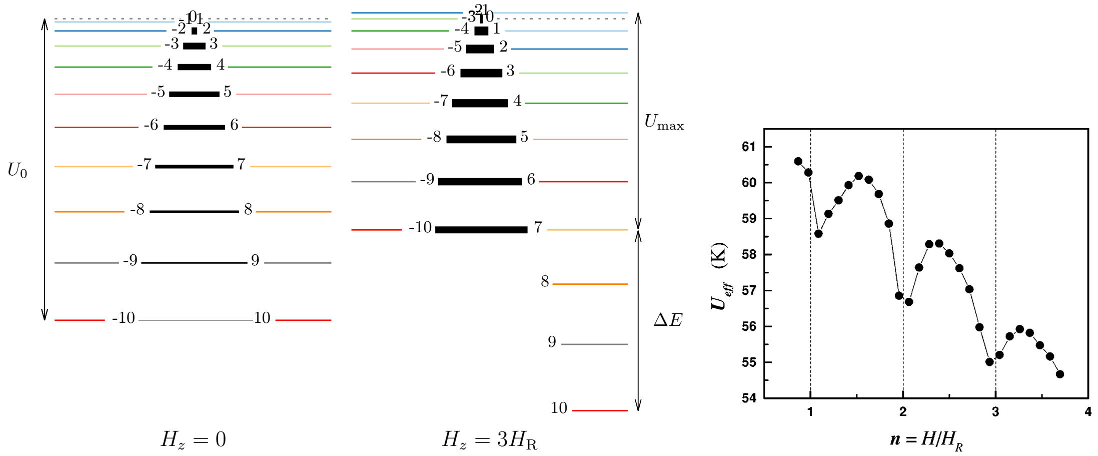

(a) Energy levels.

(b) Experimental data.

Figure 2.9: Effective barrier: 2.9(a) Spin energy levels of the Mn_{12} molecule (defined with Eq. (2.2)) under two different applied fields. 2.9(b) Experimental effective barrier vs. applied field, obtained from relaxation measurements of Ref. [22] (Figure extracted from [37]).

the stability. The Mn_{12} has a blocking temperature of 3.3 K, so it is clear that we will be dealing with very low temperatures. This has a capital importance in the case of the thermal transport because it is well known that at low temperatures, the thermal properties tend to depend strongly on the temperature, e. g., the heat capacity of phonons has the form of T^3. The specific heat of Mn_{12}-ac was first studied by Novak et al. [39] and by Gomes et al. [40]. From this measurements one can consider that other contributions to the specific heat rather than phononic are small and one can consider the heat capacity due the acoustic phonons only as

$$C_{\mathrm{ph}} = \frac{12\pi^4}{5} k_B \left(\frac{T}{\Theta_D} \right)^3 , \tag{2.12}$$

where Θ_D is the Debye temperature. The thermal diffusivity κ, defined as the ratio between thermal conductivity and heat capacity, depends on the average mean path of thermal phonons. At low temperatures the phonons are scattered mainly by impurities, implying [41]

$$\kappa \propto T^{13/3}. \tag{2.13}$$

Thus, at low temperatures, the thermal conductivity, k, dependence on temperature is $k \propto T^{4/3}$.

To understand the ignition process we need to solve the system of equations

$$\tilde{C}_{\text{ph}} \frac{\partial T}{\partial t} = \nabla \cdot k \nabla T + \Delta \tilde{E} \frac{\partial m}{\partial t}, \tag{2.14a}$$

$$\frac{\partial m}{\partial t} = -\Gamma (m - m^{\text{eq}}), \tag{2.14b}$$

where $\Delta \tilde{E} = H M_S$ is the density of magnetic energy per unit of volume, $m = M/M_S$ and $\tilde{C}_{\text{ph}}$ is the volumetric heat capacity. Both variables, m and T, are functions of $(\vec{r}, t)$ and H is an external parameter.

The first equation corresponds to the heat conduction equation with the rate of change in magnetization as source of heat ($\Delta E \frac{\partial m}{\partial t}$), while the second equation is the time evolution of the magnetization, governed by the relaxation rate Γ defined by equation (1.8), taking $\Delta E / k_B T \gg 1$ and considering U_{eff}:

$$\Gamma = \Gamma_0 \exp\left[-\frac{U_{\text{eff}}(H)}{k_B T} \right]. \tag{2.15}$$

This system of equations can not be solved analytically though, and Garanin and Chudnovsky [36] integrated it numerically and studied the ignition threshold in detail in different scenarios taking the dimensions of a sample in consideration as well. This is crucial because it turned out from early experiments that the size and geometry of the sample, the thermal coupling with the bath and the presence of gradients of magnetic field or temperature are decisive ingredients to the occurrence of magnetic avalanches.

In their work one of the key findings is that the ignition of magnetic deflagration process in molecular magnets is very different from the magnetization reversal in ferromagnets, mediated by exchange interaction and where the reversal begins with the nucleation of a small critical nucleus of opposite magnetization that spreads across the entire sample. In the case of magnetic deflagration in molecular magnets the process appears as an instability in the smooth temperature profile. I. e., the sample starts to warm up because some of the molecules in the metastable state are able to jump the barrier releasing energy, and at some point, under certain conditions, the heat produced can not be dissipated fast enough and then, abruptly, the deflagration begins with a thermal runaway. This thermal runaway needs some time to develop, the called ignition time τ_{ig}. The formation and the consequent propagation of the magnetic flame in a system with boundary temperature T_0 happens at the time τ_{ig} when the rate of spin-flip for an individual molecule Γ exceeds

$$\Gamma_{\text{c}} = \frac{8 k(T_0) k_B T_0^2}{U(H) \Delta E(H) n_i l^2}, \tag{2.16}$$

where $k(T_0)$ is the thermal conductivity at temperature T_0, l is some characteristic length of the order of the smallest dimension of the system, n_i is the initial fraction

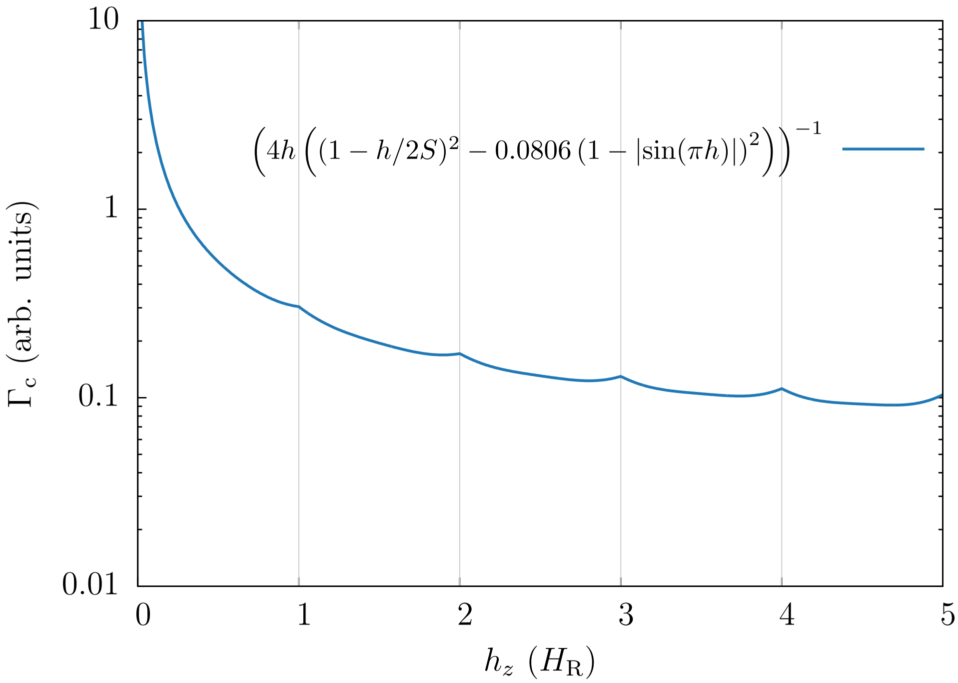

Figure 2.10: Critical rate of individual spin flipping as a function of external applied field (Eq. 2.16). At the resonant fields a small diminution of the probability can be observed.

of molecules in the metastable state, and $U(H)$ (Eq. 2.11) and $\Delta E(H)$ (Eq. 1.6) are the field-dependent energy barrier and the energy difference between the two minima of energy respectively. In the case we are interested in, $U(H)$ has dips at nH_R, meaning an increase of Γ_c at the resonant fields, i. e., the probability of ignition at nH_R would be smaller. While this is true, as we can see in figure 2.10 the augment is very small.

Fluctuations or inhomogeneities on H or T are amplified exponentially because of the Arrhenius law, resulting in that even a slight variation of these parameters can make $\Gamma \gg \Gamma_c$, which explain the abrupt and stochastic nature of the avalanche process. Nevertheless there are manners to minimize the probability of a spontaneous avalanche to study its properties, like the ignition time, its velocity and the width and temperature of the deflagration front. The obvious one is to bring the system to a metastable state “deep” enough on the energy landscape and a temperature much smaller than its blocking temperature. Once there one can try to ignite the avalanche and study its properties as a function of parameters like external field, thermal coupling, initial temperature, field gradient, etc. All the properties of the deflagration front but one can be studied in an spontaneous avalanche, the ignition time τ_{ig}.

In the same paper they studied the structure and velocity of the deflagration front and determined the width of the deflagration in the same way we did in page 5, resulting

$$l_{\text{d}} = \sqrt{\frac{\kappa_{\text{f}}}{\Gamma_{\text{f}}}}, \tag{2.17}$$

with κ_{f} and Γ_{f} being the thermal diffusivity and the relaxation rate at temperature T_{f}, for which they obtained

$$T_{\text{f}} = \frac{\Theta_D}{\pi}\left[\frac{5}{3}\frac{n_i \Delta E(H)}{k_B \Theta_D}\right]^{1/4}, \tag{2.18}$$

and, finally, the speed of the deflagration front

$$v_{\text{d}}(H) = \sqrt{\frac{4k_B T_{\text{f}} \kappa(T_{\text{f}}) \Gamma(H, T_{\text{f}})}{U(H)}} = \sqrt{\frac{4k_B T_{\text{f}} \kappa(T_{\text{f}}) \Gamma_0}{U(H)}} \exp\left[-\frac{U(H)}{2k_B T_{\text{f}}}\right]. \tag{2.19}$$

Where in $U(H)$ we will use the effective barrier (Eq. 2.11) from where the quantum characteristics will show up.

Due to the exponential dependence on the barrier height one can imagine the possibility of reaching even supersonic speeds. This was first noted in the paper of Suzuki et al. [31] where they propose the term “magnetic detonation” to refer the case where the propagation speed of the magnetic avalanche surpass the sound speed of the system. This was observed, four years later, using high field magnetic pulses in Leuven [15], in collaboration with our group. The properties of Mn$_{12}$ are somehow ideal to observe magnetic detonation due its low Debye temperature, and therefore its low sound speed —$\Theta_D \propto c_s$— ($\sim$ 2000 m/s [42]), and its electrical resistivity that avoids the appearance of Eddy currents under magnetic flux gradients (that would heat the sample promoting an early inversion, most likely without a deflagration process).

So far we have been introduced to the Mn$_{12}$-ac molecule, its magnetic and crystallographic properties, and the properties of the magnetic deflagration processes in single crystals of molecular magnets. We already know the variables involved but we still do not presented their typical values. Let us put some numbers to see the scales of what we have in hands. In the table 2.1 we can see some of the common values associated to magnetic deflagrations in Mn$_{12}$-ac single crystals.

We are ready to present a new approach to study the spatial and temporal properties of deflagration process in Mn$_{12}$-ac.

Θ_D	U_0	v_{d}	T_{f}	E_{Zeeman}	κ
38 K	65 K	10 m/s	12 K	30 μJ	10^{-5}–10^{-4} m^2/s

Table 2.1: Typical values of variables involved in magnetic deflagrations in a single crystal of Mn_{12}-ac of dimensions $\sim 1\times0.5\times0.5$ mm^3 under the conditions $\mu_0 H \simeq 1$ T, $T \ll T_B$.

2.2 Magneto-optical imaging

Imaging polarimetry techniques for magnetic flux visualization are used in a large variety of fields; from astrophysics to condensed matter physics, the polarization of light is used to determine local properties of the magnetic field.

It was Michael Faraday in an experiment in 1845 who proved for the first time the existence of an interaction between light and magnetic fields. He observed that the plane of polarization of a linearly polarized beam rotates upon passing through a piece of glass when a magnetic field is applied along the direction of propagation of the beam [43]. Before the end of the 19th century important discoveries in magneto-optical phenomena were made, e. g., Kerr effect [44] and circular and linear dichroism [45, 46]. These, among other magneto-optical effects, are the basis of a numerous techniques used to characterize magnetic and superconducting materials, on data recording, tunable polarizers, etc.

The Faraday effect is the underlying principle of the technique of magneto-optical imaging, developed in the sixties by Alers [47] and DeSorbo [48] to study the structure of the intermediate state in superconductors, and was greatly improved during the followed decade by Kirchner [49] and Huebener [50] among others (see a more complete historical development introduction in [51]). The main property of the magneto-optical imaging method is the sensitivity to the dimensionality — allowing the investigation of local dynamics with a spatial resolution of the order of 1 μm, together with the unequaled intrinsic fast temporal resolution, which enables observations on very short time scales over the whole surface of the sample.

2.2.1 The Faraday effect

The way the light propagates inside a material depend on its refractive index and its dependence on light polarization, wavelength, material temperature, electromagnetic fields, etc. In non-isotropic materials the phase velocity of light depend on the polarization of the latter and a light beam will split in two waves with different propagation velocities. The best know example of this effect can be found in the transmission of light trough a calcite crystal. Other materials that show this behavior as well are some polymers due their high anisotropy. This effect is know as birefringence and in the example of the plastics can be easily modified by bending the material, e. g., bending a CD case in front of a polarizing filter. The same idea is behind the Faraday effect. In the CD case example is the “external torsion field” what modify the original polarization of light, while in the Faraday effect is the magnetic field who does.

In the presence of magnetic fields a moving electric charge will tend to follow circular or helical paths. The sign of rotation in this paths is determined by the sign of the charge. Because of this preferred rotational direction, the propagation velocity of light through a material containing charge carriers will be different for left- and right-handed circularly polarized light. Inside a material, under a magnetic field $\vec{H}$, a linearly polarized light beam propagating parallel to the field will turn its polarization vector by an angle θ, proportional to the parallel component of the field H, the specific properties of the material V, and the distance traveled inside the material, d,

$$\theta = VHd. \tag{2.20}$$

The parameter V is called the Verdet constant. It is obvious that materials with good light transmittance and large Verdet constant are needed. But we are interested on the local magnetic properties of another materials, which do not use to fulfill both conditions at all. In that case, an indicator is needed. A number of different materials have been applied as indicators: cerous nitrate-gycerol, various europium compounds (EuS, EuSe) and bismuth-substituted iron garnets. Today, the most popular indicator is the ferromagnetic Bi:YIG film with in-plane spontaneous magnetization. We will be back on indicators when describing the actual indicator used in the setup.

In the figure 2.11 is shown the principle of the technique of magneto-optical imaging. As said above, the distribution of magnetic flux is visualized using films of magneto-optical active layers (MOLs) placed in close contact to the sample. The MOL is coated with a thin, typically 100 nm, mirror layer made of gold, silver or aluminium, on the side facing the material to investigate. This setup has the advantage of increasing the Faraday rotation because the light will have to cross the MOL two times. The Faraday rotation is monitored by an analyzer, set in crossed position with respect to the polarizer. the magnetic flux distribution at the surface of the sample is visualized as a gray-scale intensity image. In flux-free regions the linearly polarized light is reflected without a change in the plane of polarization, thus the corresponding image region will be dark because the blockage at the analyzer. On the contrary, in regions with non-zero magnetic flux the plane of polarization of the incident beam rotates following Eq. 2.20 by an angle proportional to the local magnetic field component perpendicular to the plane of the MOL. Therefore, when the reflected beam arrives at the analyzer will

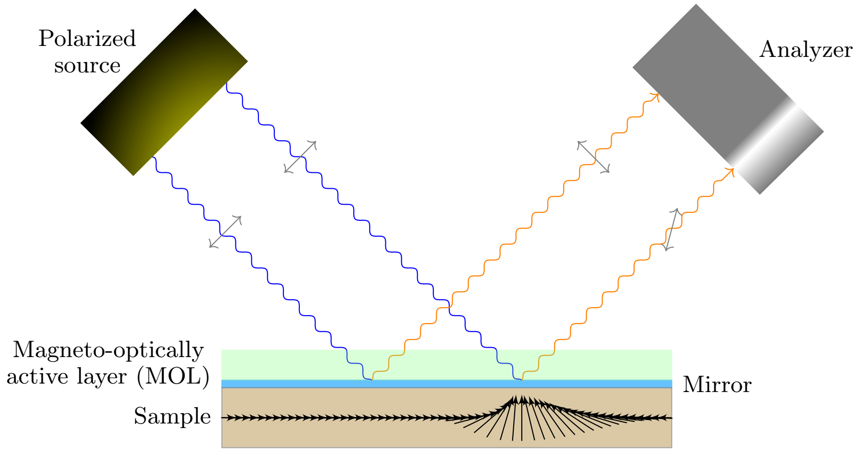

Figure 2.11: Schematic drawing of the Faraday effect. The magnetic flux distribution in the sample is visualized in the analyzer as a gray scale intensity image. The light enters the magneto-optical active layer (MOL) and is reflected at the mirror. Polarized source and analyzer are set in crossed position, so in areas where there is no flux and no Faraday rotation of the polarization takes place hence the image stays dark. On the contrary, where magnetic flux is present, the Faraday rotation modifies the polarization leading bright areas in the analyzer. The arrows inside the sample represents its local magnetization. In the experiment the incident light is perpendicular to the MOL.

pass through it. The intensity of each gray level in the obtained image is related to the Faraday rotation angle through Malus' law:

$$I = L \sin^2 2\theta, \tag{2.21}$$

where L is the intensity of the light beam at the source and the double angle 2θ accounts for the reflection on the MOL. While in the figure 2.11 the incident angle is 45° (for clarity), in the experiment the setup is with the incident light perpendicular to the MOL. Because of this, as the angle will be very small, the intensity I can be approximated

$$I \simeq 4L\theta^2. \tag{2.22}$$

The side effect of the Malus' law is that the sign of the magnetic field cannot be experimentally determined, because the relation with the intensity is $I \propto H^2$. Additionally, the intensity measured depends on the exact distribution of the incident light over the surface of the sample and in general is not homogeneous. This uneven illumination affects strongly to the measurement of magnetic fields. Additionally, at very small angles, the intensity is also very small. As we will see next, these shortcomings can be overcome by using the Magneto-Optical Image Lock-In Amplifier (MOILIA) technique developed in 2001 by Wijngaarden et al. [52].

2.2.2 Magneto-optical setup

The mangeto-optical setup used in the experiments conducted at the Vrije Universiteit Amsterdam, in the group of Dr. Wijngaarden, is schematically shown in the figure 2.12. The following description of the experimental setup in based on the description presented in the thesis of Diana Gheorghe, a former PhD student on Wijngaarden's group [53].

Light from the light source (**1**) is collimated (**2**) before being polarized by a linear polarizer (**3**) and a controlled polarization rotator (**4**) that uses the Faraday effect in a rod of special glass. Then the polarized light is split (**5**) and enters the cryostat (**6**) where is focused by the lens (**7**) and enters in the the vector magnet (**8**) onto the magneto-optical active layer (**9**). There the light passes through a MOL, reflects in the mirror layer —in close contact with the sample— and passes one last time through the MOL. The light exiting crosses again the lens (**7**) before leaving the cryostat, then crosses the beamsplitter, the analyzer (**10**) and the focusing lens (**11**) ending its trip onto the CCD camera (**12**) connected to a computer.

The light source is a Kinderman diafocus projector, model 250 AF, equipped with a 250 W lamp and a bandpass filter for 550 nm. The polarizer and the analyzer are Melles Griot dichroic sheet polarizers (03FPG007), with a wavelength range 380–780 nm and a extinction ratio of 10^{-4}. The polarization rotor is a 25 mm wide, 150 mm long SF 59 glass rod enclosed in copper coils, specially designed to generate a uniform magnetic field distribution (less than 1% inhomogeneity) inside the rod. The SF 59 glass has a large Verdet constant $V = 131 \times 10^{10}$ °/mTμm and low absorption coefficient. The modulation of the plane of polarization, by a small angle α, is done modifying the current on the coil. The beam splitter is a non-polarizing transparent plate mounted outside the cryostat.

The sample is mounted on a home made insert (not shown in the scheme), a masterpiece of enginery that allows fine tuning of the position of the sample by 6 degrees of freedom $(x, y, z, \beta, \gamma, \rho)$ —a detailed description is available in the thesis of D. Gheorghe [53]. The insert is placed inside the cryostat, in the region of homogeneous field of the magnet. The magnet is a Oxford Instruments 3-axes Vector Magnet of $\mu_0\vec{H} \in \pm[1_x, 1_y, 7_z]$ T, with a sweeping rate of $\mu_0 \mathrm{d}\vec{H}/\mathrm{d}t \in \pm[1_x, 1_y, 2.4_z]$ T/min. Out of axes, the system can safely reach a magnetic field of 1 T. The cryostat works with a constant pumping of liquid helium and can be operated in the range $T \in [1.5, 300]$ K.

As seen in Fig. 2.11, on top of the sample is attached the MOL, coated with a mirror layer. The MOL used is a bismuth-substituted yttrium iron garnet (Bi:YIG) [54], which can be used over a broader range of temperatures in

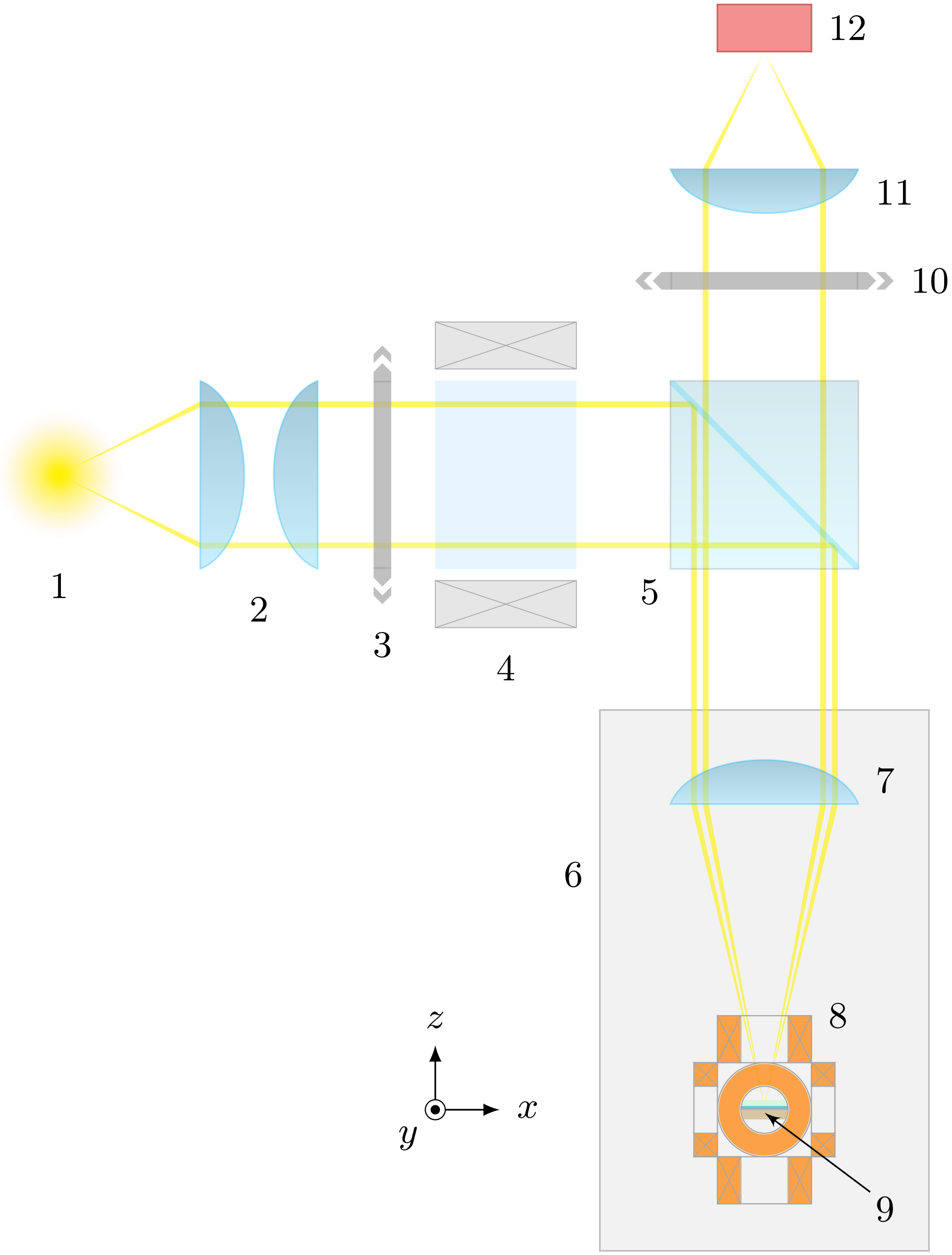

Figure 2.12: Schematic diagram of the magneto-optical setup: (**1**) Light source, (**2**) collimator, (**3**) polarizer, (**4**) polarization rotor, (**5**) beamsplitter, (**6**) cryostat, (**7**) focusing lens, (**8**) vector magnet, (**9**) MOL + mirror + sample, (**10**) polarizer (analyzer), (**11**) focusing lens, (**12**) CCD video camera connected to a computer.

comparison with the europium compounds. The Bi:YIG indicators have in-plane anisotropy. In these indicators the Faraday rotation is proportional to the out-of plane component of the magnetization vector, which is pushed out of the field by the magnetic fields underlaying sample. A side effect of the in-plane magnetization indicators is the overlap of the Faraday effect due the sample's magnetic fields, and the effect from the magnetic domains of the MOL. Nevertheless, this inconvenience can be solved by rotating the MOL. The typical properties of an active layer of Bi:YIG with a thickness of 3 μm are: a Verdet constant of the order of 10^{-2} $^\circ/\mathrm{mT}\mu\mathrm{m}$, spatial resolution (limited by the thickness and the distance to the surface of the sample, normally $\sim$ 2–3 μm) of the order of 5 μm, a saturation fields in the range of 30–200 mT, and a field sensitivity down to 10 μT.

Once the light passed through the analyzer, it is collected with a CCD camera. While they use different recording systems depending on the timescale of the experiment, we will just explain the fast analog system (remember that we are looking for deflagrations, that live in a millisecond world). The system consist in a 25 Hz Teli CCD camera (model CS8320C) with an active area of 752×582 pixels. For direct recording the camera is connected to a Hamamatsu (Argus 20) real-time image processing unit and a SONY Hi8 EVO-9650P video recorder, with a dynamic range of 8 bits and a recording speed of 25 fps (frames per second). Each frame is recorded with a corresponding timecode together with the temperature and the magnetic field at the three different axes.

Before to describe the experiments performed and the results, let us introduce briefly the MOILIA technique. The Magneto-Optical Image Lock-In Amplifier consist in the use of a polarization rotator to modulate the polarization plane by an small angle α. From equation 2.21,

$$I \simeq K + L(\alpha + \theta)^2, \tag{2.23}$$

being K an offset due to camera noise, readout offset or stray light. Choosing $\alpha = (-\alpha_0, 0, \alpha_0)$ we can determine L and θ:

$$L = \frac{I_- - 2I_0 + I_+}{2\alpha_0^2}, \tag{2.24}$$

$$\theta = \frac{I_+ - I_-}{4\alpha_0 L} \tag{2.25}$$

and

$$K = I_0 - K\theta^2. \tag{2.26}$$

The measured illumination intensity L can be considered noise-free just taking average over many images (typically 100). To determine θ, the equations 2.24

and 2.25 are solved in real time for each pixel. This technique allows to overcome the drawbacks of the typical magneto-optical imaging: the indeterminacy of the sign of the magnetic field, the strong influence of an uneven illumination, and the low sensitivity for small angles.

One more thing about the data acquisition. As it is a very important part of the process, success or failure of the analysis depend significantly on the quality of recorded videos, so I consider important to present issues related to that subject. There are two types of image acquisition in Digital Video cameras (DV): progressive scan or interlaced scan. In progressive scan the image is captured and transmitted line by line each iteration, while in interlaced scan in each iteration only every second line is transmitted. Such scan of every second line is called field. Years ago, to prevent interferences with the mains, TV receivers required displaying image at AC line frequency (50 Hz Europe, 60 Hz USA, etc.). This value is close to the 48 images per second displayed in a cinema (the films were recorded at 24 frames per second, but to prevent flickering every frame is displayed twice). The cinema cameras record in progressive, i. e., every iteration (1/24 s) an entire picture is captured. Back to TVs, the most common solution to show on them movies recorded for cinema projectors was to display images 50 times in a second alternating odd and even lines of the frame (half-frames, fields) instead of displaying 25 full frames per second. This correspond to the interlaced scan. Additional benefit was that interlaced scan requires narrower bandwidth because only the half of information is transmitted per second. Nowadays TVs show progressive images and most cameras record in progressive mode as well.

The image acquisition system we use in the experiments record videos in interlaced way at 25 frames per second. Each frame is composed from two fields captured at 1/50 s. Problem arises if captured data contains high speed motion (changes faster than 1/25 s). The effect is clear if the movie is paused in between a rapid change (Fig. 2.13).

It is obvious that this will be a crucial issue to deal with, since we are interested in magnetic deflagrations that from previous experiments in samples of similar dimensions last less than 40 ms (1/25 s). Thus we need to de-interlace the footage. There are several de-interlacing techniques: motion compensation, blending, half-sizing and line-doubling. Since we are interested in high speed phenomena and the vertical resolution is good enough, even with the half, we will use the half-sizing technique. With this technique we separate the two fields of a frame, resulting in two frames with half the height but with a temporal separation of 20 ms (1/50 s). Then, if one wants to recover the original frame size the solution is to double every line of the fields.

To de-interlace the videos I used the program VirtualDub [55] (`http://virtualdub.org`), a general-purpose media editor for fast linear operations over

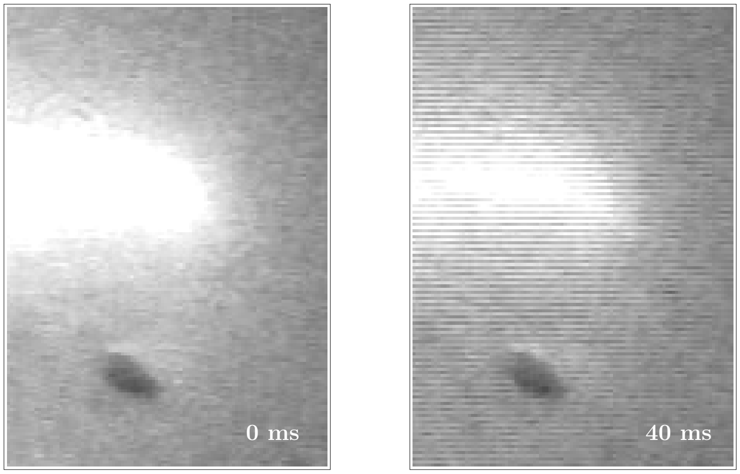

Figure 2.13: An image fragment of two consecutive frames from the experiment footage. The effect of interlaced recording can be seen already on the image on the left, while is more clear in the second image white region where odd consecutive lines remain whiter while even are already darker during the magnetization inversion process. (If the reader is using a computer then is preferable to zoom in the image, since the Moiré effect can significantly modify the effect pretended to show).

video, licensed under the GNU General Public License (GPL). In figure 2.14 we can see the de-interlace process at work. The two frames showed in Fig. 2.13 are split temporally in four by separating the two fields, and the lines of each field are doubled to keep the original vertical size (it was not necessary, but I did it). Using this technique we can double the temporal resolution of the experiment, from 40 ms to 20 ms.

2.3 Experiments

The experiments presented where performed in the group of Dr. Rinke Wijngaarden, at the Vrije Universiteit Amsterdam. The experiments where carried out by Diana Gheorghe and Alberto Hernández-Mínguez, a former student in our group. My task was to analyze in detail the images looking for any hint of a deflagration front during the magnetic avalanche.

In the experiments, the sample, a single crystal of Mn_{12}-ac of $1.2\times0.5\times0.5$ mm^3 was mounted on top of a thermometer LakeShore Cernox, model CX-1050BR (see figure 2.15). This thermometer was used as a heater to trigger the ignition of the magnetic deflagration. The MOL consisted in a layer of Bi:YIG with a thickness

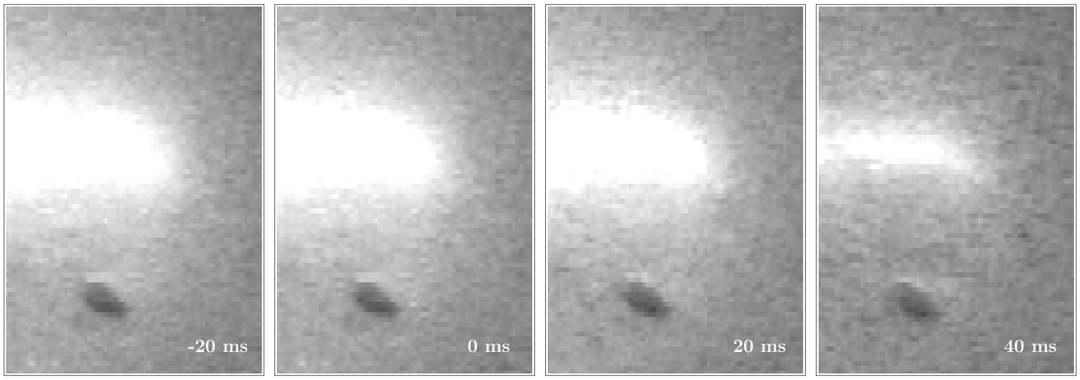

Figure 2.14: De-interlaced sequence of figure 2.13. From two consecutive frames separated 40 ms we obtain four frames separated 20 ms between each one. The vertical size is kept by doubling the height of the lines.

of 5 μm with its coated side was “glued” to the sample with 99% pure nonadecane ($C_{19}H_{40}$).

The sample is placed in this setup with its easy axis c parallel to the x axis of the magnet. Therefore, only 1 T can be applied to the sample. That fact implies that at base temperature (1.5 K) the magnetization of the sample will not be saturated (see hysteresis loops in Fig. 2.7). Thus, in order to saturate the magnetization of the sample, we will need to perform a field-cooling process from a temperature above the blocking temperature (~ 3.5 K). With the sample’s magnetization saturated along the applied field at the desired temperature (well below T_B), the field is swept up to a “negative” value. Negative meaning antiparallel to the magnetization, while in this case will be actually negative because the preparation field was taken positive. We have seen in the theoretical framework of magnetic deflagration that exists a critical rate of individual spin flipping $\Gamma_c(H,T)$ (Eq. 2.16) above which the deflagration ignites spontaneously, so, as we are interested in controlled induced deflagrations, the destination fields will be small enough to ensure no spontaneous deflagration at temperature T. To ignite the deflagration a voltage pulse is applied to the underlaying thermometer. The voltage pulses were applied using a Wavetek pulse generator, with a maximum pulse width t_p of 10 ms. The maximum voltage amplitude was 10 V, which, taking into account the resistance of the Cernox Thermometer (20 kΩ at 1.5 K), give us the maximum energy released due the Joule effect: $E_{J,\max} = V_{\mathrm{p,max}}^2 t_{\mathrm{p,max}}/R = 50\ \mu$J.

In the figure 2.16 we can see the expected evolution of the magnetization in a deflagration process and the correspondent evolution on the image formed because of the Faraday effect of the sample magnetization on the MOL. The figure represents the whole process: the sample is saturated (**1**), heated briefly once it is

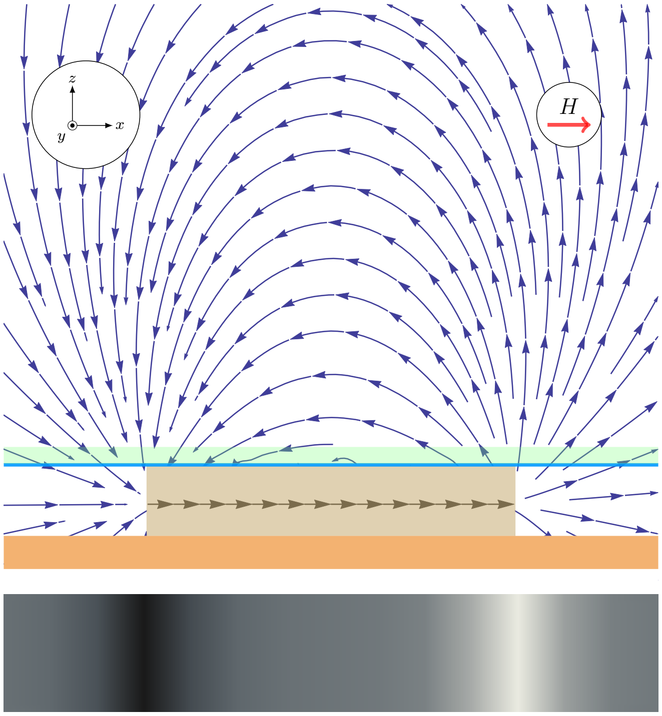

Figure 2.15: Experimental setup. The magnetic field will be applied along the x axis. The thermometer corresponds to the orange layer, the sample (with arrows representing its local magnetization) the light brown rectangle, and the mirror and the MOL the blue and light green layers respectively. The magnetic field lines of a uniformly magnetized bar are represented (blue arrows), and its correspondent magneto-optical image as well (gray-scaled image at the bottom).

in the metastable state (**2**), the magnetization inversion propagates through the sample (**3**)–(**8**). However, this accounts for the ideal case, where a narrow front is formed in one side and crosses the sample at a constant speed.

2.4 Analysis and results

A magneto-optical image obtained in the experiment ($T = 1.6$ K, $\mu_0 H = -0.1$ T, $t_\mathrm{p} = 10$ ms, $V = 10$ V) is shown in the figure 2.17. With this figure we will introduce the methodology used to analyze the de-interlaced videos. On the subfigure 2.17(a), on top of the magneto-optical image, the profile of the sample is drawn with a green line (the sample is under the MOL but we can reckon the dimensions of the sample from its magnetization). On the second subfigure 2.17(b), six different areas are highlighted with a yellow line. These areas are the regions of

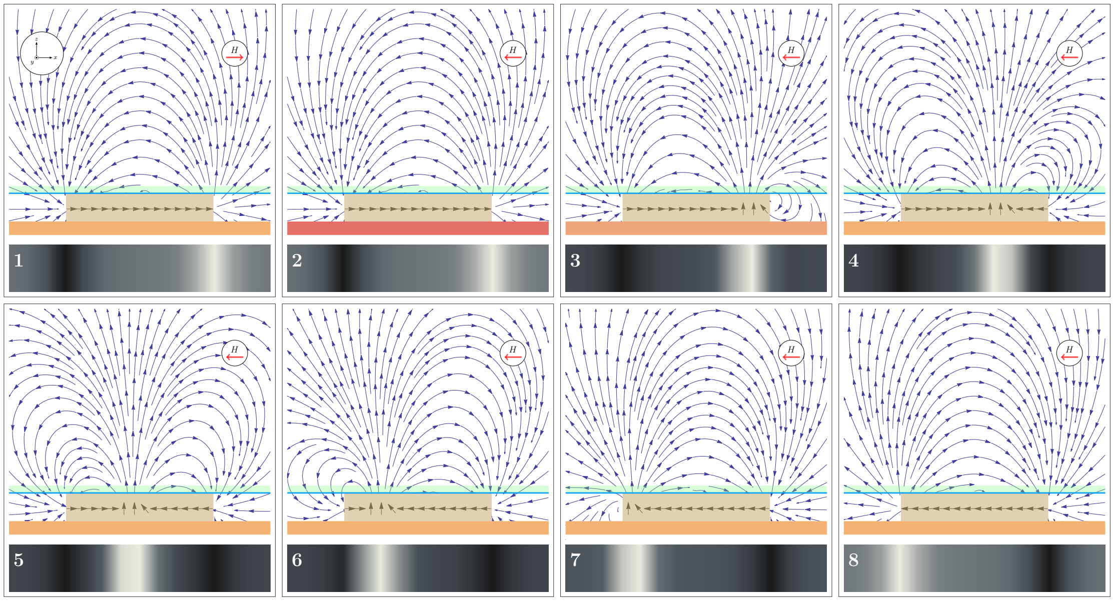

Figure 2.16: Expected evolution of the magnetization on a deflagration process. (**1**) The sample is saturated. (**2**) The magnetic field is applied antiparallel to the magnetization and the thermometer is heated for an instant. (**3**)–(**8**) The magnetization reversal front propagates through the sample. The instantaneous magnetic field lines are represented (blue arrows), and their correspondent magneto-optical image as well (gray-scaled image at the bottom).

interest (ROI) and we will analyze them every frame to study the evolution of the magnetization of the sample. We will analyze the next properties of every ROI:

1. Average gray level.
2. Standard deviation of the average.
3. Center of mass of the gray level.

The ROIs selected are: **1** and **2** at the upper and lower edge of the sample, two transverse regions **3** and **4**, and two background regions **5** and **6**. Looking at the expected magneto-optical image evolution of a magnetic deflagration (Fig. 2.16) one see why these ROIs have been selected. In a deflagration process that starts in one side of the sample, the magnetic field lines at the edges change with a delay between them. First, the edge where the deflagration has started shows a change in the “sign” of the gray level, going from white to black (or from black to white); then a white (black) front moves toward the other end which remains in the original black (white). Since the temporal resolution of the experiments is low (20 ms) the

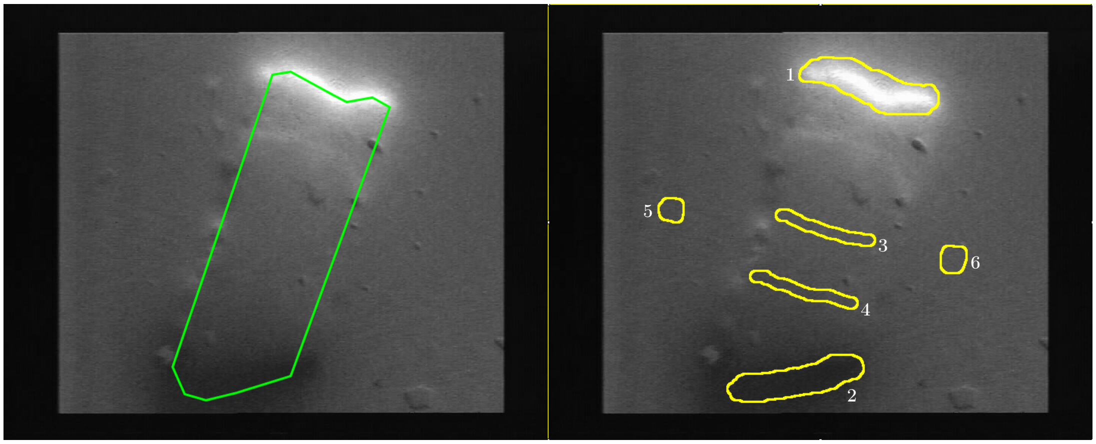

(a) Sample's profile.

(b) Selected ROIs.

Figure 2.17: Magneto-optical image of the sample: 2.17(a) Sample's profile represented with a green line on top of the magneto-optical image corresponding to $t = 0$ in experiment: $T = 1.6$ K, $\mu_0 H = -0.1$ T, $t_\mathrm{p} = 10$ ms, $V = 10$ V. 2.17(b) Selected ROIs on top of the same frame. The magnetic field is applied along the easy axis: the longest dimension of the sample.

fields used will be small to try to catch the expected "slow" deflagrations. Because of that, two ROIs where placed in the path of a deflagration process. Additionally two more ROIs where added to the analysis; two regions taken to monitor the background dynamics.

To analyze the de-interlaced videos the program ImageJ was used. ImageJ is a public domain Java image processing program [56] (`http://rsb.info.nih.gov/ij`). The program can display, edit, analyze and process many image formats. It can calculate many features of an image, from pixel value statistics to distances and angles. Actually has many options to process and analyze images. But the key feature is that provides extensibility via Java plugins and it can be scripted. A complete script was programed to analyze the videos in the quickest way, separating frame by frame and grabbing the statistical data of the selected ROIs. As we will see at the conclusion of the chapter, the time devoted to learn to script for ImageJ was very useful overall.

Back to the experiments: from the 51 times the experiment

$$\mu_0 H_x = 1\ \mathrm{T},\ T > T_B \Longrightarrow T \to T_\mathrm{ign} \Longrightarrow H_x \to H_{x,\mathrm{ign}} \Longrightarrow \text{Heat pulse } (V, t_\mathrm{p})$$

was repeated, varying the four parameters $(H_{x,\mathrm{ign}}, T_\mathrm{ign}, V, t_\mathrm{p})$, only in 33 an avalanche happened and only in 17 the avalanche was complete (one of the expected signs of deflagration): sometimes the power supplied was not enough, sometimes the temperature was not stable. To know if the avalanche was complete or not another heat pulse was sent after the experiment; we assume the deflagration is complete if a second heat pulse does not affect the magnetization. While this is not the perfect test, it is the easiest one and is reliable enough.

From the seventeen measured complete avalanches we will focus on two sets:

① $T = 1.6$ K, $\mu_0 H = -0.45$ T, $t_\mathrm{p} = [0.01, 0.1, 1, 10]$ ms, $V = [1, 10]$ V.

② $T = [1.5, 1.6]$ K, $\mu_0 H = [-0.01, -0.1, -0.3, -0.45]$ T, $t_\mathrm{p} = 10$ ms, $V = 10$ V.

From experiment set ① we will determine the reproducibility and the threshold conditions of the deflagration process. With the experiment set ② we will study the dynamics of the process under different ignition conditions, from which the dependence of the speed with the applied magnetic field will be studied and compared with the speeds observed using different techniques [13, 31, 33] and with the behavior predicted by theory [36, 57]. In the figure 2.18 the process is presented, showing the time evolution of the average gray level of ROIs **1** and **2**, together with the evolution of the de-interlaced video, frame by frame.

The data extracted from the experiment set ① is show in the figure 2.19. For the purpose of this experiment set is enough to present the data from ROIs **1**, **2** and **5**. In this set, the variable parameters are the related with the heat pulse. In order to understand the ignition condition the time span of the pulse t_p and the voltage applied V are modified. The first time span studied, $t_\mathrm{p} = 0.01$ ms, did not induced any relaxation of the magnetic moment and is not show in the figure; this indicates that (as $V = 10$ V), an energy pulse of 50 nJ is too small to promote the magnetization reversal even with $H \simeq H_\mathrm{R}$, i. e., in a very favorable situation to relax toward equilibrium. The time span was increased logarithmically every decade up to 10 ms. Despite the $t_\mathrm{p} = 0.01$ ms case, all other experiments showed a complete reversal of the magnetic moment. It is worth mentioning that the actual picture of the set-up is a little bit different than the showed in the figure 2.15. The size of the heater used (a Cernox CB-1050BR thermometer) is about the size of the sample. Let us do some calculations to estimate the amount of energy that the heater can transfer to the sample mounted on top of it. The sample surface is $1.2 \times 0.5 \ \ \mathrm{mm}^2$, while the dimensions of the thermometer specified by the manufacturer are $1 \times 0.8 \times 0.2 \ \ \mathrm{mm}^3$. We can use geometric considerations to roughly calculate the energy supplied to the sample from the Joule energy dissipated when the pulse is applied. We will consider that the heat transfer between the thermometer and the sample will be only trough the interface between them, which means that we will consider the thermometer as a hot plate with an area A with a fraction of the original power:

$$\mathrm{Power}_A = \frac{\mathrm{Power} \cdot A}{A_T} = \mathrm{Power} \cdot \frac{ab}{2(ab + ac + bc)} \simeq 0.34 \cdot \mathrm{Power},$$

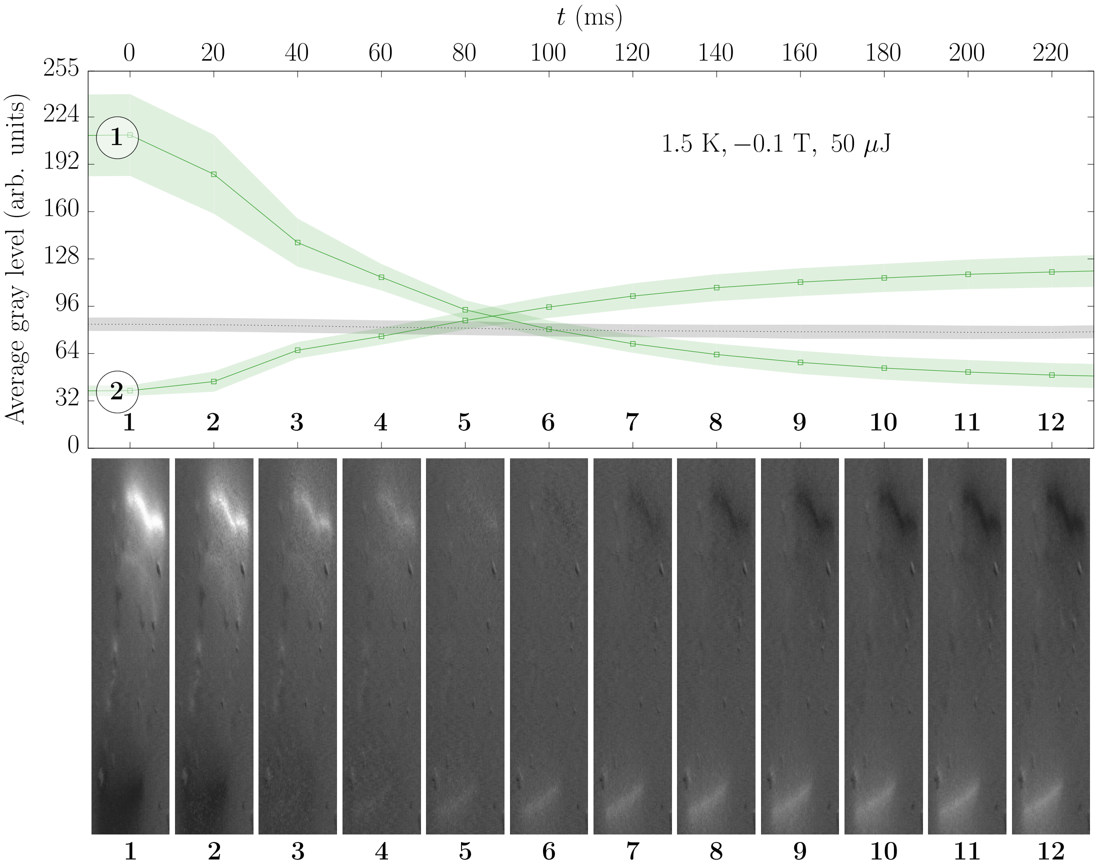

Figure 2.18: Top: Time evolution of the average gray level of ROIs **1** and **2** of the experiment $1.6\ \mathrm{K}, -0.1\ \mathrm{kOe}, 50\ \mu\mathrm{J}$. The gray line represents the average gray level of the ROI **5**. The standard deviation of the average gray level at every ROI is represented with a transparent envelope. Bottom: Every point showed in the top figure correspond to a measure in the respective frame. The frames are separated each other by 20 ms. The frame aspect ratio has been distorted for clarity.

being A_T the total area of the thermometer. As the sample do not fit entirely on top of the thermometer it will be necessary to correct again the power. The maximum area of the thermometer that the sample can cover is about the 75% of A; so the energy supplied to the sample will be at the most

$$E \lesssim \frac{V^2 t_\mathrm{p}}{R} \cdot 0.34 \cdot 0.75 = 0.255 \frac{V^2 t_\mathrm{p}}{R}, \tag{2.27}$$

which means one fourth of the energy supplied to the heater.

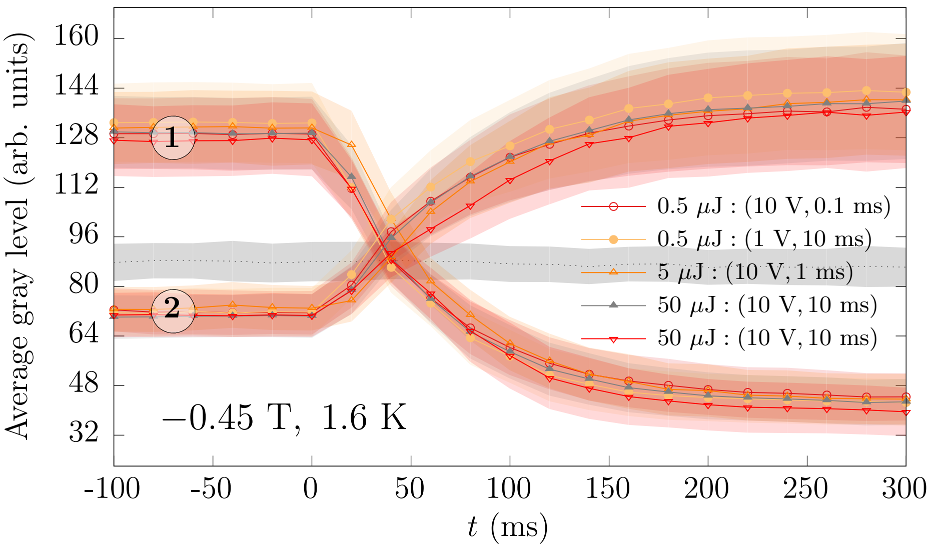

Figure 2.19: Time evolution of magneto-optical intensity at ROIs **1** and **2** in the experiment set ①. The gray line represents the average gray level of ROI **5**. The standard deviation of the average gray level at every ROI is represented with a transparent envelope.

From the figure 2.19 it follows that the dynamics of the system seem to not depend on the power supplied, in the studied range, since all the curves collapse. The origin of time $t = 0$ is chosen as the one above which the average gray level starts to change monotonically. The experimental setup did not allow to record the precise moment when the pulse was triggered so we have a lack of information of the time elapsed between the pulse and the change of the gray levels of the magneto-optical image. The ignition time depends on how fast the system is driven to the thermal instability and this depends on the properties of the pulse. A short but intense pulse can induce the ignition of an avalanche as a long but moderate one; and once the deflagration starts its dynamics does not depend on the pulse characteristics anymore. In our case we can know if the process has started or not, but not the time that needed to start. This time also depend on the metastability of the system and its thermal contact with the environment. The only thing we can extract about the ignition threshold from the experiment set ① is that a pulse of $0.255 \cdot 50$ nJ is not sufficient to ignite the self sustained process of deflagration, while pulses of $0.255 \cdot [0.5, 5, 50]$ μJ are.

Looking at the same figure we can see that the process timescale seems too large for a deflagration, and at a first glance the reader could imagine that we are observing nothing but conventional thermal relaxation induced by the heater.

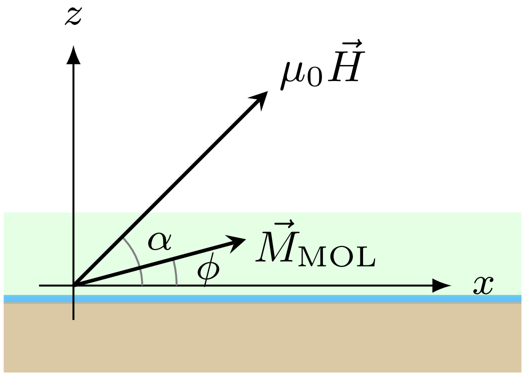

Figure 2.20: Relation between the MOL magnetization $\vec{M}_{\mathrm{MOL}}$ and the magnetic field $\vec{H}$, which forces the magnetization vector away from the easy axis of the film

Nevertheless, the first thing to be noticed regarding this scenario is that heat pulses of logarithmically increased amplitude do not enhance the relaxation rate as one should expect. But the exponential behavior reveals a thermal relaxation, so we will try to understand better what is happening in the system analyzing in detail the data. We will study the time evolution of the magnetization and from there we will estimate the temperature, speed and width of the deflagration front. There are techniques to compute the magnetization of a sample from its magneto-optical image [58, 59], but a different approach will be used here as we are interested in the variation of the magnetization relative to the saturation magnetization and not in the magnetization itself.

Before presenting the approach made to compute the evolution of the magnetization it is necessary to mention the role of the parallel magnetic field on the MOL. As said before, the MOL is a Bi:YIG film. The bismuth-substituted yttrium iron garnet is a ferrimagnet with a spontaneous magnetization, $\vec{M}_{\mathrm{MOL}}$, with the easy axis lying in the film plane. A magnetic field $\vec{H}$ applied at an angle α (see Fig. 2.20) will force the magnetization vector out to the plane. Assuming that the MOL consist of a single domain, the angle ϕ is the minimum energy angle that arises from the balance between the magnetocrystalline and the Zeeman energy [60], i. e., minimizing

$$E = K_a(1 - \cos\phi) + \mu_0 HM(1 - \cos(\alpha - \phi)), \tag{2.28}$$

which respect to ϕ, where K_a is the uniaxial anisotropy constant. As the Faraday effect is proportional to the component of $\vec{M}_{\mathrm{MOL}}$ along the light beam direction,

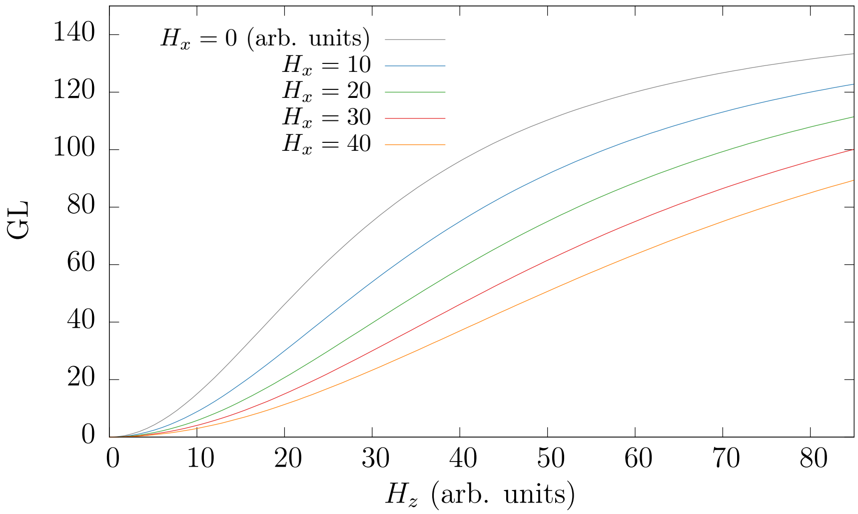

Figure 2.21: Dependence of the gray level with the parallel and perpendicular fields. The anisotropy field is set to $H_a = 30$.

which is in our case perpendicular to the film, the minimization implies

$$\theta_F \propto \sin\phi = \frac{H_z}{\sqrt{(H_a + H_x)^2 + H_z^2}}. \tag{2.29}$$

In a previous section we presented the Malus' law (2.21) which relates the intensity on the CCD camera and the squared sinus of the Faraday rotation angle. We apply Malus' law to obtain

$$\mathrm{GL} \propto \sin^2\theta_F \simeq \theta_F^2 = \frac{H_z^2}{(H_a + H_x)^2 + H_z^2}. \tag{2.30}$$

This expression, that takes into account the fact that θ_F will be small, describes well the experimental suppression of θ_F by H_x and also the saturation for large H_z. We can see this behavior in the figure 2.21. In the limit of small fields we can approximate the expression to

$$\mathrm{GL} \propto \frac{H_z^2}{(H_a + H_x)^2}, \tag{2.31}$$

that corresponds to the parabolic part of the figure 2.21. From experimental measurements the Bi:YIG anisotropy field has been determined to be $\mu_0 H_a \simeq$ 90 mT.

The experiments to study the magnetic deflagration process in Mn$_{12}$-ac suffer remarkably from this coupling between the MOL and the parallel magnetic field; because large fields are applied on the parallel direction, because the sample magnetization has an in-plane field component and because during the magnetization reversal the sensibility of the MOL is affected because this changes on the parallel local field.

Considering the misbehavior induced by the in-plane field component of the sample small, we define the magnetization of the sample as

$$M(H_x) \equiv \left(\overline{\mathrm{GL}(\mathbf{1})} - \overline{\mathrm{GL}(\mathbf{2})}\right) \cdot f(H_x), \tag{2.32}$$

where $\overline{\mathrm{GL}(\mathbf{i})}$ refers to the average gray level of the ROI $\mathbf{i}$ and $f(H_x)$ is a function to recover the right value of GL from the affected by the H_x field. As said before, we are interested in the variation of magnetization respect to the saturation magnetization. The value of M_S is taken from the magneto-optical image at $\mu_0 H_{||} = 0$ T recorded during a field sweep. The dependence of f on H_x will be determined using a physical reasoning. We will use some calibration magnetizations at the fields where we can consider the sample magnetically saturated. In the measurements of magnetic deflagrations on Mn$_{12}$-ac on the SQUID magnetometer, when one goes from the preparation field ($H \sim 3$ T) to a field between the zeroth and the first resonant field (-0.46 T), the usual sweep rate (~ 300 Oe/s) does not allow the magnetization to relax noticeably when the zeroth resonance is crossed and we can consider then that the magnetization right before the heat pulse is $M_i/M_S = 1$. In principle when the temperature is low compare to the blocking temperature (in our case $T \lesssim T_B/2$), and the sweep rate is reasonably fast (in our case ~ 150 Oe/s), M_i can be considered equal to M_S even after crossing the second resonance. Obviously, the closer we go to a resonant field, the stronger the relaxation will be and M_i will evolve towards the equilibrium before the pulse can be triggered. In reality, when a field close to a resonant field is chosen, the time the apparatus needs to reach the field without overcome it and switch off the heater of the superconducting magnet is enough to produce a remarkable relaxation. This is what happened in the experiment set ①, where $H_x = 0.98 H_R$, the initial magnetization was smaller than M_s. This maybe is not clear yet because we only have seen the time evolution of the average gray levels (figures 2.18 and 2.19), without the correction due the presence of a parallel field, and without comparing the value with M_S. The fields selected to be considered with $M_i(H_x) \cong M_S$ are $(-0.1, -0.3)$ T (from experiment set ②). We will not talk yet about the experiment set ② though.

In the figure 2.22 the magnetization temporal evolution of the experiment set ① is presented, along with a fit to every experiment. The fitting function is

$$M(t) = M_i + (M_{\mathrm{eq}} - M_i)\,(1 - \exp(-t/\tau)) \tag{2.33}$$

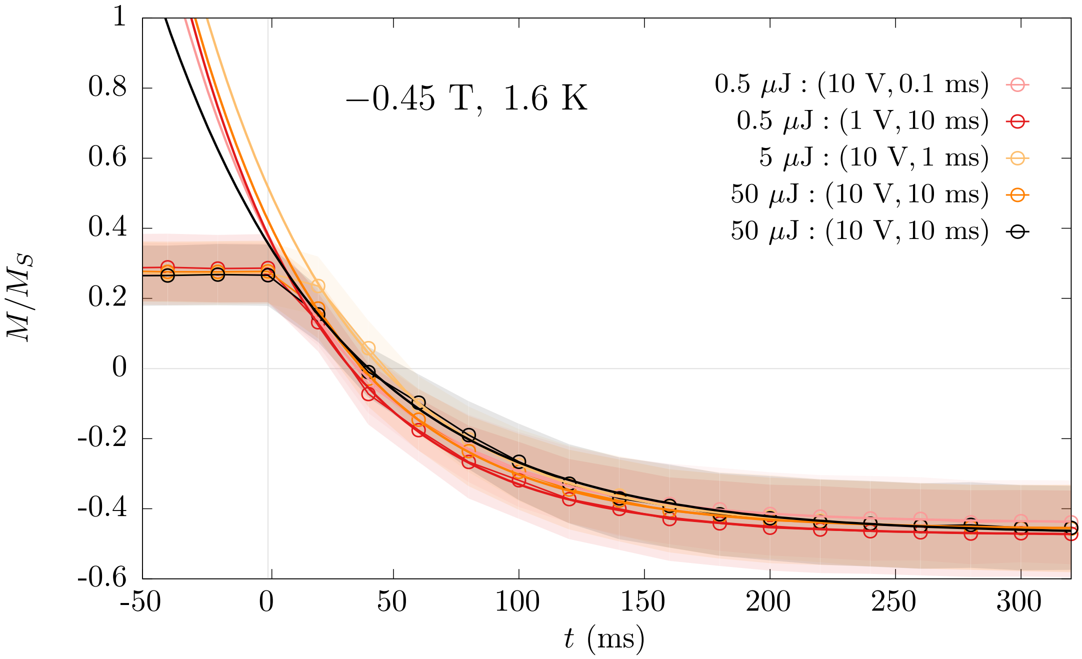

Figure 2.22: Temporal evolution of the magnetization (defined by Eq. (2.32)) divided by the saturation magnetization M_S. The solid lines represent the fit of Eq. (2.33) to the experimental curves. Experimental points are connected as a guide to the eyes only.

where M_i stands for the initial magnetization, M_{eq} is the equilibrium magnetization to which the system tends, and τ is the characteristic relaxation time. The fit is good for all the curves, giving an average value of

$$\overline{\tau} = 59.08 \pm 0.57 \text{ ms}, \tag{2.34}$$

with no apparent correlation between the pulse parameters and the value of τ. The value of M_i obtained in the fittings is wrong mainly because the uncertainty on the exact time of ignition. From the obtained characteristic times we can give a precise estimation of the temperature of the sample through Arrhenius' law:

$$\overline{T} = \frac{U(H)}{k_B \ln(\tau/\tau_0)} = 5.6837(60) \text{ K}, \tag{2.35}$$

where $\tau_0 = 6.6 \times 10^{-6}$ s is the time attempt (the inverse of Γ_0) and $U(H)$ is the effective barrier (2.11), with $U_0 = 66$ K and $b = 9$ K [38]. Actually, despite this is the precision that we can get from the fittings, has to be considered wrong because it has not taken into account the uncertainties on U_0, b, τ_0, H_a and H_R, which will raise the error. If we do error propagation analysis on the six parameters equation we will obtain

$$\overline{T} = \frac{U(H)}{k_B \ln(\tau/\tau_0)} = 5.47 \pm 0.62 \text{ K}, \tag{2.36}$$

considering the next values and their uncertainties obtained from different papers: $U_0 = 62 \pm 3$ K, $b = 8 \pm 1$ K, $\tau_0 = 6.6^{+0}_{-6.5} \times 10^{-6}$ s, $H_\mathrm{a} = 9.0 \pm 0.2$ T and $H_\mathrm{R} = 0.45 \pm 0.01$ T.

The fact that the fitting is that good suggests that all the sample is at that temperature, i. e., seems that the deflagration front width is about the size of the sample or even more. Or, the pulse applied heats the entire sample and we are in front a simple thermal relaxation. It has been mentioned before that pulses of different energy (×1, ×10, ×100) result in the same relaxation timescale so in principle the behavior can not be associated just with thermal relaxation due the increase of temperature because of the heat pulse. But we can do some calculations to check the possibility of a deflagration. Let us suppose that the external heat pulse triggers a deflagration that burns all the metastable magnetization states of the sample. That means the release of the Zeeman energy $E_\mathrm{Zeeman} = \mu_0 H \Delta M$ in the reversal of the magnetization ΔM under the magnetic field H. In the case where all the sample was prepared with the spins in the $S = -10$ state and the deflagration drove the system spins to the $S = +10$ state, the value of ΔM would be two times the saturation magnetization $M_S = N g \mu_B S$, with N being the number of molecules on the sample. To obtain the number of molecules we need the density of the $\mathrm{Mn_{12}}$-ac single crystal ($\rho = 1.84$ g/cm^3), the molecular mass ($M = 2060.3$ g/mol) and the volume of the single crystal used in the experiment ($V = 0.3 \times 10^{-3}$ cm^3):

$$N = \frac{V \rho N_A}{M} = \frac{0.3 \times 10^{-3} \cdot 1.84 \cdot 6.022 \times 10^{23}}{2060.3} = 1.6 \times 10^{17}, \tag{2.37}$$

where N_A is the Avogadro number. The reversal of the magnetization in the experiment set ① is approximately $2M_S$, as can be seen in figure 2.22. Therefore the Zeeman energy released in the reversal process is

$$E_\mathrm{Zeeman} \simeq 25 \ \mu\mathrm{J}, \tag{2.38}$$

that has to be compared with the Joule energy transmitted to the sample. As we have seen that all the pulses generate the same relaxation response we can compare the Zeeman energy with the maximum energy transmitted to the sample due the Joule effect on the heater (Eq. 2.27) in the lowest energetic pulse scenario

$$\frac{E_\mathrm{Zeeman}}{E_\mathrm{MaxJoule}} \approx \frac{25 \ \mu\mathrm{J}}{0.25 \cdot 0.5 \ \mu\mathrm{J}} = 200.$$

The Zeeman energy is more than two orders of magnitude larger than the energy supplied by the heat pulse. Hence, the increase in the temperature of the sample that rules the magnetization reversal process is mainly due the Zeeman contribution. Even more, as the ratio goes to 2 when the 50 μJ are supplied to the heater while the temperature of the sample does not show a rising (all the relaxation give the same temperature, with very low discrepancy), one can consider that: one, the heat transmission to the sample is even worst than the one fourth estimation; and two, the threshold energy to start the reversal process is much smaller than 0.1 μJ (under this conditions 0.45 T, 1.6 K).

To finally determine if the process can be considered as a deflagration we will compute the correspondent speed and width of the deflagration process. According to previous experiments, the speed of a deflagration front in Mn_{12}-ac follows

$$v_{\mathrm{d}} = \sqrt{\kappa \Gamma_0} \exp\left(-\frac{U(H)}{2k_B T_{\mathrm{f}}}\right), \tag{2.39}$$

with κ in the range of 10^{-5}–10^{-4} m^2/s [32]. Considering the temperature obtained from the fitting as the flame temperature T_{f}, and the values and uncertainties for a Mn_{12}-ac single crystal from page 45, we can compute the value of speed

$$v_{\mathrm{d}} = 26 \pm 32 \text{ mm/s}, \tag{2.40}$$

and the width of the front

$$\delta_{\mathrm{d}} = \sqrt{\kappa \tau} = 1.71 \pm 0.86 \text{ mm}, \tag{2.41}$$

approximately the size of the sample, which would explain why a narrow front of reversing spins has not seen in this case. However, the obtained speed is approximately one order of magnitude smaller than the obtained for the same field (at 2 K) in the experiments reported by Hernández-Mínguez et al. [33].

In the experiment set ② the goal was to study the dynamics of the process under different ignition conditions. In the figure 2.23 the time evolution of the average gray level of the four ROIs **1**–**4** is shown, along with the time evolution of the background (ROI **5**). Four different fields were applied at 1.6 K, while the heat pulse parameters were the same in all experiments (10 ms, 10 V). In the figure we can see how the field applied parallel to the easy axes of the sample and of the MOL affects the sensitivity. As mentioned before, the average gray levels tend to decrease with the increasing in-plane field and also due the pre-trigger relaxation that the sample presents as the ignition field approaches to the first resonant field. The first two rows of plots contain also the measurements at 1.5 K, represented in light colors.

Looking at the signals obtained in ROIs **3** and **4** we observe the absence of a clear sign associated to a propagating front. Remember that this two regions were

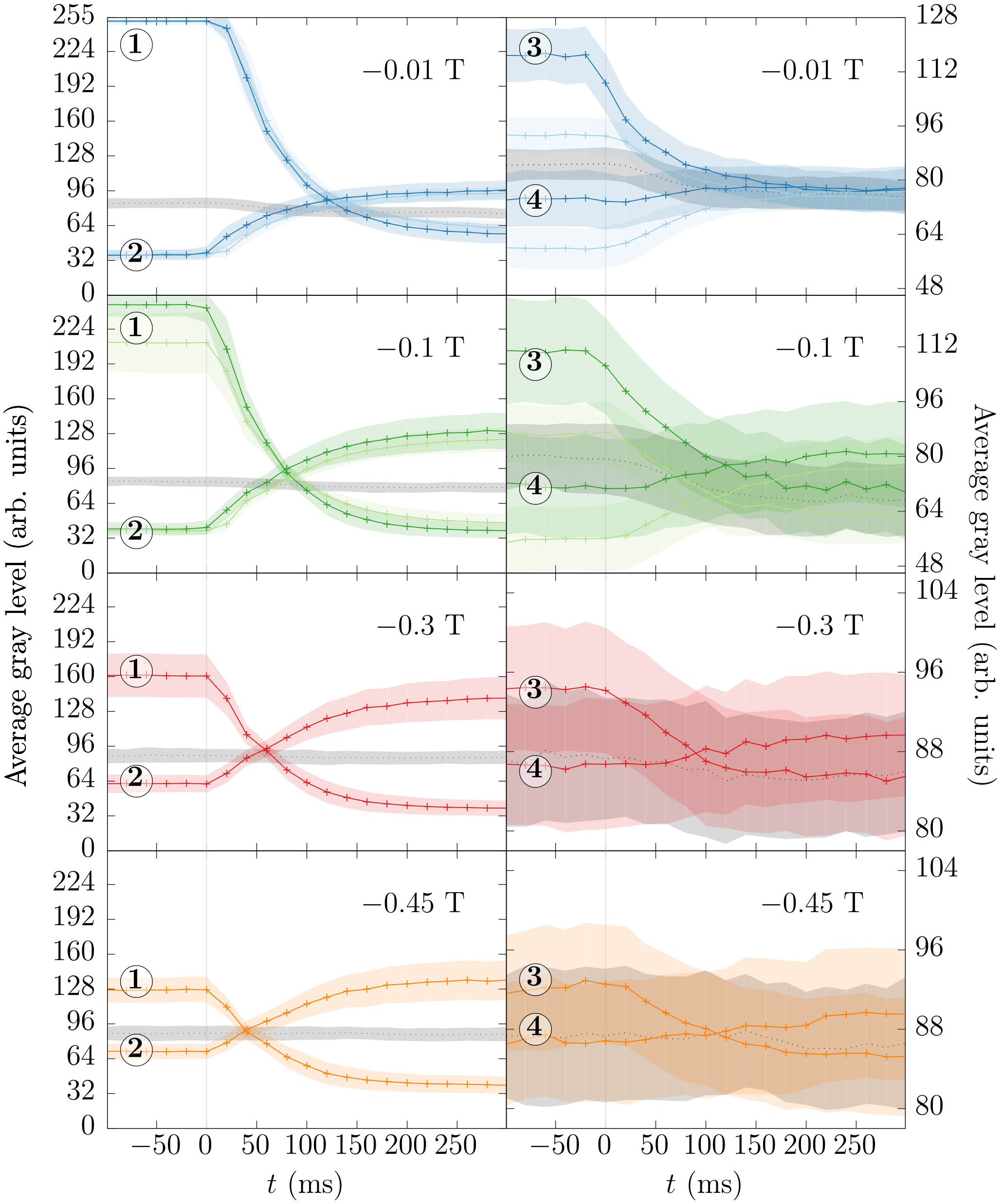

Figure 2.23: Time evolution of the average gray level of ROIs **1** and **2** (left panels) and ROIs **3** and **4** (right panels) in the experiment set ②. The gray line represents the average gray level of ROI **5**. The time $t = 0$ is defined by the frame above which the average gray level starts to change monotonically. The standard deviation of the average gray level at every ROI is represented with a transparent envelope. The expected peak originated by a propagating front passing through ROIs **3** and **4** is not observed.

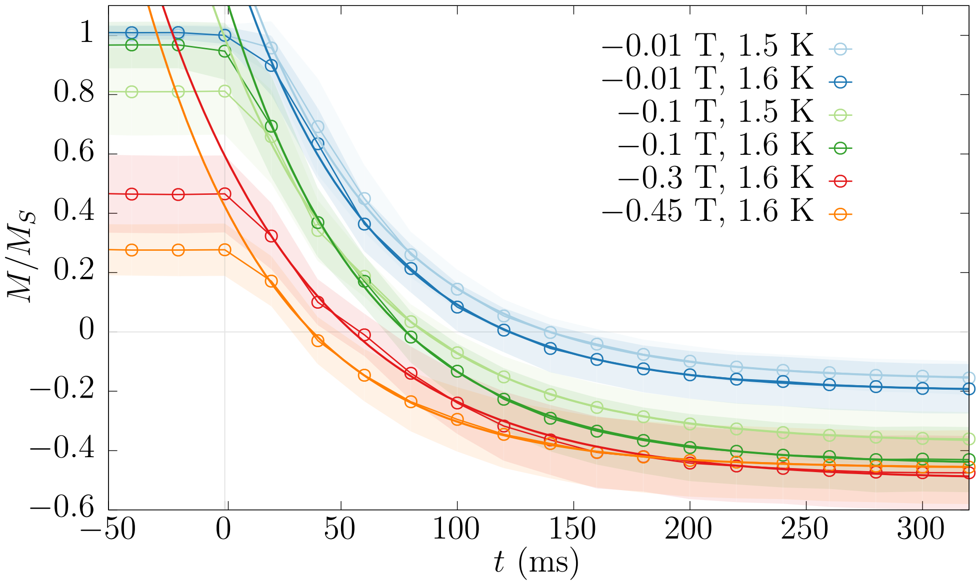

Figure 2.24: Temporal evolution of the magnetization (defined by Eq. (2.32)) divided by the saturation magnetization M_S for the experiment set ②. The solid lines represent the fit of Eq. (2.33) to the experimental curves. Experimental points are connected as a guide to the eyes only.

defined perpendicular to the expected deflagration front. If a front of magnetization change would have crossed those regions we should have obtained a peak in their gray levels.

Fig. 2.24 shows the temporal evolution of the normalized magnetization (defined using Eq. (2.32)). The fits of Eq. 2.33 revealed a surprisingly similar value of τ for the different magnetic field-temperature configurations:

Experiment	τ (ms)
−0.01 T, 1.5 K	61.8(8)
−0.01 T, 1.6 K	60(1)
−0.1 T, 1.5 K	66(1)
−0.1 T, 1.6 K	61(1)
−0.3 T, 1.6 K	70(3)
−0.45 T, 1.6 K	57(1)

The numbers in parenthesis correspond to the uncertainties from the fitting procedure. Taking into account the standard deviation of the gray levels, we can consider all the obtained values of τ equivalent. I. .e, we found that the speed of the deflagration process is independent of the magnetic field. This is in clear contradiction with the theory an the previous experiments on magnetic deflagrations. Nevertheless, what we have actually found is a limitation in the experimental technique. It was not considered during the experiments, but this results clearly imply an intermediate step in the recording procedure. The setup used was able in principle to measure changes with a temporal resolution of 20 ms, but in the experiments that used to be performed in Dr. Wijngaarden's laboratory the needs were focused in the spatial resolution, which they increase averaging several images. Therefore, we now see that the each image obtained is the result of using Eq. (2.24), but taking into it the two previous images (-80 and -40 ms), instead of computing it for every new recorded image. Therefore, this effective "moving average" spreads the temporal width of the deflagration and diffuses the intensity of the front. I.e., the effective temporal and spatial resolution arte reduced avoiding the correct measurement of the speed of deflagrations upon a certain threshold. A fast change ($\lesssim 20$ ms) would be "extended" up to 60 ms, which explains the obtained results. The slower the deflagration the better the measurement would be.

2.5 Conclusions

In this second chapter I have introduced the main subject of my thesis, the magnetic deflagration phenomenon, and also I have presented the first reported measurements of magnetic deflagrations using magneto-optical techniques.

The magneto-optical imaging method allowing the investigation of local dynamics of the magnetization with very large spacial and temporal resolutions, of the order of the 1 μm and several milliseconds. Therefore, we considered this tool a perfect candidate to the study of the propagation of magnetic deflagrations in $\mathrm{Mn}_{12}-$ac. To the date, magnetic deflagrations were studied using arrays of Hall sensors, or arrays of pick-up coils; with a spatial resolutions of tens to hundreds of micrometers respectively. However, the temporal resolution achieved using pick-up coils remains unequaled.

The results obtained in this chapter show a fast reversal of the magnetization of a $\mathrm{Mn}_{12}-$ac single crystal. The process starts at one end of the sample when the magnetic relaxation is triggered using a heater. At a certain moment, both ends of the sample have the magnetization pointing in the same direction, and finally the magnetization of the sample is fully reversed. This evidences the occurrence of a propagating front of change in magnetization, which is the hallmark of the magnetic deflagration, together with the generation of heat. This also was considered looking at the time constant associated with the magnetic relaxation at the ends.

In summary, for the first time a magnetic deflagration phenomena was registered with large spatial resolution. Improving the temporal resolution would open the doors to a detailed study of phenomena like cold magnetic deflagrations or pulsating regimes of magnetic deflagrations, both predicted theoretically [61, 62]

CHAPTER 3

Magnetic properties of Nd_5Ge_3

In this chapter are presented the magnetic and crystalline properties of the system that is the main object of study in this thesis, the intermetallic compound Nd_5Ge_3. First I will introduce briefly some of the properties of the rare-earth intermetallic compounds family R_5Ge_3 and the crystal and magnetic structure of the Nd_5Ge_3 itself, as an introduction to set the framework to show the results of the magnetic characterization measurements.

3.1 Crystalline and magnetic structure of Nd_5Ge_3

The intermetallic compound Nd_5Ge_3 belongs to the family of R_5M_3 compounds, where R correspond to rare earths and M to p-block elements. The family comprises a variety of compounds such as R_5Si_3, R_5Ge_3, R_5Ga_3, R_5Pb_3 and R_5Sn_3. While the crystal structure of these binary compounds depends upon the atomic sizes of R and M as well as the type of the p-block element, most of them crystallize in the Mn_5Si_3-type hexagonal structure [63] (a structure type with space group $P6_3/mcm$ and present in more than 400 compounds [64]). In this structure, the R atoms occupy two inequivalent crystallographic $4d$ and $6g$ sites located at (1/3, 2/3, 0) and (x_R, 0, 1/4). I. e., the layers formed by rare-earth ions are stacked along the hexagonal c-axis in an A-B-A-C sequence as is shown in Fig. 3.1 (the crystallographic structures presented in this chapter are made with the program VESTA [65]).

Due to the different near-neighbour environment associated with the two sites, this compounds typically show complicated magnetic structures. A variety of behaviours such as the coexistence of antiferromagnetic and ferromagnetic compo-

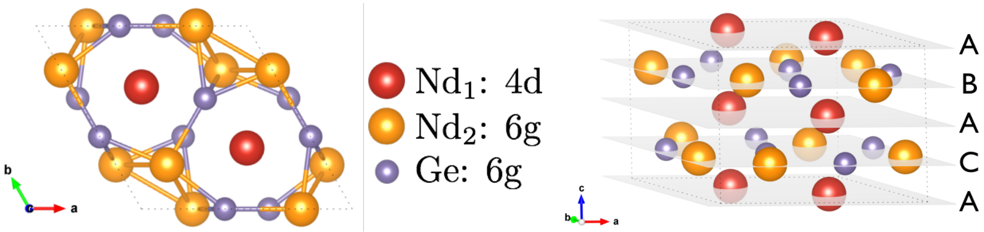

Figure 3.1: Crystallographic structure of Mn_5Si_3. In this figure, is represented the crystallographic structure of Nd_5Ge_3 with its appropriate dimensions.

nents, non-commensurate amplitude-modulated and conical spin structures, and field-induced magnetic configurations are observed.

3.1.1 The rare-earth intermetallic compounds R_5Ge_3

The R_5Ge_3 family of compounds was first studied by Buschow and Fast using polycrystalline samples [66]. The compounds R_5Ge_3 are brittle silvery metals, and fairly resistant to air oxidation. As mentioned before, this family is one of the R_5M_3 members that form an isomorphous series crystallizing in the hexagonal Mn_5Si_3-type of structure.

Fig. 3.2 shows the lattice constants ratios of the Mn_5Si_3-type members of the family R_5Ge_3. In the top panel are represented the ratios between the $a(b)$-c lattice constants of the R_5Ge_3 compounds and the $a(b)$-c lattice constants of the La_5Ge_3. The decrease observed is originated by means of what is commonly known as the “lanthanide contraction”. This phenomenon consist in a reduction of the atomic radius of the lanthanide atoms because as the 4f subshell, which is filled across these elements, is not very effective at shielding the outer shell (n = 5 and 6) electrons. It can not counter the decrease in radius caused by increasing nuclear charge. The ionic radius reduction in the lanthanide series is more than a 15%, from 103 pm for La^{3+} to 86.1 pm for Lu^{3+}, while the nuclear charge increase is a 24%, from 57 for La^{3+} to 71 for Lu^{3+}. In the bottom panel of the figure are represented the ratios between the $a(b)$ and c lattice constants of the R_5Ge_3 compounds. The ratio remains approximately constant for all members. In both panels the values corresponding to the compound Yb_5Ge_3 seem not to follow the trends of the rest of the family. The origin of this discrepancy lies in the intra-atomic interactions, that favours the filling of the sub-band by transferring an electron from the conduction bands to an f state, predominantly at the expense of the d electrons. The binding contribution of those electrons to the electronic shielding is thereby reduced, causing a substantial increase in the atomic volume.

In their study, Buschow and Fast showed bulk magnetization measurements

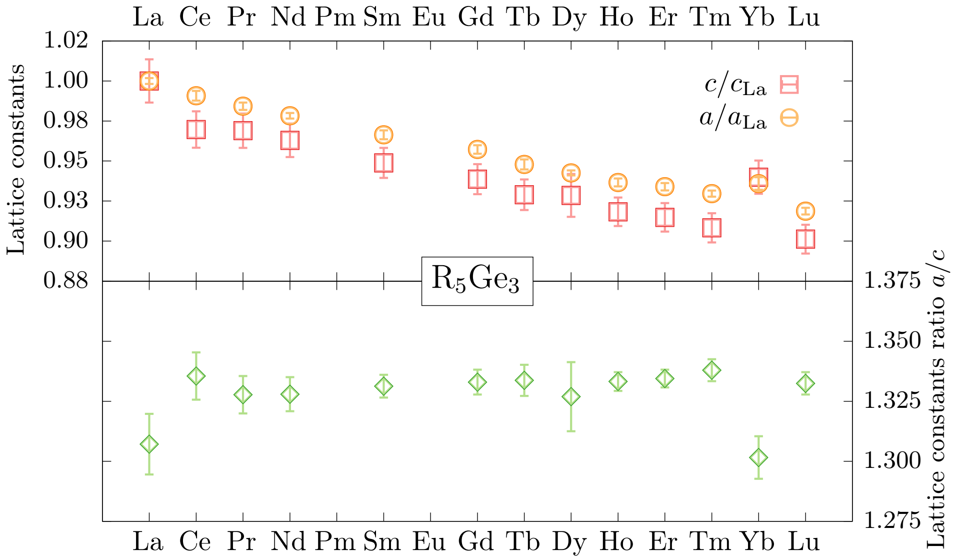

Figure 3.2: Lattice constants ratio of the Mn_5Si_3-type members of the family R_5Ge_3. No data was found for Pm_5Ge_3, and Eu_5Ge_3 crystalizes in a Cr_5B_3-type structure. Data from Springer Materials [67].

from which the magnetic ordering of different compounds was inferred: Ce_5Ge_3 and Nd_5Ge_3 as ferrimagnets and Pr_5Ge_3, Tb_5Ge_3, Dy_5Ge_3, Ho_5Ge_3 and Er_5Ge_3 as weak antiferromagnets at low temperature and exhibit a field induced metamagnetic transition (they also studied Yb_5Ge_3 and Sm_5Ge_3 but since the samples were not obtained in single phase they did not showed them in the report).

In the literature we find some papers on R_5Ge_3 polycrystalline compounds [68–79]. Nevertheless, despite the rich phenomena present in the members of the R_5Ge_3 family and their typical crystalline anisotropies, there are very few reports on single crystals. A single crystal of Ce_5Ge_3 was reported to show dense Kondo behaviour [80], Doerr et al. reported magnetostructural irreversibilities on single crystals of Gd_5Ge_3 and Nd_5Ge_3 (Ref. [81]), Tsutaoka et al. reported, on single crystals of Gd_5Ge_3 and Tb_5Ge_3, magnetization and electrical transport properties [82] and irreversible magnetic field-induced metamagnetic transitions on single crystal of Nd_5Ge_3 (Ref. [83]), and Joshi et al. reported field-induced ferromagnetic behaviour in the antiferromagnetic single crystals of Pr_5Ge_3 and Tb_5Ge_3 (Ref. [84]).

3.1.2 Magnetic structure of Nd_5Ge_3

The first magnetic experiments on Nd_5Ge_3 reported by Buschow and Fast [66] showed that, together with Ce_5Ge_3, the Nd_5Ge_3 intermetallic compound, param-

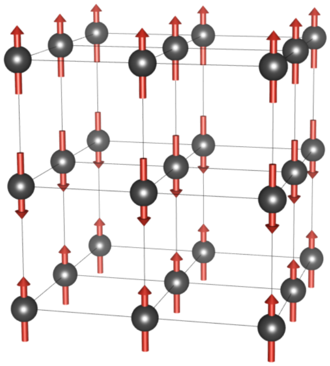

Figure 3.3: The type A antiferromagnet consists in alternately aligned ferromagnetic planes.

agnetic at room temperatures, become ferrimagnetic at low temperatures, possessing a remanent magnetic moment when studied at 4.2 K at various magnetic field strengths. The observed value for the saturation magnetization at this temperature was 1.92 μ_B per Nd atom, just 3/5 of the theoretical saturation value per Nd atom if all Nd atoms were aligned parallel to one another (and if the magnetic moment per Nd atom corresponds to the free ion value for Nd^{3+}). In their report Buschow and Fast comment that the value observed would be expected if all $6g$ Nd atoms were ordered ferromagnetically while the $4d$ were ordered antiferromagnetically. They note, however, that the saturation values in rare-earth intermetallics must be handled carefully since deviations from the theoretical values are likely to occur as a cause of partial quenching of the orbital momentum by the crystal field. Nevertheless, they indicate that the possibility of a mixture of antiferromagnetic and ferromagnetic interactions has to be considered due the positive Curie temperature observed, which suggests that a relatively weak antiferromagnetic exchange interaction might exist between magnetic sublattices, while the magnetic interactions within a certain sublattice might be relatively strong. This behaviour corresponds to layered structures like the antiferromagnetic A-type [85] and is represented in figure 3.3.

Obviously, neutron diffraction experiments were necessary in order to understand the magnetic structure of Nd_5Ge_3. Schobinger-Papamantellos and Buschow, twenty years later than the original paper from Buschow, presented a report where the magnetic properties of Nd_5Ge_3 were studied by neutron diffraction [86]. In the report the authors propose a magnetic structure that consists in a collinear double sheet structure for the Nd atoms at the $6g$ position and a canted structure for the $4d$ atoms, with the main axis of antiferromagnetism parallel to the c direction. The model proposed accounts for a saturation moments for both Nd positions of

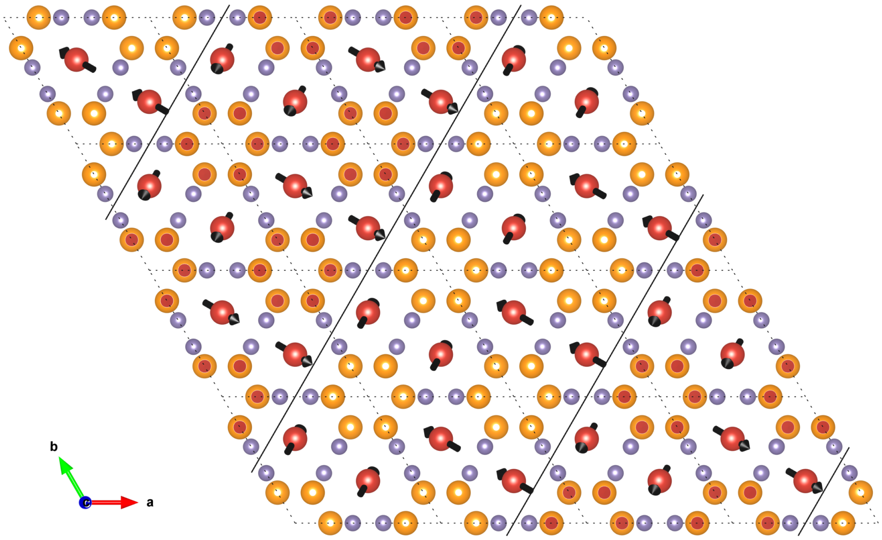

Figure 3.4: Magnetic structure of Nd_5Ge_3 at low temperature and zero applied magnetic field. Projection in the basal hexagonal plane. The $6g$ atoms (orange) order with a collinear antiferromagnetic structure along the c-axis and change sign (red dot up, white dot down) every two (110) planes (double sheet structure). The $4d$ atoms (in red) have a component in the hexagonal base that rotates 90° every (110) plane, and the c-axis compoment that changes in sign as the $6g$ atoms. This structure is proposed in Ref. [86].

1.39 and 1.34 μ_B respectively, which are well below the free ion value of 3.62 μ_B, a reduction due crystal field effects. In the model proposed the magnetic lattice is commensurate with the crystal lattice but with a cell enlargement of $4a$, $4b$, c, where a, b, and c correspond to the crystallographic axes, i. e., with a propagation vector $\vec{k} = (0.25,\ 0,\ 0)$. This model is shown in Fig. 3.4.

They studied the temperature variation of the magnetic intensity at zero applied magnetic field of the (010) magnetic reflection and the nuclear (102) reflection (the indices refer to the ortohexagonal and hexagonal unit cell respectively) (see Fig. 3.5). The 4.2 K neutron diagram of Nd_5Ge_3 in the mentioned work was characterized by a strong antiferromagnetic peak at low angles. The intensity of nuclear reflections having Nd contributions to their structure factor (such as (102) reflection) was found to be temperature independent. This fact is in apparent contradiction with the results of magnetization measurements since it excludes the occurrence of ferromagnetism below the magnetic ordering temperature, but one has to keep in mind that neutron diffraction experiments were performed at

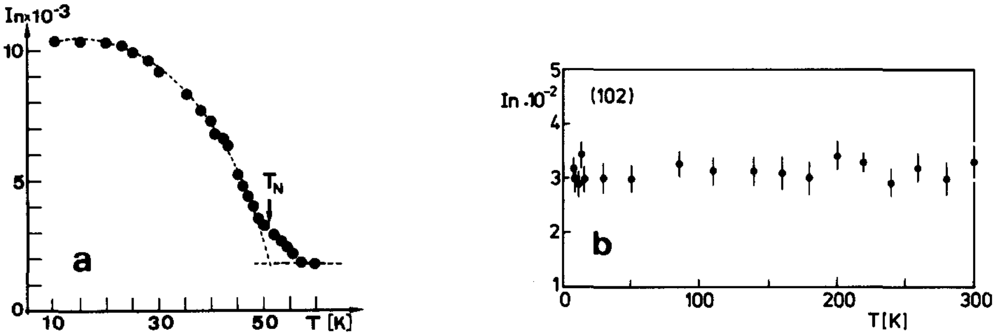

Figure 3.5: Temperature variation of the magnetic intensity of the neutron diffraction peaks. Panel a: Magnetic reflection peak (010) referred to the magnetic structure. Panel b: nuclear reflection peak (102), referred to the crystalline structure. Figure extracted from Ref. [86].

zero applied magnetic field, and this field probably induces a structural transition in the crystal (or a deformation) which accommodates the magnetic moments leading a ferromagnetic interaction between them.

According to their results the $6g$ and $4d$ symmetry positions show a different kind of magnetic order. The $6g$ atoms have a collinear arrangement along the c-axis with $\mu = 1.39(9)\ \mu_B$, the moment value in the basal plane being undefinable. By contrast the $4d$ atoms have a canted arrangement with $\mu_z = 1.16(25)\ \mu_B$ and $\mu_x = 0.7(4)\ \mu_B$. The angle describing the magnetic moment deviation from the z axis equals 31°. The refined moment values of both symmetry positions $1.39(9)\ \mu_B$, $1.34(6)\ \mu_B$ are significantly lower than the moment expected for free ion Nd^{3+}. Nevertheless, the average Nd moment observed in the saturation ($1.92\ \mu_B$) is substantially hight than each of the two Nd moments found by means of neutron diffraction. To explain this discrepancy, the authors proposed that either the field-induced magnetic transition is accompanied by a marked increase in Nd moment, or the neutron diffraction measurements where affected by a certain disorder in both Nd sublattices in zero field.

In a recent study, Vokhmyanin et al. presented new results on neutron diffraction on Nd_5Ge_3 at 10 K and room temperature [87]. In this work the proposed magnetic structure consists in a spin wave type with a wave vector $k \approx (0.187,\ 0,\ 0)$, and with the moments directed along the c-axis in both $4d$ and $6g$ positions, with a magnetic moments $2.6(1)\ \mu_B$ and $1.9(1)\ \mu_B$ respectively. This values are more reasonable to explain the saturation values of the Nd_5Ge_3.

Tsutaoka et al. outlined an investigation of the magnetic field induced irreversible AFM→FM transition by means of neutron scattering [88]. In this report they show an important result. It was suggested previously, by Maji et al. [74]

and Tsutaoka et al. [83], that the irreversible metamagnetic field induced transition could take place by a martensitic structural transition, like in Gd_5Ge_4 [89]. Nevertheless, the data obtained in this neutron diffraction study under an external magnetic field at 1.5 K showed that, while the magnetic reflections present an irreversible change by the field induced transition, the reflection peaks at the nuclear positions did not change during the isothermal magnetization process, refusing the structural change in the crystal as the origin of the magnetic phase transition nor its irreversibility.

3.2 Magnetic characterization of single crystals

In this section the magnetic characterization of single crystals of Nd_5Ge_3 is presented. The purpose is not just to reproduce the measurements already reported (some of them only in polycrystals), but also to study in detail some of the magnetic properties that will be useful in the following chapters of this thesis. The magnetic measurements performed comprise zero-field and field cooled processes, isothermal magnetization curves, temperature and frequency dependence of ac-susceptibilities, and thermoremanent magnetization relaxation.

The Nd_5Ge_3 single crystals studied in this thesis were provided by Prof. Tsutaoka from Hiroshima University. Here I describe concisely the fabrication procedure: First polycrystalline ingots are prepared by arc-melting the constituting 99.9%-pure Nd and 99.999%-pure Ge elements under high-purity argon atmosphere. Then the compounds are studied by powder X-ray diffraction to ensure they are single-phase. From that single-phase polycrystalline samples single crystals are grown by the Czochralski method using a tri-arc furnace. It should be noted that it is difficult to grow a large single crystal of Nd_5Ge_3; the grown crystal ingots tend to have small single-crystalline grains. The samples were cut from the ingots into a rectangular shape (e. g., $1 \times 1.5 \times 2$ mm^3) and annealed at 300°C for 24h in an evacuated quartz tube. Finally the crystal orientation is determined by the back-reflection Laue method. The long axis of the samples corresponds to the crystallographic c–axis.

3.2.1 The MPMS® system and its magnetometer

The magnetization measurements presented in this chapter were performed using a Superconducting Quantum Interference Device (SQUID) magnetometer, part of Quantum Design®'s Magnetic Property Measurement System (MPMS®). Here I will describe briefly the properties of this device.

The MPMS® in our laboratory is used in most of the experiments of this thesis. It was one of the first to be installed in Europe, more than 25 years ago, and, despite its age and the fact that has been improved in many non-supported ways it works flawlessly, the most part of the time. While the aim of the MPMS® is to measure magnetization using its own magnetometer (SQUID), with our device, as we will see in the next chapters, we can study also electrical transport, ferromagnetic resonance, induced magnetic deflagrations. . .

Back to the original purpose for which MPMS was made for, a schematic representation of the system is shown in Fig. 3.6. It consists of a ^{4}He dewar, with an insert that consists in turn of a cryostat with a superconducting solenoid, a tube that connects with the exterior where the sample is introduced, a set of superconducting pick-up coils in a longitudinal second-order gradiometer configuration, and the SQUID magnetometer placed at the bottom, inside a superconducting magnetic shield. The range of fields and temperatures that a given MPMS® system can reach depends on particular versions and/or upgrades. Our instrument has the following working ranges:

1. Temperature range: 1.8 – 350 K
2. Magnetic field range: up to 5 T

with a cooling rate up to 10 K/min (lower below 10 K), and a fixed magnetic field sweeping rate of 300 Oe/s with the dedicated power source (using an external power source we can also control the sweeping rate –while 300 Oe/s is still the limit due magnet's inductance).

As mentioned, the magnetization of the sample is measured with a SQUID magnetometer, that comprises of a second-order gradiometer (counter-wound pick-up coils) connected inductively to two parallel Josephson junctions in a superconducting ring. The sample is mounted in a non-magnetic sample holder and then placed on the end of a non-magnetic sample rod between the pick up coils. The movement of the sample through the gradiometer induces a current in the coils due to Faraday's law of electromagnetic induction. The SQUID then functions as an extremely sensitive current to voltage converter, outputting the change in magnetic flux measured by the pick-up coils as a voltage response. The SQUID voltage is then measured at a number of sample positions along the scan length. This SQUID response is fitted to the theoretical signal of a point-source magnetic dipole using either iterative or linear regression algorithms, and the magnetic moment of the sample is then extracted. SQUID magnetometers are capable of measuring very small magnetic moments, in our case with a resolution of 5×10^{-8} emu.

3.2.2 Isofield magnetization

It is somehow common in characterizing a magnetic material to start with the temperature dependence of the magnetization following two processes. The first

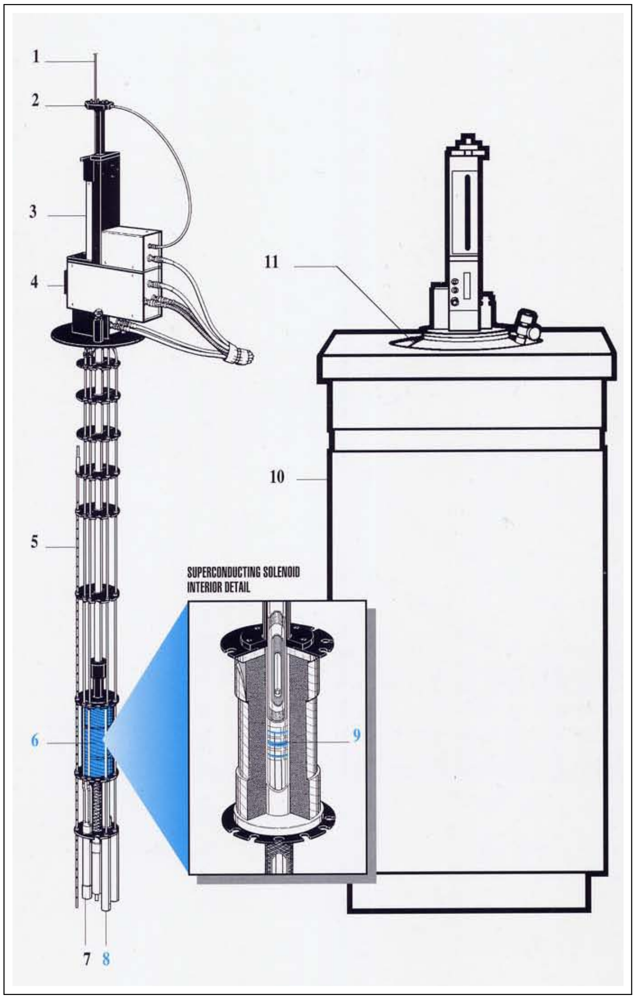

Figure 3.6: Schema of the components of the MPMS® instrument. Superconducting elements are shown in blue. Components: **1**. Sample rod, **2**. Sample Rotator (not available in our setup), **3**. Sample Transport, **4**. Probe Assembly, , **5**. Helium Level Sensor, **6**. Superconducting Solenoid, **7**. Flow Impedance, **8**. SQUID Capsule with Magnetic Shield, **9**. Superconducting Pick-up Coil, **10**. Dewar Isolation Cabinet, **11**. Dewar. Figure extracted from vendor's datasheet.

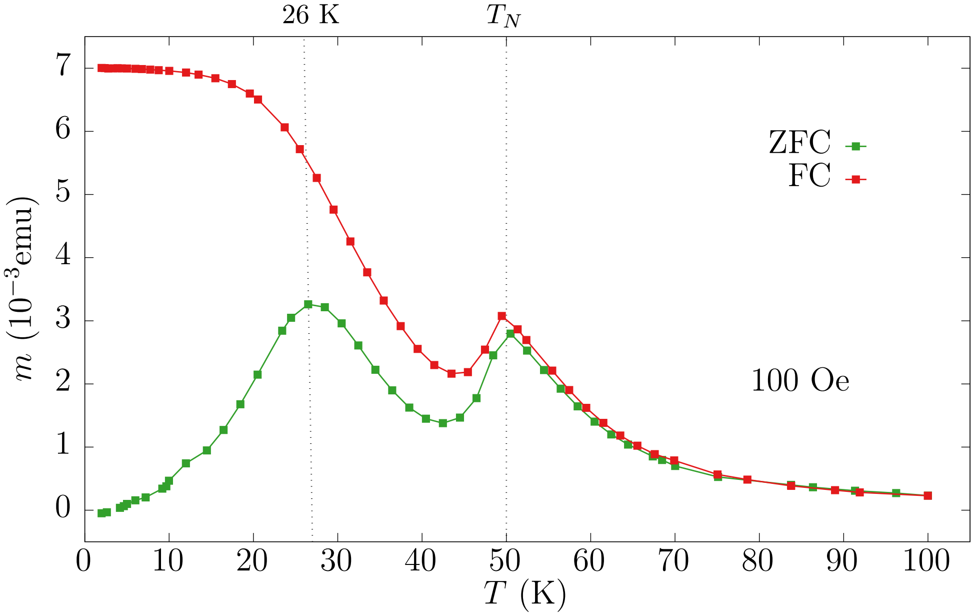

Figure 3.7: ZFC (green) and FC (red) magnetization processes with an applied magnetic field of 100 Oe along the c-axis.

process, known as zero-field cooled (ZFC) consists in cooling down the sample at zero applied magnetic field. Then, a magnetic field is applied. Usually this field is small, < 1 kOe, in order to avoid large modifications of the magnetic energy barriers of the system. With the magnetic field applied, the temperature is then raised while the magnetization is measured. The second process, known as field cooled (FC) consists in cooling down the sample but with the magnetic field applied during the process. Sometimes the magnetization is recorded during the cooling down process (known as field cooled cooling – FCC), and sometimes during the warming process (known as field cooled warming – FCW). If it is not specified, the FC is a FCW process (it is easier to warm the sample keeping a constant rate than cooling it, especially at low temperatures). The study of ZFC-FC curves is mainly focussed in the search of magnetic transitions where the system goes from paramagnetic at hight temperatures to an ordered state ferromagnetic, antiferromagnetic, ferrimagnetic, or even an unordered state like a spin-glass, as the temperature is lowered.

Fig. 3.7 shows the ZFC-FC measurements of a single crystal of Nd_5Ge_3 with an applied magnetic field of 100 Oe along the c-axis. In the ZFC process we observe two peaks. The peak at 50 K corresponds to the Néel temperature, separating the high temperature paramagnetic phase from the low temperature antiferromagnetic state. The peak that appears at 26 K has been object of many

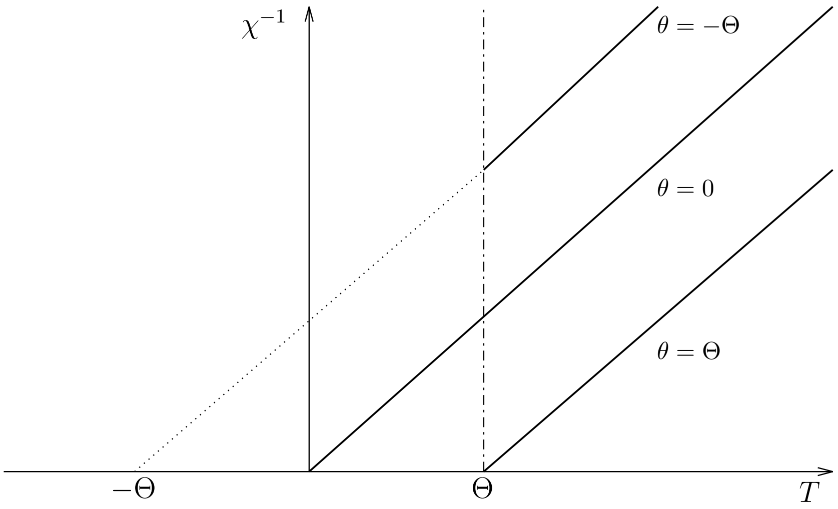

Figure 3.8: Reciprocal susceptibility against temperature. Straight lines represent the Curie-Weiss behaviour for a ferromagnet ($\theta = \Theta > 0$), a paramagnet ($\theta = 0$) and an antiferromagnet ($\theta = -\Theta < 0$).

speculations. Schobinger-Papamantellos and Buschow [86] proposed the existence of narrow Bloch walls in the ferromagnetic regions; Tsutaoka et al. [83] interpreted the peak as an indicator of a second antiferromagnetic transition, while at the end of the paper also consider the peak as a hint of weakness of the antiferromagnetic structure and suggested the possibility of the coexistence of antiferromagnetic and spin-glass states as has been proposed in Gd_5Ge_4 [90]; finally, Maji et al. [74] showed a bunch of experiments where spin-glass-like behaviour was plausible and suggested the existence of a cluster glass state below this temperature.

From the ZFC at 100 Oe we can obtain the molar DC magnetic susceptibility χ as a function of temperature, and therefore the reciprocal susceptibility χ^{-1}. In the paramagnetic state, for small applied magnetic fields, χ obeys the Curie-Weiss law,

$$\chi = \frac{C}{T - \theta}, \tag{3.1}$$

where θ is the Weiss temperature, and C is the Curie constant. If $\theta = 0$ the material is a paramagnet, while $\theta > 0$ and $\theta < 0$ mean, respectively, that the magnetic interactions in the system are of ferromagnetic or antiferromagnetic nature (see Fig. 3.8).

The magnetic molar susceptibility and the reciprocal magnetic molar susceptibility versus temperature in a 100 Oe external magnetic field for two different crystal orientations ($H \parallel c$-axis and $H \parallel c$-plane) are shown in Fig. 3.9.

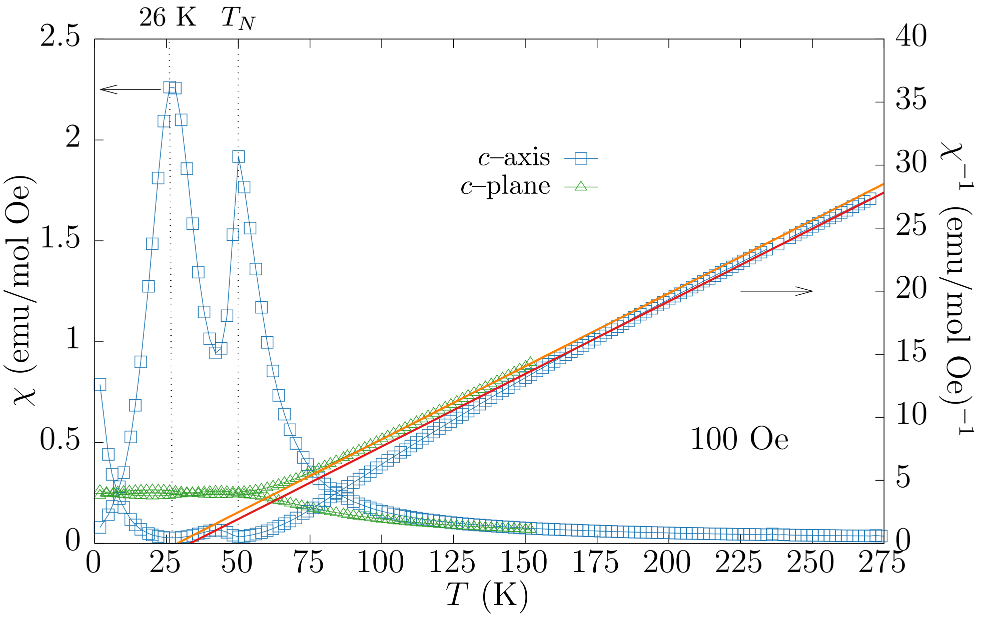

Figure 3.9: Magnetic molar susceptibility χ and reciprocal magnetic molar susceptibility χ^{-1} versus temperature in an external magnetic field of 100 Oe, for two different crystal orientations ($H \parallel c$-axis, $H \parallel c$-plane). Solid lines correspond to the fits of the data to the Curie-Weiss equation (3.1).

Well above the Néel temperature (50 K), the system magnetic susceptibility can be fitted to the Curie-Weiss equation (3.1) to get C and θ. The values obtained were:

$c-$ axis	$\mu_{\text{eff}} = 3.73(2)\ \mu_B,$	$\theta = 33(3)$ K
$c-$ plane	$\mu_{\text{eff}} = 3.715(4)\ \mu_B,$	$\theta = 28.7(3)$ K

with μ_{eff} being the effective magnetic moment per atom of Nd, which can be obtained from the Curie constant using the following expression:

$$C = \frac{nN_A\mu_0\mu_{\text{eff}}^2}{3k_B}, \tag{3.2}$$

where $n = 5$ (C is obtained in moles of Nd_5Ge_3), N_A is the Avogadro constant, μ_0 is the vacuum permeability and k_B is the Boltzmann constant. The values obtained are in agreement with those reported by Tsutaoka et al. [83]. The asymptotic positive Weiss temperature suggests dominant ferromagnetic interactions, which is plausible if the antiferromagnet is of type A with a weak antiferromagnetic interaction between ferromagnetic layers. The obtained values of the effective

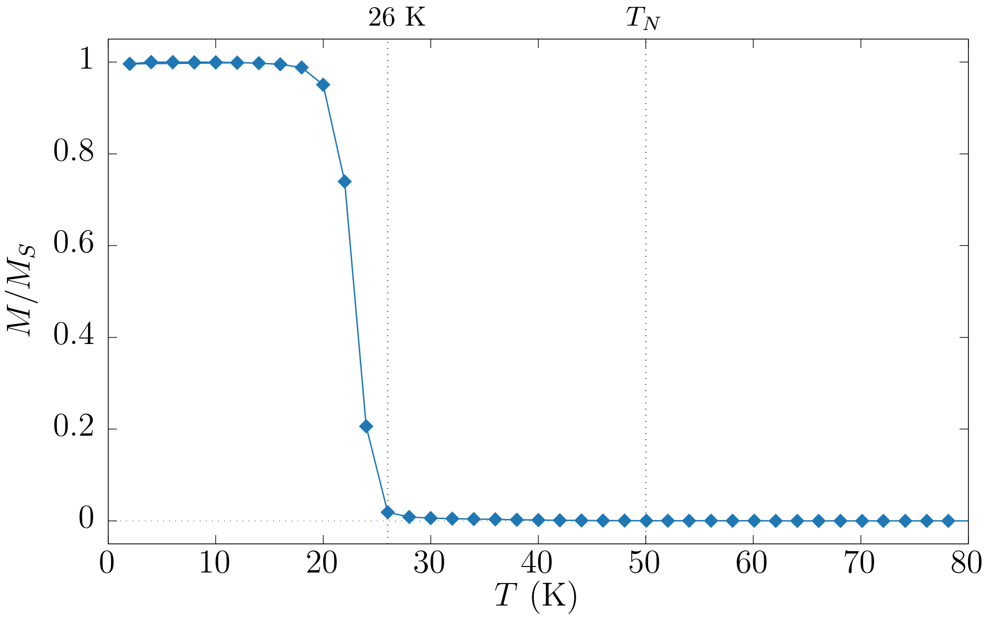

Figure 3.10: Thermoremanent magnetization (TRM) of the sample prepared in the saturated state using a FC process with 50 kOe.

magnetic moment per Nd atom coincide with the values of the magnetic moment of a free Nd^{3+} ion (3.62 μ_B).

In order to understand the nature of the peak at 26 K we performed other experiments. First we measured thermoremanent magnetization and AC-susceptibility experiments. The term thermoremanent magnetization (TRM) is given to the process of studying the dependence of the magnetic remanence (at zero applied magnetic field) with the temperature. The process starts with the sample magnetized (it can be magnetized following a FC process, or an isothermal magnetization process), then the magnetic field is removed and the magnetization is measured as the temperature is raised. Fig. 3.10 shows the TRM measurements on a single crystal of Nd_5Ge_3 after magnetizing the sample up to the saturation in a FC process with a magnetic applied field of 50 kOe. In the figure it is clear that the magnetization remains constants for $T < 20$K and goes to zero quickly before $T = 26$ K. The nature of the peak at 26 K may be related with the unblocking of magnetic clusters. In that case, due the narrow range of temperatures where the loss of remanence takes place, one may expect that: 1) the clusters are very similar (the barrier is almost identical) and/or 2) the existence of hidden mechanisms (for example self-heating of the sample) that enhances the relaxation rapidly and 3) a magnetic order-disorder transition within the clusters that destroys the energy barrier.

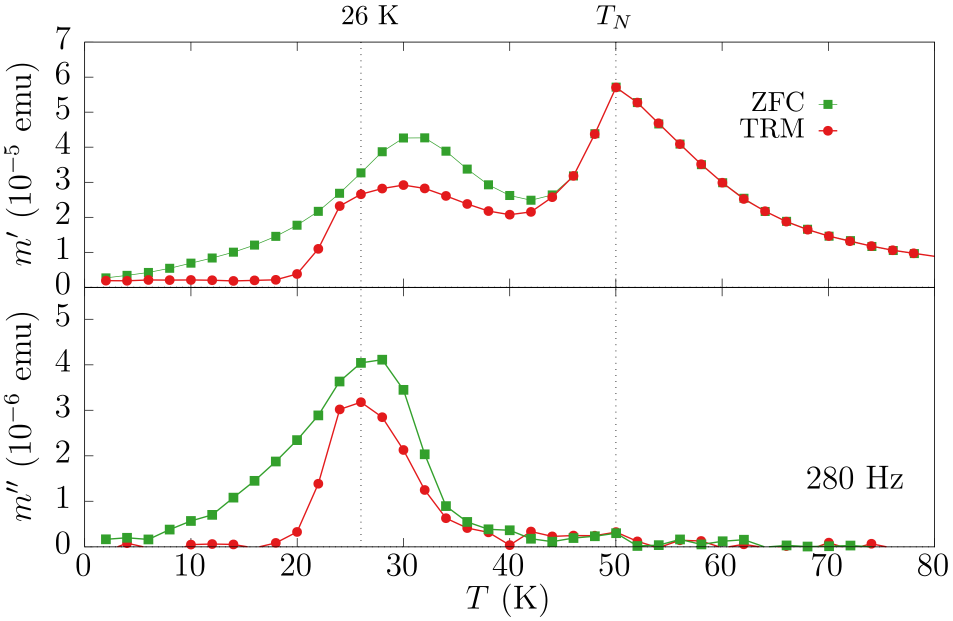

Figure 3.11: Temperature dependence of the real (top panel) and the imaginary (bottom panel) components of the AC susceptibility at $\nu = 280$ Hz at $H = 0$. Green points correspond to the sample prepared following a ZFC. Red points correspond to the sample prepared in the saturated state before setting $H = 0$ (remanent magnetization –TRM).

The AC measurements are shown in Fig. 3.11. AC measurements are an important tool for characterizing many materials because they yield information about magnetization dynamics which are not obtained in DC measurements, where the sample moment is effectively constant during the measurement time. In the limit of low frequency where AC measurement is most similar to a DC measurement; the real component of the AC susceptibility, χ' is just the slope of the $M(H)$ curve. The imaginary component of the signal, χ'', indicates the existence of dissipative processes. This dynamic measurements are a powerful tool for examining magnetic phase transitions, such as (anti)ferromagnetic transitions. We can see this at work in Fig. 3.11: we see a rapid increase in χ' as T is increased near 50 K in the ZFC and TRM curves. With mean field theory one can determine, using critical exponents, the nature of the divergence as a function of temperature and a superimposed DC applied field, allowing to distinguish between various models of magnetic interactions. Below 40 K we found differences between both ZFC and TRM curves. Below 20 K we see a magnetic response of the system to the ac magnetic field in the ZFC curve, while the TRM curve does not show any response. In a collinear AFM(FM) system with large energy barriers one does not expect to obtain magnetic susceptibility. From the TRM curve measured in DC (Fig. 3.10)

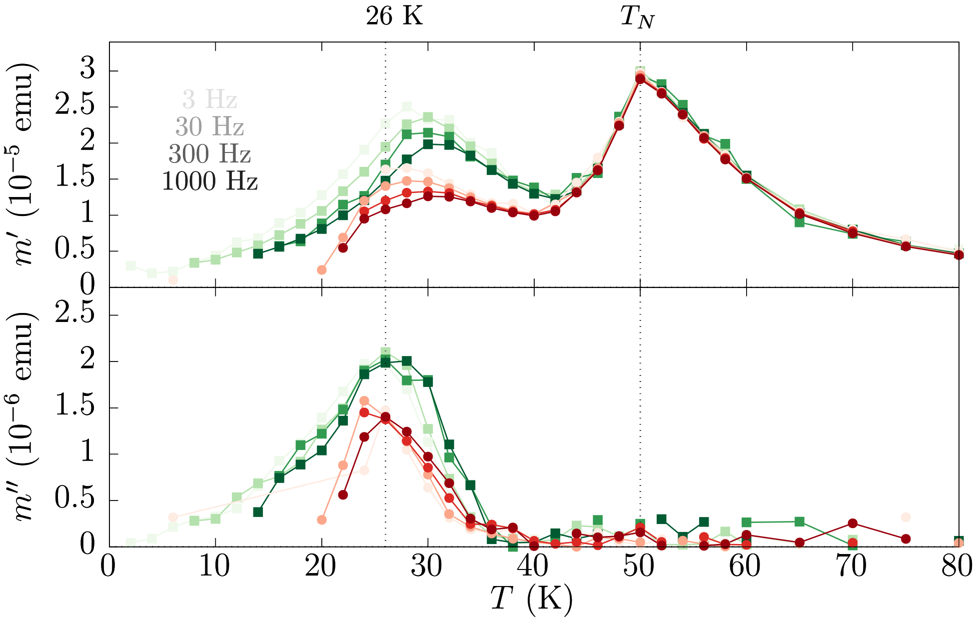

Figure 3.12: Frequency dependence of the AC measurements at $H = 0$. Top panel corresponds to the real part of the susceptibility, bottom panel correspond to the imaginary part. The preparation of the sample is the same than the previous figure, green ZFC and red TRM.

we see that below 20 K the system maintains its magnetization, i. e., is blocked in the FM saturated state. This is confirmed by the observed $\chi' \approx \chi'' \approx 0$. To explain the ZFC curve we consider the non-complete collinearity of the AFM state together with changes within the FM clusters/layers that form the A-type AFM state. It is also remarkable the difference between both ZFC and TRM curves in the range between 26 K and 40 K. Since the “shape” of both curves in that temperature range is certainly similar, we believe that what we are observing are different contributions of the same phenomenon: the susceptibility change within the FM clusters.

To the best of my knowledge, this is the first time that AC magnetic measurements on a single crystal of Nd_5Ge are reported. Maji et al. [74] presented AC susceptibility data on a polycrystalline sample which we could not reproduce in our experiments. In their measurements they found a peak on the χ'' at T_N which is not what one should expect from a antiferromagnetic phase transition [91], and also did not observed a peak in the χ around 30 K. Nevertheless they used their experiment to focus on the shift of the peak at χ'' around 30 K as a hint of a spin cluster transition. The empirical parameter $\delta_f = \Delta T_f / (T_f \Delta \log \nu)$, determines the relative shift of the spin freezing temperature. They obtained a value of 0.032 (wrongly, because they used the natural logarithm instead of the decimal); if the formula would had been used correctly they would had obtained a value of 0.089, closer to the expected for the presence of superparamagnetic clusters (~ 0.1) [92] instead of a spin glass system (~ 0.005) [93] or cluster glass systems (~ 0.01) [91, 94, 95]. The value obtained in our measurements (from peaks around 30 K in m' in Fig. 3.12) is 0.04. If we also consider the peak position of the DC measurement (the DC measurement can be treated as 1/30 Hz), we obtain a final value of $\delta f = 0.05$. This value keeps the question open about the presence of superparamagnetic clusters or the occurrence of a cluster glass system.

3.2.3 Isothermal magnetization

One of the main features of the system Nd_5Ge_3 is its magnetic field dependent dynamics. Among the members of the R_5Ge_3 family, Nd_5Ge_3 and Ce_5Ge_3 are the only compounds having remanent magnetization after the application of a magnetic field [66]. In this section I will show the magnetization curves at different temperatures, which will let the reader to understand the convenience of this system to be studied under the perspective of the magnetic deflagrations framework.

Rare-earth intermetallic compounds have large anisotropies due to the interaction of the highly anisotropic orbitals with the crystalline electric field [96]. The magnetic anisotropy of Nd_5Ge_3 was first investigated by Tsutaoka et al. [83]. In their work the magnetization curves were studied along the three crystallographic axes and under pulsed fields (up to 500 kOe). They found an easy axis of magnetization along the c-axis.

The measurements performed in our group confirm this large anisotropy (Fig. 3.13). The magnetization in the c-plane (plane perpendicular to the c-axis) increases linearly in the range of magnetic fields studied when the field is applied perpendicular to the c-axis. In the aforementioned work of Tsutaoka et al. they extended the range of fields up to 500 kOe without observing a saturation until the field was near to 400 kOe (Fig. 3.14). In the c-axis orientation, as the field is increased, we confirm the reported spontaneous metamagnetic AFM→FM transition at $H_{\text{sp-AFM}}$. Once this transition takes place the system remains in a hard FM state. When the field $-H_{\text{sp-FM}}$ is reached in the opposite direction of the magnetization of the sample, M, the spontaneous reversal of the FM occurs. These abrupt jumps in the magnetization curve are, perhaps, the most interesting aspect of this system. The fact that are large, spontaneous, abrupt, and present in two different parts of the magnetization curve, was the key factor we were looking for to study the occurrence of magnetic deflagration in systems beyond the single molecule magnets (SMM) like Mn_{12}−ac or Fe_8 (Ref. [4]).

To complete the isothermal magnetization characterization and to integrate them with the results for the temperature dependence, I measured the magnetization curves at different temperatures in the range between 2 and 60 K. Fig. 3.15

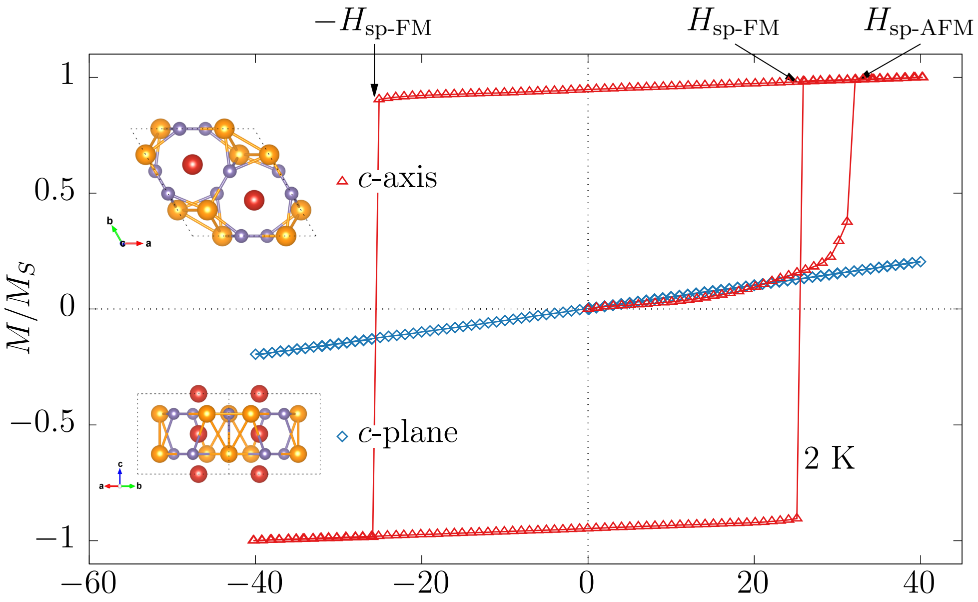

Figure 3.13: Magnetization curves along the *c*-axis and the *c*-plane at 2K, with a field sweep rate of 300 Oe/s. The spontaneous fields for the AFM→FM transition, $H_{\text{sp-AFM}}$, and for the FM reversal, $\pm H_{\text{sp-FM}}$, are marked on the top axis.

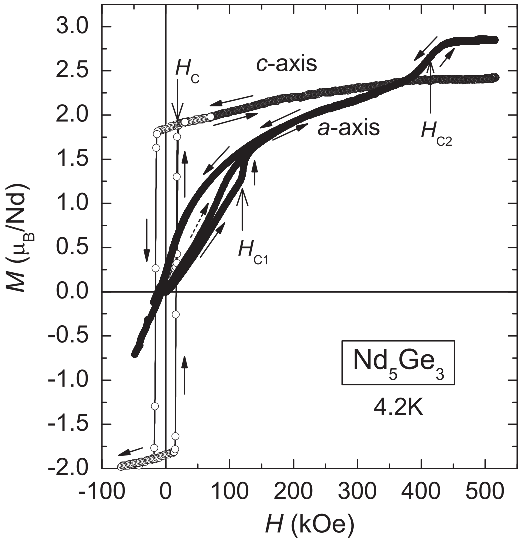

Figure 3.14: Magnetization curves along the *c*-axis and the *c*-plane at 4.2K measured in pulsed fields. Extracted from [83].

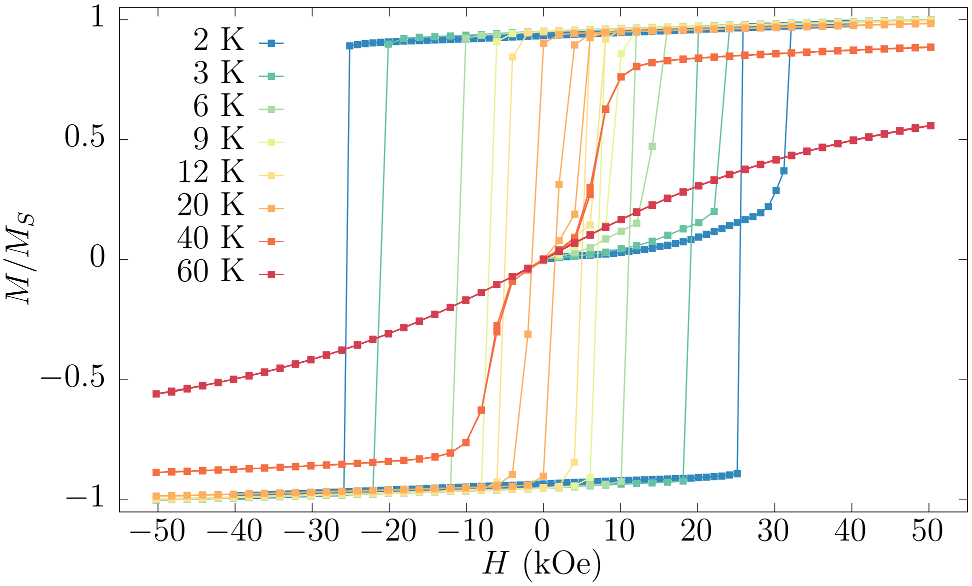

Figure 3.15: Magnetization curves along the c-axis in different temperatures in the range of 2–60 K.

show these measurements, with the magnetic field applied parallel to the c-axis and a magnetic field sweeping rate of 300 Oe/s. We can observe in the figure how the field at which the spontaneous jumps take place becomes smaller as the temperature is increased. Eventually, the magnetic remanence disappears between 20 and 40 K and the magnetic field transition does as well between 40 and 60 K. This results are in agreement with the work of Tsutaoka et al. that set the temperatures at which remanence disappears and AFM→FM transition takes place to be 26 and 50 K respectively. Note that the former was already obtained in the study of the thermoremanent magnetization (Fig. 3.10), and the later is T_N, as expected from the ZFC curve (Fig. 3.7).

3.2.4 Magnetic relaxation

Magnetic relaxation is another useful measurement to be performed on a magnetic material with hysteresis. The experiment consists in measuring the temporal evolution of the magnetization toward the thermodynamic equilibrium. Because of the magnetic hardness showed in the hysteresis loop one can infer that this system will have a slow relaxation. Magnetic relaxation in Nd$_5$Ge$_3$ have been reported by Tsutaoka et al. [83] and Maji et al. [73, 74]. In the work of Tsutaoka et al. they studied the relaxation of the remanent magnetization over time at 4.2 K. They observed a very slow relaxation, of about 0.26% of the initial magnetic moment in 15 minutes, and with a clear tendency to stabilize. Nevertheless they did not extended the study nor try to obtain magnetic parameters from this relaxation. In the works of Maji et al., on the contrary, they studied magnetic relaxation at different temperatures and magnetic fields, on a polycrystal, and found that the magnetic relaxation could be fitted to an stretched exponential. In this section I will show an study of the magnetic relaxation in a single crystal, extending the previous analysis and finding that the magnetic relaxation in Nd_5Ge_3 actually follows an extended exponential behaviour. The expression for a extended exponential magnetic relaxation is

$$M(t) = M_{\mathrm{eq}} - (M_{\mathrm{eq}} - M(0)) \exp\left(-(t\Gamma)^{\beta}\right) , \tag{3.3}$$

where Γ is the the rate of magnetic relaxation, β is the extending exponent and M_{eq} is the magnetization at the thermodynamic equilibrium. Depending on the value of β this expression corresponds to a stretched exponential ($\beta < 1$), a compressed exponential ($\beta > 1$) or, evidently, an exponential ($\beta = 1$). While the three possible cases for β drive the equation to the same final value at $t \to \infty$, M_{eq}, we can see in Fig. 3.16 how they differ at “short times”. Referred to the exponential curve, on the one hand, the compressed exponential starts “slower” and then increases rapidly the rate of relaxation and reach the final value before than the exponential curve does; on the other hand, the stretched exponential starts “faster” and then decreases rapidly the rate, reaching the final value later than the exponential curve does.

Table 3.1: Values of Γ and β for the best fits of Eq. (3.3) to the relaxation shown in Fig. 3.17

	T (K), H (kOe)	Γ ($\times 10^{-4}$ s^{-1})	β
AFM	2, 28.6	1.0	0.54
	3, 23.2	1.9	0.65
	4, 18.7	3.2	0.75
	6, 12.9	7.2	0.77
FM	3, 23.2	1.6	1.30
	4, 18.7	2.4	1.33
	5, 12.3	4.1	1.19
	6, 10.0	4.3	1.24

Fig. 3.17 shows the magnetic relaxation of the system prepared in the antiferromagnetic and ferromagnetic phases, at different temperatures and magnetic

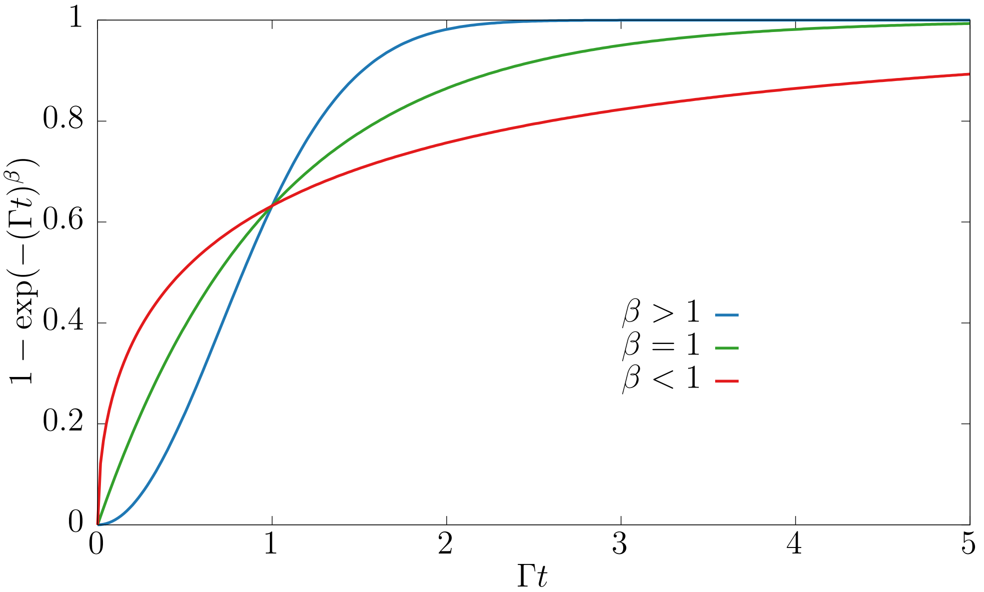

Figure 3.16: Extended exponential for $\beta < 1$ (stretched exponential), $\beta > 1$ (compressed exponential) and $\beta = 1$ (exponential).

fields. The top panel of the figure correspond to the relaxations from AFM to FM, while the bottom panel correspond to the time dependence of the reversal of the FM state. In order to observe the relaxation of the magnetization in a wide range of values and because of the large irreversibility present in the system, the fields chosen to perform the magnetic relaxation were close large enough being close to the spontaneous avalanche fields H_{sp} for each temperature and magnetic state. Table 3.1 contains the values obtained fitting the magnetic relaxation to Eq. (3.3). On the one hand, in the AFM phase the magnetic relaxation follows a stretched exponential ($\beta < 1$): the initial relaxation is enhanced and then became flatter. A distribution of barriers (even a narrow one) would lead to this kind of relaxations, the smaller barriers jump early and then the larger does. On the other hand, the FM phase follows a compressed exponential ($\beta > 1$). One possible explanation for the compressed behaviour in the FM phase is that the energy barrier to overcome is very high at the beginning, but the relaxation releases heat that enhances the relaxation rate which means more heat released and so on.

We also investigated the magnetic relaxation for fields as close to the spontaneous jump fields as possible. Fig. 3.18 shows the magnetic relaxation from the AFM state towards the equilibrium at 2 K. In the top panel are represented several fields near H_{sp}-AFM, while in the bottom panel are represented four measurements at the same magnetic field (29.1 kOe), in order to check the reproducibility

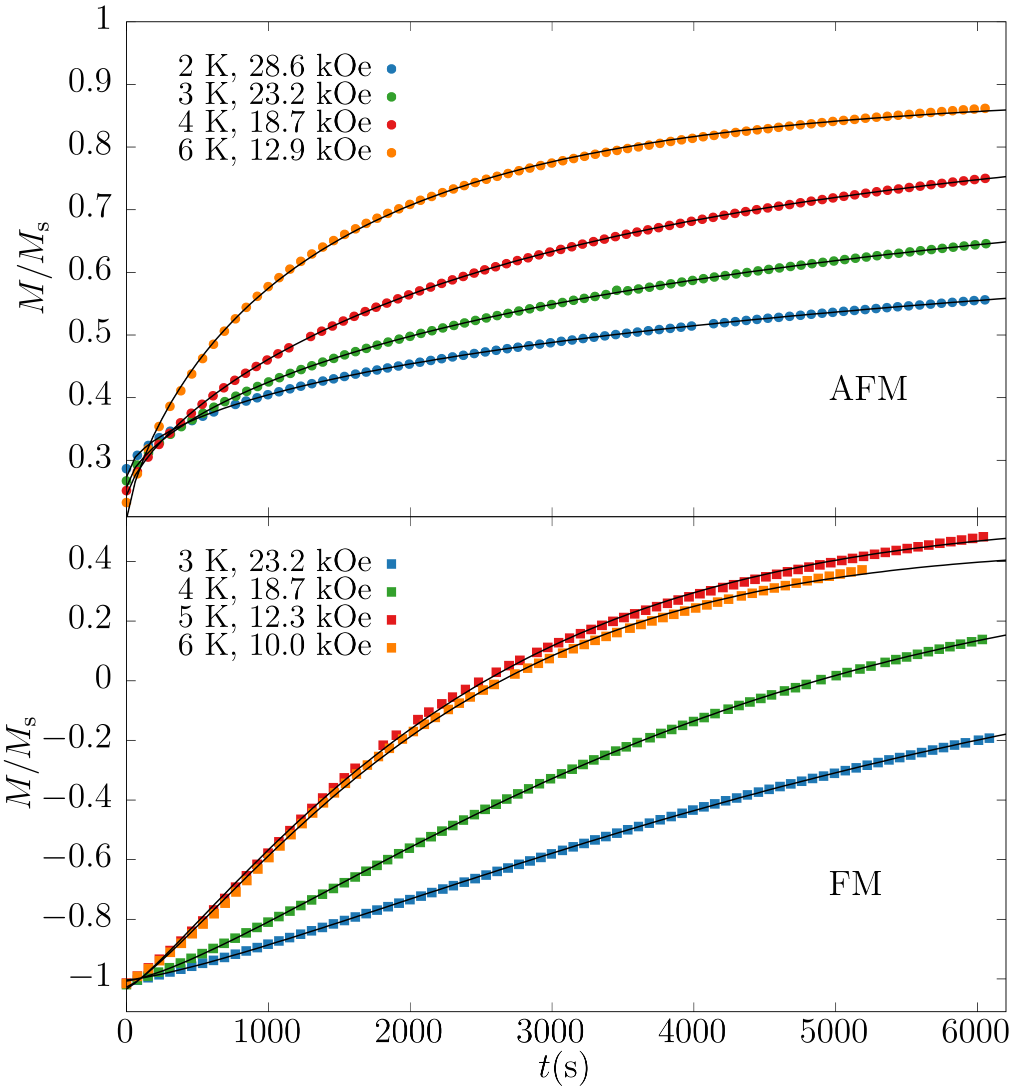

Figure 3.17: Magnetic relaxation toward the equilibrium at different temperatures and magnetic fields. The solid lines represent the fits to Eq. (3.3). The results are summarized in the Table 3.1. Top panel: initiated at the AFM state. Bottom panel: initiated at the saturated FM stated.

of the effect and the distribution in the time at which the spontaneous jump occur (for fixed T and H conditions). While I will agree with the reader that 4 realizations may not be a good statistical sample, looking also at the top panel seems plausible that the expected *incubation time* (time needed for the jump in

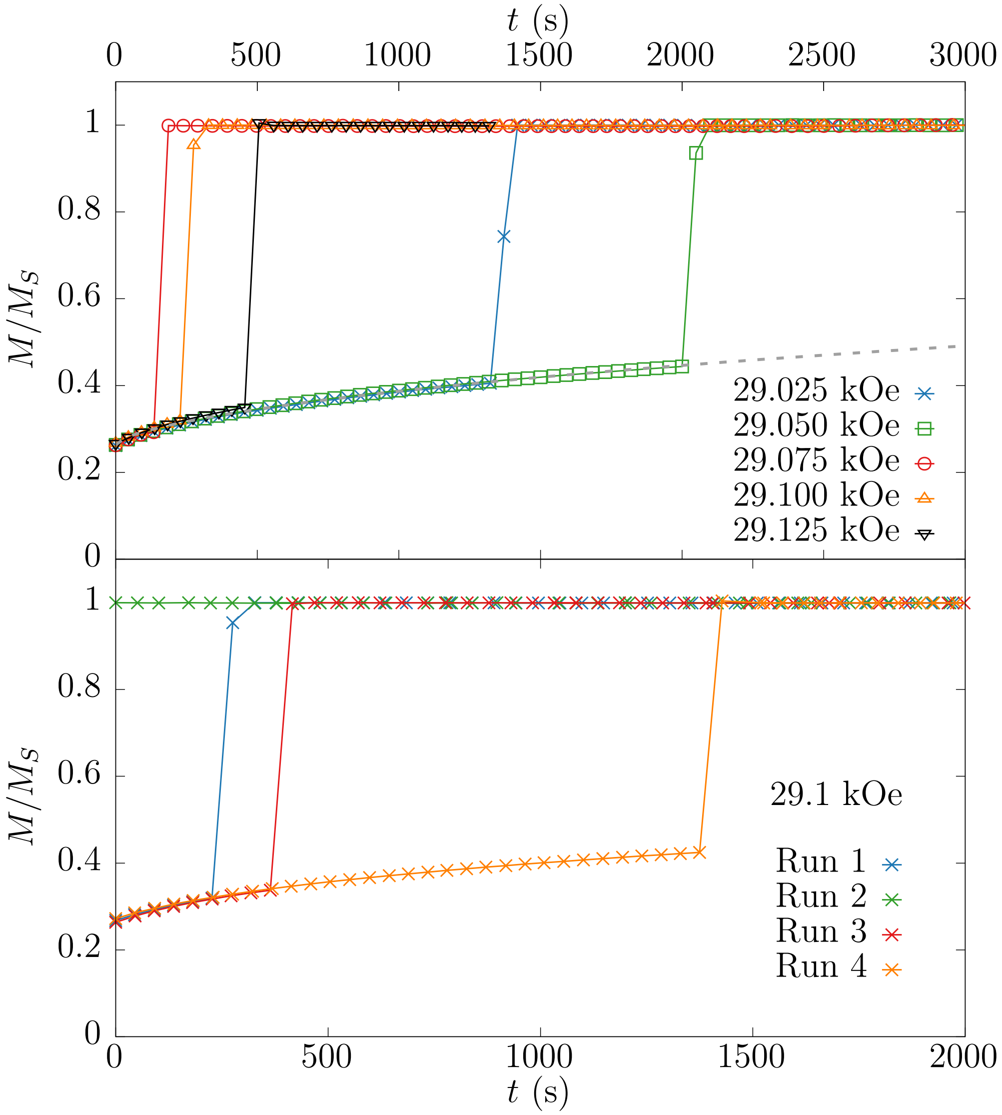

Figure 3.18: Magnetic relaxation of the AFM state towards the equilibrium in the vicinity of the critical field at 2 K. Top panel: for different applied fields. The dark gray dashed line is the fit to the extended exponential Eq. (3.3), resulting in $\beta = 0.64$, $\Gamma = 7 \times 10^{-5}$ s^{-1}. Bottom panel: reproducibility test at 29.1 kOe.

magnetization to occur) for T = 2 K and $H \approx 29$ kOe is $\lesssim 500$ s (note that Run 2 in bottom panel has an incubation time equal to 0). This time-dependent phenomena was also reported by Maji et al. in Nd$_5$Ge$_3$ polycrystals [73], so we can confirm that this is not an effect due the polycrystallinity of their samples,

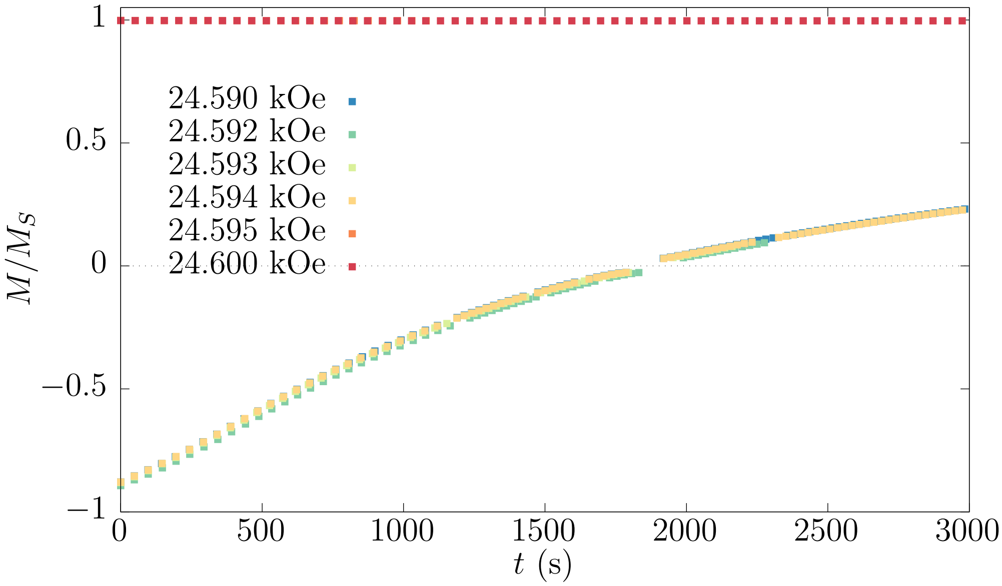

Figure 3.19: Magnetic relaxation of the FM state towards the equilibrium in the vicinity of the critical field at 2 K. Above $H = 24.594$ kOe the system relaxes before starting the experiment.

but something intrinsic of this material. It is worth to say that this kind of jump in magnetization, where both the temperature and magnetic field are kept constant, is observed in a very limited number of compounds. There are cases reported in the $Pr_{0.5}Ca_{0.5}Mn_{1-x}Ga_xO_3$ manganite [97], manganite thin films [98], $(La_{0.5}Nd_{0.5})_{1.2}Sr_{1.8}Mn_2O_7$ [99], $(La_{0.8}Eu_{0.2})_{4/3}Sr_{5/3}Mn_2O_7$ [100], and $Pr_xNa_{1-x}MnO_3$ with $x = 0.6$ and 0.75 [101, 102]. The magnetic relaxation of the FM state is shown in Fig. 3.19. In this case we can observe that the system has an extremely narrow magnetic field window of spontaneous jumps, of the order of one Oersted; above 24.595 kOe (included), the system has already relaxed before starting the measurements, while below that field the system relaxes smoothly to the equilibrium. It should be possible to observe the same time dependence of the spontaneous jump as in the AFM→FM transition, i. e., catch the FM reversal abrupt transition during a relaxation experiment, while it is not observed in our set of measurements.

3.2.5 Magnetic phases

Tsutaoka et al. presented a magnetic field-temperature phase diagram [83], based on isothermal magnetization measurements, where points are the fields which the AFM→FM magnetic field induced transition took place at a given temperature, which they named critical field H_c (see Fig 3.20). In this phase diagram we can see

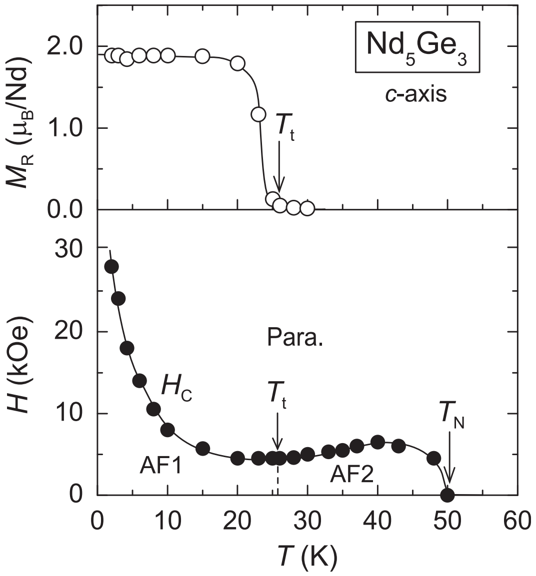

Figure 3.20: Magnetic field-temperature phase diagram of Nd_5Ge_3 and the temperature variation of the remanent magnetization M_R along *c*-axis. Extracted from [83].

a rapid decrease of the critical field as the temperature is increased. This decrease reaches a minimum around 26 K and then increases a bit up to 40 K from where it starts to diminish again until drops to 0 at 50 K. In this phase diagram they mark a region as a second AFM phase, but, in our opinion, it does not seem to be very plausible.

I want to present in this section an extension of this phase diagram, to show the different phases the system present when it is cooled down with an applied magnetic field. From the FC data it is known that a relatively small field seems to transform the system into a ferromagnet, or at least some part of it; so we decided to map the magnetization for FC processes with different magnetic fields. Fig. 3.21 shows the FC curves obtained. A clearer view of the data is presented in Fig. 3.22, where it is plotted as a heat map where the color represents the magnetization M relative to the saturation magnetization, M_S. It is evident a region where the system is fully saturated, but it is not clear if this saturation arises from an spin-flop transition where the system is still an AFM, or from the transition to the FM state. In the figure are also represented the inflection points of the isothermal FC curves, as an indicator of the boundary of this spin-flop or AFM→FM phase transition.

The phase diagram obtained by Tsutaoka et al. is not the magnetic field-temperature phase diagram of the equilibrium. The boundary presented in their

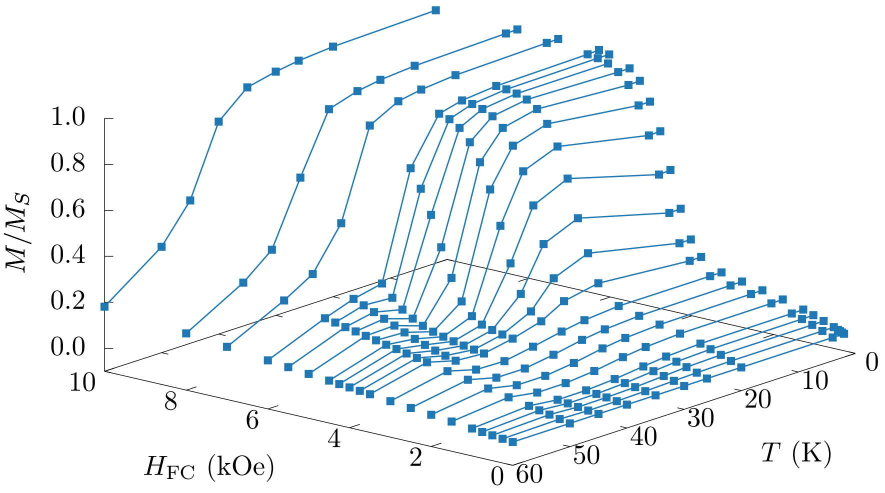

Figure 3.21: FC magnetization curves at various temperatures from 2 to 60 K, and fields from 250 Oe to 10 kOe.

phase diagram represents the points in magnetic field-temperature at which the system can be transformed by the applied magnetic field, after being prepared in the AFM state following a ZFC protocol. I. e., their process did not represent the equilibrium for a given (H, T) configuration. Instead, the phase diagram that I present in Fig. 3.23 reflects the boundaries of the equilibrium states that the system posses when it is cooled (slowly enough) with an applied magnetic field. In the phase diagram we observe how, below 26 K, the field necessary to induce the phase transition remains constant around 4 kOe. This behaviour is in contradiction with the phase diagram mentioned before, while the rest of the boundary is in good agreement. We understand this phenomenon as the blocking of AFM state when the system is cooled below 26 K in zero applied magnetic field.

3.3 Conclusions

In summary, in this chapter, I have shown an introduction to the crystalline structure Mn_5Si_3 and the properties of the family R_5Ge_3. It has been also presented the proposed models for the magnetic structure of Nd_5Ge_3. I have presented my original contribution to the study of the magnetic properties of the compound Nd_5Ge_3 as well. The new results obtained in this chapter consist in the verification in a single crystal of some of the reported phenomena in polycrystalline samples. I

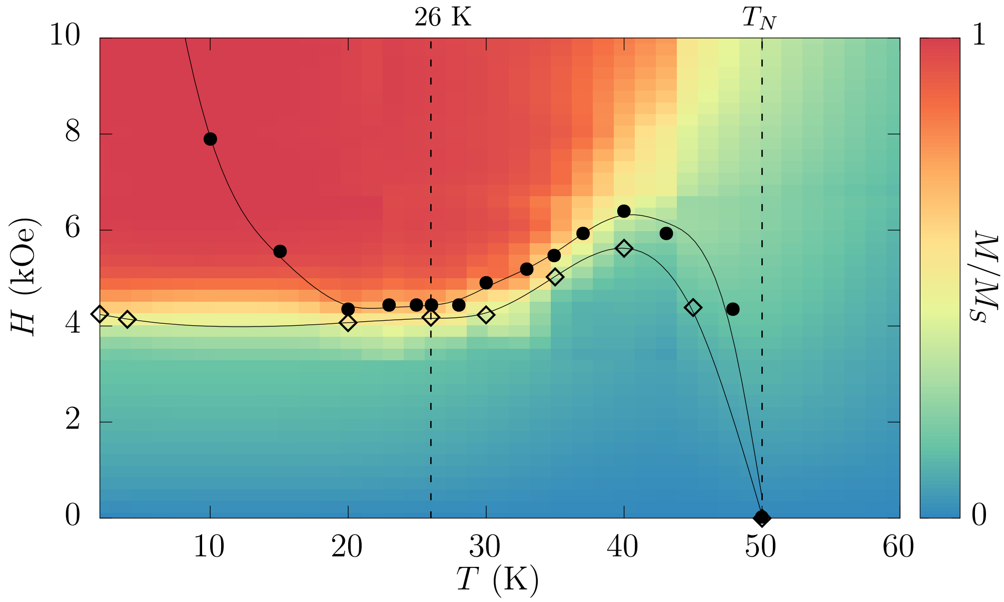

Figure 3.22: Magnetic field-temperature phase diagram. Black circles from phase diagram in Ref. [83] obtained from isothermal magnetization curves. The heat map in the background correspond to FC data. Diamonds represent the inflection point of the isothermal FC curves.

want to mention the spontaneous isothermal-isofield time dependent relaxation, showing the distribution of the incubation time for a given (H, T) configuration in the AFM→FM transition, and an extremely narrow magnetic field window for this spontaneous jumps in the case of the FM reversal. The lack of reproducibility of the ac frequency-dependent measurements in polycrystalline samples is also reported; this new measurements have allowed me to correct the estimation of the empirical parameter δ_f, reported previously to be in between the expected values of a superparamagnetic cluster and a spin cluster glass regime. The extended exponential relations in the magnetic relaxation are also presented for the first time in both magnetic phases, observing stretched and compressed behaviours for the AFM and the FM states respectively. Finally, I have contributed to extend the phase diagram, where I show the minimum field needed in a FC process to change the magnetic phase of the system from AFM to FM.

I want to finish this chapter suggesting some experiments that have not been done yet in the study of this compound. Regarding the magnetic anisotropy I would like to study the magnetization with the magnetic field applied along the c-plane after the AFM→FM transition occur. I. e., the process would be: ZFC down to $T < 26$ K, induce AFM→FM transition increasing H, set H back to 0, rotate the sample 90° and then perform an isothermal magnetization curve. Be-

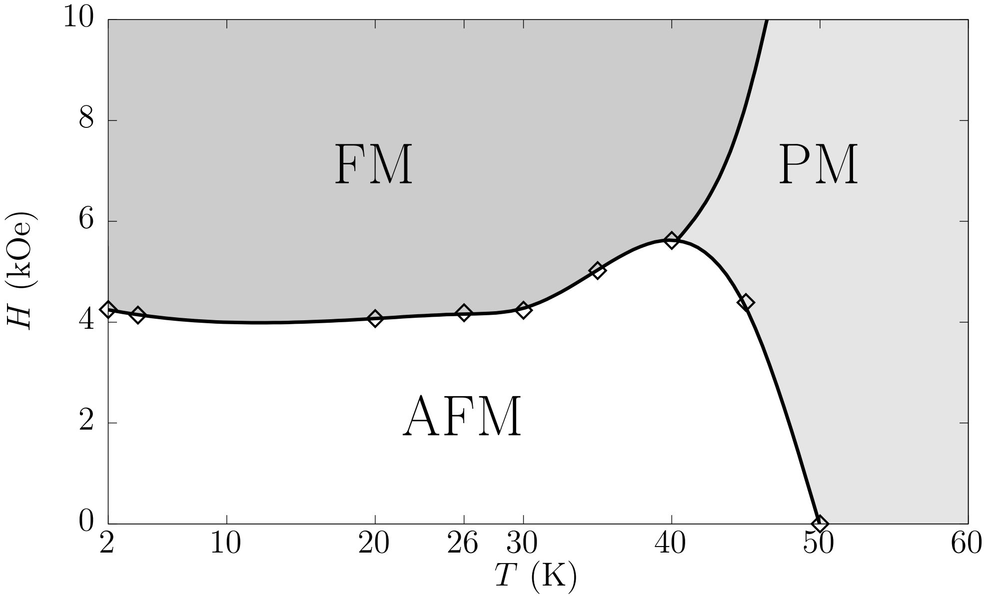

Figure 3.23: Magnetic field-temperature phase diagram. Diamonds represent the approximated inflection point of the isothermal FC curves. Three regions are defined: ferromagnetic (FM), antiferromagnetic (AFM) and paramagnetic (PM). The FM-PM curve is approximated by the inflection points in the isofield FC curves of Fig. 3.22.

cause of the large irreversibility of the magnetization one might expect that the anisotropy would be still high, but it would be interesting to measure. With respect to the phase diagram I would like to repeat the protocol, with a slower cooling rate and a higher "reseting" temperature, the first to ensure that the system is at equilibrium, and the second to guarantee that no history-effects are propagated within the experiment; and, of course, with more temperature points around 26 K. In relation to the spontaneous isothermal-isofield time dependent relaxation I would like to perform a more detailed study, obtaining the distribution of spontaneous jump times for different fields and temperatures, to try to relate them to the size of the hypothetical clusters present in the system (from the lack of Barkhausen jumps in the relaxation we only know that the clusters have to be magnetically smaller than $\sim 10^{13}\mu_B$, if they are supposed to orient with the field as a block). The last experiment that I suggest is, as commented in the magnetic phases section, to study the isothermal magnetization curves at 2 K with the system prepared following FC processes with different magnetic fields to study the dependence of the field at which of the spontaneous field-induced magnetization jumps and the size of this jumps with the initial magnetization.

CHAPTER 4

Heat capacity and electrical resistivity on Nd_5Ge_3

In this chapter I am presenting heat capacity and electrical resistivity measurements on single crystalline samples of Nd_5Ge_3. The aim of the study of this two intrinsic properties was to gain knowledge of the system, seeking a better understanding of its magnetic properties. The heat capacity measurements reveal a rich phenomena and will be of special importance in the chapter on magnetic deflagrations in Nd_5Ge_3. I will introduce first the experimental procedure and setup to measure both properties and then the results will be discussed.

4.1 Heat capacity

The temperature variation of the specific heat in zero field was measured in Ref. [83] and [74] to examine the magnetic phase transitions. Both works observed a hump around 50 K (associated to the Néel temperature) but no anomaly around 26 K, which was attributed to the existence of a spin-glass state, because of the occurrence of similar features in the $C_p(T)$ curve in other well-known spin-glass systems. In this section I will show a detailed study of the specific heat, as a function of the temperature and the magnetic field.

The specific heat measurements reported in this thesis were performed at the Physical Measurements Service, SMF ('Servicio de Medidas Físicas'). The service is integrated in the 'Servicio General de Apoyo a la Investigación' of the University of Zaragoza. SMF provides the magnetic, electric and thermal characterization of materials, in a wide temperature and magnetic field ranges. The service is open to scientists from the University of Zaragoza, other Universities and other Research

Institutions and companies. The manipulation of the equipment was done under the supervision of the SMF staff and the measurements were programed by me.

4.1.1 The PPMS® system

The heat capacity was obtained using a Physical Property Measurement System 9T (PPMS®-9T) manufactured by Quantum Design®. The PPMS® is a very versatile instrument designed for magnetic, electric and thermal measurements as a function of magnetic field and temperature. The usual temperature range is between 1.9 and 400 K. Nevertheless, as we are interested in covering the largest range possible, the Helium-3 option was used. The ^{3}He refrigerator option allows continuous temperature operation down to 0.35 K. The magnetic field range is from 0 to ±9 T, with a variable sweeping rate of 10–180 Oe/s. Besides, the system also can be operated at high vacuum conditions ($< 10^{-4}$ Torr). Another interesting characteristic is that allows both parallel and perpendicular orientations of the sample holder with respect to the applied magnetic field.

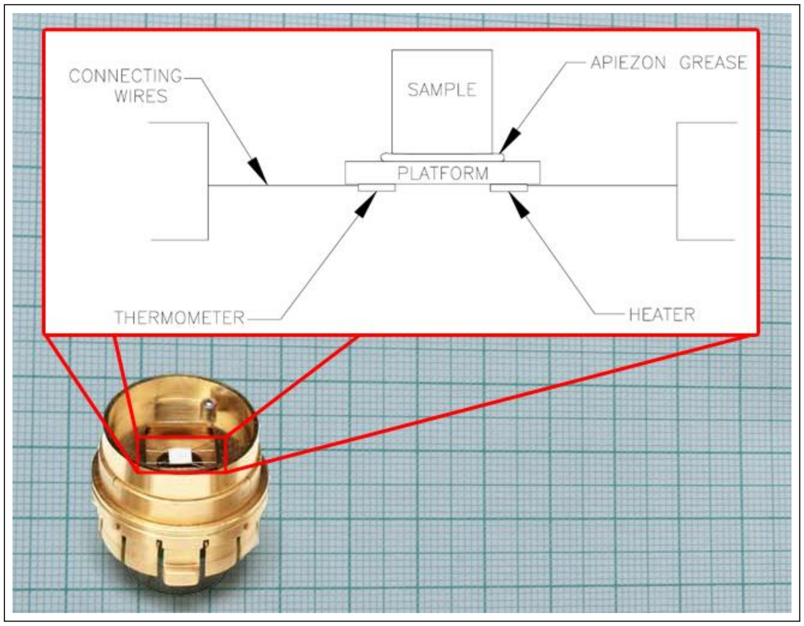

Figure 4.1: Calorimeter puck and the schematic diagram of the calorimeter. Extracted from [103].

The heat capacity puck (Fig. 4.1) provides a small micro-calorimeter platform where the sample is mounted using a standard cryogenic grease (Apiezon-N®). The sample platform is suspended by eight thin wires that act as the electrical leads for an embedded heater and thermometer. The wires also provide a well-defined thermal connection between the sample platform and the puck. An additional thermometer embedded in the puck provides a highly accurate determination of the puck temperature, and a thermal shield aids in maintaining stable sample temperature and uniformity. To ensure that heat is not lost via the exchange gas, the Heat Capacity option includes the PPMS® High-Vacuum system which maintains the sample chamber pressure near 0.01 mbar.

A single heat capacity measurement consists of several distinct stages. First, the sample platform and puck temperatures are stabilized at some initial temperature. Power is then applied to the sample platform heater for a predetermined time lapse, causing a rise in the sample platform temperature. When the power is switched off, the temperature of the sample platform relaxes toward the puck temperature. The sample platform temperature is monitored throughout both heating and cooling, providing (with the heater power data) the raw data of the heat capacity calculation. Two separate algorithms fully automate the analysis of the raw data. The most general analysis method invokes the two-tau model proposed by Hwang et al. in [104]), which assumes that the sample is not in good thermal contact with the sample platform. The values of the heat capacity and other physical parameters are determined by fitting the measured raw data to the two-tau model. In the two-tau model, the first time-constant (τ_1) represents the relaxation time between the sample platform and the puck, and the second time constant (τ_2) represents the relaxation time between the sample platform and the sample itself. A second analysis is also performed using a simpler model that assumes perfect thermal coupling between the sample and the sample platform. The heat capacity software determines which model fits better the measured data and automatically saves the values of the sample heat capacity, addenda heat capacity, thermal coupling between the sample and the platform, thermal time-constants, and other information to the data file.

The main issues that present this system regarding to heat capacity measurements are: the sample has to have a flat face to ensure a good contact; the puck has to be calibrated before a measurement with an special grease; the sample must tolerate high vacuum; and as we will see in the next chapter, the most critical issue, the fragility of the connecting wires (the wires of the sample platform of the ^{3}He heat capacity puck are thinner than the ones of the standard puck)[1].

4.1.2 Analysis and results

Figure 4.2 shows the specific heat, C, of our Nd_5Ge_3 single crystal and a polycrystalline sample of the nonmagnetic isostructural compound La_5Ge_3 (extracted form

---

[1] If the reader is interested in a more detailed description of the system and the precise procedures used in the measurements of the heat capacity I recommend to read the work of Dachs and Bertoldi [105]

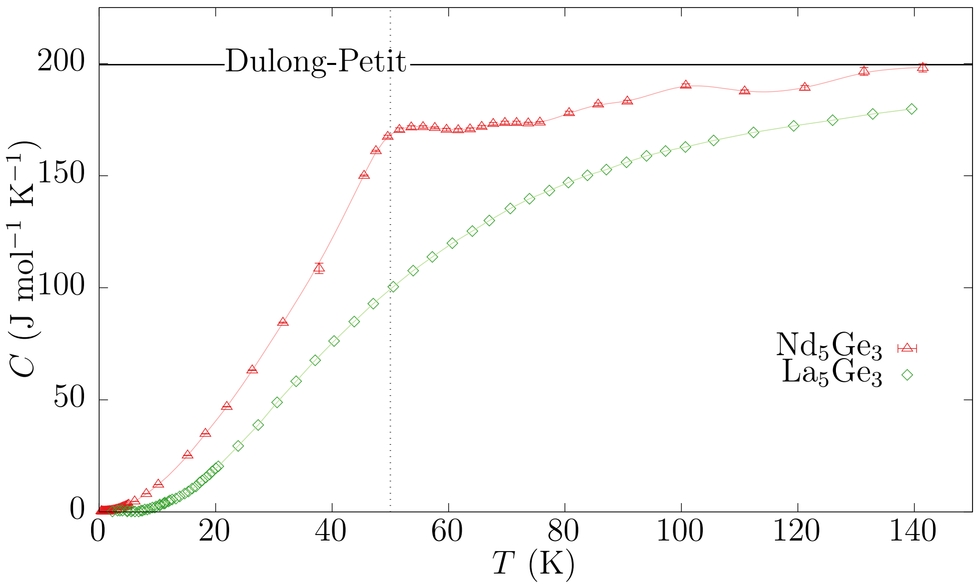

Figure 4.2: Zero-field temperature dependence of the specific heat of a single crystal of Nd_5Ge_3 (triangles) and a polycrystal of La_5Ge_3 (diamonds; extracted from Joshi et al. [84]). The lines joining the data points are guides to the eye. The vertical dotted line indicates the temperature (50 K) at which a hump is observed for Nd_5Ge_3. The horizontal solid line indicates the Dulong-Petit limit of the specific heat.

Joshi et al. [84]) as a function of temperature. The specific heat of the latter will be used as a blank and follows the expected monotonic behavior from the electronic and phononic contributions [106], while the specific heat of Nd_5Ge_3 presents a hump around $T_N \simeq 50$ K and thenceforth tends progressively to the Dulong-Petit limit.

The dependence of the specific heat of Nd_5Ge_3 with the temperature was investigated as follows. Following a ZFC process the specific heat was measured from 140 K down to 350 mK. During this process we observed the expected hump associated to the paramagnetic–AFM transition at 50 K. The next step was to measure the system in the FM state (the magnetic field will be always applied along the c-axis). It is known that cooling the Nd_5Ge_3 compound below 26 K with an applied magnetic field larger than 5 kOe leaves the system in the saturated FM state [83]. To ensure this fact we measured the specific heat following a FC in an applied field of 15 kOe, large enough for our purpose. Nonetheless our goal was to compare the magnetic contribution of the different magnetic phases to the specific heat, and the applied magnetic field could play an undesired role. Therefore, after measuring the FC process we set the magnetic field to zero and measured the specific heat of

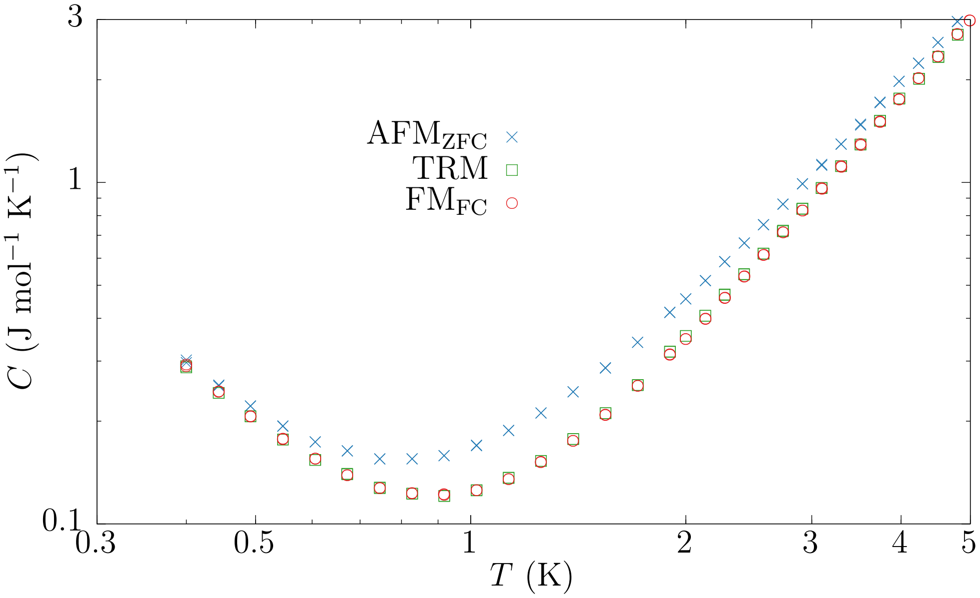

Figure 4.3: (Color online) Log-log plot of the low-temperature dependence of the specific heat of the three magnetic states: the AFM (crosses), the TRM (squares), and the FM$_{\text{FC}}$ (circles).

the ferromagnetic remanent state (TRM) as we increased the temperature. From magnetization experiments shown in the previous chapter it is known that below 20 K the TRM and the FM$_{\text{FC}}$ states are magnetically equivalent. We observed that this equivalence is also present in terms of specific heat, as it is shown in Fig. 4.3. In this figure the three data sets are plotted together showing the AFM curve and how the TRM and FM$_{\text{FC}}$ curves superimpose. Consequently, from now on we will rename the TRM state as FM state in this temperature region.

The specific heat can be assumed to be made up of four independent contributions,

$$C(T) = C_{\text{el}}(T) + C_{\text{lat}}(T) + C_{\text{hyp}}(T) + C_{\text{mag}}(T), \tag{4.1}$$

namely electronic, lattice, hyperfine and magnetic.

The contribution from phonons, C_{lat}, can be subtracted using the specific heat of the nonmagnetic isostructural compound La_5Ge_3, taking into account the different molar masses of Nd and La via the two-Debye function method [107, 108],

$$C_{\text{lat}}^{\text{Nd}_5\text{Ge}_3}(T) = C_{\text{lat}}^{\text{La}_5\text{Ge}_3}(r\,T), \tag{4.2}$$

with

$$r = \left(\frac{5M_{\mathrm{La}}^{3/2} + 3M_{\mathrm{Ge}}^{3/2}}{5M_{\mathrm{Nd}}^{3/2} + 3M_{\mathrm{Ge}}^{3/2}}\right)^{1/3} = 0.98. \tag{4.3}$$

Therefore we get

$$C(T) - C_{\mathrm{lat}}^{\mathrm{La_5Ge_3}}(r\,T) = C_{\mathrm{el}}(T) + C_{\mathrm{hyp}}(T) + C_{\mathrm{mag}}(T). \tag{4.4}$$

To determine the $C_{\mathrm{mag}}(T)$ contribution for each magnetic phase, we can attempt to model the experimental data taking into account the different terms: $C_{\mathrm{el}}(T) = \gamma T$ from free charge carriers, $C_{\mathrm{hyp}}(T) = AT^{-2}$ from the high-temperature limit of the Schottky anomaly due to the hyperfine splitting of the nuclear levels of the Nd^{3+} ions, and $C_{\mathrm{mag}}(T)$ from spin waves. The approach to study the last term was to consider the more general dispersion relations for the long-wavelength spin interactions [28: Chapter 3]. We examined the cases of AFM, FM, and type-A AFM (ferromagnetic layers antiferromagnetically coupled) states. Because of the large magnetic anisotropy and the magnetoelastic effects present in this system, we also took into account the possibility of the presence of a gap in the dispersion relation, Δ. The heat capacity contribution due the excitation of spin-waves is derived from the energy of those excitations which depends on the dispersion relation. In the low temperature limit,

$$C_{\mathrm{mag}}(T) = \frac{\partial}{\partial T}E_{\mathrm{magnon}} = \frac{\partial}{\partial T}\int_0^\infty \frac{\hbar\omega g(\omega)\mathrm{d}\omega}{\exp(\hbar\omega/k_BT) - 1}, \tag{4.5}$$

being $\hbar$ the reduced Plank constant, k_B the Boltzmann constant, ω the frequency of a spin-wave, and $g(\omega)$ the density of spin-wave states at frequency ω.

The dispersion relation for a FM, an AFM and a type-A AFM (when $T \to 0$, and considering a gap) are $\omega_{\mathrm{FM}} = Dq^2 + \Delta$, $\omega_{\mathrm{AFM}} = D|q| + \Delta$ and $\omega_{A\text{-AFM}} = D_{\mathrm{FM}}(q_x^2 + q_y^2) + D_{\mathrm{AFM}}|q_z| + \Delta$, respectively; being D the stiffness of the spin waves. In the last relation, we have a FM contribution within the layers, (q_x, q_y), and an AFM contribution between the layers, q_z (Ref. [109]). Computing the integral (4.5), the specific heat from each dispersion relation is found to be

$$C_{\mathrm{mag}}(T) = Be^{-\frac{\Delta}{T}} \begin{cases} T(12T^2 + 6T\Delta + \Delta^2) & (4.6a) \\ T^{-\frac{1}{2}}(15T^2 + 12T\Delta + 4\Delta^2) & (4.6b) \\ (6T^2 + 4T\Delta + \Delta^2). & (4.6c) \end{cases}$$

Equations (4.6a), (4.6b) and (4.6c) correspond, respectively, to the low-temperature magnetic contribution to the specific heat of the AFM, the FM, and the type-A AFM states. The usual expressions (T^3, $T^{3/2}$ and T^2, respectively) are recovered

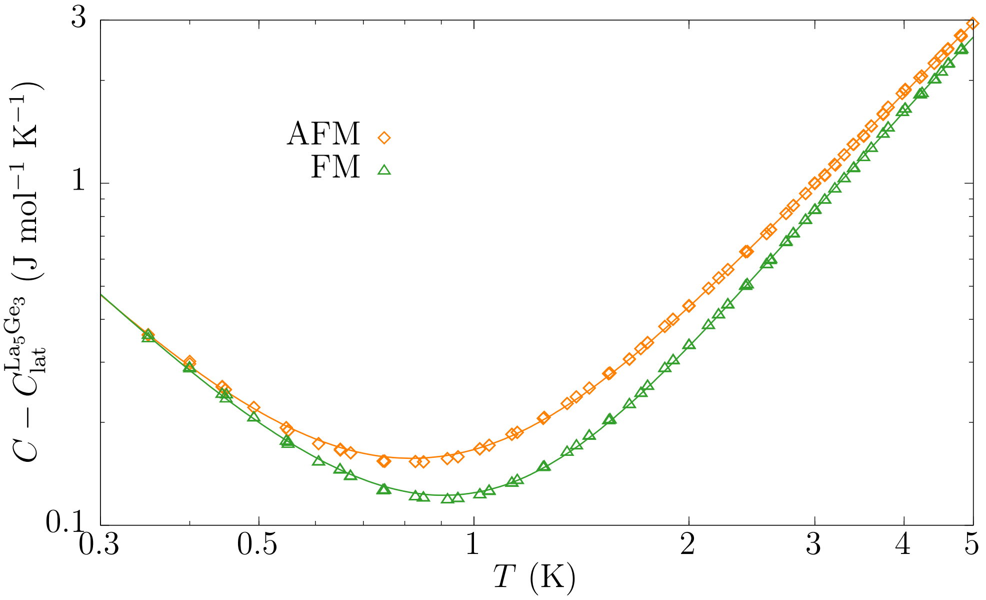

Figure 4.4: (Color online) Zero-field low-temperature specific heat for both the AFM (diamonds) and FM (triangles) states, plotted in a log-log scale to remark the differences between both states. The lattice contribution to the specific heat has been subtracted to the experimental data. The lines are the best fits of Eq. (4.4) to the data.

Table 4.1: Results of the fitting of Eq. (4.4) to the specific heat data, for both the AFM and FM states. The units are mJ/(mol K^{m+1}) where m is the power of T corresponding to each coefficient, $m = 1$ for γ, $m = -2$ for A, $m = 2$ for B. The number in parentheses is the statistical uncertainty in the last digit from the least-squares fitting procedure.

state	γ	A	B	Δ (K)
AFM	115(2)	39.3(4)	22.2(1)	4.34(8)
FM	75(1)	40.6(3)	23.1(1)	4.75(5)

when Δ is set to zero. We fitted the experimental data to the expressions with and without gap and found that, neither in the AFM nor in the FM phase, the “pure” AFM/FM contributions gave physically reasonable values for the parameters. On the contrary, in both phases the gapped type-A AFM contribution [Eq. (4.6c)] was found to fit precisely. Figure 4.4 shows the specific heat for the AFM and FM states together with the best fits of Eq. (4.4) to the data. Table 4.1 lists the coefficients of all contributions.

The mixture of interactions and dimensionalities resulting in a T^2 contribution to C_{mag} has been also considered in magnetic structures where FM droplets are found in an AFM phase [110]. In our system, nevertheless, the magnetization measurements indicate a saturated FM state, without evidence of AFM interactions. Despite I do not have a clear explanation for the presence of this term in the FM phase, the values for the parameters obtained fitting other contributions [Eq. (4.6a) and (4.6b)] do not have any physical meaning. The larger gap obtained in the FM state corresponds with the larger internal magnetic field in this phase, as it will be shown below. The values of γ for both phases are reasonable within the electronic contributions of rare earth intermetallics $\mathrm{R_5Ge_3}$ [111] and do not need extra considerations. Actually, the value of γ for the AFM state obtained is three times smaller than the obtained by Maji et al., who considered the large value of γ as an indicator of the presence of a glassy phase [74]. The reduction of the value in the FM phase with respect to the AFM can be attributed to a decrease in the density of states at the Fermi level, that would probably favour one of the electronic spin projections.

The hyperfine contribution can not be omitted to fit completely the measured specific heat. The Schottky anomaly consists in a peak originated from the (de)population of discrete energy levels. In this case, these correspond to the hyperfine split nuclear levels of the $\mathrm{Nd^{3+}}$ ions. The Schottky anomaly can be approximated to A/T^2 in its high-temperature limit, where A is related to the internal hyperfine magnetic field by the expression [110]

$$A = 5\frac{N_A k_B}{3}\left(\frac{I+1}{I}\right)\left(\frac{\mu_I H_{\mathrm{hyp}}}{k_B}\right)^2 . \tag{4.7}$$

Here I is the nuclear spin, μ_I is the nuclear magnetic moment, H_{hyp} is the internal magnetic field at the Nd site, and the factor 5 is the number of Nd nuclei per $\mathrm{Nd_5Ge_3}$ molecule. Only two isotopes of Nd have nuclear spin different from zero ($I = 7/2$), ^{143}Nd and ^{145}Nd with the natural abundances of 12.18% and 8.29%, whose nuclear magnetic moments are $\mu_I = -1.208\ \mu_N$ and $\mu_I = -0.744\ \mu_N$ respectively [112]. The hyperfine field values obtained are $\mu_0 H_{\mathrm{hyp}}(\mathrm{AFM}) = 272(2)$ T and $\mu_0 H_{\mathrm{hyp}}(\mathrm{FM}) = 276(1)$ T. The energy splitting ($\Delta E = \mu_I H_{\mathrm{hyp}}/I$) found is $\sim 2.5\ \mu$eV for both phases. We can compare this value with the splitting of other Nd compounds studied by neutron scattering. Figure 4.5 plots the hyperfine energy splitting versus the saturated ionic magnetic moment of Nd for several Nd-based compounds [113], along with the data point obtained in this thesis. The value used for the magnetic moment of the Nd ion corresponds to the one observed in the saturated FM state, $\mu_{\mathrm{Nd}} \approx 2\ \mu_B$. It is remarkable that we have obtained approximately the same splitting for both magnetic phases, $\Delta E(\mathrm{AFM}) = 2.50(2)\ \mu$eV and $\Delta E(\mathrm{FM}) = 2.53(1)\ \mu$eV, which means that the average local magnetic moment per Nd ion is roughly the same in the two phases and corresponds to the value in

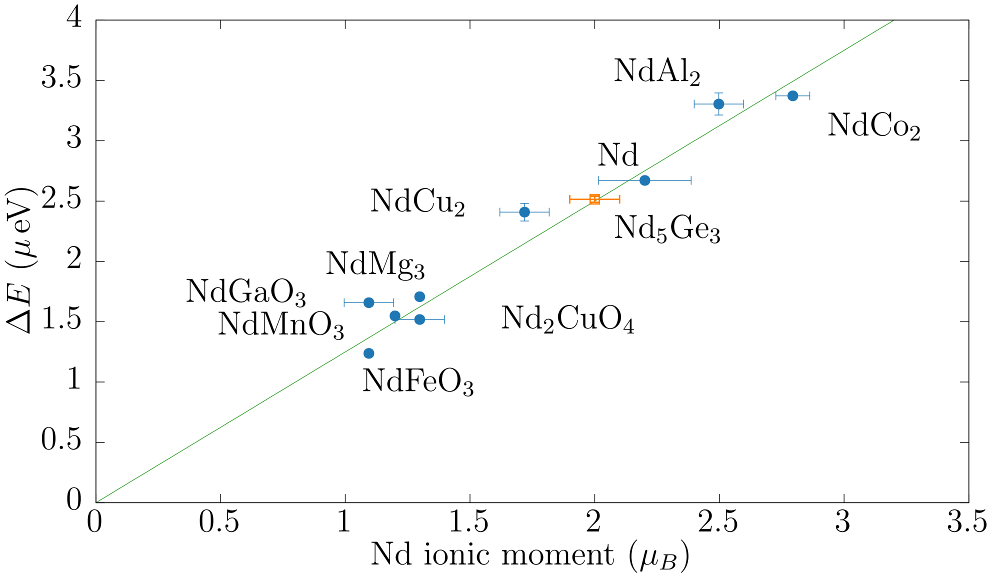

Figure 4.5: Energy splitting of inelastic neutron scattering signals in several Nd-based compounds (circles) as a function of the corresponding saturated ionic magnetic moment of Nd at low temperatures (adapted from Chatterji et al. [113]). The data point obtained in this thesis for Nd_5Ge_3 (square) is also shown.

the FM saturated state. Therefore, one may assert that the magnetic-field-induced AFM→FM transition simply flips the magnetic moments and preserves the value of μ_{Nd}.

I will show now the investigation of the temperature dependence of the magnetic contribution to the specific heat. Subtracting the analytical functions of the electronic contribution, the Schottky anomaly and the phononic contribution from the corrected La_5Ge_3 data to the total measured specific heat, we obtain $C_{\mathrm{mag}}(T)$. Fig. 4.6 shows the ZFC and TRM curves, where the latter was acquired as the sample was heated in zero applied magnetic field after it had been driven to the FM saturated state. The hump at 50 K reported in Ref. [83] and [74] now turns into a large and well-defined peak, as expected in a phase transition. This peak indicates the temperature at which the AFM ordering takes place (T_N). The inflection point observed around 26 K is in contradiction with the previously reported absence of any anomaly around this temperature, which was related to the possibility of the system to be in a spin glass state [74, 83]. Although it has to be said that in these works they did not isolate the magnetic contribution to the specific heat, and probably the subtle anomaly was obscured by other contributions.

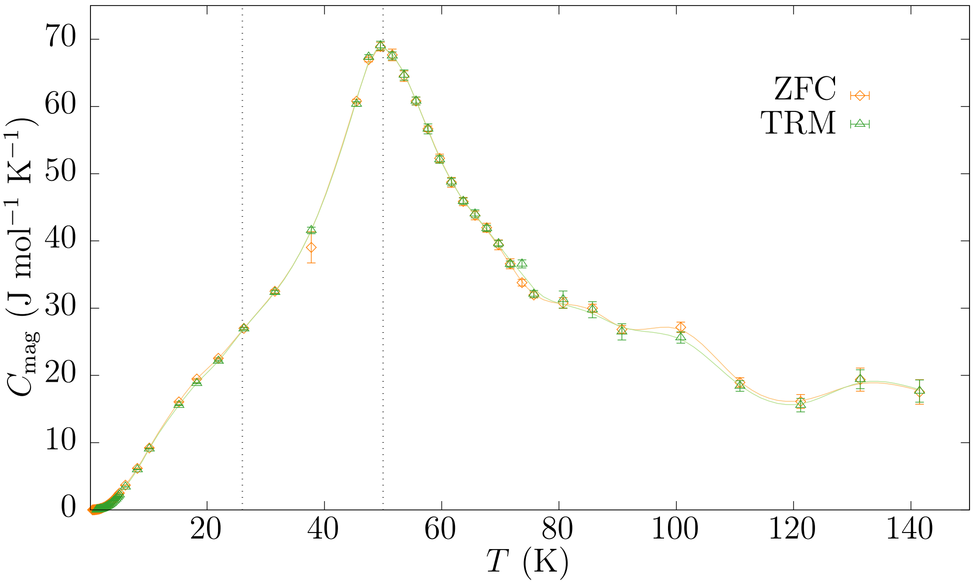

Figure 4.6: Temperature dependence of the magnetic contribution to the specific heat obtained following the ZFC and TRM processes. A maximum at 50 K and an inflection point around 26 K are highlighted with vertical dotted lines. The lines joining the data points are guides to the eye.

From $C_{\mathrm{mag}}(T)$ we can compute the magnetic entropy as

$$S_{\mathrm{mag}}(T) = \int_0^T \frac{C_{\mathrm{mag}}(T')}{T'} \mathrm{d}T', \tag{4.8}$$

where it is assumed that the magnetic entropies of AFM and FM materials at zero temperature are zero. Fig. 4.7 shows how S_{mag} attains the value of $R \ln(2J+1)$ expected for a paramagnet as the temperature grows above T_N [85]. In our case the entropy tends to $5R \ln 10$, corresponding to 5 Nd^{3+} free ions with $J = 9/2$. The actual value at which the obtained entropy tends is moderately smaller because the zero-field splitting due to the anisotropy could play a significant role even in the paramagnetic state.

Finally, the dependence of the specific heat with the applied magnetic field at fixed temperature was studied to explore the magnetic-field-induced AFM→FM transition . The system was prepared following a ZFC process from $T \gg T_{\mathrm{N}}$ down to 1.2 K, where the relative difference between the specific heat of the two phases has a maximum, and then the specific heat was measured varying the field, from 0 to 40 kOe and back to 0 Oe. Fig. 4.8 shows how a large, abrupt, and irreversible change in $C(H)$, associated with the AFM–FM transition, takes place between 16 and 17 kOe as the magnetic field increases. Two independent runs are plotted in

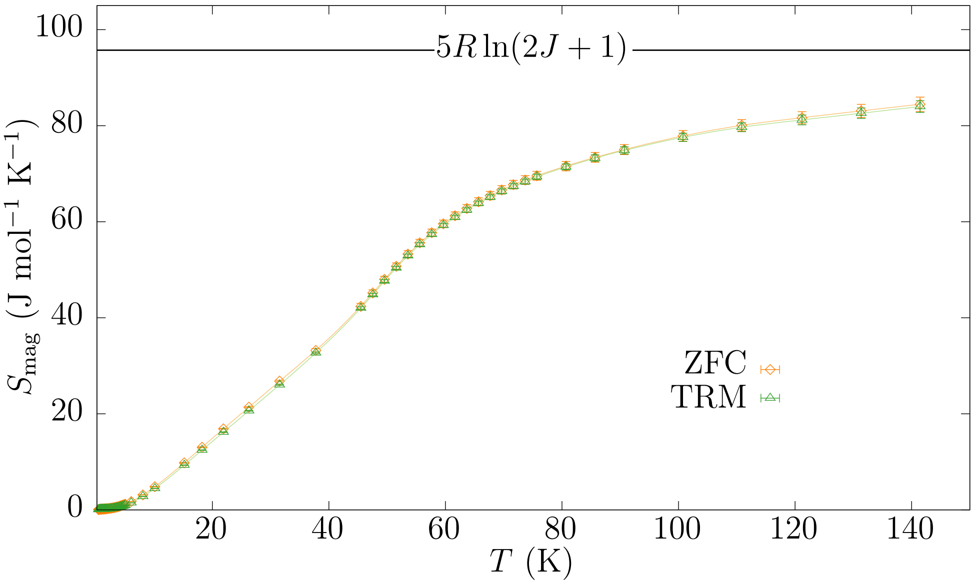

Figure 4.7: Temperature dependence of the magnetic entropy obtained for the ZFC and TRM processes. The horizontal solid line represents the value of $5R\ln(2J+1)$ for $J = 9/2$. The lines joining the data points are guides to the eye.

the figure showing the reproducibility of this transition. We also see in the figure that the decreasing dependence of the specific heat with the increasing magnetic field, above $H \approx 10$ kOe, is consistent with the behaviour of a C_{mag} term with a gap in the dispersion relation of the spin waves proportional to the applied magnetic field, $\Delta \propto H$ (see [28: Chapter 3]). Nevertheless, a change in the sign of the slope is observed in both states around 10 kOe, for which I do not have an explanation.

4.2 Electrical resisitivity

In this section I will present some results on the electrical resistivity of a single crystal of Nd_5Ge_3. To my knowledge, only a basic electrical characterization of this system is reported in literature [73]. In this work, Maji et al. present the variation of the resistance during the positive-field brach of an isothermal magnetization at 3 K in a polycrystalline sample. Nevertheless they did not report the value of the resistance and they referred the variations to the resistance in the AFM state at zero field.

Because of the observed behaviour of the specific heat we were interested in the investigation of the electrical transport properties, to see if they are as dependent

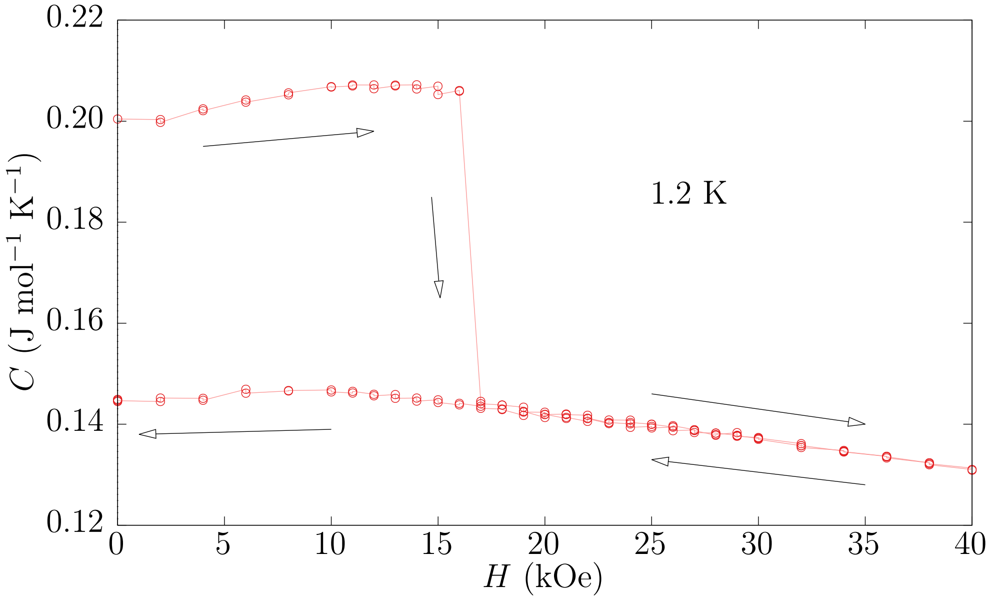

Figure 4.8: Magnetic field dependence of the specific heat at 1.2 K, starting with the system in the AFM state ($C \approx 0.2$ J mol^{-1} K^{-1}) and ending with the system in the FM state ($C \approx 0.145$ J mol^{-1} K^{-1}). Two independent runs are plotted. The lines joining the data points are guides to the eye.

of the magnetic stated as the specific heat is. Here I will show measurements of the electrical resistivity as a function of the magnetic field and the temperature. This system is a metal and therefore measuring its resistivity is difficult, even more due the small size of the sample and the implicit handicaps of the cryogenic experiments. First I will describe the experimental setups that I have designed and used in the experiments, and then I will show and discuss the results.

4.2.1 Experimental setup

To measure the electrical resistivity of the samples I had to design and made dedicated setups. The setups are designed to be placed inside the MPMS® system replacing the standard sample holder rod with a dedicated non-magnetic rod which carries 8 twisted pairs of wires on its interior. Six pairs are made of a cooper-nickel alloy (constantan). Despite its large resistance we use constantan to reduce the thermal leaks. Nevertheless, we have two pairs made of cooper in case we need to apply some current down to the sample. i. e., we use cooper cables for current/voltage and constantan cables only for voltage.

Electrical transport measurements of samples with low resistance is a tough business. And in the case that the sample is placed far from the multimeter, with

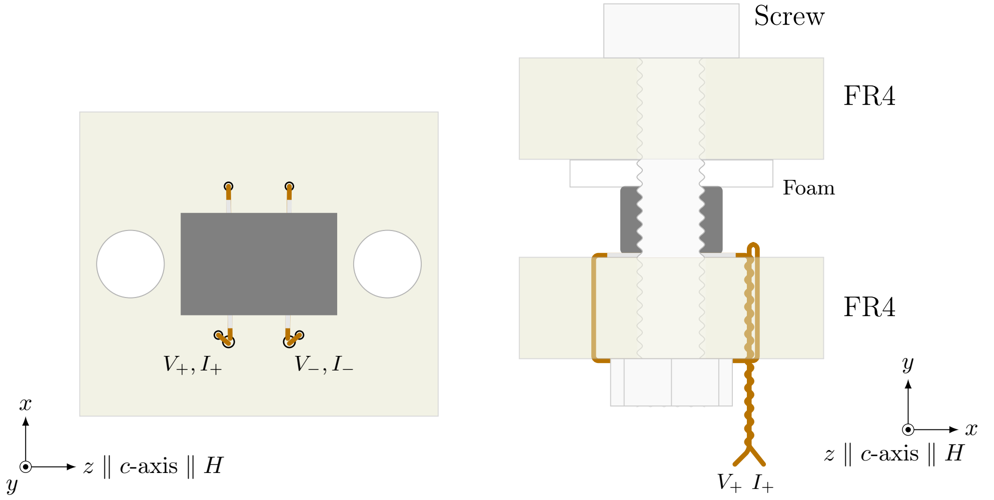

Figure 4.9: Experimental setup to measure electrical resistivity using a 2-terminal configuration. The sample (dark-gray) is pressed against two uncoated cooper wires using two pieces of FR4 and two plastic screws. A piece of foam is placed on top of the sample to ensure a good contact.

magnetic fields, thermal gradients and vacuum pumps around, is even harder. In our case, while all this inconveniences are the daily bread I had to deal with another difficulty. How to make non-permanent contacts to a sample with a size of $0.51 \times 0.51 \times 2.2$ mm^3 was a tricky problem. Silver paint do not work in this case for several reasons: the material is so flat that the paint slips; the superficial tension of the droplets together with the non-homogeneity in the concentration of silver in the paint do not permit to make small contacts; and the temperature cycles break the tiny connections. Trying spark-welding copper contacts was not an option since we had very few samples and a lot of experiment yet to perform.

Fig. 4.9 shows the setup designed to measure the electrical resistivity. The sample, in dark-gray, is centered on top of the uncoated parts of two wires ($\varnothing$ 200 μm). To avoid any movement of the wires they are "sewed" forming a loop to a piece of FR4 epoxy panel (commonly used in rigid printed circuit boards). After the loop is closed the wires are twisted in order to avoid more pick-up effects. The contact between the flat surface of the sample and the uncoated wires in obtained by pressing the sample against them. To apply pressure I used another piece of FR4 and two plastic screws. To ensure a soft accommodation I use a piece of foam on top of the sample. With this we stay away from any pinch in the sample during the (asynchronous) screwing process. The measurements were done using a Keithley® 2400 SourceMeter®, in offset-compensation mode.

This setup has obvious limitations. First of all is a two-terminal configuration,

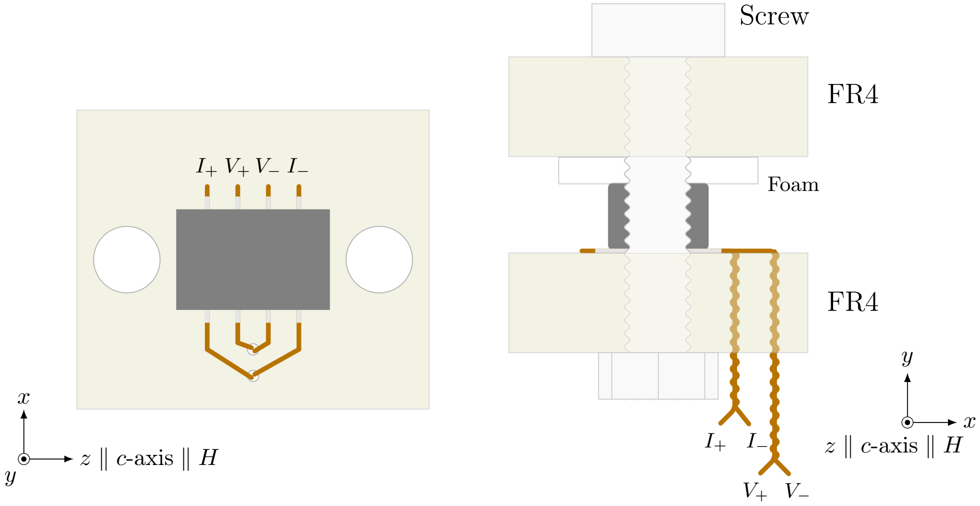

Figure 4.10: Four-terminals configuration for measuring the electrical resistivity using a setup similar to the used for two-wire measurements.

so we will be affected by the contribution of the connecting wires. In order to minimize this effect the external connections where set in four-terminal configuration, so the wires that will have contribution to the resistance will be only those included in the setup (~ 1 cm). Another limitation is that the current does not enter the system as a front but as a thin cascade from the side, which increases de effective resistivity of the sample. It has to be considered also the fact that the loop done to ensure rigidity can induce some voltage if the magnetization changes rapidly. And finally, another limitation is that covering the sample with the foam could reduce the capacity of the sample to thermalize when the magnetic relaxation processes occur.

After the first experiments we realized that we needed to get rid of some of the limitations. In the next section, and in the next chapter as well, we will mention some of the results that seemed caused by a limitation at a first glance, but revealed of a more complex origin. Back to the limitations of the two-terminal setup, I decided to dedicate some time to improve the setup and make it work in a four-terminal configuration. Fig. 4.10 shows the sketch of the new setup. In this setup we have avoided the loop, we have increased the distance that the electrons will travel, and obviously we do not have to care about the resistance of the connecting wires. This time the rigidity of the contacts was critical since there was no end for each terminal, they were just attached to the FR4 substate by a thin double layered tape. However, we checked after the experiments and the setup was still perfect. One of the vantages of measuring with a four-terminal configuration is the use of smaller currents. Since we are aware of inducing an magnetic avalanche process in

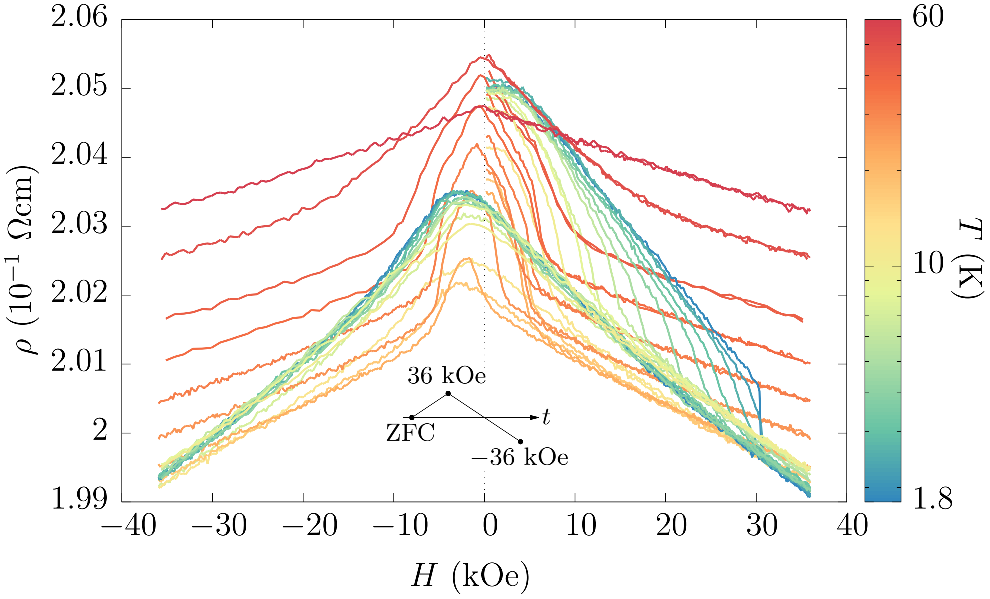

Figure 4.11: Dependence of the electrical resistivity with the temperature and the magnetic field, measured using the two-terminal configuration. The measuring protocol for each temperature is represented in the diagram.

the system by increasing the temperature we can now minimize this effect reducing the current. Note that, because of the small resistance of the system, it would be rather difficult to increase the temperature with the typical electrical currents. The electrical measurements using this configuration were performed with a Stanford Research Systems SR830 DSP Lock-In Amplifier.

4.2.2 Analysis and results

Fig. 4.11 shows the electrical resistivity versus temperature and magnetic field using the two-terminal setup. Each curve represents the process of an isothermal magnetization curve, where the starting point is reached in a ZFC process. The magnetic field sweep protocol is represented in the figure. Only the first magnetization and the reversal from positive to negative saturation curves are obtained (as they are expected to be symmetrical). In the figure we observe a decreasing trend of the magnetoresistance with the applied field, together with a displacement, with respect to $H = 0$, of the maximum of resistance in the FM state. It is important to note that, as expected, no change is observed in the FM reversal process. Since there is no change in the magnetic state it should not be any change in the electrical resistance.

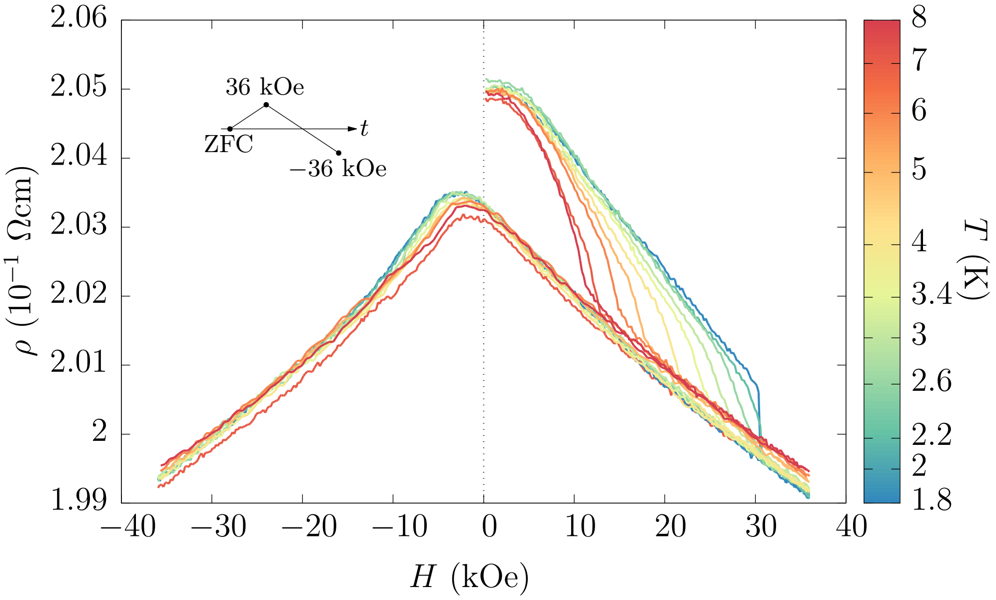

Figure 4.12: Magnetic field dependence of the electrical resistivity at low temperatures, measured using the two-terminal configuration.

Fig. 4.12 shows the low temperature resistivities of the previous figure. The magnetic field step between each point is 200 Oe. That small step implies, as was commented in the chapter dedicated to magnetization measurements, that the spontaneous magnetization jumps observed at faster sweeping rates are replaced by smooth transitions between the FM and the AFM state. Nevertheless, we can see that the curve at 1.8 K (bluest) certainly presents a jump in the resistivity at 30 kOe. In the next chapter we will study the evolution of the magnetoresistance during a continuous sweep of the field.

The results shown in Fig. 4.12 indicate a electrical resistivity of ~ 0.1 Ωcm. However, the electrical resistivity of the R_5Ge_3 compounds is expected to be comparable in magnitude to those of the pure rare earth metals [66]. Also, the electrical resistivity of several members of the R_5Ge_3 family were reported some years ago, Tb_5Ge_3 and Gd_5Ge_3 in Ref. [82]; and Ce_5Ge_3 and La_5Ge_3 in Ref. [80]. In those works, the values of the resistivities laid in the range of $\sim 10^{-4} - 10^{-3}$ Ωcm. Therefore, we need to interpret the results taking into account other sources of resistance. In this case, because of the setup used, the obvious source of resistance are the large connecting wires.

To obtain more accurate values for the resistivity of Nd_5Ge_3 I used the custom made four-terminal experimental setup explained before and shown in Fig. 4.10. The temperature dependence of the electrical resistivity obtained with this setup

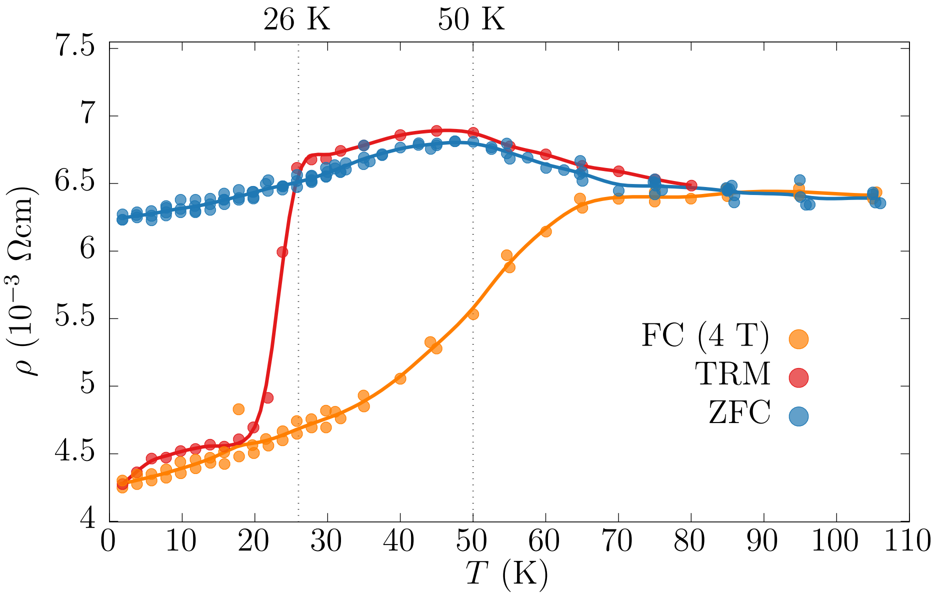

Figure 4.13: Temperature dependence of the electrical resistivity on the different different states. Lines are represented as a guide to the eyes.

is presented in Fig. 4.13. The first thing to notice is that the values lay within the expected range of $10^{-4} - 10^{-3}$ Ωcm. In the figure we can observe the behaviour of three different states with the temperature. I studied the AFM state following a ZFC protocol, then I studied the system under a magnetic field of 40 kOe, prepared following a FC process with this same field. The red curve of the figure corresponds to the last study of the electrical resistivity, in this case performing a TRM process: cooling down to the desired temperature, following a FC protocol, setting the magnetic field to 0, and then the measuring while raising the temperature. In the figure we observe that below 20 K the electrical resistivity changes slightly between the TRM and the FM, i. e., the dependence of ρ with the magnetic field is small when the system is in the FM state $\delta\rho = (\rho(0) - \rho(H))/\rho(H) \lesssim 2\%$. On the contrary, the change in resistivity between the AFM state and the FM is large enough, $\delta\rho \sim 30\%$, to incorporate the Nd_5Ge_3 compound to the large list of systems that present giant magnetoresistance (GMR). When we study the TRM process, as happens with the magnetization, we see that the electrical resistivity has a sudden and large change between 20 and 26 K. Above 26 K the dependence is the same than the obtained in the AFM curve. One can also observe that there are no marked irregularities in the trend of the ZFC curve below T_N. Nevertheless a detailed study should be done in that region, subtracting the lattice contribution, to unravel any anomaly.

4.3 Conclusions

In summary, in this chapter I have shown the study of the specific heat and the electrical resistivity in the two magnetic phases of the system Nd_5Ge_3. Definitively, the magnetic properties of this system are so important that have a huge effect in the other physical properties. From the low-temperature data of the specific heat we have modeled the different contributions to the specific heat. A magnetic T^2 contribution is found in both the ferromagnetic (FM) and antiferromagnetic (AFM) phases. This term can be understood as a mixture of FM and AFM interactions in different dimensionalities. In the case of the AFM phase this T^2 term can be attributed to a type-A AFM, while in the case of the FM phase can be interpreted as a remanence of AFM interactions. The large magnetocrystalline anisotropy of Nd_5Ge_3 is evidenced by a gapped spin-wave spectrum in both phases. The average magnetic moment at low temperature in the two magnetic phases has been obtained by means of the specific heat contribution of the hyperfine splitting of the nuclear moment of the Nd^{3+} ions. The value of this magnitude is approximately 2 μ_B in both phases, which corresponds to the saturation value of the FM state at low temperature. Hence, we state that the magnetic-field-induced transition between both states corresponds to an irreversible spin-flip transition of the Nd ions. Finally, from the magnetic field dependence we observe that the field at which the spontaneous transition takes place is remarkably smaller than the expected value from the magnetic field-temperature phase diagram. This is most likely due to the effect of being in an environment with a smaller thermal coupling (PPMS® vs MPMS®), leading to a spontaneous ignition of a thermally assisted transition at smaller fields, probably by means of a magnetic deflagration process.

Regarding the electrical resistivity experiments, I have designed different setups to measure the electrical resistivity at different magnetic fields and temperatures. The first measurements, performed with a two-terminal setup, reveal a large and abrupt change in resistance between the AFM and the FM states. The exact dependence of the electrical resistivity with the temperature for the different magnetic states, and for the TRM process, was obtained using a four-terminal setup; and reproduced in resistivity what we have observed in magnetization measurements (see section 3.2), with no difference between the FM and the TRM below 20 K, large differences between AFM and FM below 26 K, and a rapid change of the TRM in the vicinity of 26 K. In this four-terminal setup I have observed a decrease of the resistance between the AFM and the FM phases of 30%, which would add the compound Nd_5Ge_3 to the list of systems who present giant magnetoresistance.

I would like to mention that more electrical transport experiments were performed while as they are not finished or as the results are not conclusive I have preferred to not to show them in this thesis. However I want to mention them.

I studied the dependence of the electrical resistivity as a function of the lock-in frequency, and I studied the Hall effect. In both cases I found interesting phenomena but, as I have just mentioned, a deeper study has to be driven to share or to discard this results. What I was actually interested in with the Hall effect experiments was to analyze the anomalous Hall effect looking for the topological Hall effect, observed recently in the non-collinear antiferromagnet phase of Mn_5Si_3 (Ref. [114]). Another experiments that I could not perform but I consider relevant are: to study the dependence of the resistivity with the temperature after field cooling the system with different magnetic fields (the same experiment I would like to do with magnetization, and also with heat capacity); and to obtain, using the 4-wire configuration, the isothermal $R(H)$ curves with small field steps at several temperatures, to unravel the behaviour of the electrical resistivity when the field is applied in the opposite direction of the magnetization.

CHAPTER 5

Spontaneous field-induced avalanches on Nd_5Ge_3

One of the most remarkable properties of the intermetallic compound Nd_5Ge_3 is the abrupt, large, and spontaneous magnetic steps that can be induced by an external magnetic field. In the previous chapter was mentioned the occurrence of two types of this magnetic steps, the step in the metamagnetic AFM→FM transition, and the step in the reversal of the magnetization in the FM state. In this chapter the reader will find out that these abrupt field-induced jumps also are reflected in other physical properties of the compound beyond its magnetism.

5.1 Study of spontaneous avalanches in magnetism

When the temperature is well bellow 26 K the isothermal magnetization curves in a single crystal of Nd_5Ge_3 present two very abrupt jumps, as has been seen in the magnetic characterization measurements in the previous chapter. The fields and temperatures at which the AFM→FM transitions take place are represented in the aforementioned magnetic-field phase diagram reported by Tsutaoka et al. [83]. In that work, the AFM→FM transition fields (named critical field by the authors) where studied in the range of 2-60 K. Nevertheless, only for temperatures below 8 K the transitions took place abruptly and, only below 4.2 K they are complete (from AFM to saturated FM state, or from saturated FM to saturated −FM). It is important to mention that in the report, Tsutaoka et al. did not allude to the effective magnetic field sweeping rate used (it can be inferred though from the equipment they used –MPMS®– and the magnetic field steps of the isothermal magnetization curves (2 kOe), to be about 30 Oe/s).

In the isothermal magnetization curves obtained in the magnetic characterizations we found that the spontaneous avalanche fields for the AFM→FM transition, $H_{\text{sp-AFM}}$, and for the FM reversal, $\pm H_{\text{sp-FM}}$, depend on the size of the field steps used. For a given temperature, the shorter the field step, the "sooner", "softer" and "smaller" the spontaneous transition is, to the point of not being possible to consider it as a spontaneous transition. When the transition became smooth it is difficult to determine from the magnetization curves the exact magnetic field H_{sp} as so it is when the magnetic field step is too large since the transition can occur in between two steps. As we were interested in the steepest transitions (remember that we seek determining if the Nd_5Ge_3 compound belongs to the family of materials with magnetic deflagration phenomena), we will study them using a single field step, i. e., we will sweep the magnetic field without measuring the magnetization of the sample in between. Nevertheless to know the exact H_{sp} we will need to monitor the magnetization of the sample in some way and record the magnetic field at the precise moment at which the magnetization changes abruptly. As the change in magnetization we expect to observe is somehow rapid we can measure it using a pick-up coil surrounding the sample. The electromotive force (induced voltage) generated in a circuit within a time-dependent magnetic field is given by Lenz's law,

$$\varepsilon = -\frac{\mathrm{d}\Phi}{\mathrm{d}t}, \tag{5.1}$$

where Φ is the magnetic flux that crosses the total surface defined by the circuit. In the case of a magnetic sample of area S inside an applied magnetic field H perfectly surrounded by a N-turns coil, the expression will be in a first approximation

$$\varepsilon = -\frac{\mathrm{d}}{\mathrm{d}t}(N \cdot S \cdot B) = -N\frac{\mathrm{d}}{\mathrm{d}t}(S \cdot \mu_0(H + M)), \tag{5.2}$$

from which, in our case, as S do not depend on time and during the transition $\dot{H} \ll \dot{M}$, we get

$$\varepsilon \approx -\mu_0 N S \frac{\mathrm{d}M}{\mathrm{d}t}. \tag{5.3}$$

From the relaxation experiments performed by Maji et al. it is known that the transitions take place in a time-window of less than 10 seconds [73]. The single crystal samples of Nd_5Ge_3 have a magnetization saturation of is 57 emu/g, a density of 7.11 g/cm^3, and a typical size of $1 \times 1.5 \times 2$ mm^3. So, the expected minimum voltage induced in a 3-turns pick-up coil transitions will be

$$\varepsilon \sim -\mu_0 \cdot 3 \cdot 1.5\ \mathrm{mm}^2 \cdot \frac{\Delta M}{\Delta t} = \begin{cases} -0.23\ \mu\mathrm{V} & (\mathrm{AFM} \to \mathrm{FM}) \\ \mp 0.46\ \mu\mathrm{V} & (\mathrm{FM\ reversal}), \end{cases}$$

where the ΔM considered in the AFM→FM transition is from $M = 0$ to $M = M_S$, while in the FM reversal ΔM is from $M = \pm M_S$ to $M = \mp M_S$. The expected voltage values are certainly small, and worst, they are close to the value of the voltage constantly induced in the same pick-up coil by the sweeping magnetic field during the magnetization curve:

$$\varepsilon \sim -\mu_0 \cdot 3 \cdot 1.5\ \mathrm{mm}^2 \cdot (\pm 300\ \mathrm{Oe/s}) = \mp 0.13\ \mu\mathrm{V}. \tag{5.4}$$

However, as this "extra" contribution is maintained all along the isothermal magnetization curve it should be easy to subtract from the measurement of ε. x

5.1.1 Experimental setup

To study the spontaneous field-induced magnetic jumps the experimental setup consisted of: a 3-turns pick-up coil, placed surrounding the center of the sample, and mounted in a sample transport rod designed for electrical transport measurements; an amplification stage, which output signal (V_{amp}) is sent to a fast data acquisition card connected to a computer; and a multimeter to monitor the value of the magnetic field, connected to the same computer. An schematic diagram of the experiment setup is represented in Fig. 5.1.

Because the expected induced voltage was small and with a contribution from the applied magnetic field that would need to be subtracted we decided to use a dedicated amplification stage, with the shortest possible wiring between the coil and the amplifier. I designed a setup, mounted directly on top of the sample transport rod with an instrumentation amplifier. The instrumentation amplifier chosen was the INA128P because its precision, high common-mode rejection (50 dB at G=100, f=100 kHz), low settling time (9 μs at G=100), wide bandwith (200 kHz at G=100) and large slew rate (4 V/μs). The connection diagram is shown in Fig. 5.2. The induced voltage in the coil (C) is the input of the instrumentation amplifier. The output is connected to the analog input of a data acquisition card (AI). To reduce the noise in the output signal I used two 13 V lead-acid batteries in series as the power supply of the amplifier. The reference level of the system, Ref, is the voltage point between the batteries, and is connected to the ground. Following the recommendations of the manufacturer, when the differential source impedance is low, the bias current return path can be connected to one input, what I did with the 10 kΩ resistor connected to the + input. The gain of this instrumentation amplifier can be calculated with the following expression:

$$\mathrm{G} = 1 + \frac{50\ \mathrm{k}\Omega}{R_{\mathrm{G}}}. \tag{5.5}$$

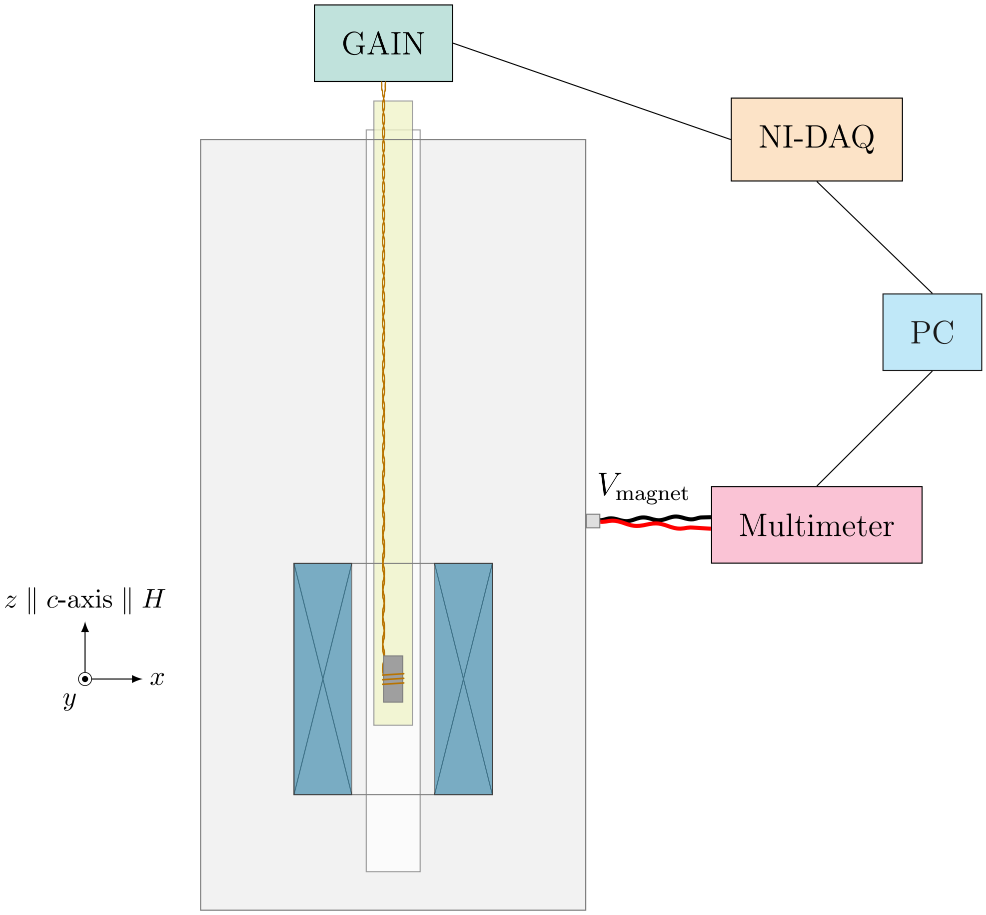

Figure 5.1: Schematic diagram of the experimental setup. The sample (dark-gray), surrounded by a 3-turns pick-up coil (cooper) is placed, using a dedicated sample rod (lime-yellow), in the center of the superconductor solenoid (dark-blue) of the MPMS® system (light-gray). The signal collected by the pick-up coil is amplified (GAIN) and measured with a National Instruments™ data acquisition card (NI-DAQ) controlled by a computer (PC). The magnetic field is determined by the analog voltage output V_{magnet} (Multimeter).

5.1.2 Analysis and results

Using the National Instruments™ LabVIEW program I programed a protocol to obtain, for different temperatures, the spontaneous fields H_{sp} in both the AFM→FM and the FM reversal processes. The protocol for each temperature consisted of the next sequence of steps:

1. Set $H = 0$ and $T = 100$ K. Wait 300 s when (H, T) stable.

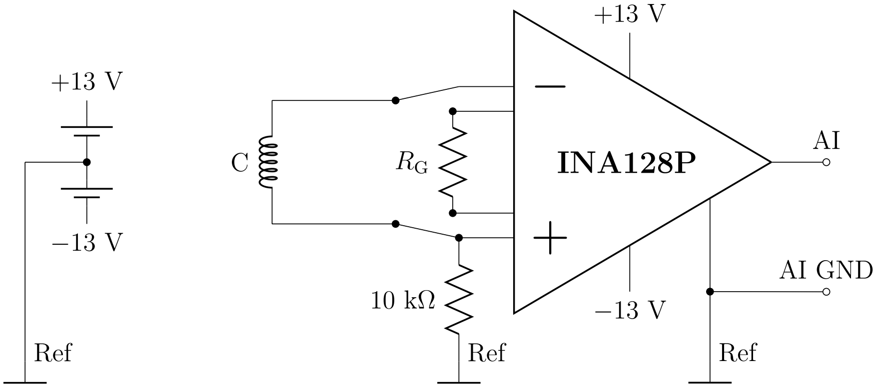

Figure 5.2: Connection diagram of the amplification stage ($\times(1 + 50\ \text{k}\Omega/R_\text{G})$) of the induced voltage in the coil (C). The output is connected to the analog input of a data acquisition card (AI). The power supply are two 13 V lead-acid batteries in series. The reference level of the system, Ref, is the voltage point between the batteries.

2. Set T. Wait 300 s when T stable.
3. Measure magnetization.
4. Set $H = 40$ kOe.
5. Monitor H and V_amp (Record $H_\text{sp-AFM}$ when a peak is detected in V_amp).
6. Measure magnetization.
7. Set $H = -40$ kOe.
8. Monitor H and V_amp (Record $H_\text{sp-FM}$ when a peak is detected in V_amp).
9. Measure magnetization.

The purpose of the measurement of the magnetization at steps 3, 6 and 9 is to ensure the system is in the AFM state at step 3, in the saturated FM state at step 6, and in the "negative" saturated FM state at step 9. With this we try to determine, the initial and final state of the system before and after each expected spontaneous transition/reversal.

This kind of large, sudden, and self-sustained processes commonly receive the name of avalanches. From now on, I will refer to the magnetic abrupt complete transitions as magnetic avalanches. The results of the study of the spontaneous avalanche fields, H_sp, in the AFM→FM transition, and in the FM reversal, as a function of the temperature are shown in the left panel of Fig. 5.3. I have to

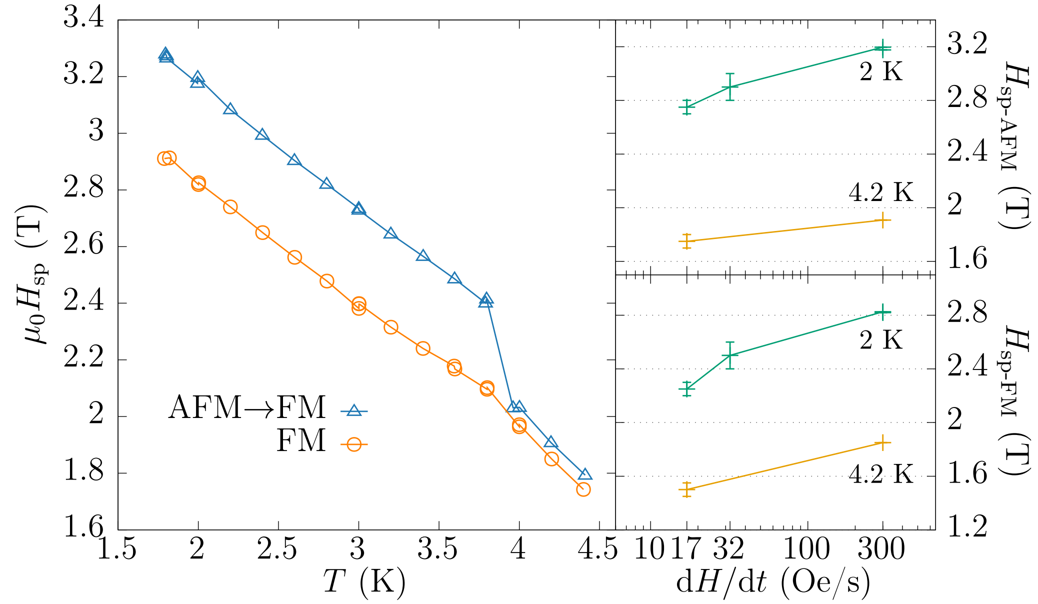

Figure 5.3: Spontaneous avalanche field. Left panel: spontaneous avalanche field as a function of temperature with a magnetic field sweeping rate of 300 Oe/s. Right panels: spontaneous avalanche fields (top: AFM→FM, bottom: FM) for two temperatures, as a function of the effective sweeping rate. Lines are represented as a guide to the eyes.

mention that, as was shown in the previous chapter, the field-induced changes in magnetization in Nd_5Ge_3 only occur when the field is applied along the c-axis, so all the experiments regarding magnetic avalanches will be with the magnetic field pointing in the c-axis direction. Back to the figure we can observe some interesting phenomena. We can see how the spontaneous avalanche field decreases when the temperature is increased in a clear linear fashion for both processes, an almost constant separation in field between them, a sudden change in the spontaneous avalanche field of the AFM→FM process right below 4 K, and a precise reproducibility of the fields (some temperatures have more than one measurement). Also as mentioned in the introduction of this section, we can see in the right panels of Fig. 5.3 how the values of the H_{sp} fields obtained with this procedure are substantially larger than those obtained in the isothermal magnetization curves. A curve with field steps of 1 kOe is equivalent to a sweeping rate of 17 Oe/s, while one with steps of 2 kOe is equivalent to a 32 Oe/s sweeping rate. Because during the isothermal magnetization curve the jump can occur between two measurements, or during a measurement, we assign an error to the determination of H_{sp} of half of the step size.

The reproducibility of H_{sp} does not depend on the temperature. One should expect that as the temperature increases, it does the “noise” in H_{sp} if its main origin is due the random thermal relaxation of some part of the sample. Instead, it looks like the sample has very few thermal relaxation but when one happens at a given field it makes the entire system to change its magnetization.

The sudden change in the spontaneous avalanche field for the AFM→FM process that occurs between 3.8 and 4 K with $\mathrm{d}H/\mathrm{d}t = 300$ Oe/s could be also present, in a minor scale, in the 17 Oe/s measurements, since the ratio $H_{\text{sp-AFM}}/H_{\text{sp-FM}}$ shows a marked decrease between the values obtained at 2 and 4 K. In the case the decrease actually appears in the same temperature range would be an indicator of some interesting phenomena happening in the AFM phase. If there were a similar clear jump in the FM reversal process one could blame to a change in the thermal bath (an increase in the cooling power would imply an increase of the values of spontaneous field), but as there is no such effect I believe that must be something related to the magnetization dynamics of the AFM phase, like there were two contributions to start the avalanche, and below some temperature one of the contributions fade out.

Below 4 K we found that the ratio $H_{\text{sp-AFM}}/H_{\text{sp-FM}}$ is between 1.13 and 1.16 for all the magnetic field sweeping rates. That means that, while the exact value of H_{sp} depends on $\mathrm{d}H/\mathrm{d}t$, it affects equally to both magnetic jumps. At the moment of the spontaneous avalanche, the magnetization of the two states is very different. In the AFM phase, as the temperature is reduced, the pre-jump magnetization relaxation become smaller for a given field, but in the FM phase the magnetic relaxation is negligible in this range of temperatures (see Fig. 3.15). Therefore, even if the ΔM plays a role in the determination of the ignition point of the avalanche, its contribution has to be small because we do not observe an increase on $H_{\text{sp-AFM}}/H_{\text{sp-FM}}$ when temperature decreases. There are more factors that affect the ignition condition, like the thermal diffusivity (that depends on the temperature), the energy barrier to overcome (which depends on the magnetic field), the relaxation rate (that depends on the energy barrier and the temperature of the system) and the energy released in the relaxation (which depends linearly with the magnetic field and the magnetization change, ΔMH). The ignition condition for the magnetic avalanches was derived in a work of Garanin and Chudnovsky [36]. Despite they focus on the case of single molecule magnets, we can use their derivation to explore the spontaneous avalanche ignition conditions in our material.

The spontaneous avalanches occur when the system produces locally more heat than it is able to release to the environment or transport to further parts of the system. The equation describing the evolution of the temperature of the system,

$$\frac{\mathrm{d}T}{\mathrm{d}t} = \frac{1}{C}\frac{\mathrm{d}\Delta E}{\mathrm{d}t} + \nabla \cdot \kappa \nabla T, \tag{5.6}$$

accounts for the heat produced by the magnetic relaxation, $\mathrm{d}\Delta E/\mathrm{d}t$, and for the heat diffusion across the system $\nabla\cdot\kappa\nabla T$. Because $\Delta E \propto \Delta M$ and $\mathrm{d}M/\mathrm{d}t = f(T)$, the integration of Eq. (5.6) can not be done analytically. Nevertheless, after some assumptions on the boundary conditions and the timescales involved in the process (details in Ref. [36]), a new equation for the temperature evolution is obtained,

$$\frac{\mathrm{d}T}{\mathrm{d}t} = \frac{\Delta\tilde{E}}{C}\cdot\Gamma\cdot\Delta M - \Gamma_d(T-T_0), \tag{5.7}$$

where $\Delta\tilde{E}$ is the energy released per unit of magnetization, Γ corresponds to the magnetic relaxation rate, ΔM is the change in magnetization that is produced in a relaxation, Γ_d is the rate of heat dissipation and T_0 is the temperature of the thermal bath. It is possible to obtain the critical relaxation rate at which the spontaneous avalanche will ignite, imposing that the temperature evolution defined by Eq. (5.7) starts growing from T_0, i. e., having the minimum with respect to temperature equal to 0 at $T = T_0$,

$$\left.\frac{\mathrm{d}\dot{T}}{\mathrm{d}T}\right|_{T_0} = \frac{\Delta\tilde{E}}{C}\cdot\left.\frac{\mathrm{d}\Gamma}{\mathrm{d}T}\right|_{T_0}\cdot\Delta M - \Gamma_d = 0, \tag{5.8}$$

and obtaining therefore,

$$\left.\frac{\mathrm{d}\Gamma}{\mathrm{d}T}\right|_{T_0} = \frac{C\Gamma_d}{\Delta\tilde{E}\cdot\Delta M}. \tag{5.9}$$

If the system possesses a unique magnetic barrier $U(H)$, the relaxation would obey the Arrhenius formula

$$\Gamma = \Gamma_0\exp\left(-\frac{U(H)}{k_BT}\right), \tag{5.10}$$

implying the critical relaxation rate that lead to a spontaneous avalanche to be

$$\Gamma_{\mathrm{sp}} = \frac{8C\kappa_0k_BT_0^2}{\Delta\tilde{E}\cdot\Delta M\cdot U(H)\cdot l^2}, \tag{5.11}$$

where Γ_d has been substituted by $8\kappa_0/l^2$, with κ_0 and l being the thermal diffusitivity at T_0 and the characteristic length of the smallest dimension of the sample respectively. Again, considering a unique barrier in the system and $\Delta\tilde{E} = H$, we will have an spontaneous avalanche when $\Gamma(H,T_0) = \Gamma_{\mathrm{sp}}$, i. e.,

$$H\cdot U(H)\exp\left(-\frac{U(H)}{k_BT_0}\right) = \frac{8C\kappa_0k_BT_0^2}{\Gamma_0l^2\Delta M}. \tag{5.12}$$

This equation does not takes into account the fact that the magnetic field is being swept. When the magnetic sweeping rate is large and the system is at low temperature we can consider that the magnetization has no time to relax, so we can apply the last equation as a first approximation (infinite sweeping ratio). In the chapter dedicated to the study of magnetic deflagrations in Nd_5Ge_3 we will get the ingredients needed to compute this expression and find the expected values of H_{sp} as a function of the temperature. For now we can anticipate that the relation works reasonably well in our case, despite the fact that this expression was originally derived for a single molecular magnet crystal very different from our system.

Nevertheless, in the meantime, we can obtain some valuable information taking a deeper look at the experimental behaviour of H_{sp}. The data obtained suggest a linear dependence of the spontaneous avalanche field with the temperature. To relate both variables, the first thing that one may consider is the relation between the relaxation rate and the temperature and the energy barrier (which depends of the applied magnetic field). Let us suppose that exists a critical magnetic relaxation rate, that only depends on the energy barrier and the temperature

$$\Gamma_{\mathrm{sp}} = \Gamma_0 \exp\left(-U(H_{\mathrm{sp}})/k_B T\right) . \tag{5.13}$$

While it seems like I am going to obtain the same relation presented before, note that now we are not considering the thermal dynamics on the sample explicitly. The isothermal magnetization measurements for the different crystallographic axes presented in the chapter 3 showed that the Nd_5Ge_3 compound resembles a system with uniaxial anisotropy. The magnetic energy barrier of a uniaxial anisotropy system is

$$U(H) = U_0 \left(1 - \frac{H}{H_a}\right)^2 , \tag{5.14}$$

with U_0 as the energy barrier at zero applied magnetic field, and H_a as the anisotropy magnetic field at which the barrier is suppressed. With some basic algebra we obtain

$$H_{\mathrm{sp}} = H_a \left(1 - \sqrt{\frac{k_B T}{U_0} \ln\left(\frac{\Gamma_0}{\Gamma_{\mathrm{sp}}}\right)}\right) . \tag{5.15}$$

The fit of experimental data to Eq. (5.15) is shown in Fig. 5.4. The results obtained are:

$$\begin{array}{r|l} \text{AFM}\to\text{FM} & \mu_0 H_a = 5.19(1)\ \text{T}, \quad \gamma = 0.075(1)\ \text{K}^{-1} \\ \hline \text{FM-reversal} & \mu_0 H_a = 4.73(1)\ \text{T}, \quad \gamma = 0.081(1)\ \text{K}^{-1} \end{array} .$$

where $\gamma \equiv k_B/U_0 \ln\left(\Gamma_0/\Gamma_{\mathrm{sp}}\right)$.

Let us consider if those values have physical sense. On the one hand. the value of Γ_{sp}, given the reproducibility of the phenomena and the sweeping rate of the magnetic field, is expected to be about 1 Hz or more. Therefore, taking

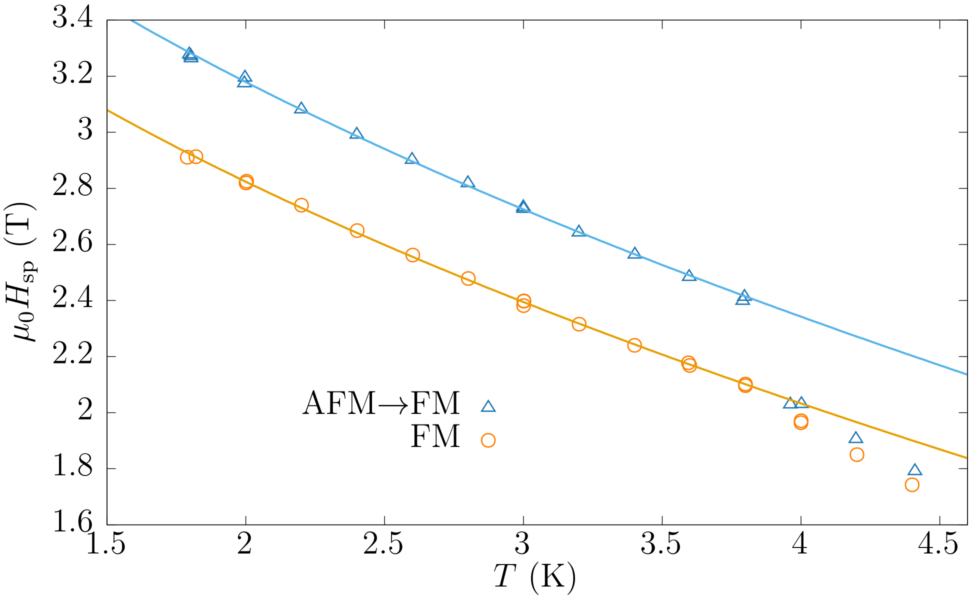

Figure 5.4: Spontaneous avalanche field as a function of temperature with a magnetic field sweeping rate of 300 Oe/s. Lines represent the fit to Eq. (5.15) below 4 K.

$\Gamma_0 = 10^7$ s^{-1} in Nd_5Ge_3 from Ref. [73], the values of γ will be always much smaller than one since it is reasonable, given the large anisotropy, a zero field energy barrier U_0 of hundreds of Kelvin. On the other hand, looking at the trend of H_{sp} one may expect a value of H_a around 50 kOe.

It is clear from these fits that one have to consider only temperatures lower than 4 K to obtain such a precise likeness. Taking into account this constrain in the fits it definitely looks like there is something above 3.8 K, in both states. In the work of Tsutaoka et al. (Ref. [83]), one can observe, looking at the isothermal magnetization curves, that the separation between what they call H_c and H_d ($H_{\text{sp-AFM}}$ and $H_{\text{sp-FM}}$ for us if they would had used a continuous sweeping rate of 300 Oe/s) is reduced around 4 K and then increases again when the temperature is raised. The origin of this discontinuity may be attributed to a change in the thermal properties of the bath or of the sample, but the heat capacity of the sample does not show any discontinuity as we have already seen in chapter 4, so the most plausible explanation is the change of the MPMS®'s cooling power. Above the boiling temperature of liquid helium (4.2 K) the systems maintains the temperature of the sample space stable by using the gas heater to warm the incoming helium gas evaporated from the main reservoir. Below that point, the temperature is stabilized controlling the pressure over of the liquid helium condensed in a pot. The large difference in the required control mechanisms in both temperature regimes may be translated to an abrupt change in the cooling power, which would explain the discontinuity observed in H_{sp} around the crossover temperature.

In summary, the fact that the experimental points can be fitted precisely to Eq. (5.15) is a remarkable hint that leads to the possibility of describing the magnetic energy barrier as the one of a system with uniaxial anisotropy, and also points to consider that the thermal transport properties do not play a crucial role in the moment when this spontaneous avalanches occur (in the range where the points fit to the expression).

5.2 Spontaneous avalanches in magnetostriction

Another interesting property of many rare-earth compounds is their magnetoelastic phenomena, which in certain cases shows irreversibilities. In this section, I want to present briefly the study of the magnetoelasticity phenomena in a single crystal of Nd_5Ge_3 reported by Doerr et al. [81], for a better understanding of the compound, and to show the reader the rich phenomena this system posses. In their experiments Doerr et al. observed a strong magnetostructural irreversibility induced by the applied magnetic field. The reported results on thermal expansion for the c-plane and the c-axis are shown in Fig. 5.5. They followed two protocols, first a ZFC (black points) and then a TRM at the lowest temperature (red points) –they do not commented in the paper the magnitude of the field applied but it is said that the fields are applied in the direction of the axis under study. In the

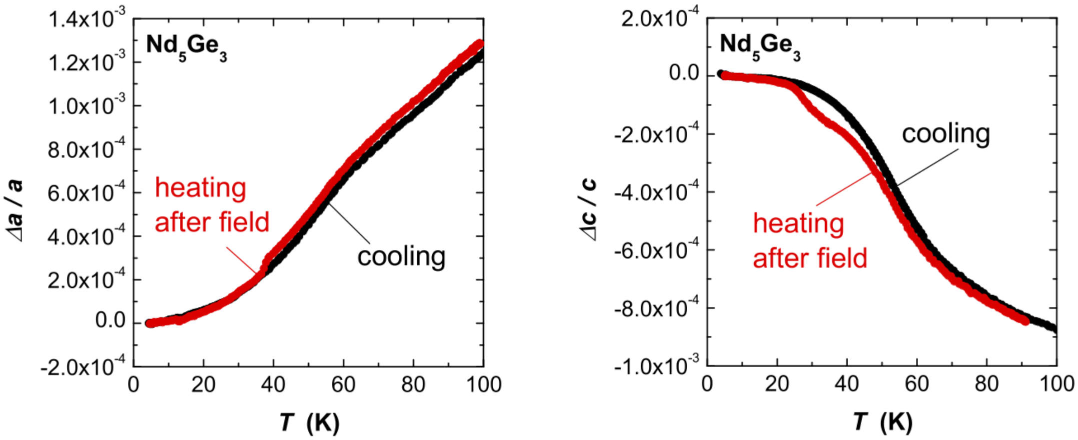

Figure 5.5: Thermal expansion of Nd_5Ge_3 under ZFC (black) and TRM (red) protocols, with the magnetic field applied along the axis under study. Left panel: thermal expansion along the c-plane. Right panel: thermal expansion along the c-axis. Extracted from Ref. [81].

c-plane (in this case a-axis), the system expands as the temperature is increased with an inflection point at the Néel temperature $T_N = 50$ K, and there is no difference between the ZFC and the TRM protocols. On the contrary, in the c-axis they see how the system shrinks that dimension when warming up. In the ZFC this only happen for $T \gtrsim 26$ K, while in the TRM above $T \gtrsim 20$ K starts decreasing, then has an step around 26 K and then smoothly tends to the value of the ZFC curve, which reaches at T_N. Bellow 26 K the c-axis of the system is “frozen” no matter what, and has a first contraction before 40 K if there is no magnetic field applied, then contracts more and more with an inflection point at T_N.

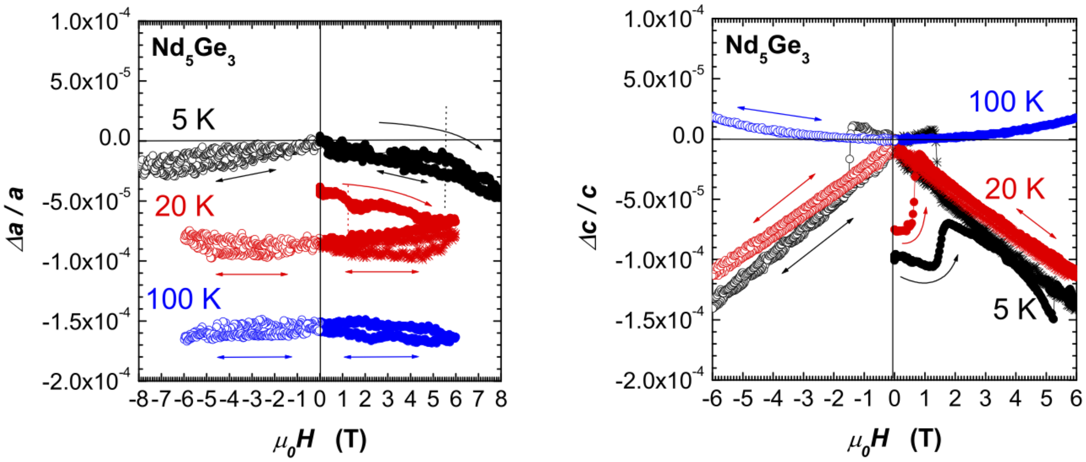

Figure 5.6: Longitudinal magnetostriction of Nd_5Ge_3 Left panel: thermal expansion along the c-plane. Right panel: thermal expansion along the c-axis. Extracted from Ref. [81].

The results on longitudinal magnetostriction are presented in Fig. 5.6, and reveal the magnetic field-induced origin of the marked irreversibility not observed in the thermal expansion. In the c-plane the dependence of the longitudinal magnetostriction with the applied field has the same behaviour at three different temperatures, and do not shows irreversibility. On the contrary, in the c-axis, for the three temperatures represented we can see three very different behaviours. Focusing in the 5 and 20 K curves we observe how the system starts contracting with the applied magnetic field up to a field at which presents an abrupt elongation which is not recovered in the process of setting the field back to 0. We also see that, in the curve at 5 K, the system presents an irreversibility when crossing the zero magnetic field, elongating the sample instead of contracting it, up to a point in field where it contracts suddenly, remaining in that contracting tendency until the field is again applied in the contrary direction. We believe that this is a clear indication that this behaviour is caused by the interaction of the magnetization

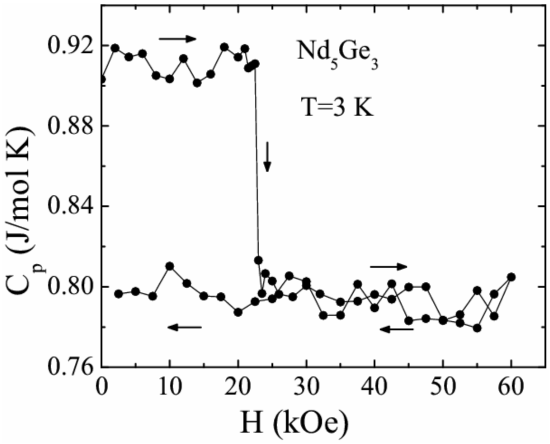

Figure 5.7: Magnetic field dependence of the specific heat of a polycrystalline sample of Nd_5Ge_3 at 3 K. Extracted from Ref. [73].

and the applied field: the sign of the magnetostriction is defined by $-H \cdot M$, being M the magnetization along the chosen axis.

I have included this results in this chapter because, while in the Fig. 5.6 are not observed complete avalanches, I am absolutely convinced that it is just due the fact that the measurements where performed too slowly. My hypothesis is that this system has spontaneous field-induced elongation(contraction) avalanches during the AFM→FM(FM) processes, precisely because the abrupt change in M in both.

It worths to mention again (see the end of Sec. 3.1.2) that this magnetoelastic transitions do not correspond to a change in the crystalline structure of the system like the one observed in a similar rare-earth compound Gd_5Ge_4 (Ref. [115]). This is confirmed by neutron diffraction experiments performed at low temperature under an external magnetic field [88].

5.3 Study of spontaneous avalanches in heat capacity

Abrupt variations in the specific heat of Nd_5Ge_3 were first reported by Maji et al. using a polycrystal [73]. Their results are shown in Fig. 5.7. They observed a large and very sharp decrease of the specific heat at the field at which they observed the AFM→FM transition in the isothermal magnetization curve. In the previous chapter I have shown the magnetic field dependence of the specific heat at 1.2 K in which the same phenomena is observed. However, the field where the abrupt

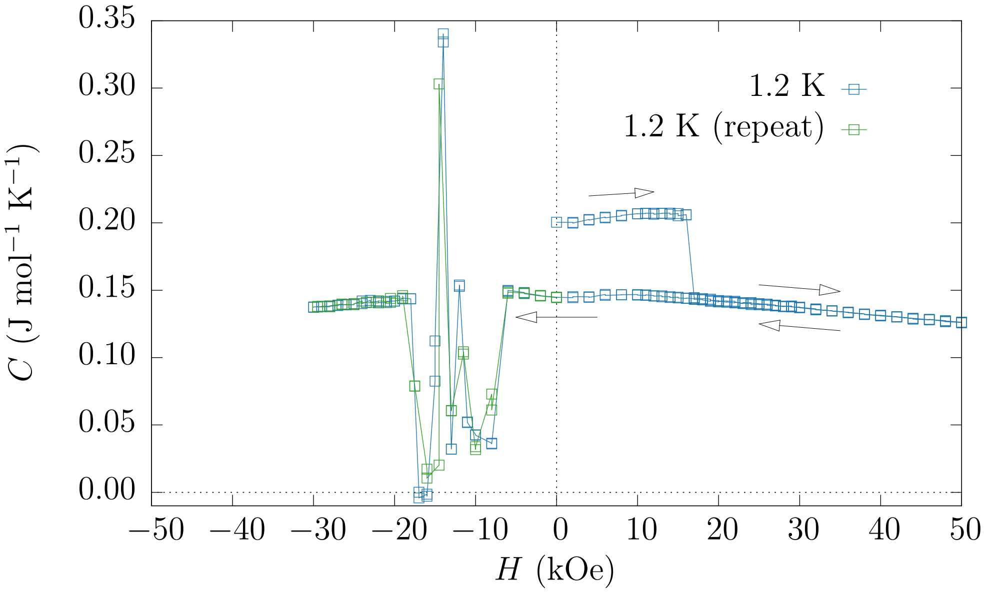

Figure 5.8: Magnetic field dependence of the specific heat at 1.2 K, starting with the system in the AFM state. Two independent runs are plotted for $H < 0$. The lines joining the data points are guides to the eye.

transition takes place is very different from what can be extrapolated from the fits of the spontaneous magnetic avalanche fields (see Fig. 5.4) and from the obtained in the isothermal magnetization curves (see Fig. 3.13). Therefore we found interesting to study the dependence of the spontaneous specific heat jumps as a function of the temperature.

5.3.1 Analysis and results

The first thing we tried was to measure the large change in the specific heat induced by the external applied field. From specific heat measurements as a function of temperature we find that around 1.2 K the relative specific heat between the AFM and FM phases has a maximum. Fig. 5.8 shows two independent runs of the isothermal magnetization process at 1.2 K. The process starts preparing the system in the AFM state following a ZFC protocol. Then the specific heat is measured in equidistant magnetic field steps up to $H = 50$ kOe and from there down to −30 kOe. I will focus first on the positive branch of the magnetic field. The magnetic field at which the specific heat has the sudden drop lays between 16 and 17 kOe. As it was just mentioned, these values of field do not agree with what one may expect extrapolating the behaviour of the spontaneous avalanche fields vs. temperature shown in a previous section. The first thing to consider is

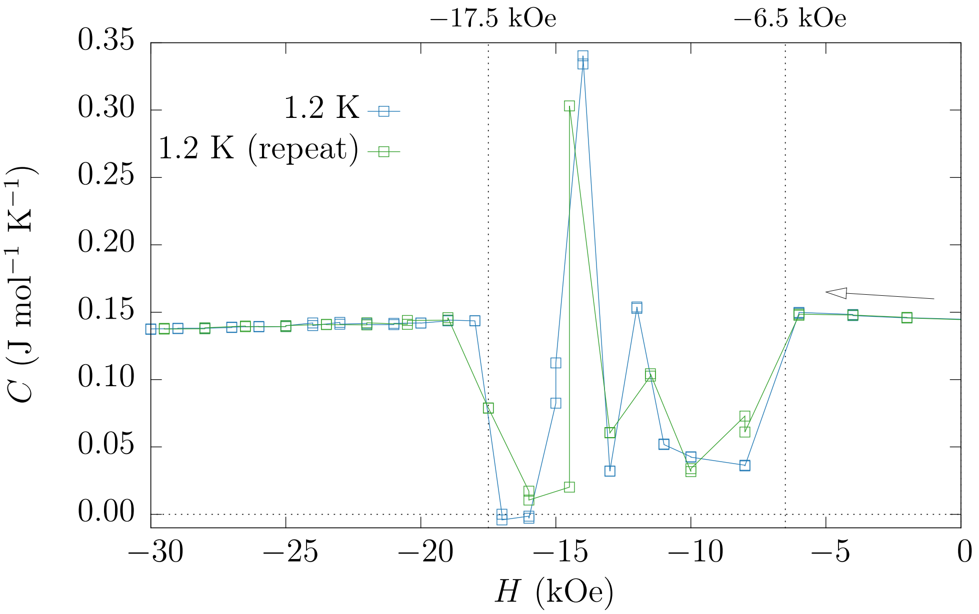

Figure 5.9: Magnetic field dependence of the specific heat at 1.2 K, starting with the system in the FM state oriented in the "positive" direction. Two independent runs are plotted. The lines joining the data points are guides to the eye.

the possibility of that this spontaneous transition has not been spontaneous but induced. I. e., we look for the possibility that the heat pulse sent to the sample to measure the specific actually triggers the avalanche. Nevertheless, the amount of power is tiny ~ 4 nW and therefore is hard to count it as the main reason of the large shift of the spontaneous avalanche field. However the heating effect is there and can not be excluded to explain a reduction. Another plausible explanation is to consider that the large difference in the thermal bath properties between the two experimental setups (MPMS® for magnetic measurements, versus PPMS® for specific heat measurements) can strongly affect how thermally-assisted abrupt transitions develop, as it has been observed in other systems [7, 116]. The thermal conductivity of the bath in the PPMS® is negligible because the high vacuum on the sample space. We believe that the difference on how the sample is thermalized in both systems is large enough to explain the reduction we observe.

Now I'll focus on the negative field part of Fig. 5.8, which is zoomed in Fig. 5.9. In this figure is represented the magnetic field dependence of the specific heat at 1.2 K, starting with the system in the FM state oriented in the "positive" direction. Two independent runs are plotted to show the reproducibility of the irregularities. We find that between −6 and −18 kOe, the specific heat measurements seem erroneous or extremely noisy. But if we look in detail we can see how the repro-

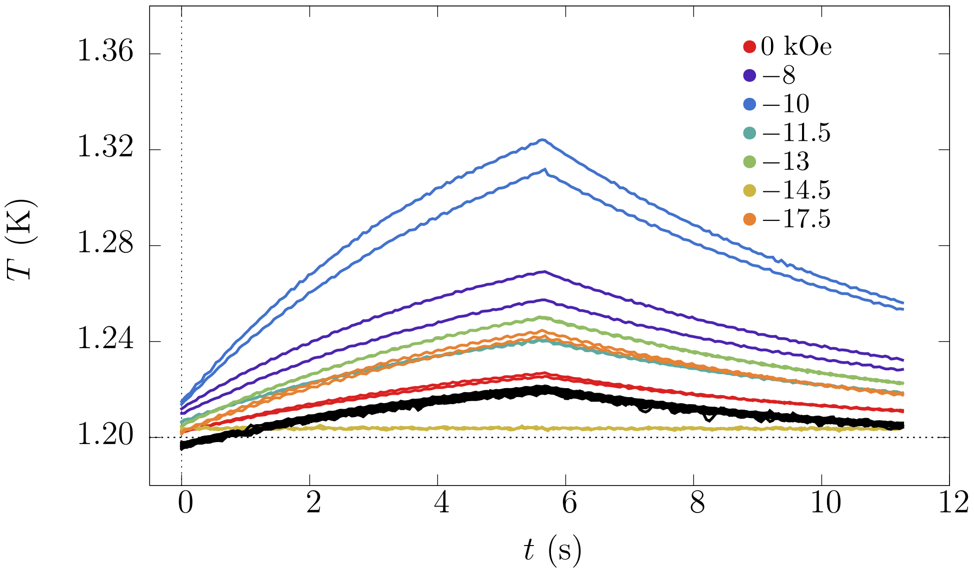

Figure 5.10: The thermal response of the sample to the heat pulse applied to obtain C for different applied magnetic fields. The curves correspond to the green points of Fig. 5.9. Black curves represent the rest of measurements not specified in the legend. Red curves correspond to the measurements at 0 kOe.

ducibility even in the “chaotic” region is large, so we can not consider these points as noise.

The thermal response of the sample to the heat pulse applied to obtain C for different applied magnetic fields is shown in Fig. 5.10. The curves are the thermal response from which are obtained the values of the specific heat for the green points presented in the previous figure. The curves whose fields lay inside the “chaotic” region are colored while the curves of the fields outside this region are shown in black color. We see that the black curves are certainly similar, unlike the colored ones. However, the color curves do not look like erroneous measurements. There are two main possible origins for this behaviour, and both are related with the sample. First let me remember the reader that the sample is fully magnetized in the opposite direction of the magnetic field that is being applied at this moment. This implies that the sample is far from the equilibrium and that any thermal perturbation has the potential to enhance the exothermic magnetic relaxation. As has been already mentioned, to extract the heat capacity of the sample, the PPMS® system fits the obtained temperature curves to a set of equations. Those equations are derived considering a single source of heat: the square heat pulse delivered by the heater placed at the sample holder. Therefore, an additional source of heat would make the results erroneous. If the amount of heat released in the magnetic

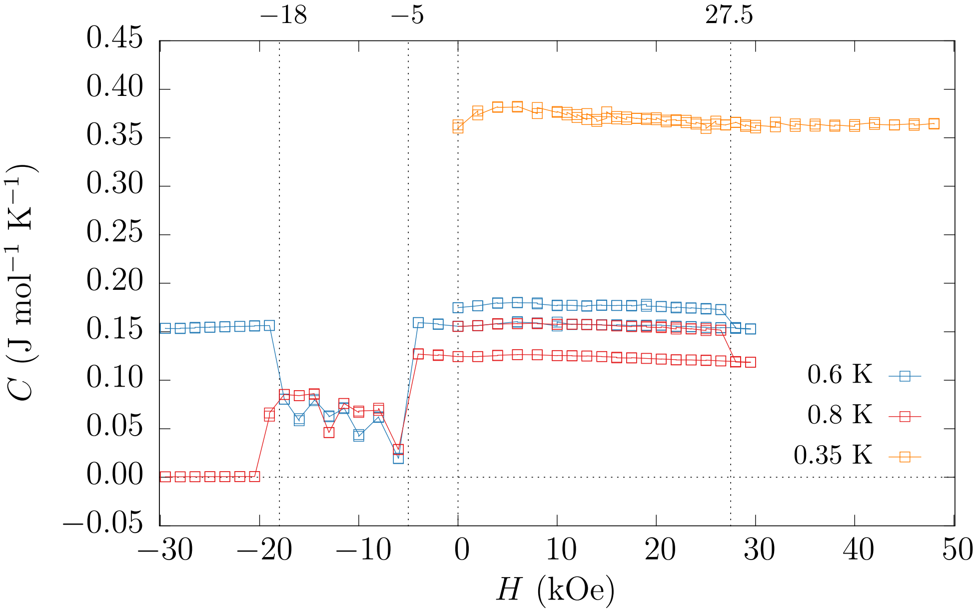

Figure 5.11: Magnetic field dependence of the specific heat at different temperatures, starting with the system in the AFM state. The curve for 0.35 K was not obtained in the negative magnetic field branch. The lines joining the data points are guides to the eye.

relaxation is small, and only occurs while the heat pulse is applied, then one could expect the measurement system to yield a smaller heat capacity value, since the system appears to be heated "more than expected". This is consistent with what is observed in Fig. 5.9, but still the behaviour seems too erratic to consider only the "self heating" origin. The second origin of the inconsistency can be a deviation of the c-axis with respect to the direction of the magnetic field, which would result in a torque to the sample platform, changing the properties of the carefully calibrated connecting wires and therefore assigning a wrong value of the specific heat. Once the magnetization of the sample is reversed the torque diminishes and the measurements recover the expected behaviour (above 18 kOe).

I measured the heat capacity as a function of magnetic field following the same protocol at 0.35, 0.6 and 0.8 K and I found the same problem (see Fig. 5.11) (the curve for $T = 0.35$ K was not obtained in the negative magnetic field branch). In this figure we see that definitively something happened at 0.8 K at −20 kOe. Sadly, this measurements were done overnight and we found the next morning that what actually had happened was that the sample platform broke (see Fig. 5.12).

When looking at the fields at which the AFM→FM transition and the FM reversal takes place (we consider the field where the measurements recover the consistency as the field of FM reversal) we find that they are systematically smaller

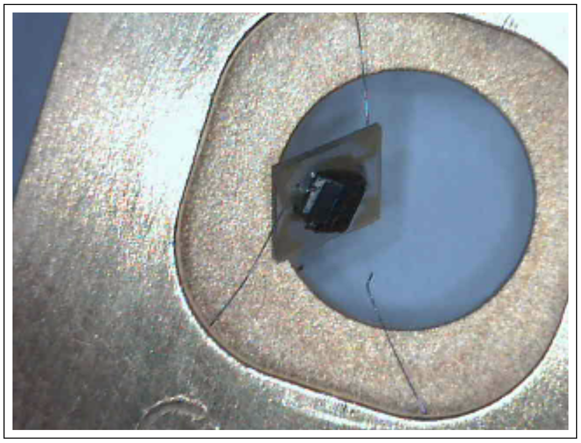

Figure 5.12: The calorimeter after the magnetic torque break the connecting wires of the platform.

than expected.

5.4 Study of spontaneous avalanches in resistivity

The electrical resistivity of Nd_5Ge_3 is the last of the physical properties where field-induced abrupt changes have been reported by Maji et al. using a polycrystal [73]. In their results, they report a sharp decrease of a normalized electrical resistivity at the field at which they observed the AFM→FM transition in the isothermal magnetization curve (see Fig. 5.13). In the previous chapter I have shown the

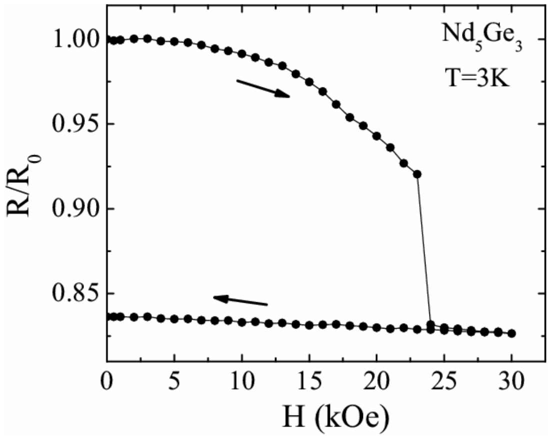

Figure 5.13: Applied magnetic field dependence of the normalized electrical resistance of Nd_5GE_3 at 3 K. Extracted from Ref. [73].

magnetic field dependence of the electrical resistivity at different temperatures. Those measurements were obtained following the isothermal magnetization curve, every 200 Oe (which is equivalent to a sweeping rate of ~ 3 Oe/s). Because of the small size of the magnetic field steps the system does not show abrupt changes in magnetization, except at the lowest temperature measured (1.8 K). Therefore we were interested in measuring the electrical resistivity as a function of time when the magnetic field is being swept at the fastest rate available. In our case the maximum rate is 300 Oe/s.

5.4.1 Experimental setup

To measure this small signals fast I used the amplification stage that I showed in the first section of this chapter (see Fig. 5.2), together with the four-terminal configuration (see Fig. 4.10); connecting the V^+, V^- lines to the inputs of the instrumentation amplifier, and applying a fixed current of 10 mA between I^+ and I^-. The data is recorded with a rate of 100 kHz using a National Instruments™ data acquisition card NI-DAQ 6010® controlled by a computer. I did with LabView the programs to control the acquisition process, and to coordinate the capture with the magnetic field-temperature protocols running in the MPMS®.

5.4.2 Analysis and results

Because of the large reproducibility observed in H_{sp} in the magnetic avalanches we can try to catch a spontaneous avalanche in resistance by tracking the magnetic field and capturing the voltage when H is around the expected H_{sp}. We acquire the signal during 10 seconds, so we have a magnetic field window of 3 kOe for each temperature. At the capturing rate of 100 kHz we will get exactly one million of points in this ten seconds-window. Fig. 5.14 shows one of the measurements performed: At 1.8 K, with the sample in the AFM state, the magnetic field is set to 4 T with a rate of 300 Oe/s; then, 1500 Oe before the $H_{\mathrm{sp}}(1.8\ K)$ obtained in the magnetic avalanches, the voltage is monitored during 10 seconds. The points obtained are represented with light blue lines. Even without smoothing the data (dark blue line) we clearly observe the step in the voltage. Looking at the data carefully we discovered hidden something very interesting. In the inset of the figure we can see how, at the moment of the “jump” of the resistance (voltage), an extraordinary large pulse of voltage is detected, first positive an then negative. I checked the data finding that this was not noise since nothing similar was captured during the rest of 10 seconds. In the inset we define t_a as the duration of the avalanche process. It is important to remember that Maji et al. indicated that the spontaneous avalanches last less than 10 seconds. I doubt they could imagine that the time span of the avalanches would be of the order of $\sim 100\ \mu$s. Fig. 5.15 shows

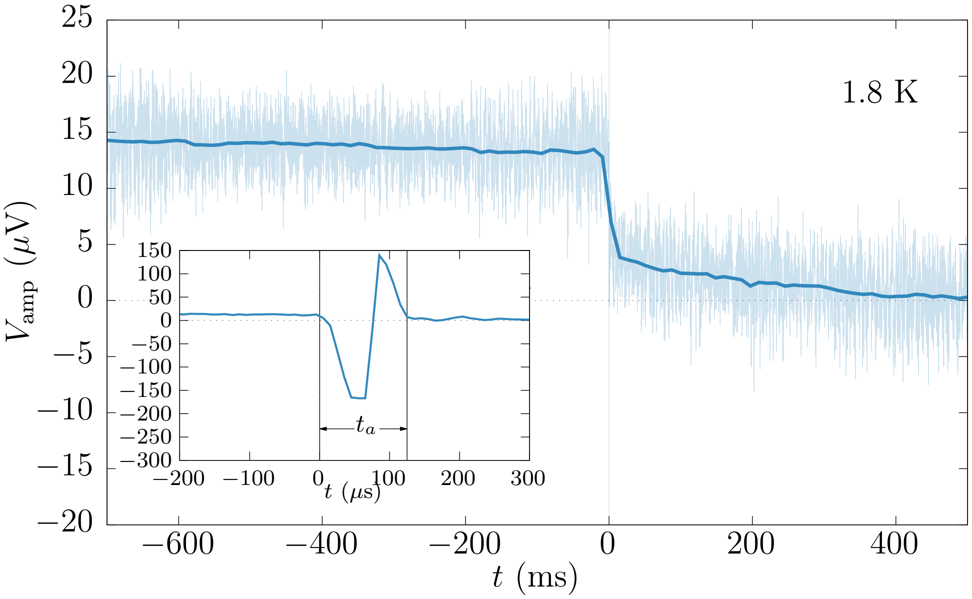

Figure 5.14: Time evolution of the voltage in the sample during a magnetic field ramp from 0 to 4 T at 1.8 K. The dark blue line represents the data smoothed. The inset shows a narrow window around $t = 0$.

the smoothed data of the change in resistance (voltage) during the AFM→FM transition for different temperatures. Because we track continuously the magnetic field, we can assign easily the magnetic field as the coordinate and plot the curves not versus time but versus field.

The burst of voltage detected resembles the spontaneous voltage generation (SVG) phenomena reported in different rare-earth intermetallic compounds like $Gd_5Si_2Ge_2$ (Ref. [117]), $La(Fe_{0.88}Si_{0.12})_{13}$ and $SmMn_2Ge_2$ (Ref. [118]), and $Tb_5Si_{2.2}Ge_{1.8}$ (Ref. [119]). In those materials the generation of voltage last tens of seconds as do the changes in magnetization, and the SVG appears triggered by the magnetic field but by the temperature as well. The origin of this phenomena is not clear yet, in some materials it is related to coupled magnetostructural transitions, in some to latent heats and magnetocaloric effects. I will now present the results obtained together with a discussion of the origin of this voltage peaks. Fig. 5.16 shows the voltage peaks observed when zooming in the discontinuity. In this figure the time for each curve has been shifted taking 0 as the begining of the negative peak. The reader will notice the tendency of the peaks to become smaller and wider as the temperature is increased, probably keeping constant the area. As observed in the peak at 1.8 K shown in a previous figure, the peaks come in pairs, one peak down followed by one peak up. I checked that this down-up signature of the peaks depend on the sign of the magnetic field (or the sign of the change

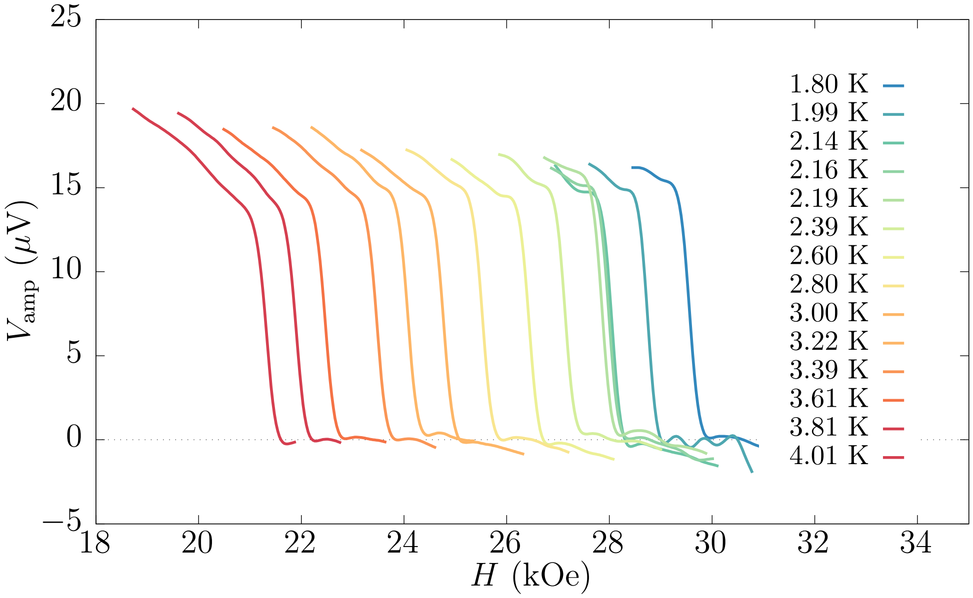

Figure 5.15: Smoothed voltage signal in the AFM→FM transition for different temperatures.

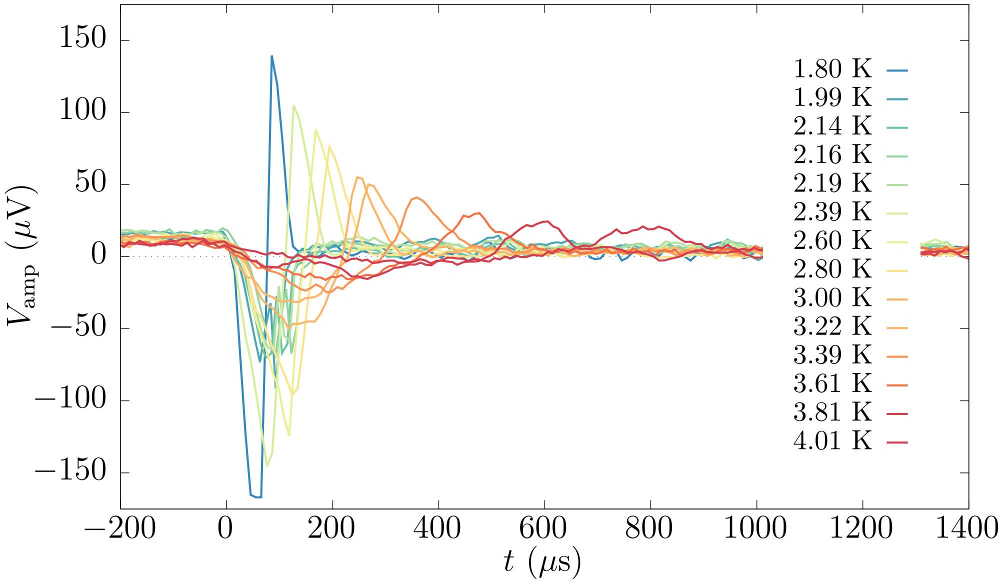

Figure 5.16: Voltage peaks detected during the transition AFM→FM for different temperatures.

in magnetization that in our case, bellow 26 K is the same thing). Nevertheless what I suspect is that in reality it depends on the direction of the change of the magnetization. Therefore it would be like an effect of induction of voltage in the system following the Lenz law. The curious aspect is that there is no loop in the setup of the 4-terminal configuration except, perhaps, the possibility that due the low resistance of the sample it closes the loop somehow on its interior.

If this voltage burst is a phenomenon that depends on the change of magnetization of the sample then we should be able to observe it in the change of the direction of magnetization during the FM reversal as well; however, the DC resistivity measurements did not reveal any discontinuity when the samples magnetization is reversed (see Fig. 4.12). Nevertheless, as we are dealing with voltage bursts that last less than one millisecond, it is impossible that would be observed during a DC measurement that takes more than one second to give a single voltage value. As we suspected, when the sample reverses its FM magnetization, a down-up(up-down) peak is also observed in the measured voltage. Due the large voltage of the peaks we can use them as a trigger in the acquisition process. This way we can measure with a higher temporal resolution a narrower time-window. The following experiments were recorder using an acquisition rate of 1 MHz during 3 ms.

To unravel the behaviour of this peaks in the FM reversal we can try to study them without applying any current to the system. I. e., to see if is a process linked to a voltage induction in a “accidental” pick-up coil we will measure the temporal evolution of the voltage between the different terminals of the 4-terminal configuration. We name the terminals as follows,

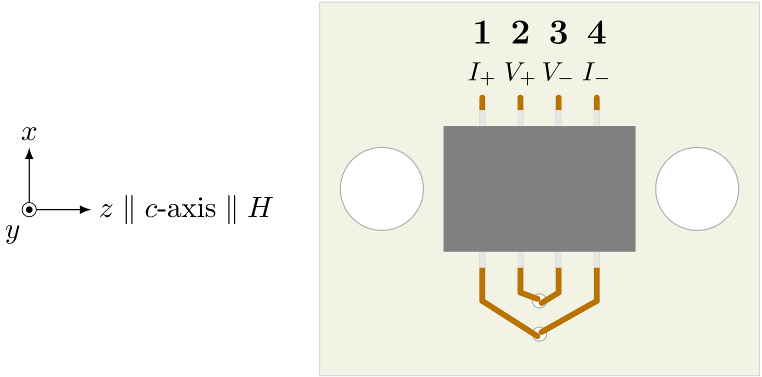

.

A representation of the voltage peaks obtained in this last experiment is shown in Fig. 5.17. I did not could extend the study as a function of the terminal for the AFM→FM transition, but based in what is observed for the FM reversal, I expect the same tendencies. In the figure we can already estimate that the area of the signals is related with the distance between the terminals. We can compute the ratios for the FM reversal areas and compare them with the ratios of the distances between the terminals:

1 − 3	**1 − 2**	**2 − 3**		**2 − 3**	**1 − 2**	**1 − 3**
1.6	2.6	3.5	**1 − 4**	3	3	1.5
	1.5	2.2	**1 − 3**	2	2	
Area		1.3	**1 − 2**	1		**Distance**

We see they are in a excellent agreement taking into account that the ratio of distances is roughly estimated. It is very difficult to measure exactly the distance between the terminal when the sample is pressed agains them; even the "electrical" distance between terminals may not correspond to the shortest one in the z direction.

Gathering all the data, we have so far found that the peaks appear both in the AFM→FM transition and in the FM reversal. We have seen that the peaks are symmetric respect to zero voltage when the field being "positive" or "negative" depending on the sign of magnetic field. We have observed that for a given $\mathbf{a}-\mathbf{b}$ terminal choice the heigh and width of the peaks is modified depending on the temperature (or indirectly on H_{sp}). The area enclosed by the peaks is conserved in this measurements, pointing to a relation with the change of the magnetization, since this is approximately the same in the magnetic avalanches for $T < 4$. We have also found that the ratio of the area enclosed by the peaks obtained for two different $\mathbf{a}-\mathbf{b}$ terminal choices, corresponds in a good approximation to the ratio of the physical separation between those. In summary, considering the shape of the signal and the properties just mentioned, it looks like the sample together with the terminals form a circuit of the type,

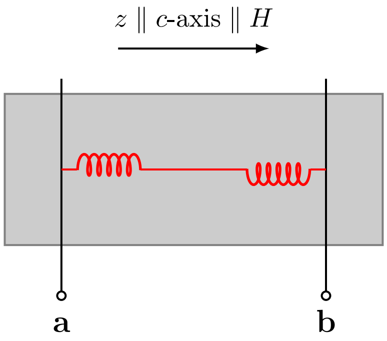

,

where the gray rectangle corresponds to the sample, $\mathbf{a}-\mathbf{b}$ are two of the four terminals, and the red solenoids represent the contribution of the sample. Note that the solenoids are wired in opposite directions between each other. In this

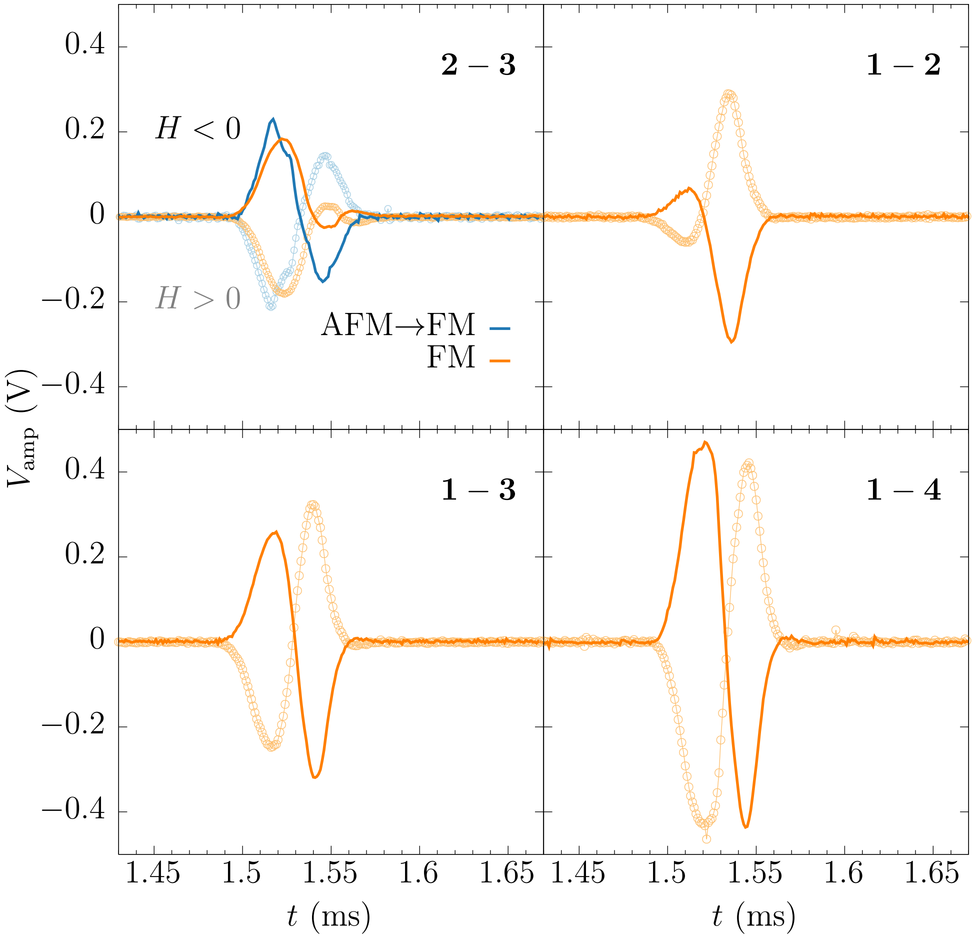

Figure 5.17: Voltage peaks detected during the AFM→FM transition and the FM reversal at 1.8 K. Top-right legends mark the terminals involved. The dark(light) curves correspond to measurements with $H < 0 (H > 0)$.

configuration, with the solenoids just at the terminals (that would correspond more likely to a single coil), we can precisely reproduce the obtained voltage curves considering a propagating front of magnetization change. Fig. 5.18 shows the induced voltage in two coils, connected in series and wired in opposite directions, when a magnetic dipole crosses them at constant speed. The three panels presented in the figure are different realizations for different distances between the coils, which in the case of our experiment would be different distances between the terminals. Taking a look at Fig. 5.17 one can see that it can be reproduced with a very simple model, while the real dynamics are not understood.

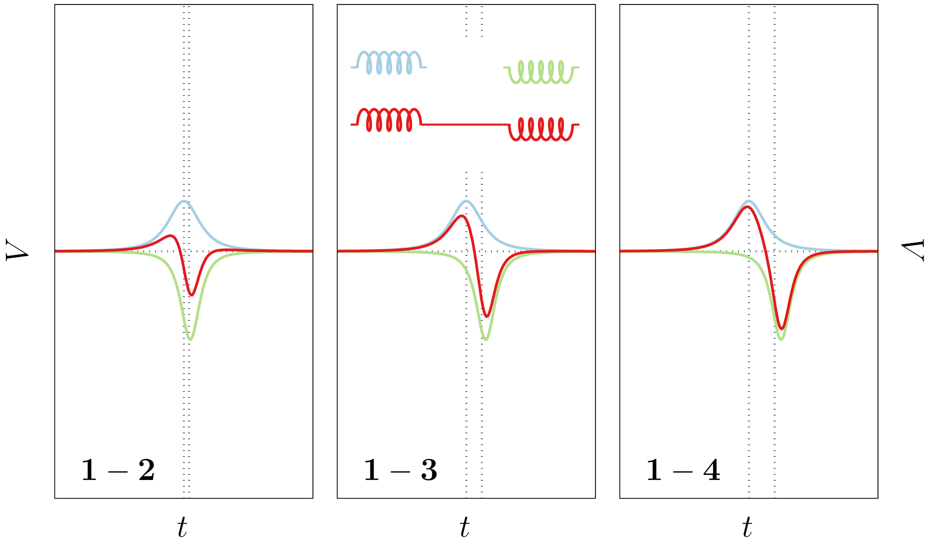

Figure 5.18: Signal expected of two similar 1-turn coils (blue and green curves), wired in opposite directions and connected in series (red curves), when a magnetic dipole crosses them at constant speed. The panels represent the signals as a function of the distance between the terminals, increasing from left to right.

It has been suggested in Ref. [117–119], that these spontaneous voltage peaks observed in different intermetallic compounds are originated due the Seebeck effect,

$$\varepsilon = -S\nabla T, \tag{5.16}$$

where S is the Seebeck coefficient of the material. This equation relates directly the voltage generated at a certain moment with the temperature gradient between the contacts, i. e., the shape of the peaks would represent one to one the temporal evolution of the hermal gradient between the chosen terminals during the magnetic avalanche. Because the timespan of the phenomena is of the order of hundreds of microseconds we know that the heat generated in the sample during the avalanche can not be thermalized in such a short period of time. We can explain the first down(up) peak because the large thermal gradient if the avalanche has set a propagating heat front, but we can not explain the following up(down) peak because we expect almost no thermal gradient between the terminal when this front reach the second one. Therefore, while the shape of the peaks resemble those observed in SVG materials, we can not conclude their origin. The main difference between their peaks and ours is the timescale, which is precisely what do not let us to explain the process as a thermoelectric phenomenon. Besides, it think that is also important to mention that in those works they found that the

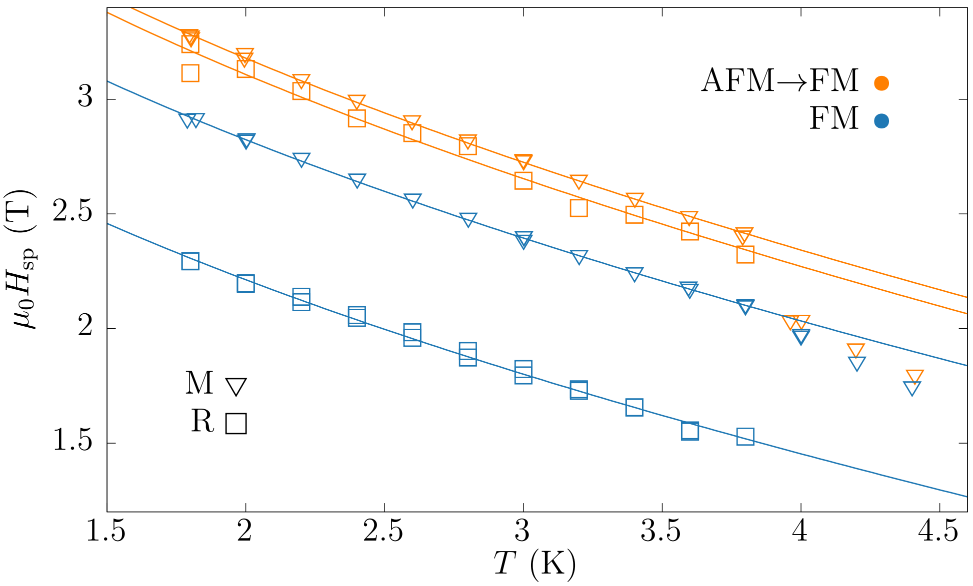

Figure 5.19: Spontaneous avalanche field as a function of temperature with a magnetic field sweeping rate of 300 Oe/s, from magnetization (triangles) and resistance (squares). Lines represent the fit to Eq. (5.15).

"sign" of the peaks depend on the sign of the change in magnetization, for which they do not give an explanation. Is very difficult to explain that dependence with just thermoelectric effects because that would imply that those effects had a directionality that depends on the sign of the magnetization change. Nevertheless, it is well known that the "direction" of changes in magnetization, if any, is always the same and is determined usually by sample's properties like the shape, impurities, dislocations… or external conditions like thermal and/or field gradients.

Finally, considering the abrupt changes in resistance in the AFM→FM transitions shown at the beginning of this section, together with the voltage peaks obtained in both the AFM→FM transition and in the FM reversal, we can plot the fields at which they occur as a function of the temperature, as we did the the spontaneous magnetic avalanches in magnetism in the first section of this chapter (see Fig. 5.3). Fig. 5.19 shows the spontaneous avalanche field versus the temperature. In the plot are represented the data from magnetic avalanches and the data just obtained from resistance avalanches and voltage induction. In the AFM→FM transition, the spontaneous fields obtained are very similar while in the FM reversal they differ significantly. However, the difference between the spontaneous fields in the FM reversal is maintained in the measured range of temperatures ($\approx$ 6 kOe). The main reasons to this difference could be the different size of the samples and/or a change in the thermal properties of the setup between both experiments. The dimensions of the sample used in this resistance experiments are approximately $0.51 \times 0.51 \times 2.2$ mm^3 while the dimensions of the one used in the magnetic avalanches were approximately $1 \times 1.5 \times 2.3$ mm^3. Nevertheless, seems like the FM reversal is more sensitive to changes in the sample size and/or in the thermal coupling with the bath with respect to the AFM→FM transition, probably because the energy released is bigger in the first ($\Delta M_{\mathrm{FM}} \gtrsim 2\Delta M_{\mathrm{AFM}\to\mathrm{FM}}$). Fitting the values of this last experimental results to Eq. (5.15) we obtain,

$$\begin{array}{r|l} \text{AFM}\to\text{FM} & H_a = 5.1(1)\ \text{T}, \quad \gamma = 0.077(3)\ \text{K}^{-1} \\ \hline \text{FM-reversal} & H_a = 4.04(3)\ \text{T}, \quad \gamma = 0.103(1)\ \text{K}^{-1} \end{array}.$$

5.5 Conclusions

In summary, in this chapter I have shown the magnetic field-induced spontaneous abrupt changes that occur in different physical properties of the intermetallic compound $\mathrm{Nd_5Ge_3}$. Magnetism, specific heat, elasticity and resistance are the physical properties that experiment spontaneous and abrupt changes during isothermal magnetization process. Besides the study of magnetoelastic effects, I performed the experiments to study the magnetic field-temperature dependence of those spontaneous changes.

Magnetism was the first of the physical properties of $\mathrm{Nd_5Ge_3}$ reported to show this spontaneous jumps. Nevertheless, to the best of my knowledge, in this thesis is presented the first explicit study of this phenomena. I have designed a setup to measure the exact magnetic field at which the jumps take place. This setup consists of a 3-turns pick-up coils which signal is amplified right at the end of the sample transport rod using an instrumentation amplifier. I have found an almost linear dependence of the spontaneous avalanche field H_{sp} with temperature; a sudden change of this linear behaviour between 3.8 and 4 K; a constant "distance" in magnetic field between the $H_{\text{sp-AFM}}$ and $H_{\text{sp-FM}}$, and a good agreement of the experimental values with a toy model that relates H_{sp} to the temperature using the supposition of a thermally activated magnetic relaxation over a single effective uniaxial energy barrier. I have also presented some results regarding the influence of the sweeping rate of the magnetic field used during the isothermal magnetizations.

The magnetoelastic transitions shown in literature are not stepped, but as I argued in the corresponding section, the reason is the slow effective sweeping rate of the magnetic field. I am convinced that the same experiment repeated with a faster sweeping rate would present a clear jump in the dimensions of the sample.

I have commented also the dependence of the “sign” of the magnetoelastic effect with the magnetization of the sample, the applied field and the magnetic state. In the AFM→FM transition the system elongates, while in the FM reversal suffers a contraction.

Specific heat spontaneous jumps are also presented in this chapter. However, the experimental values obtained for H_{sp} do not match with the ones from magnetization measurements, being smaller in the first case. The different thermal coupling in the two experimental setups is considered to be the most affecting aspect. To measure heat capacity is desired that the heat transmission only occurs between the sample and the measuring platform. Therefore, the sample, in the high vacuum conditions of the PPMS®, can barely release to the thermal bath the heat produced by magnetic relaxation and surpass the relaxation rate condition at smaller magnetic fields.

The last physical property reported to show spontaneous jumps is the electrical resistance. In this chapter, using the four-terminal configuration presented in the previous chapter, together with the amplification stage presented in the spontaneous magnetization avalanches section, I have observed jumps in the temporal evolution of the resistance during the AFM→FM transition and, perhaps more surprising, large voltage peaks during this transition and during the FM reversal. Some considerations about the origin of those peaks are discussed in the last section of this chapter, while the question remains open. I consider really interesting to extend the experiments on the electrical resistivity of the sample. With better electrical contacts, measuring along different crystallographic directions, studying the effect at slower sweeping rates and also during isofield magnetization curves. I think that the spontaneous voltage generation observed is this material could bring important clues to the understanding of the phenomena behind.

CHAPTER 6

Magnetic deflagrations on Nd_5Ge_3

In the preceding chapters I have presented how at low temperatures, the metamagnetic transition and the reversal of the magnetization in the highly anisotropic compound Nd_5Ge_3 occur abruptly –rather than being smooth processes. These abrupt changes are commonly known as magnetic avalanches. When the propagation of the local change of the magnetization is mediated by the on-site heat released and occurs at subsonic speed, the magnetic avalanche process is called *magnetic deflagration*. As was mentioned in the first chapter of this thesis, deflagration in the reversal of magnetization were first reported in molecular magnets (see Ref. [3] and references therein). This phenomenon is also found in systems with a rapid magnetic phase transition. Deflagration in metamagnetic transitions has been observed first in manganites [5], and later in the intermetallic compound Gd_5Ge_4 (Ref. [8]), where the transition is induced by a change in the crystallographic structure.

Studying the spatial and time-resolved evolution of spontaneous magnetic avalanches with a set of pick-up coils and thermometers, we found that those spontaneous magnetic avalanches propagate across the sample. In this chapter, I will report fast magnetic deflagration phenomena occurring in both antiferromagnetic and ferromagnetic phases in a single crystal of the intermetallic compound Nd_5Ge_3, being the first case of a system in which this deflagration phenomenon occurs in two different magnetic phases, and also being the first time that is observed in a ferromagnetic material.

Here I present an investigation of spontaneous and induced magnetic deflagrations in Nd_5Ge_3. Because of the "uncontrollable" nature of the spontaneous avalanches the study was focused on the induced ones, which were investigated as a function of the applied field and temperature. The induction of the deflagrations consists in the application of a short burst of heat, injecting a current pulse into

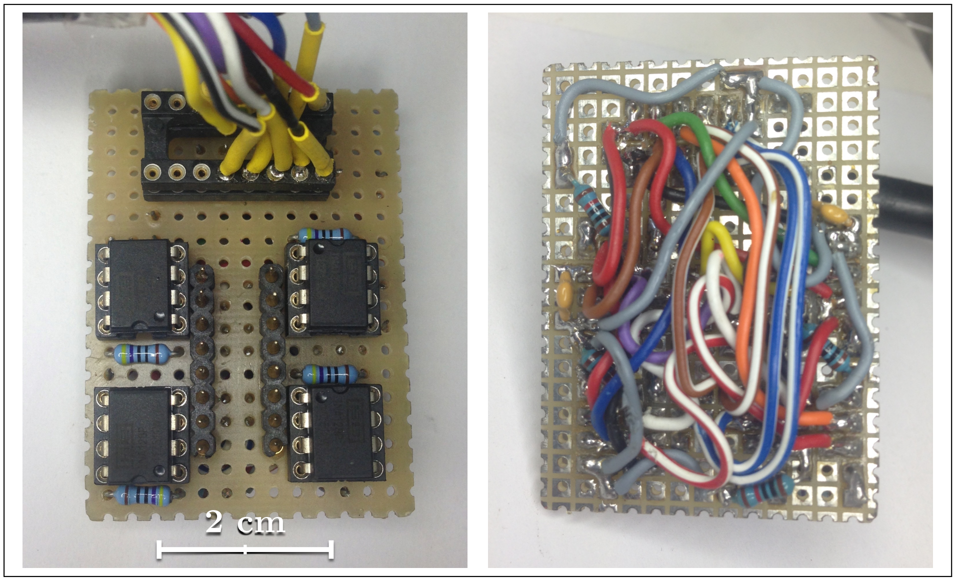

Figure 6.1: Front and back photos of the amplification stage board. The sample transport rod has a 16-pin socket at the end that is plugged into the board. The circuit for each amplifier is shown in Fig. 5.2.

a resistor placed at one end of the sample. The complete experimental setup will be shown in the first section of this chapter. In the section dedicated to the presentation to the measurements and their interpretations I will illustrate that the observed deflagrations fit well with the theory of magnetic deflagration, although it was derived for very different magnetic systems. Because of the good fitting to the theory, I will conclude this chapter showing how I extrapolate the deflagration speed to larger fields pointing out the possibility of reaching the supersonic regime (magnetic detonation) within feasible experimental conditions.

6.1 Experimental setup

To study the spatial and time-resolved evolution of the magnetic jumps I designed an evolution of the experimental setup to measure the spontaneous avalanches in magnetism shown in the previous chapter. The new setup consists of four 2-turns independent pick-up coils placed along the sample, and one resistor at each end, all together mounted at the end of a sample transport rod designed to electrical transport measurements. The amplification stage setup described in Chap. 5 is replicated for each one of the four coils (see Fig. 6.1). The output signal of the coil Ci , Vi_{amp}, is sent to a fast data acquisition card connected to a computer. The voltage across the resistor Ri is recorded using another data acquisition card

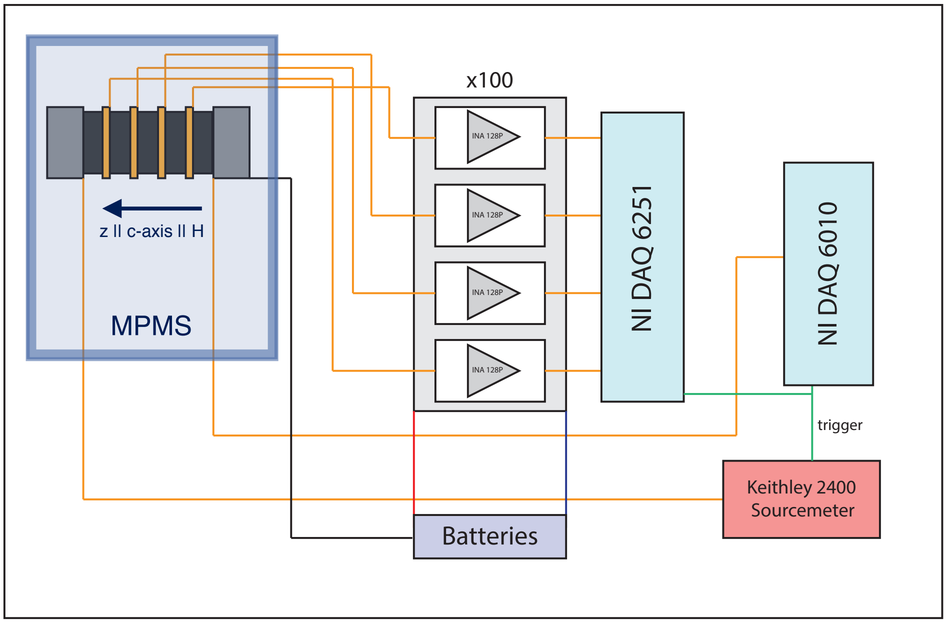

Figure 6.2: Schematic diagram of the experimental setup. The sample (dark-gray), surrounded by four independent 2-turns pick-up coils (cooper), with two resistors at the ends (gray), is placed inside the MPMS® system (light-blue), pointing in the direction of the applied magnetic field. The voltage induced at each pick-up coil is amplified (INA128P) and measured with a National Instruments™ data acquisition card (NI-DAQ 6251, light-green) controlled by a computer. The voltage at the resistors is recorded with a data acquisition card (NI-DAQ 6010, light green). The amplifiers are powered by two lead-acid batteries (gray-blue). A current pulse is sent with a Keithley 2400 Sourcemeter (red), which triggers the capture by the acquisition cards.

connected to another computer. To induce the deflagrations, one of the resistors is connected to a Keithley 2400 Sourcemeter programmed to send a current pulse. Fig. 6.2 shows a schematic diagram of the entire experimental setup. While it is not present in the diagram, another multimeter is used to monitor the magnetic field in real time, as in the original setup dedicated to the study of spontaneous avalanches. Fig. 6.3 shows two pictures and a schematic drawing of the setup of coils and resistors described. The goals in the designing process were to obtain four coils of almost identical properties (the properties of a coil are defined by the area it surrounds, the number of turns, and the "width" defined by those turns), and to place them equidistant along the sample. The way I found to fulfill these requirements was to print on a plastic sheet a sketch of the sample, together with marks where the coils should be. Those marks correspond to the black circles at

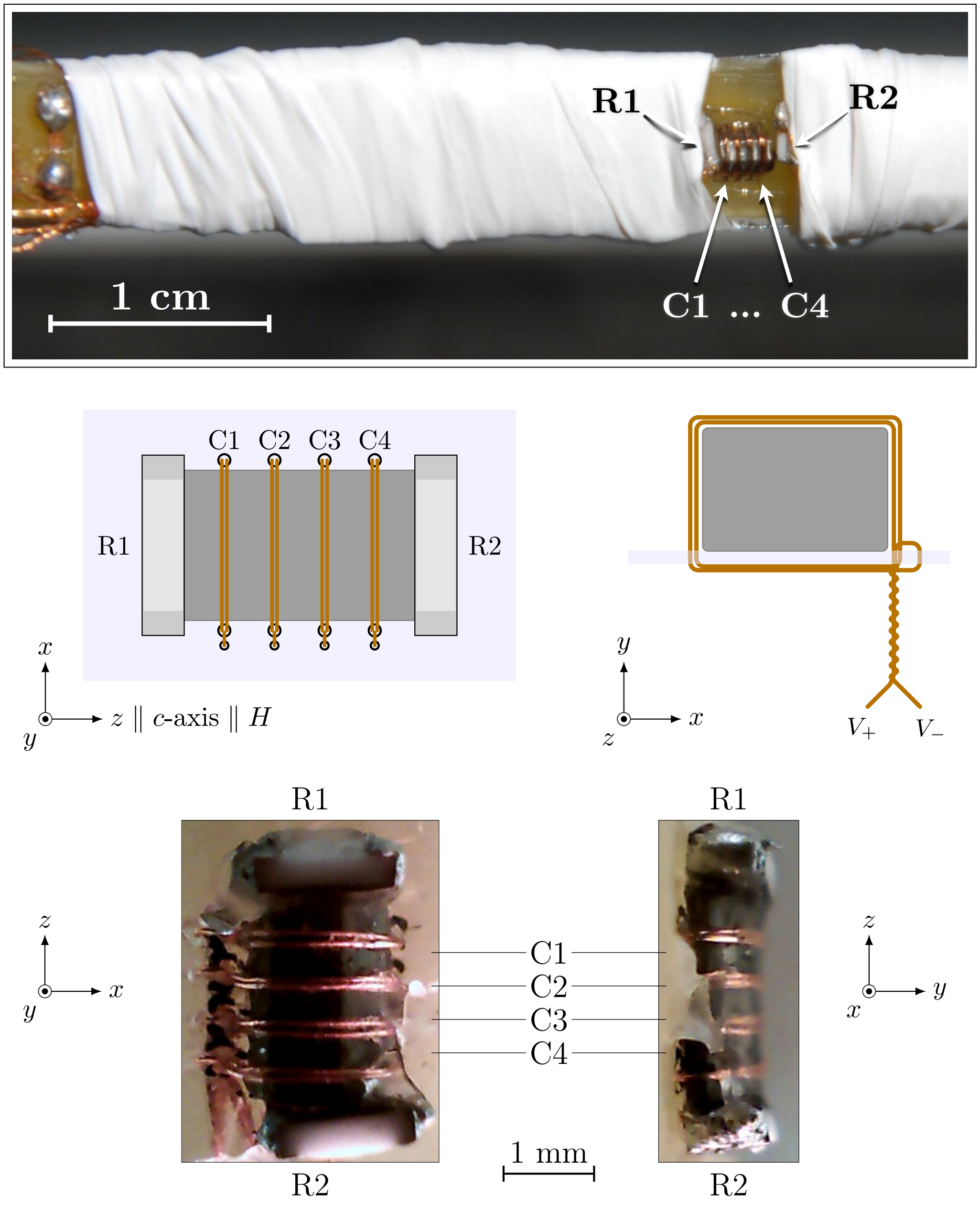

Figure 6.3: Photos and schematic drawing of the experimental setup: two resistors Ri ($i = 1, 2$), and four independent equidistant 2-turn pick-up coils Cj ($j = 1, \dots, 4$) that sew the sample (dark-gray rectangle) on a thin plastic layer (light-blue rectangle). The middle-right picture shows the loops defined by one coil.

the sides of the sample shown in the drawing on Fig. 6.3. The next step was to "sew" the sample to the plastic sheet using a coated cooper wire (⌀ 50 μm), doing two loops per coil. A tiny third loop is needed to ensure that all coils are almost equal. One resistor is placed at each end of the sample. Surface-Mount Device (SMD) resistors, made of ruthenium oxide, with a room temperature resistance of ~ 1 kΩ and dimensions $0.8 \times 0.4 \times 1.5$ mm^3 were used. Obviously, this "sewing" process is not automated. The setup was done entirely by hand, and it is worth to mention that was a challenge because of the sizes, complexity, and materials involved. A close-view of the setup is shown in two pictures at the bottom of Fig. 6.3 together with the scale.

As we have seen in the previous chapter spontaneous avalanches occur at a precise magnetic field H_{sp} for a given temperature. Therefore a way to trigger the process below that field is needed to study the magnetic field dependence of the avalanche. Several methods have been used for this purpose, from surface acoustic waves to heat pulses [5, 8, 13]. In our case one of the resistors at the ends of the sample (Fig. 6.3) acted as a thermometer (R2), and the other one acted as a trigger to ignite the avalanches (R1). The trigger consists in a single current pulse, generated with a Keithley 2400 Sourcemeter. In order to keep constant the amount of energy generated by this pulse for different temperatures and magnetic fields, the resistance of R1 is measured before sending the pulse. Then the current amplitude is set to produce 100 mW during 10 ms.

The resistor used as a thermometer was calibrated using the temperature of the MPMS® system as reference. The amplitude of the current used to measure the resistance was 60 μA.

Besides the measurements involving the dedicated setup presented in this chapter, magnetization measurements were also carried out. Those measurements were done using the SQUID magnetometer of the MPMS® system. As I explained in the previous chapter, measuring the magnetization before and after the avalanche is important in order to fully understand the dynamics of the phenomenon.

6.2 Analysis and results

6.2.1 Spontaneous magnetic deflagrations

Fig. 6.4 shows the time-resolved measurements of the spontaneous FM reversal that occur at 5 K. In the figure we can see how the first coils to present a rise are the coils number four and three, followed in order by coils two and one This is consistent with a propagating front of change in magnetization with a definite direction. Looking at the data we can consider that the spontaneous avalanche started within coils three and four. If we normalize each curve by its maximum we observe that

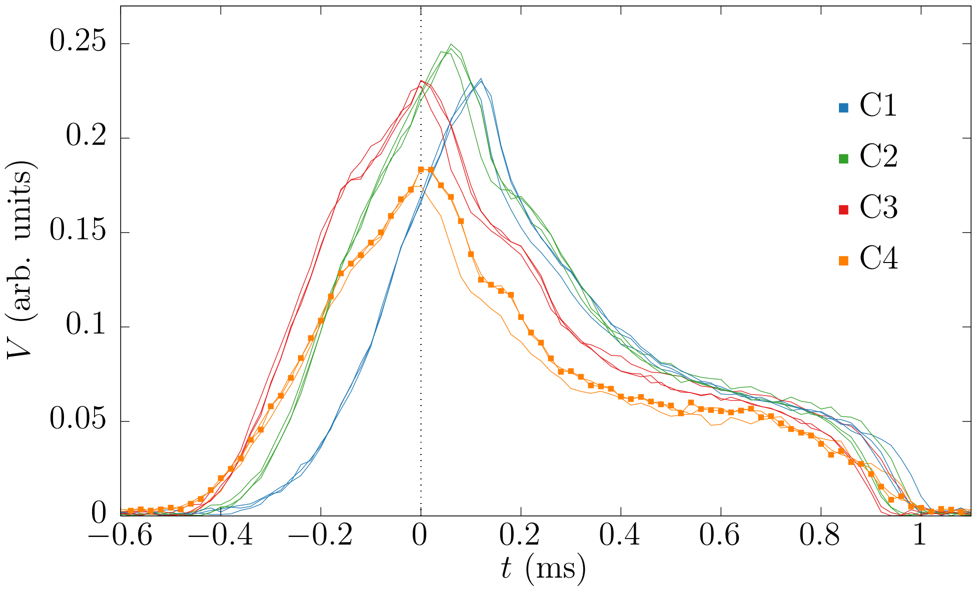

Figure 6.4: Time-resolved measurements of the spontaneous FM reversal at 5 K. In the figure are represented three independent runs, with each run centered at the maximum voltage of coil 4. The number of points measured is shown in one of the signals of coil 4. All three spontaneous avalanches took place at 16.57 kOe.

curves from coils three and four overlap (see Fig. 6.5). The reproducibility of this spontaneous avalanche is unexpectedly hight, as can be observed in the figures. Three independent measurements were performed and all three match very well. Even more, two of the measurements were obtained sweeping the magnetic field from −4 T to 4 T, and one sweeping the magnetic field in the oposite direction. Obviously the curves obtained in both procedures have different sign because of the sign of ΔM so the curves presented in the figures are the absolute values of the induced voltage. It is clear from the figures that the dynamics do not depend on the direction of the magnetic field. It starts always near the R2 end of the sample, and propagates towards R1. It is worth to mention that the resistor at R2 is acting as a thermometer, which could imply that the current used to measure the voltage drop on it causes some instabilities in the proximity of the sample, somehow inducing the start of the spontaneous avalanche at that end.

The shape of the induced voltage curves is maintained in all the coils and has some peculiarities. Although the different coils present a rise at very different times, all go back to zero at a similar time. It is remarkable as well the presence of a "plateau" at the second half of the curve. The signal looks like made of at least two distinct contributions. We will focus on the study of signal's shape in

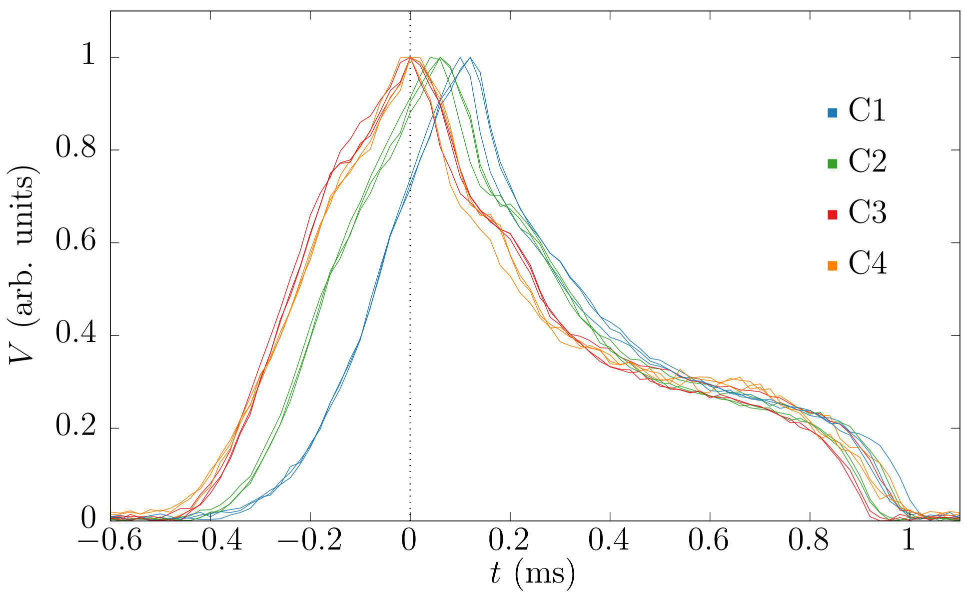

Figure 6.5: Time-resolved measurements of the spontaneous FM reversal at 5 K. Each curve is normalized by its maximum voltage. Curves from coils four and three overlap.

the next chapter.

6.2.2 Induced magnetic deflagrations

As it has been explained in the introduction, to study systematically the process of this magnetic avalanches as a function of different magnetic fields and temperatures we need to avoid the spontaneous jumps. The experimental procedure to study the induced magnetic avalanches is the following. To study the AFM→FM transition process, the system is cooled in zero applied magnetic field from 70 K to a certain T value, and then a magnetic field $H_{\mathrm{ig}} < H_{\text{sp-AFM}}$ was applied. The trigger is sent while the voltage induced by the magnetic flux change in the pick-up coils, Ci, and the temperature of the thermometer, R2, are recorded. To determine the amount of magnetization change produced in the induced avalanche, the magnetization was measured immediately before the trigger and right after the acquisition time-window was closed. I repeated the whole procedure at different magnetic fields, H_{ig}, and temperatures until the trigger has no effect, because the metastability is not large enough to ignite the avalanche (low fields) [120], or because the avalanche take place spontaneously before (high fields). To study the FM reversal process I set the temperature T and then a magnetic field of -40 kOe is applied, large enough to ensure the complete transition AFM→FM. Next, the system is driven

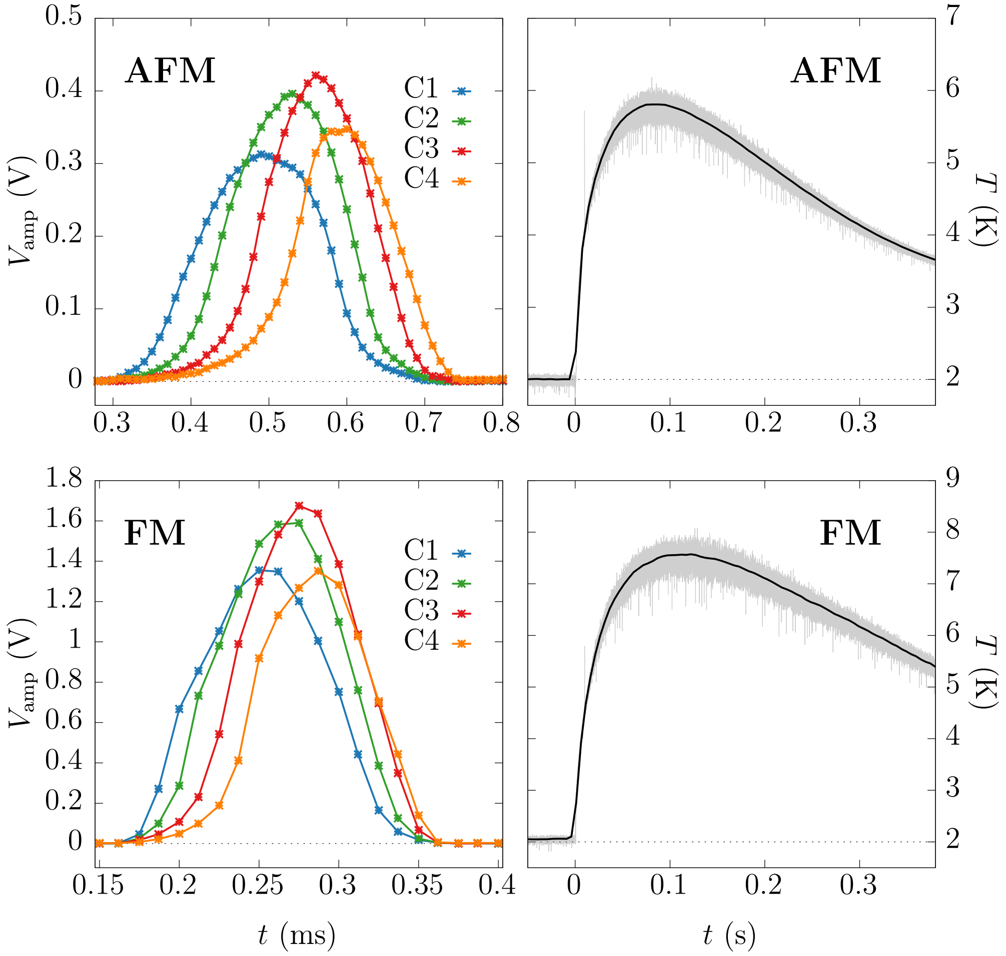

Figure 6.6: Temporal evolution of the voltage induced in the four pick-up coils (left panels) and the temperature change registered in the thermometer R2 (right panels). Measurements performed at 2 K and 24 kOe. Top panels correspond to the AFM→FM transition. Bottom panels correspond to the FM reversal. The scales are different in each plot. The black line in the temperature curves represents the data smoothed. Lines in the induced voltage are represented as a guide to the eyes.

to the desired $H_{\text{ig}} < H_{\text{sp-FM}}$ value, where the magnetization-trigger-recording-magnetization procedure is performed. I repeated the whole method at different magnetic fields and temperatures.

Fig. 6.6 shows the signals obtained during the AFM→FM transition and the FM reversal, at the same magnetic field-temperature conditions, 2 K and 24 kOe.

On the left side of the figure are represented the induced voltages (amplified) in the four independent pick-up coils. The first thing to remark is that in both processes, it is very clear the propagation of the change in magnetization. The first coil to detect a change is the coil C1 (which is the nearest to the trigger), followed in order by the coils C2, C3 and C4. We can see that the signals obtained during the AFM→FM transition are almost four times smaller and two times wider than those obtained during the FM reversal. Since $V(t) \propto \mathrm{d}M/\mathrm{d}t$, the area comprised by each curve is proportional to the amount of change in magnetization. We can do a simple calculation considering the peaks as triangles of heigh h and base b, and compare their areas,

$$A_{\mathrm{AFM}} = \frac{1}{2} b_{\mathrm{AFM}} h_{\mathrm{AFM}} \approx \frac{1}{2} 2 b_{\mathrm{FM}} \frac{1}{4} h_{\mathrm{FM}} = \frac{1}{2} A_{\mathrm{FM}}, \tag{6.1}$$

which, in agreement with magnetization measurements, means that we are measuring directly the change in magnetization, $\Delta M \approx 2M_S$ in the FM reversal and $\Delta M \approx M_S$ in the AFM→FM transition. Since the trigger is sent at $t = 0$ for both measurements, we also have to mention that the elapsed time until the magnetization (voltage) changes abruptly in the FM reversal is approximately the half of the elapsed time in the AFM→FM transition. On the right side of Fig. 6.6 we find the temperature uprise at the thermometer R2, for both processes as well. Note the different time scale used in the measurements of T in reference to the measurements of the voltage in the pick-up coils (this is the reason why I used two distinct data acquisition cards, to be able to track both with enough density of points). We observe some differences between the temperature evolution of the two processes. The first is the maximum temperature achieved, approximately 6 K in the AFM→FM and 8 K in the FM. The second is the cooling trend, more pronounced in the AFM→FM. This is consistent with the amount of energy released during the processes, which, considering only magnetic energy, is approximately the double in the FM reversal than in the AFM→FM process since $\Delta E = (\Delta M)H$, and since both measurements were performed at the same applied magnetic field of 24 kOe. Given the spatial propagation of the magnetization change, this large and stepped increase of temperature is the second ingredient to consider the magnetic avalanches that occur in the $\mathrm{Nd}_5\mathrm{Ge}_3$ as magnetic deflagrations.

Before studying the dependence of the deflagration properties with the applied magnetic field I conducted a reproducibility test of the FM reversal. Fig. 6.7 shows seven independent measurements of the inducted voltage during the FM reversal at 2 K and $H_{\mathrm{ig}} = 18$ kOe (from now on, H_{ig} will refer to the *ignition field*, i.e, the field at which the trigger is sent). Actually, four of the seven runs were measured with $H_{\mathrm{ig}} = -18$ kOe, and as happened with the spontaneous FM reversal at 5 K shown in Fig. 6.5, neither the shape nor the "order" of the coils are affected. The main difference between this results and the spontaneous ones is

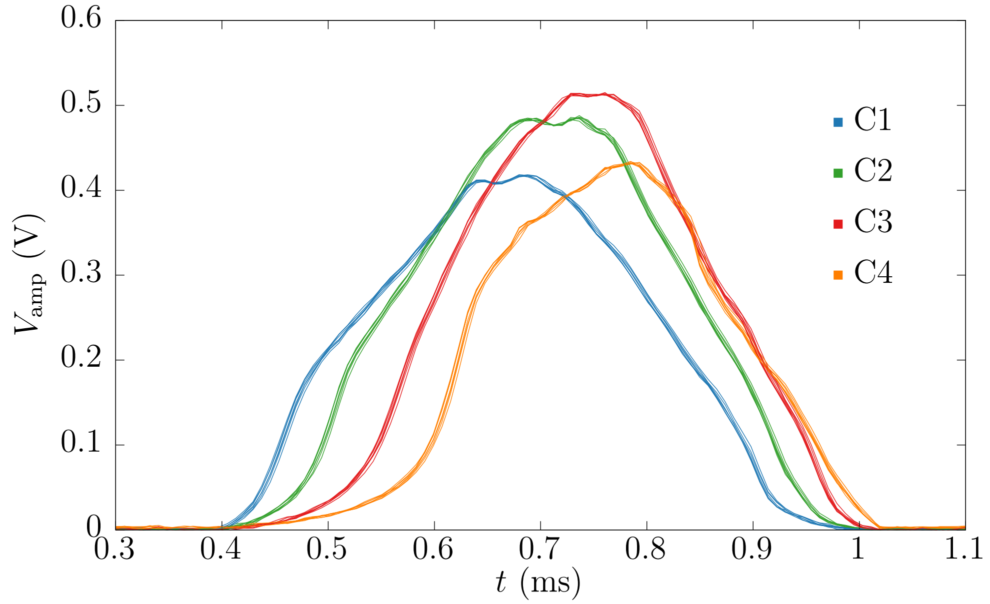

Figure 6.7: Reproducibility test. Time-evolution of the induced voltage on the coils for seven independent triggered FM reversals at 2 K and 18 kOe. The trigger is sent at $t = 0$.

that in this case we know that the elapsed time is in a very good approximation the same for all. Certainly, this results point to consider that the dynamics of the magnetic deflagration in Nd_5Ge_3 is highly deterministic.

Fig. 6.8 presents the time-resolved measurements of the FM process at 2 K as a function of the ignition field H_{ig}. The top panel comprises the voltage generated in the coils (only coil C3 is shown for clarity). In this panel we observe how, as H_{ig} increases, the time elapsed between the trigger ($t = 0$) and the rise in the signal decreases, the height of the signal increases and the width of the peak shrinks. The temperature increment in the thermometer placed at the end of the sample is shown in bottom panel of Fig. 6.6. Looking at this temperature data we observe the presence of a threshold in the occurrence of the process. For low fields the process can not be induced by the trigger (we kept the energy released by the trigger constant for all fields, $E_{trig} = 1$ mJ), but above a certain magnetic field, the avalanche process can be observed in the signals of the coils (Fig. 6.6) and also in the signal of the thermometer.

We can see this threshold effect with greater clarity in Fig. 6.9, where the signals of the coil C3 and the thermometer R2 are presented together for three consecutive fields. For $H_{ig} = 11$ kOe the coil signal does not show any relevant peak, while the thermometer presents a rise. The origin of this increase in the temperature is the

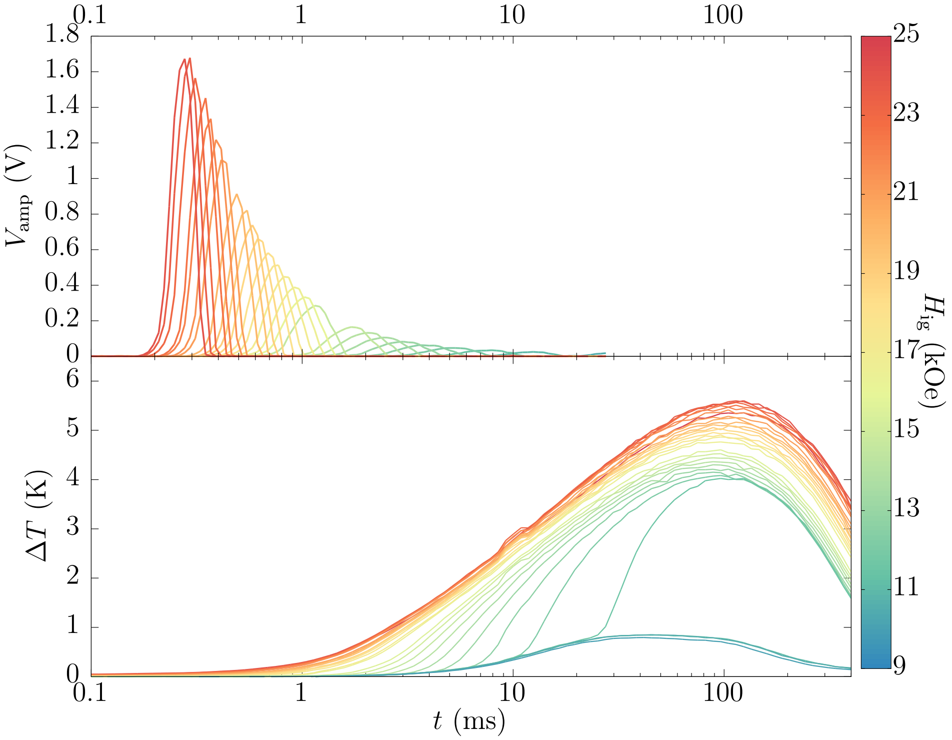

Figure 6.8: Time-resolved measurements of the induced FM process as a function of H_{ig} at 2 K. In all measurements the trigger was sent at $t = 0$. Top panel: voltage generated in coil C3 (amplified). Bottom panel: temperature increment in R2. The two panels share the color code, that corresponds to the magnetic field.

energy released by the trigger plus the heat generated by the thermally assisted magnetic relaxation. Nevertheless, we can see in the bottom panel of Fig. 6.6 how, for $H_{\mathrm{ig}} \leq 11$ kOe, the increments in temperature are equivalent, meaning that the contribution of the induced magnetic relaxation is very small if the avalanche process has not occurred. This was also observed few years ago in single crystals of Mn_{12}−ac by Subedi et. al [120]. As the magnetic field is increased up to 11.5 kOe and above, an increase in the temperature is observed before a peak appears in the coil signal, and a rapid increase of the temperature takes place when the avalanche process occurs and is detected by the coil. An interesting feature is that this rapid increase is the expected response for an abrupt heat front.

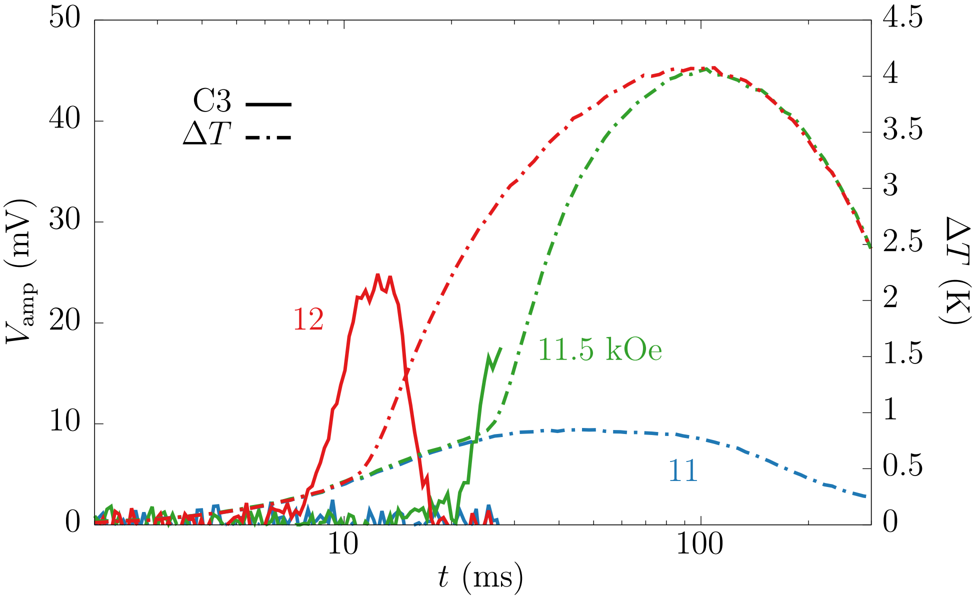

Figure 6.9: Three temperature measurements at consecutive increasing fields (dashed lines), along with their respective coil C3 signal (solid lines).

6.2.3 Analysis of flame temperature

Fig. 6.10 shows the maximum temperature increment, $\Delta T_{\max} = T_{\max} - T_0$, during the AFM→FM transition and the FM reversal at 2 K. We observe, as for the speeds, a reduction when the field is in the vicinity of H_{sp}. The goal pursued placing a thermometer at the end of the sample is to determine the production of heat and its dependence with the magnetic field. In my opinion, in any of the previous works where magnetic deflagrations were studied, the temperature uprise was analyzed in detail. One of the key factors is that the temperature measured is substantially smaller than the expected temperature reached during the magnetic deflagration process. Fig. 6.11 shows the temperature at the deflagration front, T_f, obtained solving numerically the equation

$$(\Delta M)H = \int_{T_0}^{T_f} C(T')\mathrm{d}T', \tag{6.2}$$

with $T_0 = 2$ K, and using the specific heat measurements presented in Chap. 4. In the figure we observe that the flame temperature is almost three times the maximum temperature measured by R2. The origin of this difference can be attributed to the different heat capacities and mass of the sample and the thermometer, and a bad thermal coupling between them. Let us do some numbers. First we will assume that the energy that receives the resistive part of the thermometer R2 is

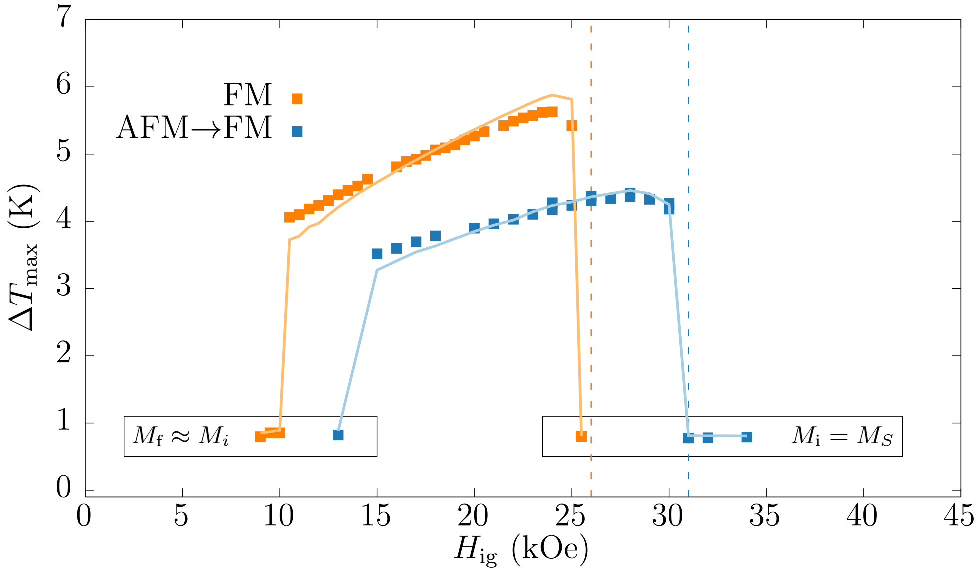

Figure 6.10: Maximum temperature increment, $\Delta T_\mathrm{max} = T_\mathrm{max} - T_0$, during the AFM→FM transition and the FM reversal measured at 2 K. The vertical dashed lines correspond to the respective spontaneous deflagration magnetic fields H_sp The highlighted region at low fields correspond to “under-threshold” fields for which a 1 mJ heat pulse did not ignited the avalanche. The lines correspond to the maximum temperature increase considering the energy received at R2 as a fraction of the energy released at R1 and the magnetic energy generated in the deflagration processes.

a fraction of the energy released due Joule effect during the trigger in R1 plus a fraction of the magnetic energy generated in the sample,

$$\Delta E_\mathrm{R2} = \alpha Q_\mathrm{R1} + \xi \Delta M H, \tag{6.3}$$

being α and ξ the fractions corresponding to the energies generated by the resistor R1 and by the sample, respectively. Because of the geometry of the setup we expect $\alpha \ll \xi < 1$. In this approximation I did not considered any contribution of the thermal bath; because of the time scale of the process (around milliseconds) it can be considered isolated in a first approximation. The resistive component of the resistors used is approximately one milligram of ruthenium dioxide. The temperature increase that would experiment that component, given an increase in the energy can be obtained solving

$$\Delta E_\mathrm{R2} = \frac{m}{M}\int_{T_0}^{T_\mathrm{max}} C_\mathrm{R2} \mathrm{d}T = \frac{m}{M}\frac{\gamma_\mathrm{R2}}{2}T^2 + \frac{m}{M}\frac{\beta_\mathrm{R2}}{4}T^4 \Big|_{T_0}^{T_\mathrm{max}}, \tag{6.4}$$

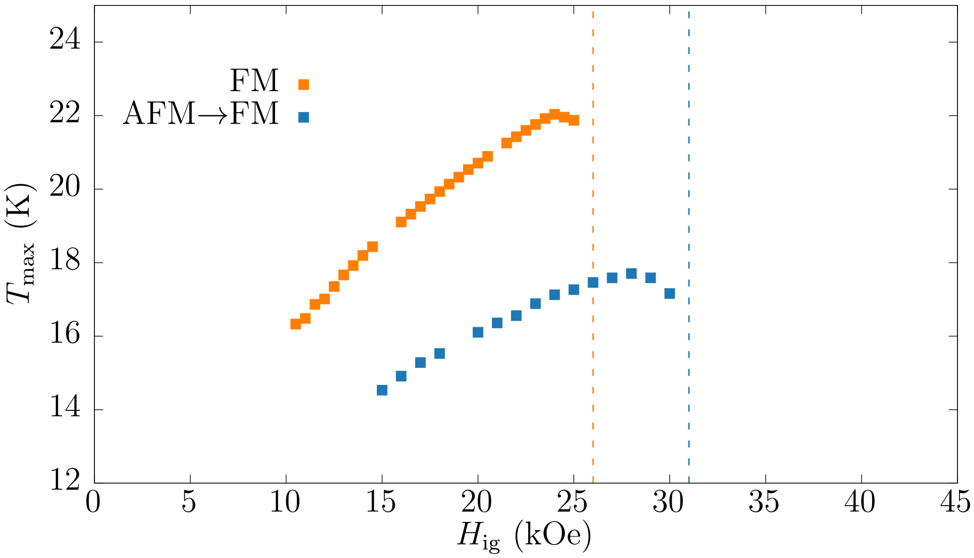

Figure 6.11: Expected temperature of the deflagration front during the AFM→FM transition and the FM reversal measured at 2 K. The vertical dashed lines correspond to the respective spontaneous deflagration magnetic fields H_{sp}.

where ΔE is the energy increment, T_0 is the initial temperature, γ and β are the electronic and phononic contributions to the specific heat, m is the mass of the RuO_2 in R2 and M its molar mass. Solving Eq. (6.4) for T_{max}, we get four solutions. Only one of this solutions is positive and real,

$$T_{\mathrm{max}} = \sqrt{\sqrt{\left(\frac{\gamma_{\mathrm{R2}}}{\beta_{\mathrm{R2}}}\right)^2 + \frac{4M}{m\beta_{\mathrm{R2}}}\left(\alpha Q_{\mathrm{R1}} + \xi \Delta M H\right) + T_0^4 + 2\frac{\gamma_{\mathrm{R2}}}{\beta_{\mathrm{R2}}}T_0^2} - \frac{\gamma_{\mathrm{R2}}}{\beta_{\mathrm{R2}}}}. \tag{6.5}$$

Now we can use all the known values: $\gamma_{\mathrm{R2}} = 5.77$ mJ/mol K^2, $\beta_{\mathrm{R2}} = 0.0225$ mJ/mol K^4 (Ref. [121]), $m = 10^{-3}$ g, $M = 133$ g/mol, $Q_{\mathrm{R1}} = 1$ mJ, and $T_0 = 2$ K, together with the ΔM at each field (known from the pre-trigger and post-trigger measurements performed with the SQUID magnetometer), to compute T_{max} as a function of the magnetic field using α and ξ and the fitting parameters. Fig. 6.10 shows the curves obtained using:

AFM→FM	$\alpha = 0.08$	$\xi = 0.38$
FM-reversal	$\alpha = 0.08$	$\xi = 0.34$

.

The values for both processes are nearly equal. We can expect this since the considerations made were independent of the magnetic state. Furthermore, the predicted

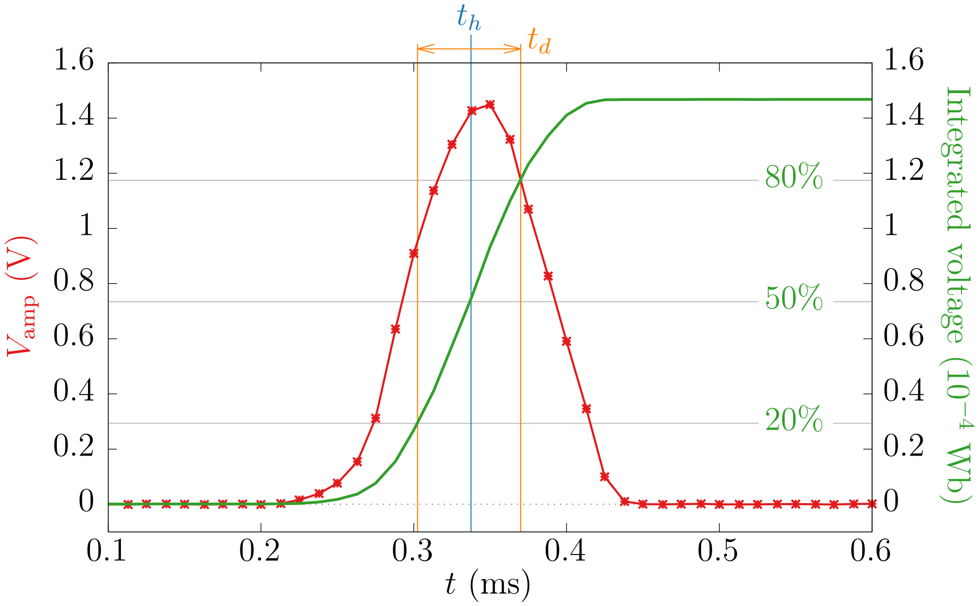

Figure 6.12: Voltage induced in coil 3 at 2 K and 23 kOe (red) and its integrated curve (green). The speed is calculated using the difference of the time at half hight of the integrated voltage, t_h, between two coils. In some references it is also defined a "deflagration time" as t_d.

relation between α and ξ is recovered. In summary, I have shown that when the properties of the thermal contact between the sample and the thermometer, together with the thermal properties of the last, are considered, the temperature values obtained are compatible with the higher temperature associated to the deflagration phenomenon.

6.2.4 Determination of the propagation speed

Using the definitions presented in Fig. 6.12 we obtain the speed of the propagating avalanche as $v_{ij} = d_{ij}/\Delta t_{ij}$, where d_{ij} is the distance between the coils i and j, and $\Delta t_{ij} = t_{h_j} - t_{h_i}$ is the time delay between the half heights of the integrated voltages of coils i and j. In some references, when only one coil is used to measure the deflagration phenomenon, a "deflagration time" t_d is defined, from which the propagation speed is estimated [9, 13, 33].

The obtained values of v_{exp} as a function of H_{ig} for the AFM and FM processes are plotted in the Fig. 6.13. In this figure we can see how the speed rapidly increases with H_{ig} –this results confirm that we are not dealing with domain wall motion, since the speed of a domain wall scales lineraly with the applied field, $v_{DW} \propto (H - H_c)$, being H_c the coercive field (see Ref. [122, 123]). On the contrary

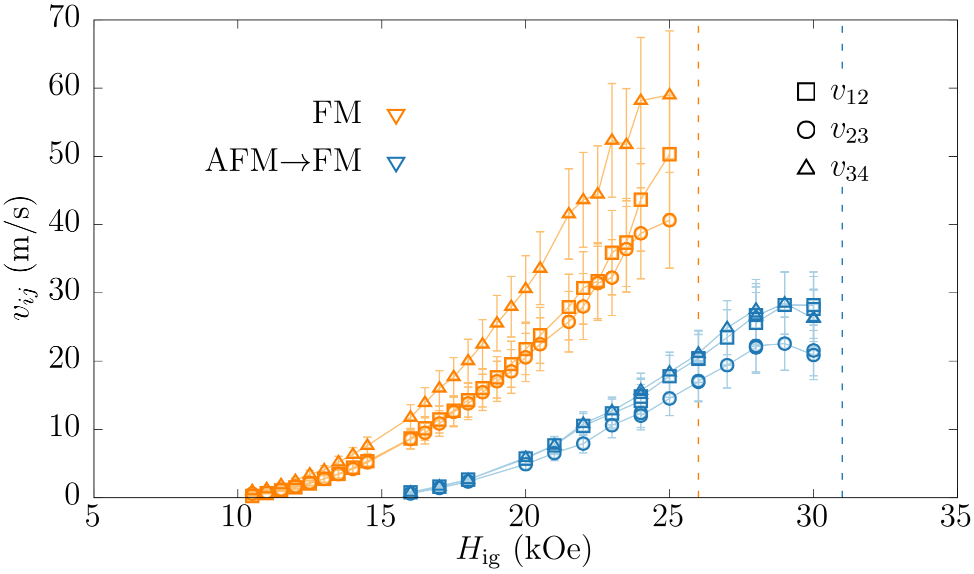

Figure 6.13: Experimental speed of the front between coils i and j as a function of the ignition field. The vertical dashed lines correspond to the respective spontaneous deflagration magnetic fields H_{sp}.The lines correspond to the respective linear fits.

as H_{ig} gets closer to H_{sp} (dashed vertical lines), the speed decreases slightly. This decrease in the velocity of propagation of the front is due to the loss of total magnetization change in the process, because of the thermal magnetic relaxation that occurs before the trigger. This magnetic relaxation also generates firewall zones in the crystal that effectively slow down the propagation of the deflagration front. It is the same picture of a wildfire, once a part of the sample is relaxed (burned) it acts as a barrier to the propagation of the magnetization change front.

In Fig. 6.13 we can observe that the speed of the front changes along the propagation. Surprisingly, the obtained speeds seem to follow the trends

$$\begin{aligned} \mathrm{FM}: &\quad v_{34} > v_{12} \gtrsim v_{23} \\ \mathrm{AFM} \rightarrow \mathrm{FM}: &\quad v_{34} \approx v_{12} > v_{23}, \end{aligned}$$

where, in any case, the speed at the extremes of the sample is larger than the speed at the center. This intriguing behaviour will be understood using a toy model.

Let us consider the setup shown in Fig. 6.14 made of a magnetic sample of length l, surrounded by two independent pick-up coils of radius r_{c}, separated a distance d between each other, and placed at a distance e to the end of the sample. Let us consider a magnetization change front of width δ moving trough the sample at a constant speed v_0.

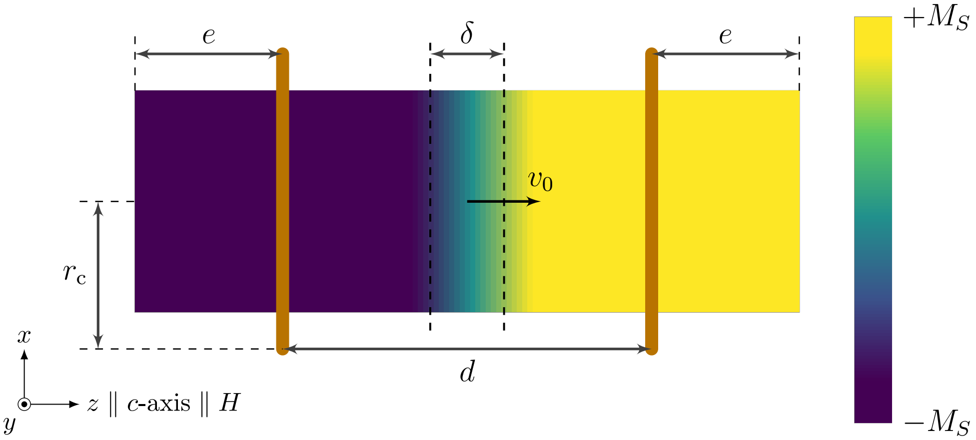

Figure 6.14: Definitions used in the toy model to explain the large speed obtained when using the "exterior" coils.

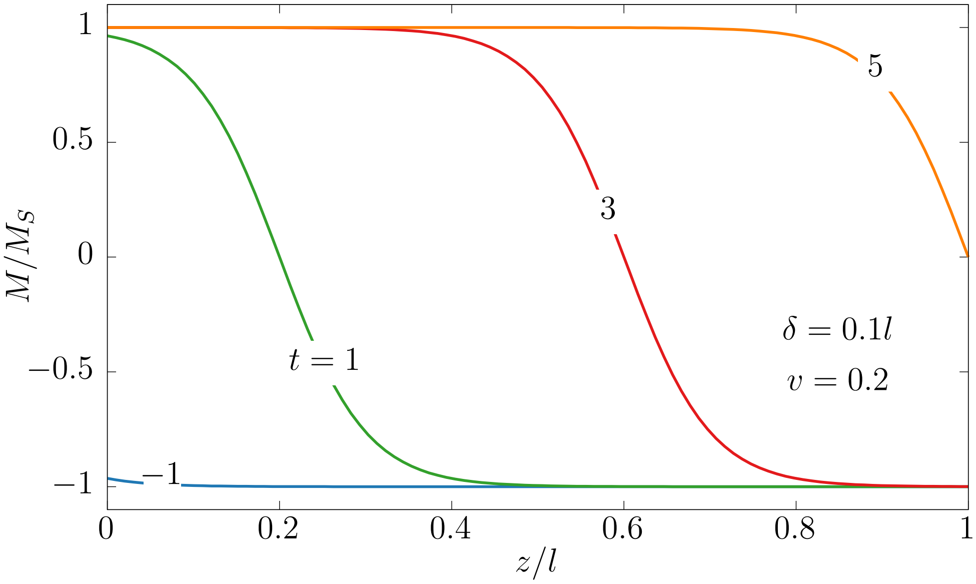

Figure 6.15: Spatial and temporal dependence of the magnetization of a sample of length l described by Eq. (6.6) with a propagating magnetization change front of witdh $\delta = 0.1l$ which covers the length the sample in 5 units of time ($v_0 = 0.2$).

The temporal evolution of the magnetization in our case can be modeled with

$$M(z, t; v_0; \delta) = M_S \tanh\left(-\frac{z - v_0 t}{\delta}\right), \tag{6.6}$$

which describes the propagation with time of a change of the magnetization from $-M_S$ to M_S (being M_S the saturation magnetization). Fig. 6.15 shows the temporal and spatial dependence of Eq. (6.6) considering a sample of length l in which a front of width $\delta = 0.1l$ covers its length in 5 units of time ($v_0 = 0.2$). In the figure, δ corresponds to the width in which the magnetization is reduced by an $\sim 80\%$. E. g., at $t = 3$, a bit more than two fifths (0.4) of the sample can be considered to have relaxed from $-M_S$ to M_S while one fifth of the sample is still "unburned", and in between them is the front where the magnetization is being changed.

With this description of the spatial and temporal evolution of the magnetization we can derive the voltage that a coil surrounding the sample would measure. The voltage induced at time t in a coil with radius r_c placed at $z = p$ when a magnetic change occurs along its axis is defined by

$$V(t,p) = \int_{-\infty}^{\infty} \frac{Ar_\mathrm{c}^3}{\left(r_\mathrm{c}^2 + (z-p)^2\right)^{3/2}} \frac{\mathrm{d}}{\mathrm{d}t} M(z,t,v_0,\delta)\mathrm{d}z, \tag{6.7}$$

where A is a constant and

$$\frac{Ar_\mathrm{c}^3}{\left(r_\mathrm{c}^2 + (z-p)^2\right)^{3/2}} \tag{6.8}$$

is the sensitivity of a coil. Substituting M from Eq. (6.6) we obtain

$$V(t,p) = A\frac{v_0}{\delta}M_S \int_0^l \frac{r_\mathrm{c}^3}{\left(r_\mathrm{c}^2 + (z-p)^2\right)^{3/2}} \operatorname{sech}^2\left(-\frac{z - v_0 t}{\delta}\right)\mathrm{d}z. \tag{6.9}$$

The infinite limits of integration of the integral are reduced to 0 and l because M is only defined in the sample.

With this equation we now can compute how the position of the coil with respect to the sample and the width of the front affect to the measured speed. I computed two curves $V(t,p)$ for different times at two fixed positions $p = e$ and $p = l - e$, with a front of fixed width δ and speed v_0. Because of the lack of material in the left(right) vicinity of the coil the curves are not symmetric. Measuring the time delay between the maximum of the curves we obtain $v = d/\Delta t$, exactly like I do to obtain the speed from the experimental curves. In this case, since I now exactly that the speed is v_0, I get the amount of overestimation. In Fig. 6.16 we can see this overestimation because of the mentioned factors. In our experimental setup we have $e/r_\mathrm{c} \lesssim 1$. Therefore this toy model can explain a measured value up to a $\sim 20\%$ larger than the "true" one. This effect becomes smaller as the width of the front become narrower and narrower. In summary, due the proximity to the edge of the sample and the width of the propagating avalanche, the shapes of the signals of coils C1 and C4 have their height reduced and are also shifted to the "center". Therefore the most reliable coils to be used to define the speed of propagation are the coils C2 and C3.

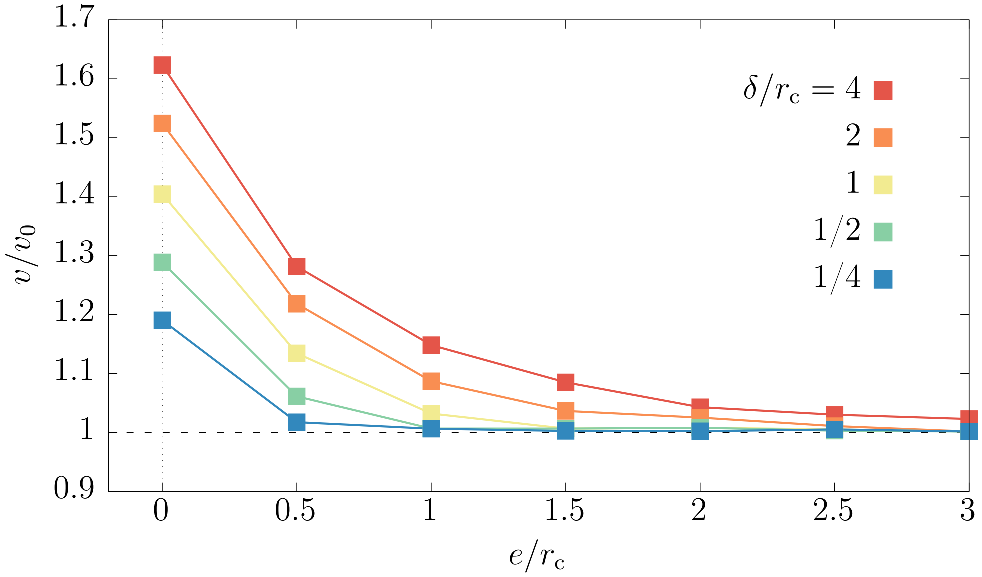

Figure 6.16: Overestimation of the speed of a front of width δ when its obtained using the time delay of two coils separated a distance d and both at at distance e to the edge of the sample.

Now I want to review briefly the theory of magnetic deflagration presented in the first chapter of this thesis. The theory formulated by Garanin and Chudnovsky in Ref. [57] establishes the dependence of the propagation speed of the front on the magnetic field, H (H_ig in our experiments), as

$$v(H) = \sqrt{\left(\frac{1}{\tilde{\varepsilon}_0} - 1\right) \kappa_f \Gamma_0 e^{-W_f}}, \tag{6.10}$$

with

$$\tilde{\varepsilon}_0 = \frac{1}{(\Delta M)H} \int_T^{\left(\frac{W_f}{1+W_f}\right)T_f} C(T')\mathrm{d}T', \tag{6.11}$$

and

$$W_f = \frac{U(H)}{k_B T_f} \tag{6.12}$$

Here T_f is the temperature of the propagating front (or "flame" temperature), $U(H)$ is the energy barrier, Γ_0 is the attempt frequency, $(\Delta M)H$ is the Zeeman energy released and C is the specific heat. This expression is obtained considering that the thermal diffusivity κ is independent of temperature in the range of T_f, i. e., $\kappa(T) \approx \kappa(T_f) \equiv \kappa_f$. As mentioned in the begining ot this section, the value of T_f is obtained solving the equation

$$(\Delta M)H = \int_{T}^{T_f} C(T')\mathrm{d}T'. \tag{6.13}$$

Instead of using approximations fo $C(T)$ we can take profit of the precise specific heat measurements presented in Chap. 4, to obtain numerically T_f for every field H_{ig}.

A phenomenological energy barrier $U(H)$ is obtained from isothermal magnetization measurements following the procedure described in the work of Hernàndez et. al with Mn_{12}, where the authors demonstrated how the energy barrier can be straightforwardly calculated due to the exponential behaviour of the magnetic relaxation in the Mn_{12} system (Ref. [23]). Let me reproduce the procedure as an introduction to the adaptation that I am going to use. The relaxation of a system of identical and independent barriers follows the equation

$$\frac{\mathrm{d}M}{\mathrm{d}t} = -\Gamma\left(M - M_{\mathrm{eq}}\right), \tag{6.14}$$

where, at temperature T and magnetic field H, the rate of thermally assisted magnetic relaxation Γ follows the Arrhenius formula:

$$\Gamma(H, T) = \Gamma_0 \exp\left(-\frac{U(H)}{k_B T}\right), \tag{6.15}$$

with Γ_0 being the *attempt frequency* which accounts for the relaxation from the thermal phonon bath. Therefore we can solve the equation for $U(H)$,

$$U(H) = k_B T \ln\left(\frac{\Gamma_0\left[M_{\mathrm{eq}} - M(H(t))\right]}{\dfrac{\mathrm{d}}{\mathrm{d}t}M(H(t))}\right), \tag{6.16}$$

where $M(H(t))$ corresponds to the magnetization at time t during an isothermal magnetization curve.

The fact that we are dealing with experimental data sets some constrains to the use of this expression. The sensitivity of measurements is the first issue, followed by the limitations derived from using numerical finite differences to compute $\mathrm{d}M/\mathrm{d}t$, and by the accuracy in the determination of M_{eq}. These constrains define three regions in the obtained $U(H)$. In the ranges of fields where the system barely relax: when $\mathrm{d}M/\mathrm{d}t \approx 0$ while $M_{\mathrm{eq}} \not\approx M$, or when $M_{\mathrm{eq}} \approx M$ (and therefore dM/d$t \approx 0$), the energy barrier values are not well defined because of the large errors introduced by the experimental limitations. Nevertheless, between these regions, the energy barrier dependence with the applied magnetic field gives us the phenomenological behaviour of $U(H)$. The key factor of the procedure relies on the scalability of $U(H)$ with T in those intermediate regions. If the theoretical $U(H)$ relation is known previously it can be checked following this procedure as it will fit the regions where $U(H)$ forms a scaling function with T. In a system with uniaxial anisotropy, the energy barrier along its easy axis is

$$U(H) = U_0(1 - H/H_a)^2, \tag{6.17}$$

being U_0 the energy barrier at zero-applied field and H_a the anisotropy field [28]. Then one can try to fit Eq. (6.17) to $U(H)$ in the range of H between the "noisy" intervals.

The procedure just explained is only valid for the case of an exponential relaxation over a single energy barrier, however, as shown in Chap. 3, the magnetic relaxation of Nd_5Ge_3 follows an extended exponential behaviour:

$$M(t) = M_{\text{eq}} - (M_{\text{eq}} - M(0))\exp(-(t\Gamma)^{\beta}), \tag{6.18}$$

with

$$M(t) \equiv M(H,T,t) \quad \text{and} \quad M_{\text{eq}} \equiv M(\infty).$$

Therefore, in the following paragraphs I will introduce how this procedure can be adapted to our case. To obtain $U(H)$ in our system we first derive the differential magnetic relaxation law in the case defined by Eq. (6.18),

$$\frac{\mathrm{d}M}{\mathrm{d}t} = -\Gamma_{\text{inst}}\left(M - M_{\text{eq}}\right), \tag{6.19}$$

where $\Gamma_{\text{inst}} \equiv \beta\Gamma(t\Gamma)^{\beta-1}$ is defined as the instantaneous relaxation rate. We will define a certain time t_0 for which $\Gamma_{\text{inst}} = \Gamma$, which, using Eq. (6.18) gives the relation

$$M(t_0) = e^{-\frac{1}{\beta}^{\frac{\beta}{\beta-1}}}(M(0) - M_{\text{eq}}) + M_{\text{eq}}. \tag{6.20}$$

This condition implies that, at time t_0, the magnetic relaxation of the system cannot be distinguished from an exponential relaxation with a rate Γ. Therefore the procedure to obtain $U(H)$ can be applied (assuming the thermal relaxations to be governed by Arrhenius formula).

Fig. 6.17 shows the isothermal magnetization curves from which we will derive $U(H)$. To avoid the spontaneous avalanches, the field sweeping rate was reduced to ∼ 20 Oe/s. On the positive magnetic field branch are shown the magnetization

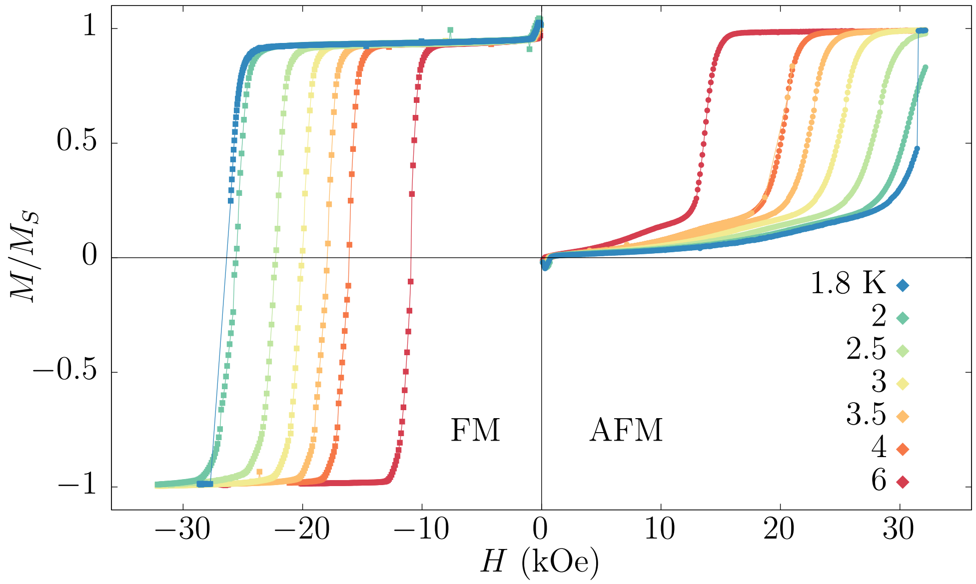

Figure 6.17: Magnetization curves at different temperatures for the two different magnetic phases, measured at a magnetic field sweeping rate of ∼20 Oe/s.

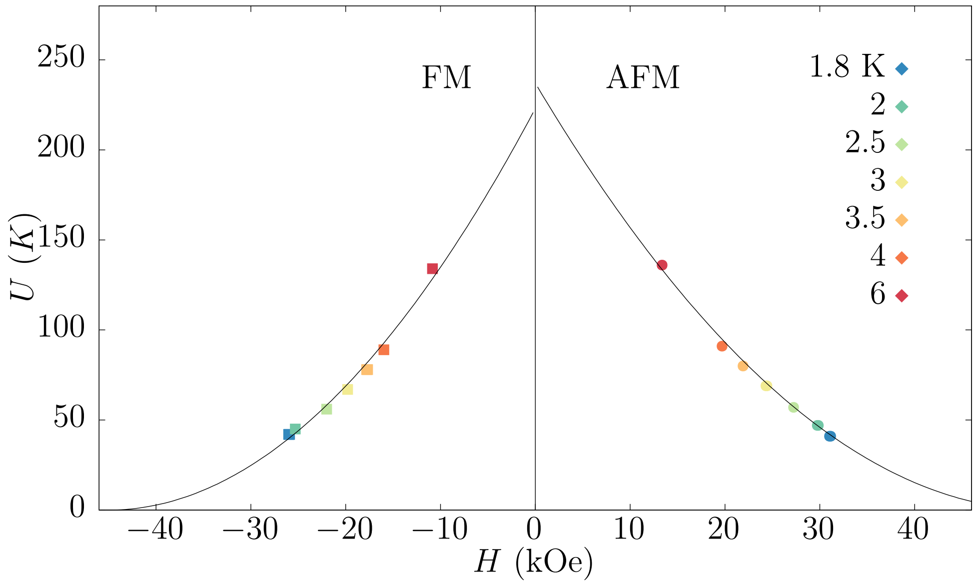

Figure 6.18: Energy barrier as a function of the magnetic applied field, computed using Eq. (6.16) around the values of $M(t)$ that satisfy Eq. (6.20)

Table 6.1: Values of the parameters used to fit the magnetic field dependence of the energy barrier. The number in parenthesis is the statistical uncertainty in the last digit from the least-squares fitting procedure.

state	U_0 (K)	H_a (kOe)
AFM	237(4)	53.1(6)
FM	223(7)	45(1)

curves with the system initially in the AFM state while on the negative field branch the magnetization curves correspond to the system in the FM state.

Using Eq. (6.16) for those values of the instantaneous energy barrier $U(H)$ (arising from Γ_{inst}), that corresponds to $M(t) \simeq M(t_0)$, we obtain the phenomenological energy barrier represented by the marks shown in Fig. 6.18. As a first approach, and because of magnetic properties of Nd_5Ge_3, we fit these values to the expression of an uniaxial anisotropy barrier (Eq. (6.17)). Despite its simplicity the fits are good, therefore we assume the energy barrier of Nd_5Ge_3 has the phenomenology of a uniaxial anisotropy barrier. The fits are represented by solid lines in figure 6.18 and the obtained parameters are shown in Table 6.1.

The aim with this adaptation to the procedure of Hernàndez et. al is to obtain an approximate effective energy barrier to be used to compute the speed of the propagating front in the deflagration process. However, this energy barrier can not be used to describe the magnetic relaxation of this intermetallic compound at a constant temperature that takes places in broad timescale. The strong non-linear dynamical behavior of this avalanche is mostly determined by the thermal dependence of the relaxation rate. This fact makes the broad timescale present in a stretched exponential law (at a constant temperature) to collapse on a single event that can be described by a single effective energy barrier.

Back to the fit of the experimental data to the theory of magnetic deflagration, the only unknown parameter in Eq. (6.10) is κ_f. This equation can be rewritten as

$$v = \sqrt{\kappa_f} \cdot f(H; H_a; U_0; \Gamma_0). \tag{6.21}$$

Therefore, if the experimental data matches the theoretical expression, one should expect a linear dependence between the v_{exp} and the function f.

Fig. 6.19 shows the dependence of the experimental speed of the front, measured using the signals from coils 2 and 3, on the ignition magnetic field. In Fig. 6.20 we plot the experimental speed v_{exp} versus the function f for both the AFM and FM processes, along with the corresponding linear fits of Eq. (6.21). Since the reduction of the total magnetization change that occurs for fields near H_{sp} can induce firewalls that would reduce the speed of the front, we do not take into account them in the fits. We associate the non-linearity at small values to slow-

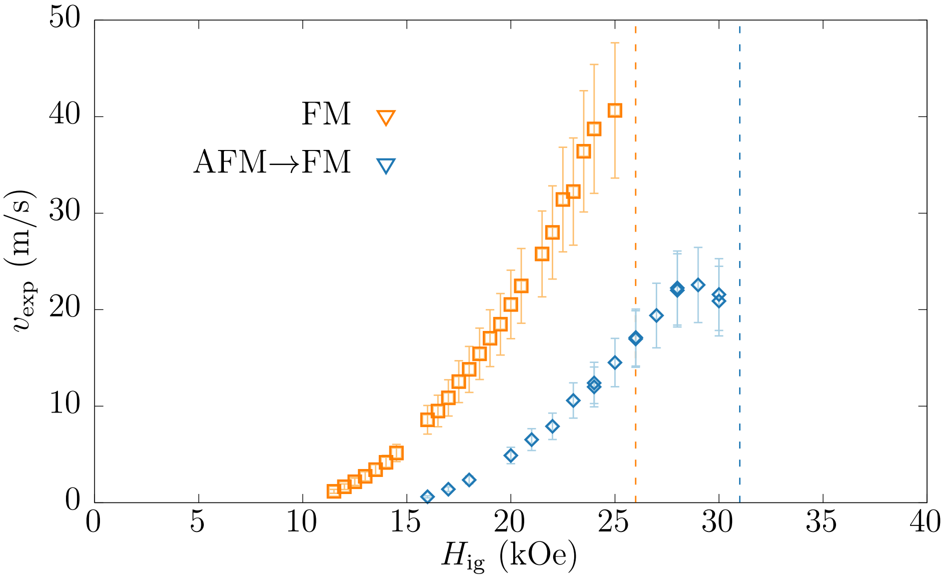

Figure 6.19: Dependence of the experimental speed of the front (v_{23}) on the ignition magnetic field. The vertical dashed lines correspond to the respective spontaneous deflagration magnetic fields H_{sp}

deflagration processes where the thermal bath plays an important role [120]. The values of κ_f obtained for each phase are The results obtained are:

$$\begin{array}{r|l} \text{AFM}\to\text{FM} & \kappa_f = 8.5(8) \times 10^{-4}\ \mathrm{m}^2/\mathrm{s} \\ \hline \text{FM-reversal} & \kappa_f = 9.6(9) \times 10^{-4}\ \mathrm{m}^2/\mathrm{s} \end{array} .$$

being of the expected order of magnitude for a metallic compound [124]. We obtain a slightly higher thermal diffusivity in the FM phase, which we consider consequent with the lower heat capacity and electrical resistance of this state.

The results just presented correspond to the study of thermally induced magnetic avalanches at 2 K. Moreover I explored the induced deflagrations at different temperatures. I found that for $T \ll 26$ K, at a given field $H_{\mathrm{ig}} < H_{\mathrm{sp}}(T)$, the induced deflagration process does not depend on the initial temperature. When the Zeeman energy and the energy barrier are large, which is the case of Nd_5Ge_3, the theory of magnetic deflagrations indicates a negligible dependence of the speed of the front with the initial temperature. Nevertheless the dynamics of magnetic deflagrations are largely affected by changes in ΔM. Actually, the condition $T \ll 26$ K mentioned above translates into a temperature independent ΔM.

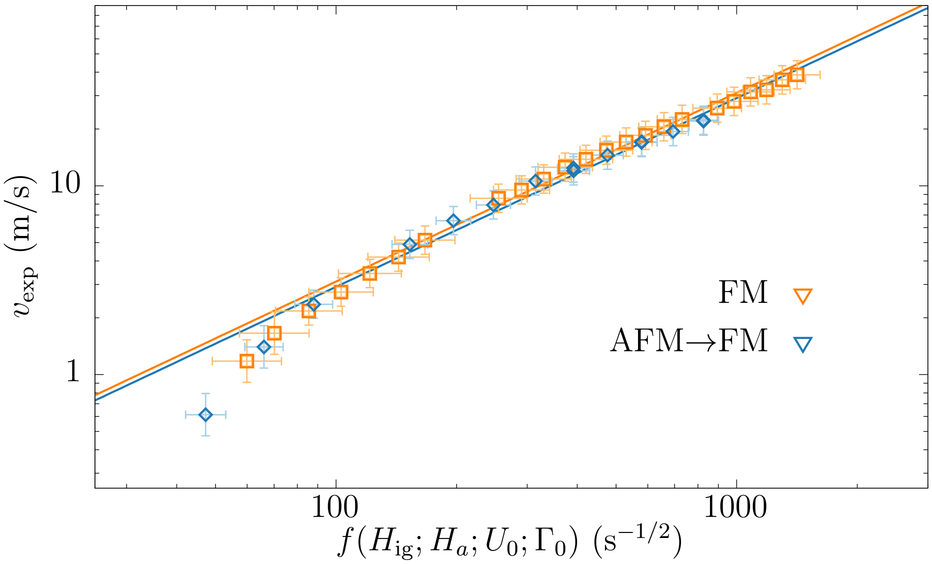

Figure 6.20: Log-log plot of the experimental speed versus the theoretical function f [Eq. (6.21)]. Only the experimental speeds with maximum ΔM are used. The lines correspond to the respective linear fits.

Using the obtained values for the thermal diffusivity we can estimate the deflagration front width $l_d \sim \kappa/v$, getting $l_d \sim 1$ mm for the lowest speed and $l_d \sim 10$ μm for the fastest. Nevertheless, if we compare the calculated shape of the curves for different front widths using the model presented in Pag. 143, with the induced voltage curves obtained experimentally, we found that the experimental data suggests fronts broader than the estimated using the expression κ/v. To explain this discrepancy I consider the thermal contact of the boundaries of the sample with the environment and, as stated in a recent paper by Jukimenko et al. [125], the bending of the front by the dipolar field, as the main reasons of finding, in terms of coil detection, wider fronts. I. e., it is possible that the width of the front of magnetization change has the size estimated by the ratio between the thermal diffusivity and the propagation speed, but if the front is not perfectly flat (for the given reasons) then the signal obtained in a pick-up coil would correspond to a front with a wider effective width.

Finally, one of the most promising aspects of deflagration in this material is evidenced in Fig. 6.21. With the parameters of the system I plot the theoretical front speed as a function of the magnetic field, taking ΔM equal to the maximum experimental value for all the range of fields (which is equivalent to consider the environment temperature equal to zero). Along with the theoretical curves are

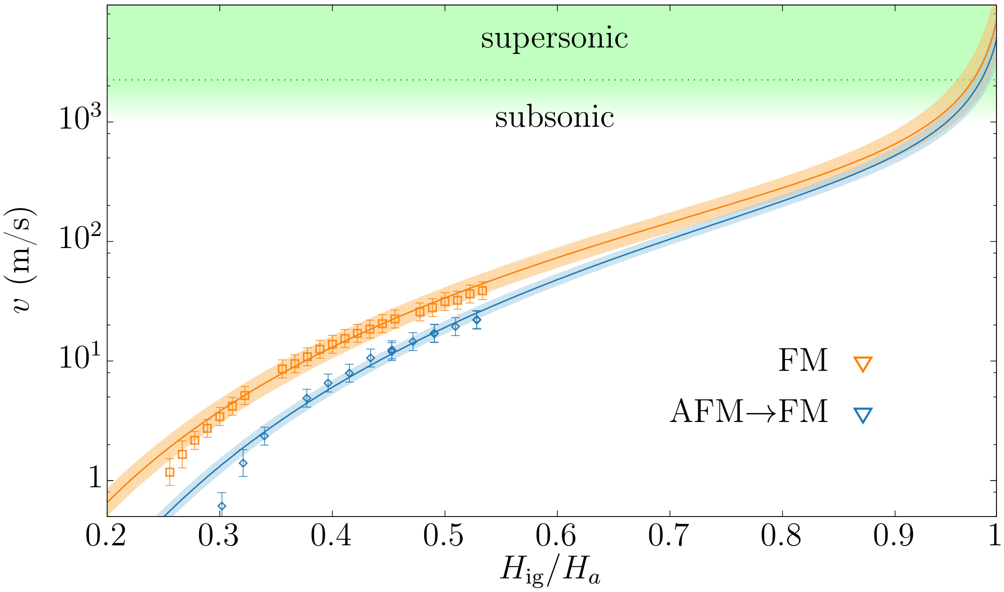

Figure 6.21: Projection of the theoretical speed (lines) at $T = 0$, with their uncertainties (transparent envelopes). The points correspond to the experimental data with maximum ΔM.

plotted the experimental data with maximum ΔM. From the theory of magnetic deflagration we can see how the exponential dependence of the speed on the barrier opens the possibility of reaching supersonic speeds. This was first noted in the the work of Suzuki et al. [31] where they propose the term "magnetic detonation" to refer the case where the propagation speed of the magnetic avalanche surpass the sound speed of the system. That prediction was observed some years later by Decelle et al. using high field magnetic pulses [15]. In the case of Nd_5Ge_3, because its low electric resistivity, we can not use high field magnetic pulses. The induced eddy currents would increase the temperature of the sample, implying: 1) a decrease in $H_{\rm sp}$ (which determines the maximum speed at a given temperature) and 2) a decrease of the "burnable" magnetization due the induction of thermal relaxation, which would also reduce the speed; much more if this relaxation sets some firewall regions.

Taking a look at the extrapolation of $v(H)$ shown in Fig. 6.21 it seems possible to reach this supersonic regime in a commercial dilution refrigerator with a base temperature of tens of millikelvin and with magnetic fields up to 50 kOe. The large and magnetic moment of Nd_5Ge_3 would benefit the investigation of the subsonic to supersonic transition.

6.3 Conclusions

In this chapter I have presented the first evidences of magnetic deflagration phenomena in Nd_5Ge_3, being the first case of a system in which the phenomenon is observed in two distinct magnetic phases, and also the first case for a ferromagnetic system.

To study the magnetic deflagrations I designed a setup that consists of four independent pick-up coils placed equidistant along the sample, one thermometer at one end, and one trigger at the other end. I have to say that the making of this setup was one of the trickiest aspects of this thesis. The signal of each coil is amplified using an amplification stage, specifically designed to be mounted right on top of the sample transport rod of the MPMS® system. Both the signals of the thermometer and of the four coils were obtained simultaneously during the induced magnetic avalanches. Moreover, the time scale used was different in the two acquisitions, being larger in the case of the thermometer (500 ms) than in the case of the coils (20 ms).

The magnetic deflagration phenomena is shown to occur in the spontaneous magnetic avalanches. The spontaneous magnetic deflagrations presented occur in a definite direction, starting around R2 and propagating towards R1. The reproducibility was found to be remarkable. Nevertheless, the shape of the signals obtained did not correspond with the expected ones, indicating some hidden dynamics.

In this chapter, the attention is focussed in the study of the dependence of the phenomenon with the applied magnetic field. To be able to study that dependence I triggered the process at a given *ignition field*, H_{ig}, smaller than the spontaneous deflagration field H_{sp}. From the comparison between the measurements of the magnetic deflagrations of the both the AFM→FM and FM processes, we observe that, as expected, the area under the induced voltage peaks is proportional to the change in magnetization. I have also presented reproducibility tests in the induced FM reversal, resulting to be very high. From the temperature measurements we can see the presence of a threshold in the ignition of the deflagration process, i. e., given the same heat pulse, the process only takes place for certain values of H_{ig}. Regarding to the temperature, I have also presented an analysis of the maximum temperature registered by the thermometer R2 during the deflagrations, being able to explain the large difference between the observed temperature and the expected temperature reached in the sample during the deflagration process.

The speed of the deflagration front is obtained from the voltage curves. However, using a toy model it is shown that due the size and position of the coils with respect to the sample, the most reliable speed is the obtained using the two central coils C2 and C3. With this speed I proceeded to study the likeliness that the magnetic deflagrations in Nd_5Ge_3 could be explained using the theory developed for single molecule magnets. In this investigation we obtained an effective barrier $U(H)$ to describe the system. It is worth to mention, that, as we found in the previous chapter, the compound Nd_5Ge_3 can be well described using the magnetic energy barriers of a system with uniaxial anisotropy. Using this effective barrier, I have shown that the fit of the theory to the experimental speeds is certainly good. That good agreement allows us to point out the possibility of studying the transition from magnetic deflagration to magnetic detonation within reasonable experimental conditions.

CHAPTER 7

Seeking spontaneous magnetic detonations on Nd_5Ge_3

In the last chapter of this thesis, I will present the experimental details and results obtained in the sought of magnetic detonations on a single crystal of Nd_5Ge_3.

As we have just seen in the previous chapter, the speed is a rapidly increasing function of the magnetic field. The maximum speed at a given temperature depends in the combination of two factors, both closely related to the temperature. The first factor is the change in the amount of "burnable" magnetization as the magnetic field is swept. For large temperatures, during the magnetic field sweep, some regions of the sample could have change their magnetization by thermal relaxation, reducing the amount of energy to be released by a deflagration, and perhaps setting firewalls to the propagation of the same. The second factor that determines the maximum speed of the magnetic deflagrations is the greatest magnetic field achievable. In Chap. 5 I presented the results of the dependence of the spontaneous deflagration field, H_{sp}, with the temperature. As we saw, the lower the temperature, the larger the spontaneous deflagration field. The first factor can be overcame using a faster magnetic field sweeping rate (note that as the sample has a large electrical conductivity we will find limitations with the sweeping rate as well), while the only solution for the second is to use a different cryostat rather than the MPMS® to access the millikelvin range.

In the description of the magnetic deflagration phenomena presented in the first chapter of this thesis it was mentioned how the exponential dependence of the propagation speed on the barrier height could open the possibility of reaching even supersonic speeds. Four years after Suzuki et al. coined the term "magnetic detonation" [31], the first experimental observation of the supersonic regime was obtained by Decelle et al. [15]. In the last years, some theoretical papers have appeared considering different aspects of this supersonic propagation, by the group of Prof. Bychkov [126–128] and by the group of Prof. Garanin [61].

In this chapter I will present the experimental setup used to study the spontaneous magnetic deflagrations in a ^{3}He$-^4$He dilution refrigerator. As the reader is about to see, unexpected results were obtained at very low temperatures. To try to unravel the nature of these surprising measurements, I conducted measurements of the spontaneous deflagrations in a Quantum Design® PPMS® system too, to consider dependences of the results with the specific characteristics of the equipment used. However, the experiments performed in both systems confirmed the unforeseen temperature dependence of the spontaneous deflagrations in Nd_5Ge_3 for temperatures below 1.5 K.

7.1 The ^{3}He–^{4}He dilution refrigerator

Before describing the equipment I would like to say a few words about the principle of operation of a dilution refrigerator. Later we will recall these mechanisms when trying to understand the experimental results. The principle of operation of the dilution refrigerator is based in the phase separation of a mixture of the two stable isotopes of helium when is cooled below a critical temperature. This critical temperature, T_c, is a function of the concentration of of ^{3}He in the mixture, measured above 0.86 K. Below T_c, two phases appear: a lighter "concentrated phase", rich in ^{3}He, and a heavier "dilute phase", rich in ^{4}He. The concentration of ^{3}He in each phase depends with the temperature. Fig. 7.1 shows the phase diagram of the ^{3}He$-^4$He mixture. The phase diagram defines three distinct regions. A region with normal fluids ^{3}He and ^{4}He, which, below the lambda line becomes a region with Fermi fluid ^{3}He and superfluid ^{4}He. For concentrations larger than 6.6 %, a forbidden region appears for temperatures below the tricritical point (marked in the plot at 0.86 K). A cooling procedure is also shown in the figure, drawn with a dashed line. The color points lay along it and will be used later in the explanation of the operation of the system. The initial ^{3}He concentration used in the considered cooling procedure is 50 %, which corresponds to the concentration of ^{3}He in the mixture that we have in our dilution refrigerator.

The principle of operation of the dilution refrigerator relies in the different enthalpy of the the ^{3}He in the two phases, which opens the possibility to obtain cooling power by evaporating the ^{3}He from the concentrated phase into the dilute phase. The properties of the liquids in the dilution refrigerator are described by quantum mechanics and the details will not be described here. However, it is helpful to regard the concentrated phase of the mixture as liquid ^{3}He, and the dilute phase as ^{3}He "gas". The ^{4}He which makes up the majority of the dilute phase is inert, and the ^{3}He 'gas' moves through the liquid ^{4}He without interaction.

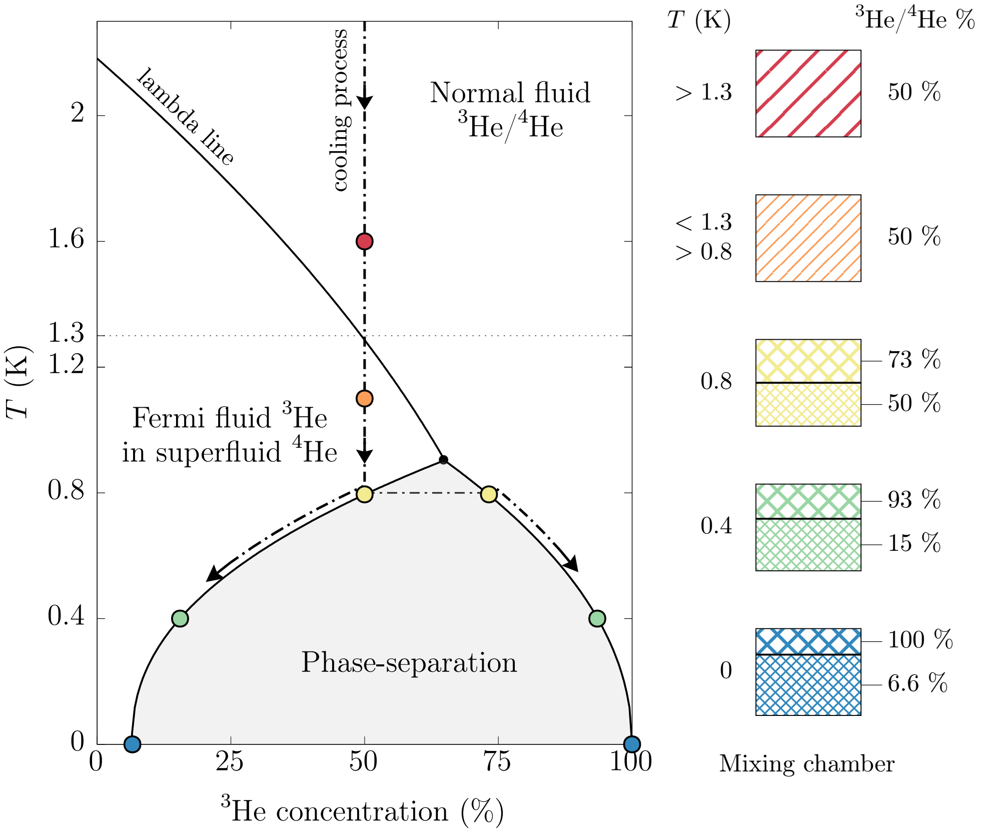

Figure 7.1: Temperature-^{3}He concentration phase diagram of the ^{3}He$-^4$He mixture (main plot), and state of the mixing chamber at different temperatures (right figures). The phase diagram defines three regions: fluid mixture of ^{3}He and ^{4}He, Fermi fluid ^{3}He in superfluid ^{4}He, and a forbidden region highlighted in light-gray. The color phase diagram points lay along the cooling procedure for a initial ^{3}He concentration of 50 %. Each different mixing chamber state correspond to the respective colour mark. The percentages in the mixing chambers correspond to the concentration of ^{3}He. Below a critical temperature (0.8 for 50 %), the black lines define the boundary between the light concentrated phase (top) and the heavy diluted phase (bottom). The changes in the volume fraction accounts for the condensation of the ^{3}He "gas".

This 'gas' is formed in the mixing chamber at the phase boundary. This process continues to work even at zero temperature because the equilibrium concentration of ^{3}He in the dilute phase is still finite (6.6 %). However, the base temperature is limited by other factors, and in particular by the residual heat leak and heat exchanger performance.

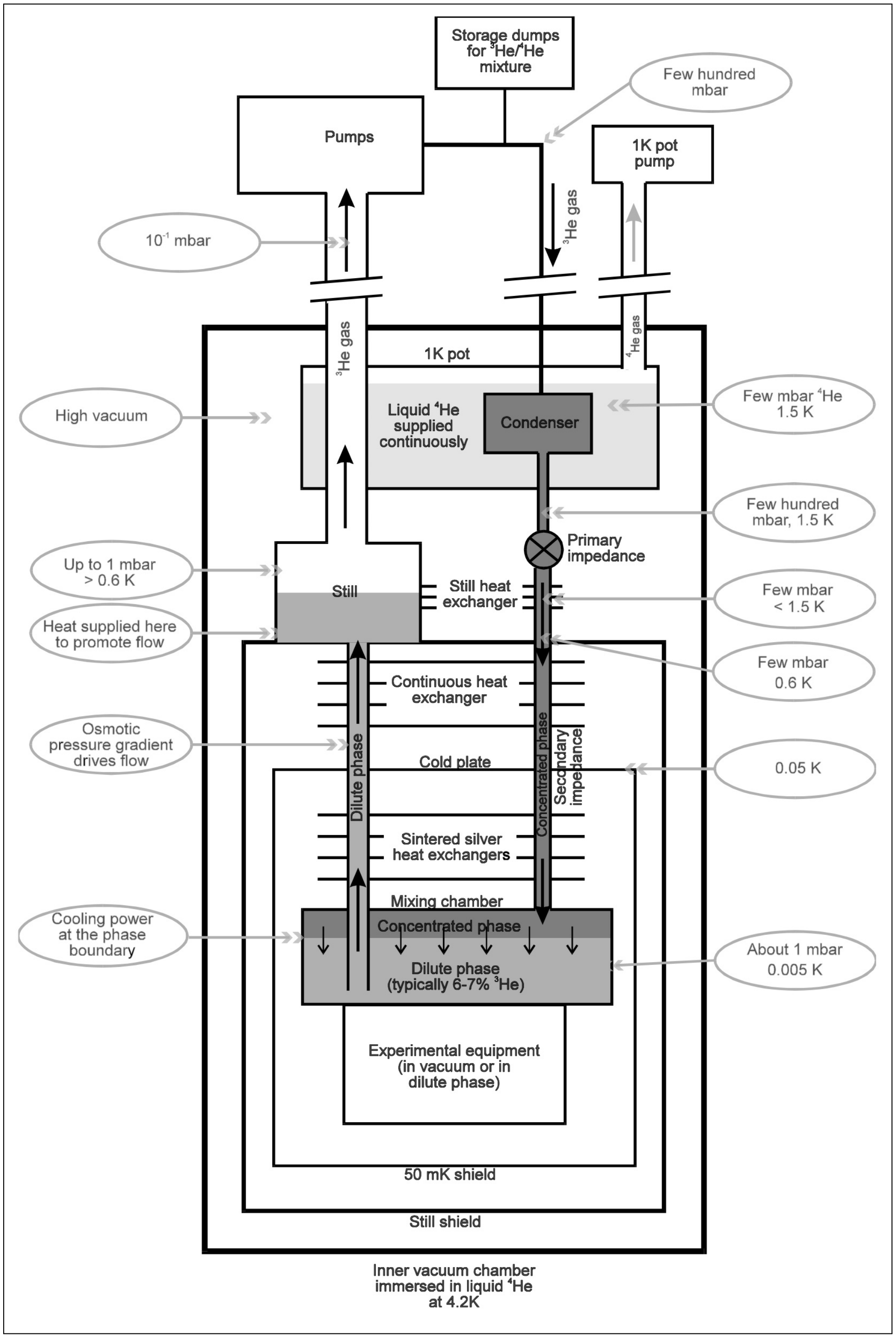

Figure 7.2: Schematic diagram of a typical continuously operating dilution refrigerator. Extracted from [129].

I will now describe the procedure to operate the refrigerator in a continuous mode[1]. A dilution refrigerator is a complex and expensive system. It uses ^{3}He, with its prohibitive prices, and consumes huge amounts of liquid helium and liquid nitrogen. Fortunately, the ^{3}He$-$^{4}He mixture is kept in a close circuit and is rarely refilled. The system has a maze of valves and connections to manipulate making it really tricky to operate manually. The complexity of the system comes from the different agents and steps involved in the cooling procedure. The cryostat has three main layers: one liquid nitrogen chamber, surrounding one liquid helium chamber, which surrounds the inner cooling system. Besides this thermal and radiation protection, during the operation of the dilution refrigerator the nitrogen is used as well in a primary 77 K cold traps where the mixture is cleaned by the condensation of impurities. While it also serves as a thermal and radiation protection, the liquid helium that surrounds the inner cooling system is explicitly used in the "cleaning" (via a secondary 4.2 K cold trap) and the cooling procedure of the mixture; and is also used to keep the temperature of the superconducting coils at 4.2 K.

Fig. 7.2 shows a schematic drawing of a typical continuously operating dilution refrigerator, with each part involved in the cooling process named, together with indications of the typical pressure and temperature values along the procedure. When the refrigerator is started, the 1 K pot is used to condense the ^{3}He$-$^{4}He mixture into the dilution unit. This 1 K pot is continuously filled with liquid helium from the liquid helium chamber (not shown in the diagram). It is not intended to cool the mixture enough to set up the phase boundary but only to cool it to 1.2 K. In order to get phase separation, the temperature must be reduced to below the phase separation temperature defined for a given ^{3}He concentrations (see Fig. 7.1). The still is the first part of the fridge to cool below 1.2 K. It cools the incoming mixture before it enters the heat exchangers and the mixing chamber, and phase separation typically occurs after a few minutes. Gradually, the rest of the dilution unit is cooled to the point where phase separation occurs. It is important for the operation of the refrigerator that the ^{3}He concentration and the volume of mixture is chosen correctly, so that the phase boundary is inside the mixing chamber, and the liquid surface is in the still; as mentioned before, the concentration of our mixture is of 50 %. In a continuously operating system, the ^{3}He must be extracted from the dilute phase (to prevent it from saturating) and returned into the concentrated phase keeping the system in a dynamic equilibrium. The ^{3}He is pumped away from the liquid surface in the still, which is typically maintained at a temperature of 0.6 to 0.7 K. At this temperature the vapour pressure of the ^{3}He is about 1000 times higher than that of ^{4}He, so ^{3}He evaporates preferentially. A small amount of heat is supplied to the still to promote the required flow. The

---

[1] A more detailed description of the ^{3}He$-$^{4}He dilution refrigerator can be found in Ref. [130]

concentration of the ^{3}He in the dilute phase in the still therefore becomes lower than the one in the mixing chamber, and the osmotic pressure difference drives a flow of ^{3}He to the still. The ^{3}He leaving the mixing chamber is used to cool the returning flow of concentrated ^{3}He in a series of heat exchangers. In the region where the temperature is above about 50 mK, a conventional counterflow heat exchanger can be used effectively, but at lower temperatures than this, the thermal boundary resistance (Kapitza resistance) between the liquid and the solid walls increases as T^3, so the contact area has to be increased as much as possible. This is often done by using sintered silver heat exchangers. The room temperature vacuum pumping system is used to remove the ^{3}He from the still, and compress it to a pressure of a few hundred millibar. The gas is then passed through filters and liquid nitrogen/liquid helium cold traps (not shown in the diagram), to remove impurities, and returned to the cryostat, where it is pre-cooled in the main helium bath and condensed on the 1 K pot. The primary impedance is used to maintain a high enough pressure in the 1 K pot region for the gas to condense. The experimental apparatus is mounted on or inside the mixing chamber, ensuring that it is in good thermal contact with the dilute phase. In our case is mounted inside the mixing chamber, so the sample will be immersed in a helium fluid. All connections to the room temperature equipment are thermally anchored at various points on the refrigerator to reduce the heat load on the mixing chamber and give the lowest possible base temperature. The common procedure to control the temperature is set the system to work with the maximum cooling power pumping the ^{3}He while applying heat in the still. Then, once the system is at its base temperature, T_B, a PID controller operates the heater in the mixing chamber to maintain the temperature $T > T_B$ stable. The temperature control is difficult at very low temperatures, so the experiments are preferably performed in “one temperature direction”. The temperature of the crucial parts of the system like the 1 K pot, the still, the mixing chamber, and the liquid helium and nitrogen tanks are monitored using calibrated RuO2 thermometers.

7.2 Experimental setup

The dilution refrigerator in our lab is a top-loading Kelvinox TLM 40, manufactured by Oxford Instruments, with a base temperature of $\sim$ 30 mK and a superconducting NbTi coil to produce magnetic fields in the z direction. A ~ 1 % homogeneity in the magnetic field is ensured in the ± 2 cm region respect to the center of the magnet. The energization of the magnet is done with the 4G Magnet Power Supply, made by the company Cryomagnetics, Inc. The limits in the usage of this power supply are determined by the physical limitations and safety protocols of the superconducting coil. The range of magnetic field strengths that we can

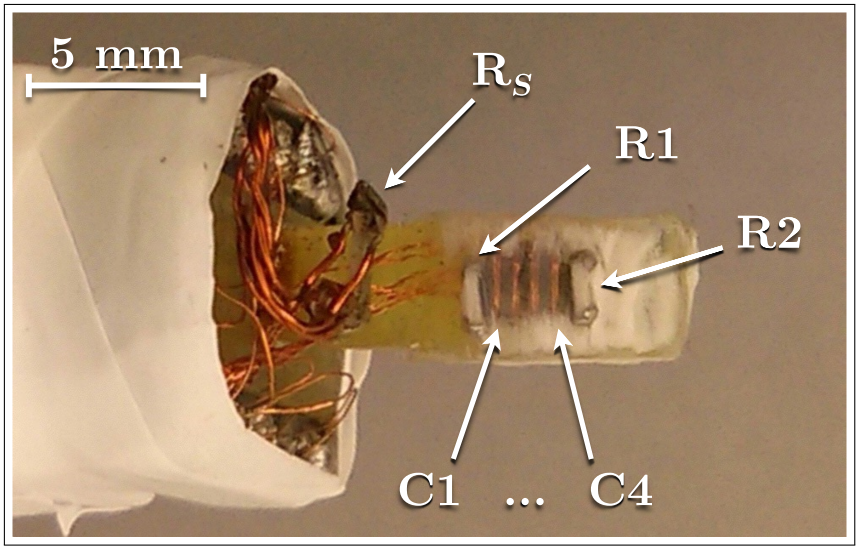

Figure 7.3: Photo of the experimental setup: two resistors, Ri (i = 1, 2); four independent equidistant 2-turn pick-up coils, Cj (j = 1,...,4), that sew the sample on a thin plastic layer; and a calibrated RuO_2 thermometer, R_S, that measures the temperature at the sample space.

obtain in this dilution refrigerator is comprised between ±50 kOe, with a variable sweeping rate up to 300 Oe/s (1.8 T/min). The measurements of the temperature at the crucial parts of the dilution refrigerator are performed using the ac bridge circuit AVS-46, manufactured by RV-Elektroniikka Oy. This equipment is primarily designed for low temperature thermometry with a very-low power dissipation. The temperature controller is a TS-530, made by RV-Elektroniikka Oy, and the heater in the mixing chamber is powered with a PS2603 Dilution Refrigerator Power Supply, fabricated by Oxford Instruments.

Fig. 7.3 shows a picture of the setup of coils and resistors used to measure the spontaneous magnetic deflagrations. The system's thermometer controlled by the AVS-46 appears in the photo as R_S. The design of the setup is almost identical to the design shown in the previous chapter. Nevertheless, this setup is better in every aspect: the coils are even more similar between them, the loops are sewed tighter, the thermometers are placed closer to the edges and with less tin in the soldering points, and the length of each connecting wire is substantially reduced. Working at 30 mK requires an extra effort in every detail. The amplification stage circuit described in Chap. 6 is used in this experiments. Nevertheless, keeping the circuit structure, I had to made a new connection to place the amplification stage as close as possible to the exit of the cryostat's connections. Because we expected to deal with very fast deflagrations, the amplified signal of each coil Ci, was sent to a 4-channel Tektronix DPO2014B oscilloscope connected to a computer. This oscilloscope has a sampling rate of 100 MHz and stores up to 1 GS/s (gigasamples per second). However, while the temporal resolution, 10 ns, is very good for our purposes, it digitalizes the voltage with 8-bits resolution (256 levels). The voltage across the resistor Ri is recorded using the data acquisition card NI-DAQ 6010, connected to the same computer.

The protocol to measure the spontaneous deflagrations was the next, first the system is cooled with zero applied magnetic field down to its base temperature, T_B. Then the magnetic field is swept up to 50 kOe with a sweeping rate of 300 Oe/s. With this first sweep we expect to observe an AFM→FM deflagration. Once the system is at T_B and 50 kOe, the temperature is slowly raised while the magnetic field is swept back and forward between 50 and −50 kOe with the same sweeping rate. This procedure should let us to observe temperature dependence of the FM reversal spontaneous deflagrations, obviously if for a given temperature the spontaneous deflagration field $H_{\rm sp}$ is smaller than 50 kOe. The number of AFM→FM measurements was expected to be extremely limited due the difficulty and cost (economic and in time) of increasing the temperature of the sample up to $T > 50$ K. To try to reduce the time and the difficulty of increasing in a controlled way the temperature of the sample we decided to try to set the temperature of the mixing chamber to the temperature of the 1 K pot and then slowly pull up the entire insert while controlling the temperature of the sample space and the temperature of the other critical parts of the refrigerator. This procedure increases rapidly the temperature of the sample, as we wanted. When the insert is pushed back down the sample starts reducing its temperature rapidly, also as we wanted. The problems appear when the insert approaches the mixing chamber. Even performing the operation with extreme caution, the temperature of the mixing chamber increases enough to force the need of repeating the entire "proper" cooling procedure. Therefore, I could not increase the number of AFM→FM transitions as much as I wanted. However, we are about to see that I was able to obtain a large number of spontaneous deflagrations in the FM reversal process, covering a wide range of temperatures.

7.3 Analysis and results

On the one hand, the results obtained in Chap. 5 indicated the increasing dependence of the spontaneous deflagration field H_{sp} with the decreasing temperature. On the other hand, in the fit of the theoretical speed to the experimental propagation speed showed in the previous chapter one finds that for $H_{\rm ig} \gtrsim 0.95 H_a$ the expected propagation speed is of the order of the speed of sound. Considering both, one expects that lowering the temperature enough, the supersonic regime could be reached.

Two different aspects surprised us in the seek of magnetic detonations. The first was that I was not able to observe induced voltage peaks in the first magnetization curves. Because of the difficulty and cost just explained, I only tried to observe them five times. The first three experiments were done at base temperature, and the other two at two different temperatures, both below 1 K. There were four possibilities to explain this unexpected behaviour: a) Either the AFM→FM spontaneous magnetic deflagration did not occurred below 50 kOe; b) it occurred at low fields and the induced voltage was too small to trigger the capture; c) the AFM→FM magnetic transition becomes smooth, or d) simply the transition did not take place at ultra-low temperatures.

The second surprising aspect of this measurements in the dilution refrigerator is that I did not find magnetic detonations, but large reproducible jump discontinuities in the spontaneous deflagration fields. In this section I will investigate in detail the stepped discontinuities, also with measurements of the spontaneous magnetic deflagrations performed in a PPMS®. The comparison between the measurements done in those very different systems is the key factor that let me to present a new and unexpected phenomenon in the Nd_5Ge_3 intermetallic compound.

7.3.1 Jump discontinuities in the spontaneous deflagration field

Fig. 7.4 shows the results of the spontaneous deflagration field, H_{sp}, versus temperature experiments in the dilution refrigerator. Three independent experiments are shown in this figure. One experiment consisted in measuring the spontaneous deflagrations with the sample “naked”, while in the other two the sample was covered with grease. Before mentioning the aim of measuring this different “thermal coupling” conditions, I want to focus the attention to the clear and unexpected jump discontinuities in the spontaneous deflagration field that appear at 1.3 and 0.9 K. Note that the stepped discontinuity at 1.3 K is large $\sim$ 5 kOe. Below 0.6 K it seems that another small step appears, while it is not very clear in this experiments. From the three independent measurements we find a large reproducibility of the phenomenon. The “noise” in H_{sp} is different in each of the four regions defined by the jump discontinuity temperatures. Above 1.3 K the uncertainty of H_{sp} is small (almost all points follow a monotonic curve). Between 1.3 and 0.9 K, the points seem to follow a definite curve but with an increased dispersion. Below 0.9 K the value of H_{sp} appears to become independent of the temperature, with a dispersion that is reduced below 0.6 K.

With the study of the spontaneous deflagration field for different “thermal coupling” conditions I tried to observe the effect of a change in the heat exchange

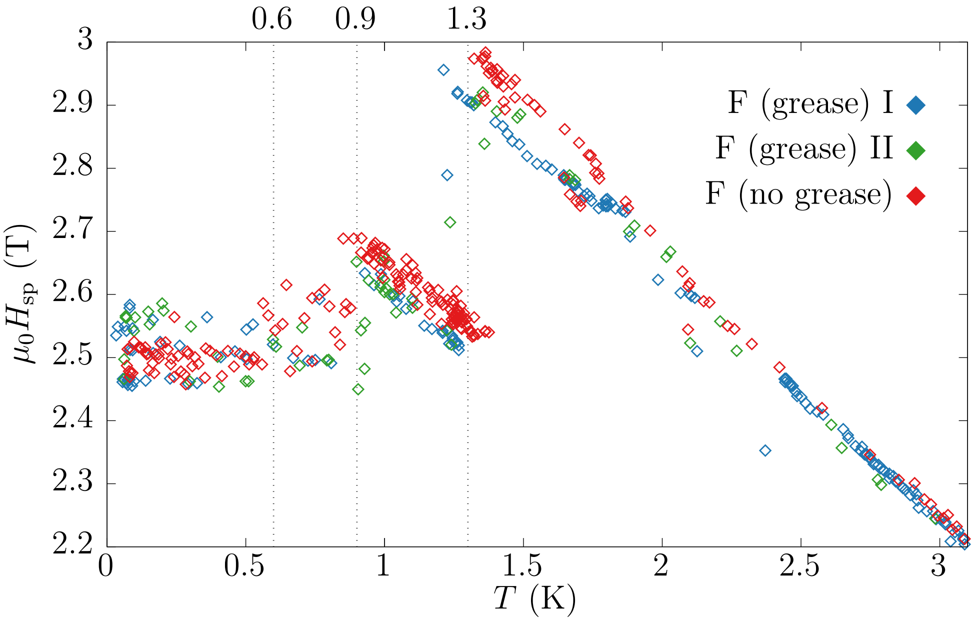

Figure 7.4: Log-linear plot of the spontaneous deflagration field as a function of the temperature. Three independent experiments are presented. The green and blue diamonds correspond to experiments where the sample was covered with grease. The experiment without grease is represented using red diamonds. We observe clear jump discontinuities around 1.3 and 0.9 K, in all three experiments. An apparent third discontinuity is observed around 0.6 K.

properties between the sample and the thermal bath. In Chap. 5 it was already pointed out how, for the same system, the spontaneous deflagration field should shift to lower values as the thermal contact with the environment became poorer. Moreover, it was also indicated a necessary increase of the uncertainty of H_{sp} due thermal fluctuations, that given the reduced effectiveness of the sample to release the heat generated in the magnetic transition (relaxation), derive in a thermal runaway that produces the deflagration. These two expected features are observed in Fig. 7.4. As the temperature is reduced we observe how the spontaneous deflagration fields obtained with the “naked” sample are larger than ones obtained with the sample covered with grease. However, the second feature, the increase in the uncertainty of H_{sp} seems to be relevant only at the lowest temperatures. Besides the aim of this study was to check this two hypothesis, it is worth to mention that the occurrence of the stepped discontinuities are found at the same temperatures, and with the same change in magnitude.

I will now try to determine the origin of the jump discontinuities. The first question to answer is if the amount of change in magnetization is the same in all the spontaneous deflagrations. Incomplete avalanches at certain temperatures could

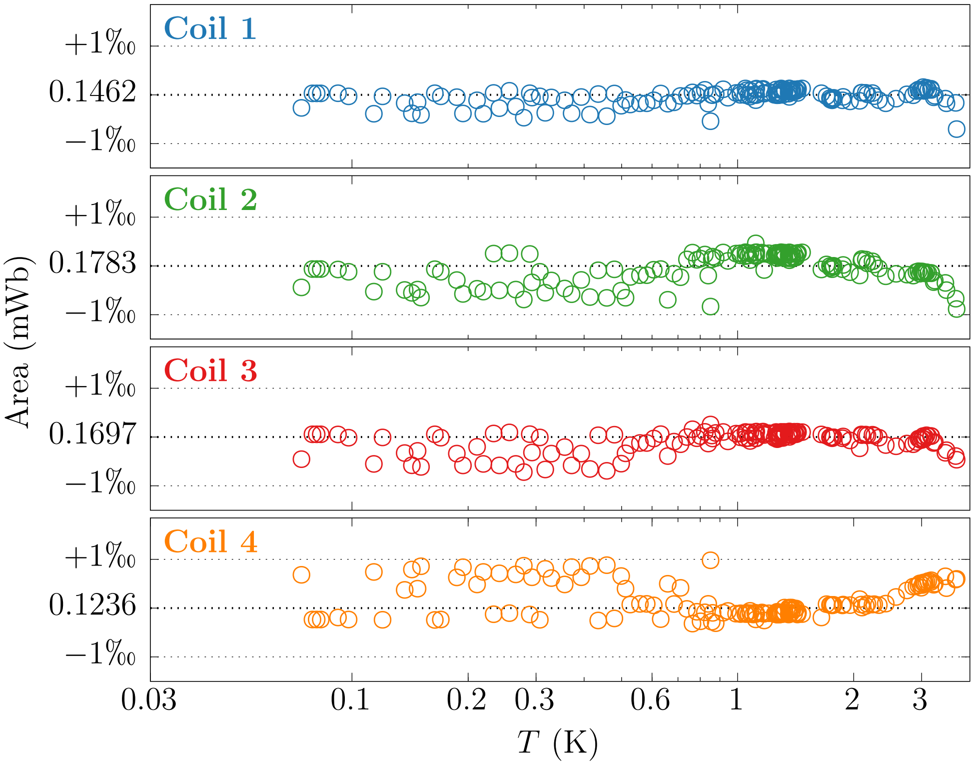

Figure 7.5: Log-linear plot of the area defined by the signals of the four independent coils, as a function of the temperature. The area remains constant in the whole range of temperatures, with deviations less than 1‰, indicating that in all the observed spontaneous deflagrations the change in magnetization is the same.

explain changes in the $H_{\mathrm{sp}}(T)$ curve. Our dilution refrigerator has not incorporated a magnetometer by default (we have a dedicated SQUID magnetometer, designed by my advisor [131], but it can not be operated together with the sample holder that I needed to study the deflagrations). Therefore, unlike the measurements done in the MPMS® system (see Chap. 6), we do not have direct measurements of the magnetization after the spontaneous deflagration. However, we can know the magnitude of the change in magnetization of the sample during the deflagration, just studying the area below the induced voltage curves of the coils. As the coils are very similar to those used in the previous chapter, and the gain of the amplification stage is the same, we know the expected area associated to a certain change in magnetization. Comparing for a given temperature the values of the areas obtained in the induced deflagrations in the MPMS® together with the spontaneous ones obtained in the dilution refrigerator, we find that they are completely compatible. I. e., we confirm that, at "high" temperatures (~ 2 K) the change in magnetization observed in the FM reversal corresponds to the complete reversal of the saturation magnetization. Once we know this at high temperatures we can compare the areas for all the spontaneous deflagrations in the whole range of temperatures. Fig. 7.5 shows the area defined by the signals of the four independent coils as a function of the temperature. We observe that, within a 1‰, the area remains constant in the entire temperature range. We do not observe any relevant discontinuity in the areas. Therefore, we have found that the ΔM involved in all the spontaneous deflagrations measured corresponds to the complete reversal of the magnetization saturation, and consequently we have discarded the hypothetical influence of incomplete deflagrations on the stepped discontinuities.

The second question to answer in the determination of the nature of these jump discontinuities is if there exists any discontinuity in the thermal properties of the sample. Based on the specific heat experiments shown in Chap. 4 we can discard abrupt changes in the thermal properties of this compound, at least in the range covered by the specific heat measurements (0.3–140 K). Just to mention, I did not found stepped changes in the $C(T)_{\mathrm{FC}}$ as a function of the temperature, and the erratic behaviour found around the H_{sp} in the $C(H)_{\mathrm{FM}}$ curves was already explained and clearly associated to a misalignment between the sample and the applied magnetic field.

The last question I tried to answer is if there exists any discontinuity in the thermal bath. The ^{3}He concentration-temperature phase diagram shown in the description of the $^3\mathrm{He}-^4\mathrm{He}$ dilution refrigerator (see Fig. 7.1) has a important event at 1.3 K, for an initial ^{3}He concentration of 50% (which is exactly the ^{3}He concentration that we have in the mixture at room temperature). At 1.3 K the ^{4}He of the mixture has a transition from a fluid to a superfluid state. This transition is so relevant in the properties of the thermal bath that we believe that can explain the stepped discontinuity at 1.3 K. Also, following the cooling process in the phase diagram, we see how around 0.8 K the $^3\mathrm{He}-^4\mathrm{He}$ suffers a second abrupt change, enters the immiscibility region where the ^{3}He separates in a diluted and a concentrated phases. The second observed jump discontinuity is found around 0.9 K, so again we believed that the phase change in the mixture could be the origin of the stepped discontinuity in the spontaneous deflagration field. There are no more abrupt changes in the mixture below the phase separation curve so we can not explain the discontinuity at 0.6 K.

If the nature of the jump discontinuities is completely related to the changes in the $^3\mathrm{He}-^4\mathrm{He}$ mixture, then one should not observe them when performing the same experiment in a cryostat that reach temperatures below 0.8 K without using a mixture. As was mentioned in the description of the measurements of heat capacity (Chap. 4), the PPMS® system, with the ^{3}He option, can reach 0.35 K.

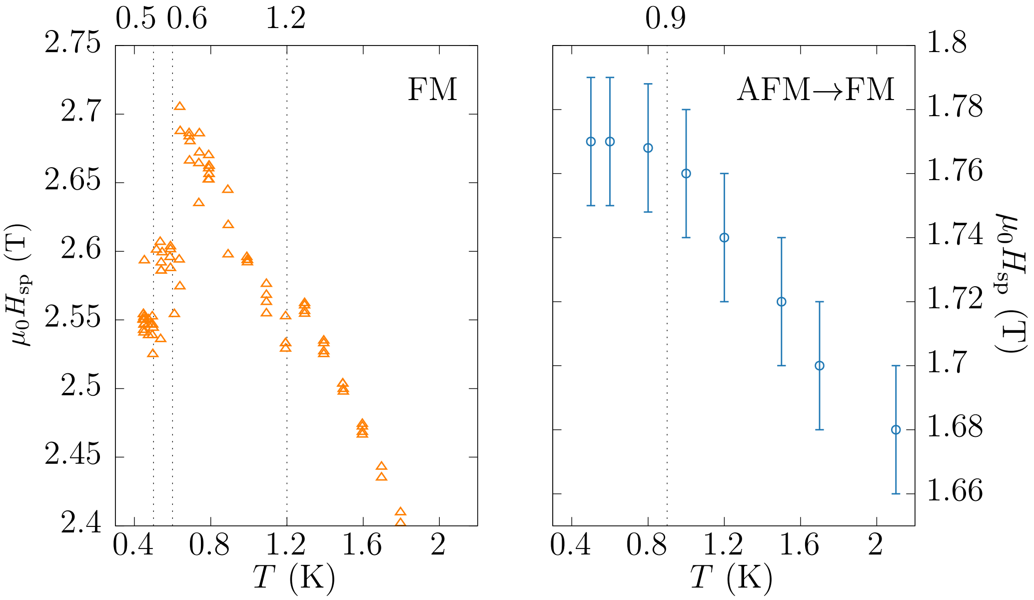

Figure 7.6: Spontaneous deflagration field as a function of the temperature measured in a PPMS® with the ^{3}He option. Left panel: FM reversal experiments. Right panel: AFM→FM experiments.

Also, unlike in the dilution refrigerator where the sample was immersed in fluid, in the PPMS® the sample is only in thermal contact with the sample holder in a high vacuum environment (0.9 mTorr). As in the case of the specific heat experiments, the following results were obtained in the Universidad de Zaragoza. Because of the specifications of the equipment, the experimental setup to study the spontaneous deflagrations in the PPMS® consisted in a single 3-turns coils, centered in the sample, and a resistor placed at one end. The induced voltage of the coil and the voltage drop in the resistor were measured with the same equipment as the one used in the dilution refrigerator, with the Tektronix DPO2014B oscilloscope and the NI-DAQ 6010 data acquisition card respectively.

Fig. 7.6 shows two panels with the spontaneous deflagration fields in the FM reversal (left panel), and in the AFM→FM transition (right panel). Let me start commenting the right panel. As the reader can see, for the first time in this thesis, error bars are used in the determination of the spontaneous deflagration field (in all the previous measurements the uncertainty was smaller than the size of the marks). The reason for those error bars is that the deflagrations were not observed as peaks in the induced voltage, but as “slow” changes in the resistor. The error bar corresponds to the uncertainty in the determination of the magnetic field since it was being swept while the change in resistance was recorded “manually”.

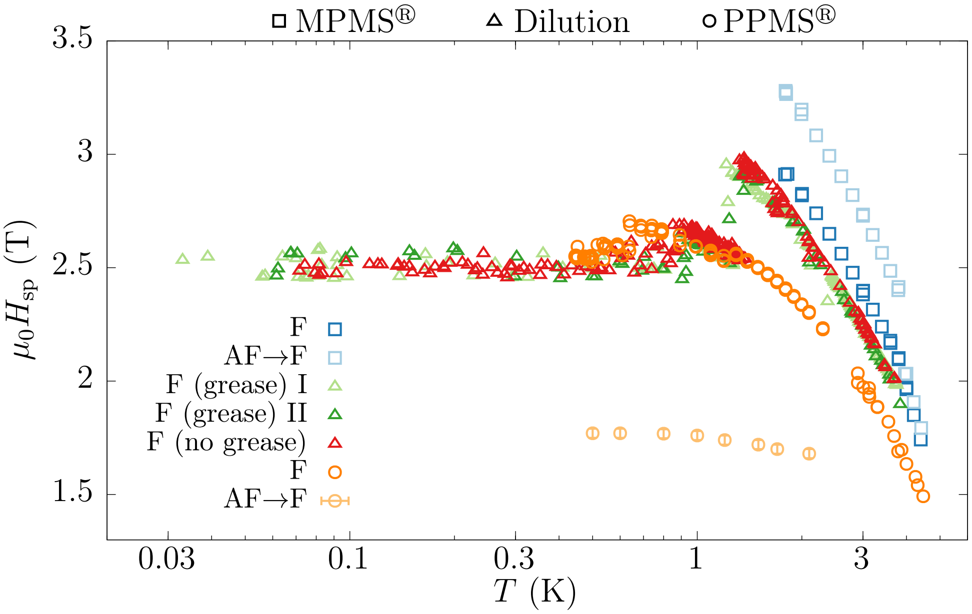

Figure 7.7: Log-linear plot of the spontaneous deflagration field as a function of the temperature measured in three different equipments: MPMS® (squares), ^{3}He$-^4$He dilution refrigerator (triangles) and PPMS® (circles).

In the panel we observe a plateau below 0.9 K. Nevertheless, due the large error bars, I can not ensure it. The values obtained for $H_{\mathrm{sp-AFM\to FM}}$ are much smaller than the ones obtained in the MPMS® system. Even taking into account the high thermal isolation present in the PPMS® I can not explain such a reduction.

The left panel shows the spontaneous deflagration fields for the FM reversal as a function of the temperature. Unexpectedly, we observe jump discontinuities as in the dilution refrigerator experiments. Nonetheless, the magnitude of the step is much smaller in this case. We can see a jump discontinuity at 1.2 K, and two more at 0.6 and 0.5 K. The discontinuity around 0.9 K observed in the dilution refrigerator is not found in these experiments. The environment is so different between both cryostats that the only explanation is that those jump discontinuities around 1.2 and 0.6 K are an intrinsic property of the sample. I consider that the fact that the step around 0.9 has disappeared, and the one around 1.3 has largely reduced its magnitude, mean the conjunction of the discontinuities associated with the Nd$_5$Ge$_3$ and with the ^{3}He$-^4$He mixture.

A summary of all the spontaneous deflagrations measured in the different equipments is shown in a log-linear plot in Fig. 7.7. In this figure is evident the rich phenomena that we have found in this system.

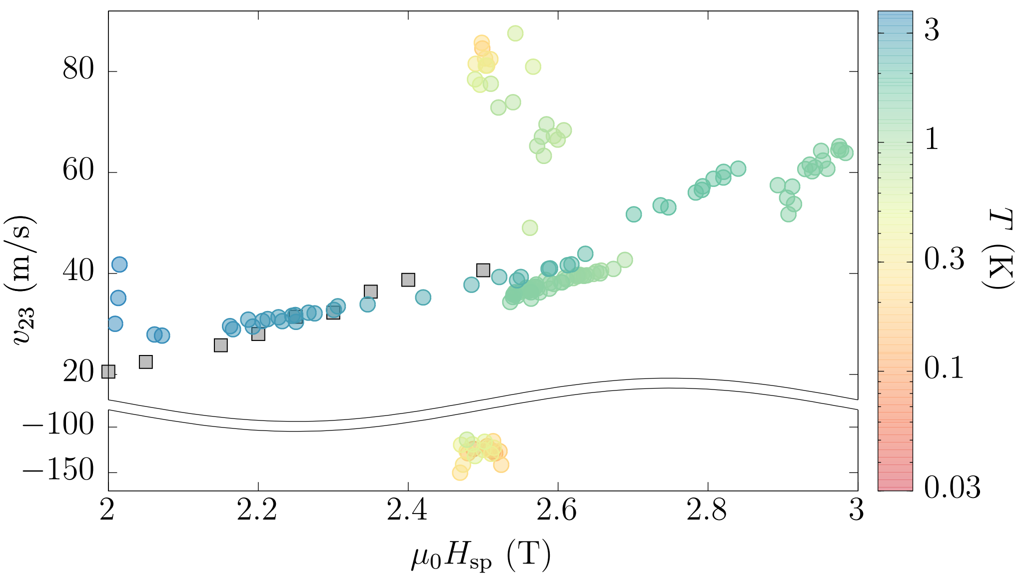

Figure 7.8: Speed of spontaneous deflagrations as a function of the spontaneous deflagration field, H_{sp}. The measurements correspond to the experiment with the sample “naked”. The color represents the temperature at which the deflagration took place. The vertical axis is broken between −80 and 15 m/s to show in detail the two distinct regions of the speeds. The gray squares correspond to speed of the induced deflagrations at 2 K in the MPMS®.

7.3.2 Anisotropic magnetic deflagrations

Following the procedure shown in the previous chapter to determine the propagation speed of the induced magnetic deflagrations, we obtain the speed of the spontaneous deflagrations. Fig. 7.8 shows the dependence of the speed with the spontaneous deflagration field in the experiment with the sample “naked”. Because the jump discontinuities, it is obvious that we did not reached the supersonic regime; actually, we barely double the fastest speed obtained in the induced deflagrations. Nevertheless, looking at the figure we observe some strange phenomena. For certain temperatures, the speed is either two times larger for the same given field (points around 2.5 T), or three times larges in the oposite direction (around the same field of 2.5 T, bottom part of the plot). This anomalies are also observed in the speeds of the experiments where the sample was covered with grease. In the plot are also represented the propagation speed of the induced deflagrations at 2 K, showing how the speed is mainly defined by the magnetic field at which occurs the deflagrations, being spontaneous or induced.

To understand the observed dependence of the propagation speed with the mag-

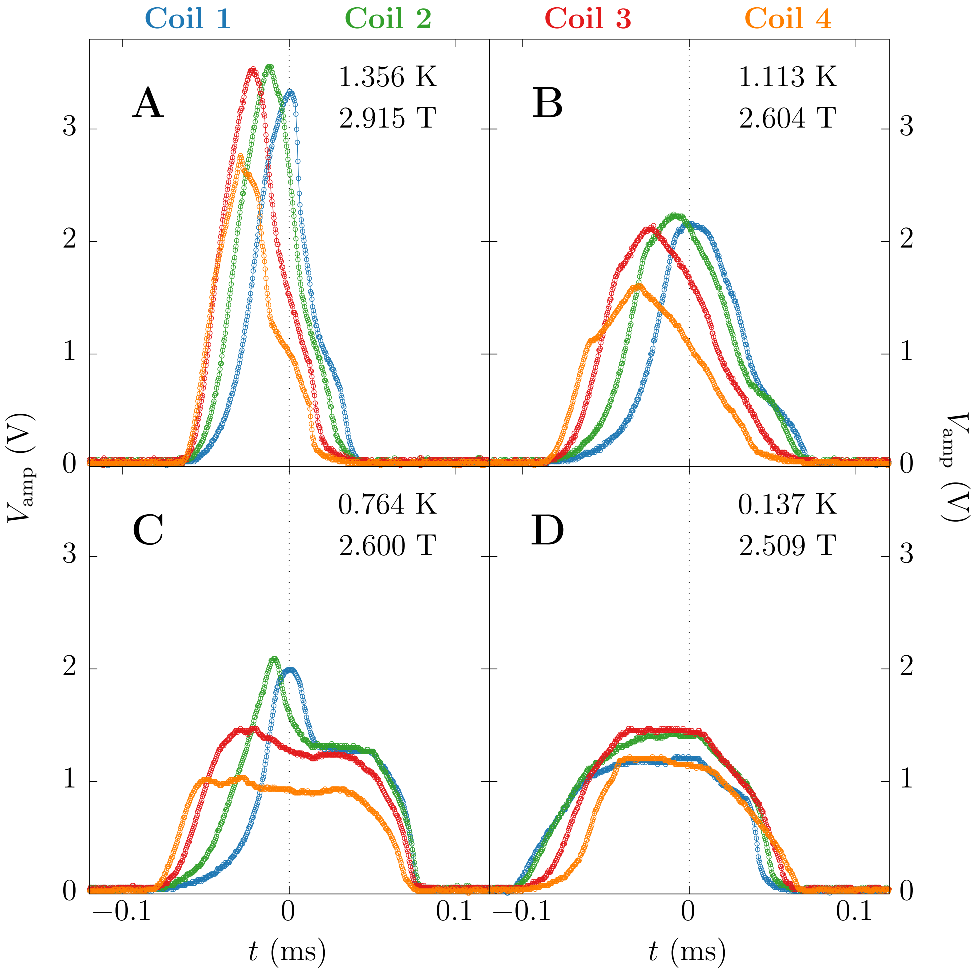

Figure 7.9: Temporal evolution of the four characteristic induced voltage shapes in the four 2-turn independent pick-up coils. The time scales have the zero set at the time where the Coil 1 has its maximum.

netic field and temperature I checked one by one the shapes of the induced voltage signals. I will show, referred to the experiment with the “naked” sample, the four different type of shapes that I found to appear in the temperature range. These four types are shown in Fig. 7.9. From **A** to **D**, each shape correspond to a decreasing temperature. The curves at the highest temperature **A** have the shape that we already observed in the spontaneous deflagrations in the AFM→FM process at 5 K, measured in the MPMS® (Pag. 133). Nevertheless it does not correspond to the shape of the induced deflagrations. It has to be mentioned that besides the different shapes, the main difference between the AFM→FM spontaneous deflagration curves and the curves of the FM reversal induced deflagrations was their reversed order, i. e., the propagating front of magnetization change moved through the sample in opposite directions. The fact that we are obtaining the same shape in the spontaneous FM reversal indicates that the spontaneous deflagrations have a preferred starting point at the end closer to the pick-up coils number 3 and 4. This is supported by three of the four shape types presented in the figure. Before commenting the intermediate temperatures I will discuss the shape of the type shown in the **D** panel. We observe that the order has changed, being the pick-up coils 1 and 2 the firsts to register a change in the magnetization. This shape occurs only at the lowest temperature range, and I believe to be a side effect of the measurement of the temperature at the resistor R1. The resistor R1 is placed right at the end that is closer to the coil 1 (see the experimental setup shown in Fig. 7.3). The current used to measure the temperature was 20 μA, which implies a heat dissipation of $\lesssim 1$ μW. Certainly it is a tiny amount of power, but one can not discard that at ultra-low temperatures this heat promote the appearance of a spontaneous deflagration, moreover taking into account the observed change in the shape and "direction" of the induced voltage signals.

Comparing the panels **B** and **C** we observe that both spontaneous deflagrations occur at the same magnetic field, 2.6 T. Nevertheless the shapes are completely different. This is the best proof that the parameter that control the shape of the curves is the initial temperature rather than the magnetic field. The shape of the curves at 1.113 K (**D**) looks similar to the shape of the **A** ones, but when studying the whole set of curves I found that they have to be considered different. The curves that have the shape of this type (**B**) are always smother than the **A** curves.

Finally, I want to center the attention on the shape defined by the curve shown in the **C** panel. All the rest of shapes showed certain internal structure (which is maintained repeating the process with the same experimental conditions, as we have seen in the different reproducibility tests shown in the previous chapter), but the internal structure of this shape is so evident that I have to consider that as a hint of some hidden properties of this system. Taking a look at the curves we can distinguish three main features. The first is that the induced voltage drop suddenly in all the four coils almost at the same time. The second attribute is the almost flat response observed in the totality (coil 4) or in parts of the curves (coils 3 to 1). The last characteristic is the presence of a marked peak "embedded" in the enveloping plateau. It worths to mention that the curve shape observed at the lowest temperatures share the first two properties.

To explain this features I suggest that the thermal conductivity of the Nd_5Ge_3 and/or the speed of the deflagration front are highly anisotropic. An schematic diagram of the propagation of a magnetic deflagration in a system with a large

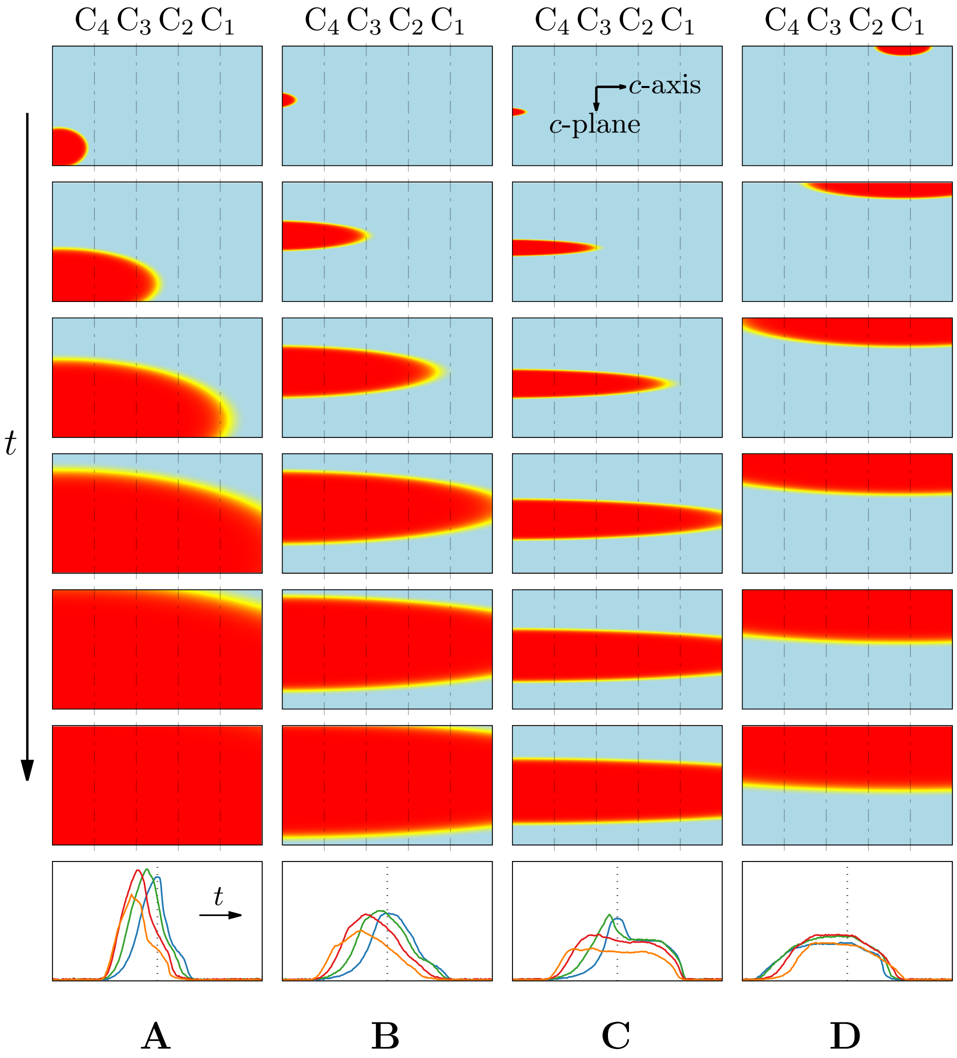

Figure 7.10: Schematic diagram of the propagation of magnetic deflagrations in a sample with anisotropic thermal conductivities and/or anisotropic magnetic deflagration speed, as a function of the initial size of the deflagration front. The four shapes observed, **A**. . . **D**, can be approximately obtained considering a simple ellipsoid model.

anisotropy in the heat transport properties is shown in Fig. 7.10. In these diagrams are considered the time evolution of deflagration fronts defined by ellipsoids, with different initial sizes and origins. The ratio between the semi-axis represent the anisotropy of the system. The shape that we are considering, **C**, would be compatible with the response of the set of coils to a magnetic deflagration of the type **C** of the diagram. I. e., an elongated deflagration front that propagates rapidly across the c-axis, resulting in a sequential peaked detection by the coils, followed by the lateral movement of the deflagration front, which would give the synchronous flat response of the coils. The shape **D** obtained in the ultra-low temperatures could be reproduced following the **D** schema. At “high” temperatures the initial front would be larger, implying a propagation through the sample as a whole (schema **A**). This schema results in a sequential peaked response when the front reaches the center of each coil, as observed in the shape **A**. Despite being a simple model, it explains reasonably well the experimental shapes. Therefore, I consider that what I have observed in the shape of the magnetic deflagrations is an indirect measure of the large anisotropy in the thermal transport and properties of the Nd_5Ge_3. I have to mention that anisotropic magnetic deflagrations where investigated theoretically in an squared sample of a single molecule magnet by Dion et al. in Ref. [127], and studied experimentally in Gd_5Ge_3 single crystals cut along different directions by Saül et al. in Ref. [9]; however, in this work they characterized the propagation properties along each axis, but they did not observed a combined deflagration propagating at different speeds in different directions.

I have extended the shape classification to the whole set of spontaneous magnetic deflagrations measured in the dilution refrigerator, including also the ones obtained in the MPMS® and PPMS® systems. Fig. 7.11 shows up to seven different shapes found to appear in the experiments performed in the three different cryostats (**A**. . . **G**). Note that the first four shapes corresponding to the dilution refrigerator (panel **A** to **D**), are obtained at different temperatures than the ones just shown in the previous figures.

Fig. 7.12 shows the discrete spectrum of shapes as a function of temperature for the different spontaneous deflagration experiments: **i)** MPMS® AFM→FM, **ii)** MPMS® FM reversal, **iii)** Dilution no-grease, **iv)** Dilution grease, **v)** PPMS®. Each measured spontaneous deflagration is represented with a mark using the colors defined by the labels of the shapes shown in Fig. 7.11. The vertical dashed lines correspond to the temperatures of the jump discontinuities shown in Fig. 7.5. These spectra reveal interesting phenomena. The first aspect we notice is that the jump discontinuities observed in the spontaneous deflagration field are also present in the shapes. The second remarkable detail is that each shape occurs in a rather defined region of temperature. Both characteristic are very clear in the spectrum obtained in the dilution refrigerator with the sample not covered with grease, **iii**. In the spectra **iv** and **v** the range of appearance of the different shapes is also defined, but the overlapping in temperatures is much larger. It seems obvious that in more thermally isolated systems (the sample covered with grease in the dilution refrigerator, and in high vacuum in the PPMS®), the conditions for the thermal runaway are more propitious. In those systems, during the magnetic relaxation

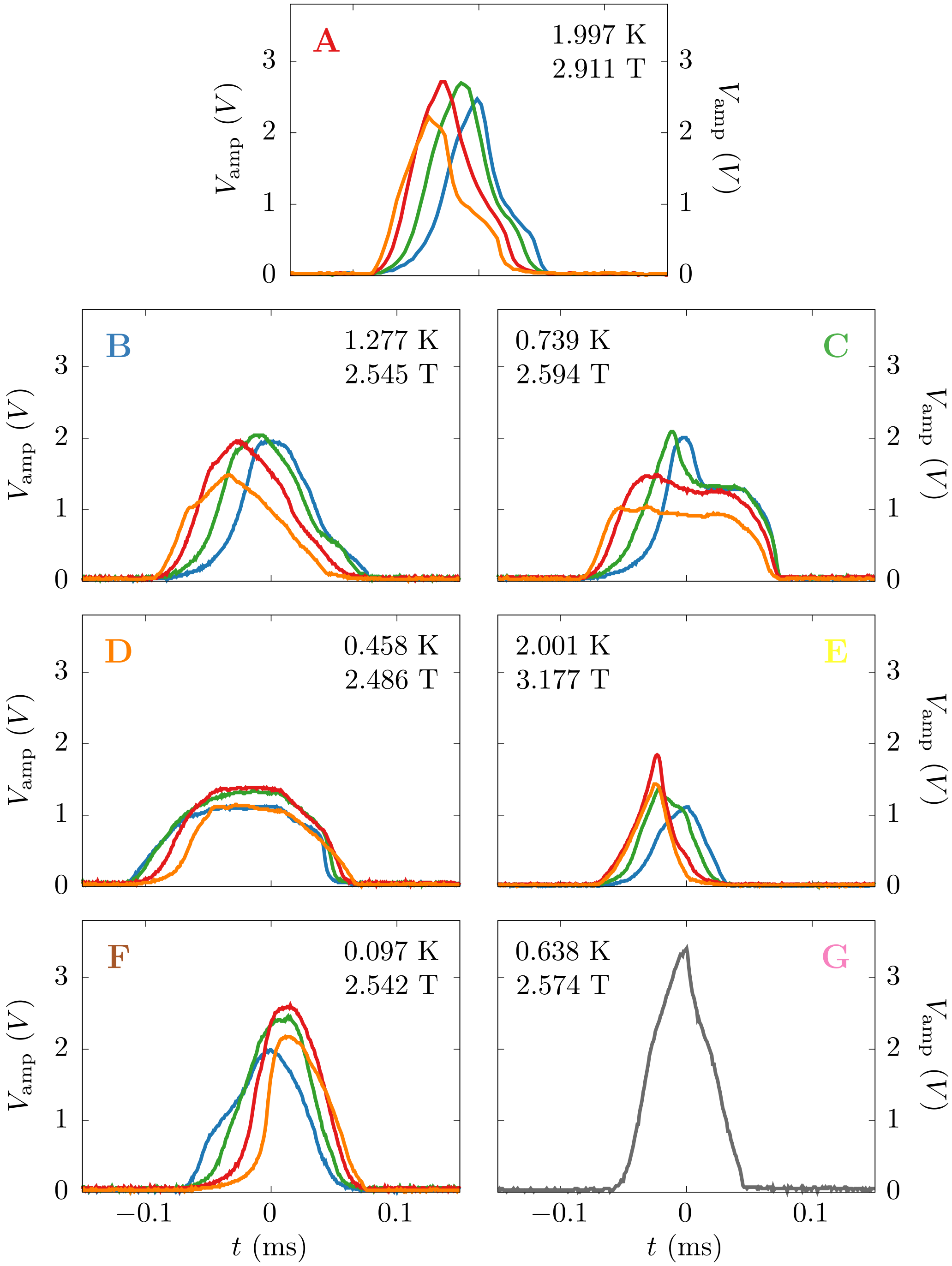

Figure 7.11: Time dependence of the seven distinct induced voltage shapes observed in the spontaneous deflagration experiments carried out in different equipments. The individual shapes are named from top to bottom, from left to right, as **A**. . . **G**.

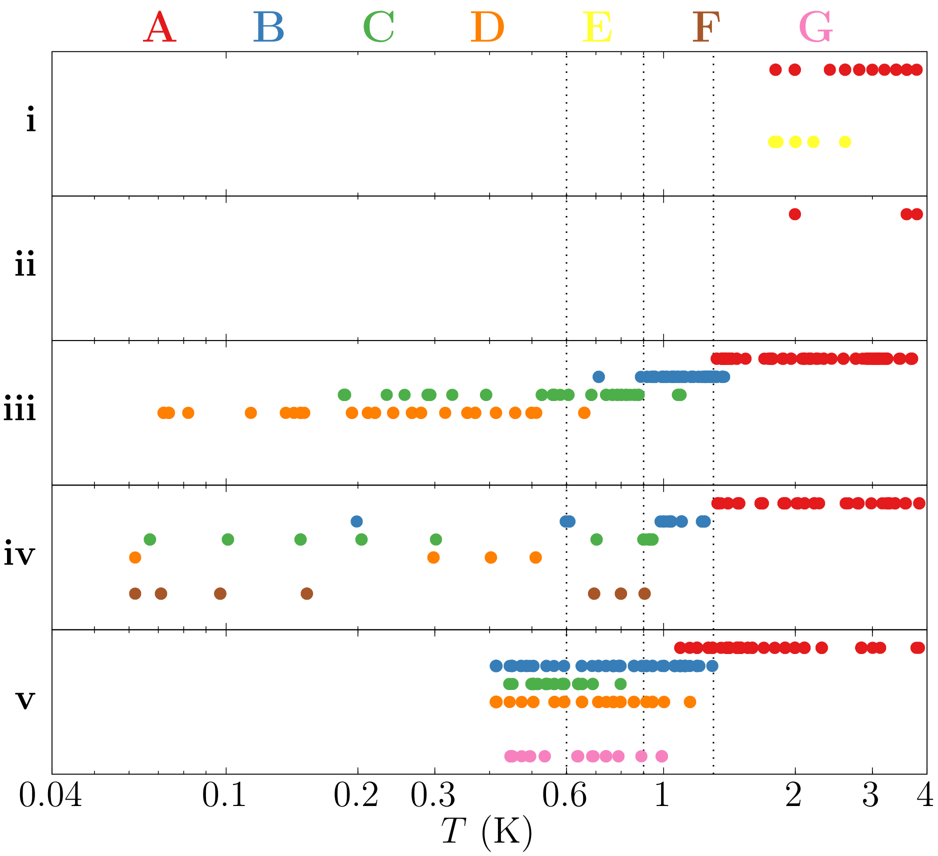

Figure 7.12: Discrete spectrum of shapes as a function of temperature for the different spontaneous deflagration experiments: **i)** MPMS® AFM→FM, **ii)** MPMS® FM reversal, **iii)** Dilution no-grease, **iv)** Dilution grease, **v)** PPMS®. The labels **A**. . . **G**, and their colors, correspond to the shapes shown in Fig. 7.11. The vertical dashed lines are the temperatures of the jump discontinuities in the spontaneous deflagration field presented in Fig. 7.5.

that precedes the magnetic deflagrations, due the reduced thermal coupling to the cold bath, the formation of the deflagration front is favoured, increasing the probability to occur in more than one place at the same time. I. e., the "effective" size of the deflagration front when the system is isolated is expected to have a larger variability than in the case of a well thermalized system. Therefore considering the model based on ellipsoids in which the shape is determined by the anisotropy and by the initial size of the deflagration front, one can explain reasonably well the overlapping occurrence of the different shapes as a function of the temperature in the two mentioned systems.

Nevertheless, I do not have an explanation for these stepped discontinuities in the shape of the signals as a function of the temperature. As with the jump discontinuities in the spontaneous deflagration field, the fact that appear at the same temperatures in two clearly distinct systems (dilution refrigerator vs. PPMS®) makes me suspect that we are in presence of a new physical property of the Nd_5Ge_3 system. Please note that the measurements of the specific heat covered the range of temperatures where we are observing this stepped discontinuities, without reporting any abrupt anomaly. However, I want just to note that at 1.2 K the system has its minimum of heat capacity.

7.4 Conclusions

The goal initially pursued in this chapter was to reach the supersonic regime of the propagation of the magnetization change front in the FM reversal and/or in the AFM→FM transition. The experimental conditions required theoretically to obtain magnetic detonations made me move from the MPMS® system to the $^3He-^4He$ dilution refrigerator. The operation of the dilution cryostat that we have in the group is fully manual, and the complexity of the system is certainly high because the number of delicate steps in the cooling procedure. Due the extreme conditions of ultra-low temperature measurements, I made from scratch a new experimental setup of coils and resistors, being better than the previous in every aspect.

In the first measurements of spontaneous magnetic deflagrations we already got an unexpected result. We could not observe magnetic deflagrations in the AFM→FM transition. Moreover, jump discontinuities appear at definite temperatures in the FM reversal spontaneous deflagration fields. I check the reproducibility of these jumps, also modifying the "thermal coupling" between the sample and the environment repeating the experiments with the sample covered in grease. First I considered the abrupt changes that experiment a $^3He-^4He$ mixture (with a ^3He concentration of 50%) at 1.3 and 0.8 K. Being the first the ^4He fluid-superfluid temperature transition and the second the phase separation of the ^3He fluid in two phases with very different concentrations. However, as I repeated the experiments in a PPMS® using a ^3He option obtaining again some of the jump discontinuities, I presented my hypothesis that this stepped discontinuities are related to intrinsic properties of the sample. Then I proceeded to study the dependence of the speed with the spontaneous magnetic deflagration field. Since the obtained results were very difficult to justify I explored all the obtained induced voltage curves. I found that, in the experiment with the sample not covered with grease, four distinct shapes are repeated in all the induced curves. I extended the study of the shape of the induced voltage signals to the whole set of measurements of spontaneous magnetic deflagrations obtained in the three different equipments (MPMS®, PPMS®

and ^{3}He$-^4$He dilution refrigerator); finding up to seven different shapes. Looking this shapes in detail I came to propose a model of a system with a large anisotropy on its thermal transport properties, at which different initial conditions of the spontaneous deflagration process, lead to very different shapes in the induced voltages of the coils. Since the model describes well the results and because we already know that the intermetallic compound is very anisotropic in many of its physical properties, I consider the observed shapes as the first experimental evidence of the anisotropic thermal transport properties in Nd_5Ge_3.

Nevertheless, I do have no explanation either for the jump discontinuities of the spontaneous deflagration fields, or for the stepped discontinuities of the occurrence of the distinct shapes. A deeper study, involving other physical properties of the system, like electrical resistivity or magnetism, should be conducted in the range of theses discontinuities, in order to unravel their origin. However, the specific heat measurements performed (shown in Chap. 4) did not revealed any abrupt anomaly at these temperatures.

In summary, this chapter is a clear example of serendipity. Trying to obtain magnetic detonations in the Nd_5Ge_3 compound, I found very interesting stepped discontinuities.

General conclusions and future work

I want to conclude this thesis dissertation summarizing the results presented in the different chapters, together with some thoughts about future experiments.

This thesis is based in two very different magnetic materials with a common property. Under certain conditions their magnetization changes are described by the magnetic deflagration phenomena. My original contribution to the investigation of the magnetic deflagrations on the single molecule magnet Mn_{12}−ac consist in studying, for the first time, the deflagration phenomenon using magneto-optical imaging. The results obtained revealed in images the spatial and temporal dependence of the reversal of the magnetization. Moreover, the images were analyzed in detail, finding that the measuring procedure was acting as a low-pass filter. Therefore, improving the image recording protocol (loosing a bit of resolution on the spatial distribution of magnetization), I expect to observe with clarity a magnetic front of deflagration, being able to study its dynamics under different magnetic field-temperature conditions, for example we could study the theoretical predictions when a transverse magnetic is applied in addition to the longitudinal field. Of course, there are other aspects where improvements can/must be made: a longer rectangular sample, with a flat surface, and a smaller heater, for example.

The second material object of study in this thesis is the intermetallic compound $\mathrm{Nd}_5\mathrm{Ge}_3$. This material possesses many interesting physical properties. While the goal of this thesis was to unravel if the reported magnetic avalanches were in reality magnetic deflagrations, I conducted different experiments, with the solely intention of acquire as much knowledge as possible about the material in order to understand the nature of the deflagration phenomena. In the literature there were very few studies on single crystalline samples of this compound, so this thesis has also contributed to expand the knowledge on the material, beyond its magnetic properties. The reason to explain why I needed to fully understand the properties of this system is that is the first time that magnetic deflagrations are observed in two distinct phases of a magnetic material, and also the first time that are reported to occur in a ferromagnet.

In the study of the different physical properties I have found rich phenomena. The $\mathrm{Nd}_5\mathrm{Ge}_3$ presents abrupt transitions in almost every physical property explored. This is an indication of the strong coupling between the different properties with the magnetic structure and its interaction with an external applied field. I have found spontaneous jumps in the heat capacity and in the electrical resistivity. I have observed a rare phenomenon of spontaneous voltage generation when the magnetization changes. In the specific heat measurement I have obtained unexpected AFM contributions even with the system in the FM phase. In the magnetization relaxation experiments I have reported spontaneous jumps in the magnetization, with the magnetic field and the temperature being constant. Certainly, this system is plenty of rich phenomena. And on top of all, the magnetic deflagration.

In different chapters of this thesis I have studied the spontaneous and induced deflagrations, as a function of the magnetic field and/or the temperature. The fit of the theory to the experimental speeds was good enough to encourage us in the hunt for magnetic detonations, because the extrapolation of the fitted curve. Nevertheless, in a clear case of serendipity, instead of reaching the supersonic deflagration regime, what I found was jump discontinuities in the spontaneous deflagration fields. To understand their origin I repeated the experiments in a very different cryostat, finding that, while some of the features could be affected by the thermal bath, the spontaneous deflagration field presented stepped discontinuities that had to be related to intrinsic properties. Was then when, looking at the shape of the induced voltage curves obtained with the pick-up coils, I found that the deflagrations in this system seem to be highly anisotropic.

One important part of the work done during my predoctoral period was dedicated to the design and fabrication of the different experimental setups, some of them certainly tricky to fabricate and manipulate. Also, while are not described in this dissertation, in the seven years that I have been in the group I have investigated many other things. Unfortunately, very few of them ended in satisfactory results and had to be abandoned. I want to mention three: the study of the Doppler Rotational Effect in single crystals of YIG, where I designed a complete pneumatic setup using a dental turbine inside a special cryostat (a turbine with a rotating speed of 360.000 rpm, indeed); the study of the reduction of the Curie temperature on magnetite nanoparticles, in collaboration with Dr. Prozorov in the Ames National Lab (Ames, Iowa); and the fabrication of large arrays (~ 32) of Hall sensors to measure the spatial propagation of magnetic deflagrations, done during my stay with Dr. del Barco in the University of Central Florida (Orlando, Florida).

I want to say some words about the future work that I think that has to be done after this thesis. I would investigate in detail the electrical properties of the Nd_5Ge compound, from Hall measurements to Seebeck effect. I am convinced (actually, I already have some data) that many interesting things are waiting to be discovered in this system. Moreover, taking into account that in this system we can “activate” two different stable magnetic states with temperature (warming up to 70 K) and with field (cooling with 5 kOe), I found very interesting to study the change in the electrical properties between both states. Another proposal is to extend the study of magnetic deflagrations to other materials: I am certainly sure that this intermetallic compound is not the only ferromagnet that possess magnetic deflagration phenomena. Therefore I motivate the study of similar compounds (all with very large magnetic anisotropies), as $CeFe_2$, Y_2CoMnO_6, $R_6Co_{1.67}Si_3$ with (R= Tn, Nd), or some Heusler alloys, for example.

List of Publications

Thesis publications

[1] D. Villuendas, D. Gheorghe, A. Hernández-Mínguez, F. Macià, J. M. Hernàndez, J. Tejada, and R. J. Wijngaarden, "Magneto-optical imaging of magnetic deflagration in Mn12-Acetate", EPL (Europhysics Lett. 84, 67010 (2008)

[2] D. Villuendas, J. M. Hernàndez, and T. Tsutaoka, "Heat capacity study of the magnetic phases in Nd5Ge3 single crystal", arXiv:1504.04252 (2015) - Accepted in JMMM

[3] D. Villuendas, J. M. Hernàndez, S. Vélez, and T. Tsutaoka, "Multiphase magnetic deflagrations in a Nd5Ge3 single crystal" (2015) - Submited to PRB

[4] D. Villuendas, J. M. Hernàndez, "Anisotropic magnetic deflagrations in Nd5Ge3" (2015) - In preparation

Other publications

[1] A. Hernando, D. Puigdomènech, D. Villuendas, C. Vesperinas, and A. Plastino, "Zipf's law from a Fisher variational-principle", Physics Letters A, 374(1), 18–21 (2009)

[2] A. Hernando, D. Villuendas, C. Vesperinas, M. Abad, and A. Plastino, "Unravelling the size distribution of social groups with information theory in complex networks" ,The European Physical Journal B 2010, 76 1, pp 87-97 (2010)

Bibliography

[1] I. Glassman, *Combustion* (Academic Press, New York, 1996) (cit. on p. 1).

[2] W. J. Brown, "Thermal Fluctuations of a Single-Domain Particle", Phys. Rev. **130**, 1677–1686 (1963) (cit. on p. 4).

[3] M. P. Sarachik, "Magnetic Avalanches in Molecular Magnets", in *Mol. magnets*, edited by J. Bartolomé, F. Luis, and J. F. Fernández, NanoScience and Technology (Springer Berlin Heidelberg, Berlin, Heidelberg, 2014) Chap. 5, pp. 113–127 (cit. on pp. 5, 127).

[4] T. Leviant, A. Keren, E. Zeldov, and Y. Myasoedov, "Quantum ignition of deflagration in the Fe8 molecular magnet", Phys. Rev. B **90**, 134405 (2014) (cit. on pp. 5–6, 66).

[5] F. Macià, A. Hernández-Mínguez, G. Abril, J. M. Hernàndez, A. García-Santiago, J. Tejada, F. Parisi, and P. V. Santos, "Observation of phonon-induced magnetic deflagration in manganites", Phys. Rev. B **76**, 174424 (2007) (cit. on pp. 6, 127, 131).

[6] F. Macià, G. Abril, A. Hernández-Mínguez, J. M. Hernandez, J. Tejada, and F. Parisi, "Magnetic fingerprints of the very fast jumps of colossal magnetoresistance in the phase-separated manganite La0.225Pr0.40", Phys. Rev. B **77**, 012403 (2008) (cit. on p. 6).

[7] F. Macià, G. Abril, J. M. Hernandez, and J. Tejada, "The role of thermal coupling on avalanches in manganites.", J. Phys. Condens. Matter **21**, 406005 (2009) (cit. on pp. 6, 113).

[8] S. Vélez, J. M. Hernàndez, A. Fernàndez, F. Macià, C. Magen, P. A. Algarabel, J. Tejada, and E. M. Chudnovsky, "Magnetic deflagration in Gd5Ge4", Phys. Rev. B **81**, 064437 (2010) (cit. on pp. 6, 127, 131).

[9] S. Vélez et al., "Anisotropic magnetic deflagration in single crystals of Gd5Ge4", Phys. Rev. B **85**, 054432 (2012) (cit. on pp. 6, 141, 173).

[10] S. McHugh et al., "Effect of quantum tunneling on the ignition and propagation of magnetic avalanches in Mn12 acetate", Phys. Rev. B **76**, 172410 (2007) (cit. on pp. 6, 21).

[11] S. McHugh, R. Jaafar, M. P. Sarachik, Y. Myasoedov, A. Finkler, E. Zeldov, R. Bagai, and G. Christou, "Magnetic avalanches of minor fast-relaxing species of Mn12 acetate", Phys. Rev. B **80**, 024403 (2009) (cit. on pp. 6, 21).

[12] S. McHugh, B. Wen, X. Ma, M. P. Sarachik, Y. Myasoedov, E. Zeldov, R. Bagai, and G. Christou, "Tuning magnetic avalanches in the molecular magnet Mn12-acetate", Phys. Rev. B **79**, 174413 (2009) (cit. on p. 6).

[13] A. Hernández-Mínguez, J. M. Hernàndez, F. Macià, A. García-Santiago, J. Tejada, and P. V. Santos, "Quantum Magnetic Deflagration in Mn12-Acetate", Phys. Rev. Lett. **95**, 217205 (2005) (cit. on pp. 6, 20–21, 38, 131, 141).

[14] F. Macià, J. M. Hernandez, J. Tejada, S. Datta, S. Hill, C. Lampropoulos, and G. Christou, "Effects of quantum mechanics on the deflagration threshold in the molecular magnet Mn12-acetate", Phys. Rev. B **79**, 092403 (2009) (cit. on p. 6).

[15] W. Decelle, J. Vanacken, V. V. Moshchalkov, J. Tejada, J. M. Hernàndez, and F. Macià, "Propagation of Magnetic Avalanches in Mn12-Ac at High Field Sweep Rates", Phys. Rev. Lett. **102**, 1–4 (2009) (cit. on pp. 6, 25, 152, 155).

[16] V. K. Pecharsky and K. A. Gschneidner, "Structure, magnetism, and thermodynamics of the novel rare earth-based R5T4 intermetallics", Pure Appl. Chem. **79** (2007) `10.1351/pac200779081383` (cit. on p. 6).

[17] T. Lis, "Preparation, structure, and magnetic properties of a dodecanuclear mixed-valence manganese carboxylate", Acta Crystallogr. Sect. B Struct. Crystallogr. Cryst. Chem. **36**, 2042–2046 (1980) (cit. on pp. 9, 12).

[18] A. Caneschi, D. Gatteschi, and R. Sessoli, "Alternating Current Susceptibility, High Field Magnetization, and Millimeter Band EPR Evidence for a Ground S=10 State in [Mn12012(CH3COO)16(H20)4]2CH3COOH*4H20", J. Am. Chem. Soc. **113**, 5873–5874 (1991) (cit. on pp. 9, 11).

[19] R. Sessoli, D. Gatteschi, A. Caneschi, and M. A. Novak, "Magnetic bistability in a metal-ion cluster", Nature **365**, 141–143 (1993) (cit. on p. 9).

[20] J. R. Friedman, M. P. Sarachik, J. Tejada, and R. F. Ziolo, "Macroscopic Measurement of Resonant Magnetization Tunneling in High-Spin Molecules", Phys. Rev. Lett. **76**, 3830–3833 (1996) (cit. on p. 10).

[21] J. R. Friedman, M. P. Sarachik, J. Tejada, J. Maciejewski, and R. F. Ziolo, "Steps in the hysteresis loops of a high-spin molecule", J. Appl. Phys. **79**, 6031 (1996) (cit. on p. 10).

[22] J. M. Hernàndez, X. X. Zhang, F. Luis, J. Bartolome, J. Tejada, and R. F. Ziolo, "Field tuning of thermally activated magnetic quantum tunnelling in Mn12-Ac molecules", Europhys. Lett. **35**, 301–306 (1996) (cit. on pp. 10, 21–22).

[23] J. M. Hernàndez, X. X. Zhang, F. Luis, J. Tejada, J. R. Friedman, M. P. Sarachik, and R. Ziolo, "Evidence for resonant tunneling of magnetization in Mn12-acetate complex", Phys. Rev. B **55**, 5858–5865 (1997) (cit. on pp. 10, 146).

[24] L. Thomas, F. Lionti, R. Ballou, D. Gatteschi, R. Sessoli, and B. Barbara, "Macroscopic quantum tunnelling of magnetization in a single crystal of nanomagnets", Nature **383**, 145–147 (1996) (cit. on p. 10).

[25] R. Moroni, C. Cartier dit Moulin, G. Champion, M.-A. Arrio, P. Sainctavit, M. Verdaguer, and D. Gatteschi, "X-ray magnetic circular dichroism investigation of magnetic contributions from Mn(III) and Mn(IV) ions in Mn12-ac", Phys. Rev. B **68**, 064407 (2003) (cit. on p. 10).

[26] D. A. Garanin, "Spin Tunneling - a Perturbative Approach", J. Phys. a-Mathematical Gen. **24**, L61–L62 (1991) (cit. on p. 14).

[27] F. Hartmann-Boutron, P. Politi, and J. Villain, "Tunneling and magnetic relaxation in mesoscopic molecules", Int. J. Mod. Phys. B **10**, 2577–2637 (1996) (cit. on p. 14).

[28] E. M. Chudnovsky and J. Tejada, *Lectures on Magnetism (with 128 Problems)* (Rinton Press, Inc., Princeton, New Jersey, 2006), p. 224 (cit. on pp. 19, 84, 89, 147).

[29] C. Paulsen and J. G. Park, "Evidence for Quantum Tunneling of the Magnetization in Mn12-Ac", in *Quantum tunneling magn. – qtm '94*, edited by L. Gunther and B. Barbara (Springer Netherlands, Boston, 1995) Chap. Part III, pp. 189–207 (cit. on pp. 19, 21).

[30] A. Hernández-Mínguez, "Avalanchas en sistemas de espines: deflagración magnética cuántica y nueva ley de relajación.", PhD thesis (Universitat de Barcelona, 2009) (cit. on p. 19).

[31] Y. Suzuki et al., "Propagation of Avalanches in Mn12-Acetate: Magnetic Deflagration", Phys. Rev. Lett. **95**, 147201 (2005) (cit. on pp. 20, 25, 38, 152, 155).

[32] J. M. Hernàndez, P. V. Santos, F. Macià, A. García-Santiago, and J. Tejada, "Acoustomagnetic pulse experiments in LiNbO3/ Mn12 hybrids", Appl. Phys. Lett. **88**, 012503 (2006) (cit. on pp. 21, 46).

[33] A. Hernández-Mínguez, F. Macià, J. M. Hernàndez, J. Tejada, and P. V. Santos, "Phonon-induced quantum magnetic deflagration in Mn12", J. Magn. Magn. Mater. **320**, 1457–1463 (2008) (cit. on pp. 21, 38, 46, 141).

[34] D. Villuendas, D. Gheorghe, A. Hernández-Mínguez, F. Macià, J. M. Hernàndez, J. Tejada, and R. J. Wijngaarden, "Magneto-optical imaging of magnetic deflagration in Mn12-Acetate", EPL (Europhysics Lett. **84**, 67010 (2008) (cit. on p. 21).

[35] S. McHugh, R. Jaafar, M. P. Sarachik, Y. Myasoedov, H. Shtrikman, E. Zeldov, R. Bagai, and G. Christou, "Experimental determination of the dipolar field in Mn12-acetate", Phys. Rev. B **79**, 052404 (2009) (cit. on p. 21).

[36] D. A. Garanin and E. M. Chudnovsky, "Theory of magnetic deflagration in crystals of molecular magnets", Phys. Rev. B **76**, 054410 (2007) (cit. on pp. 21, 23, 38, 105–106).

[37] E. Del Barco, J. M. Hernàndez, M. Sales, J. Tejada, H. Rakoto, J. M. Broto, and E. M. Chudnovsky, "Spin-phonon avalanches in Mn12-acetate", Phys. Rev. B **60**, 898–901 (1999) (cit. on pp. 21–22).

[38] M. Sales, J. Hernandez, J. Tejada, and J. Martínez, "Time-dependent heat capacity of Mn12 clusters", Phys. Rev. B **60**, 14557–14560 (1999) (cit. on pp. 21, 44).

[39] M. A. Novak, R. Sessoli, A. Caneschi, and D. Gatteschi, "Magnetic properties of a Mn cluster organic compound", J. Magn. Magn. Mater. **146**, 211–213 (1995) (cit. on p. 22).

[40] A. M. Gomes, M. A. Novak, R. Sessoli, A. Caneschi, and D. Gatteschi, "Specific heat and magnetic relaxation of the quantum nanomagnet Mn12Ac", Phys. Rev. B **57**, 5021–5024 (1998) (cit. on p. 22).

[41] D. A. Garanin and V. Lutovinov, “Absorption of sound and kinetic coefficients of elastic bodies”, Ann. Phys. (N. Y). **218**, 293–324 (1992) (cit. on p. 22).

[42] M. Leuenberger and D. Loss, “Spin tunneling and phonon-assisted relaxation in Mn12-acetate”, Phys. Rev. B **61**, 1286–1302 (2000) (cit. on p. 25).

[43] M. Faraday, “Experimental Researches in Electricity. Nineteenth Series”, Philos. Trans. R. Soc. London **136**, 1–20 (1846) (cit. on p. 26).

[44] J. Kerr, “On Rotation of the Plane of the Polarization by Reflection from the Pole of a Magnet”, Philos. Mag. **3**, 321 (1877) (cit. on p. 26).

[45] A. Cotton, “Dispersion rotatoire anomale des corps absorbants”, Compt. Rend. **120**, 1044 (1895) (cit. on p. 26).

[46] P. Zeeman, “On the influence of Magnetism on the Nature of the Light emitted by a Substance”, Philos. Mag. **43**, 226 (1897) (cit. on p. 26).

[47] P. Alers, “Structure of the Intermediate State in Superconducting Lead”, Phys. Rev. **105**, 104–108 (1957) (cit. on p. 26).

[48] W. DeSorbo, “Study of the Intermediate State in Superconductors using Cerium Phosphate Glass”, Phys. Rev. Lett. **4**, 406–408 (1960) (cit. on p. 26).

[49] H. Kirchner, “High-resolution magneto-optical observation of magnetic structures in superconductors”, Phys. Lett. A **26**, 651–652 (1968) (cit. on p. 26).

[50] R. Huebener, R. Kampwirth, and V. Rowe, “Magneto-optical observation of the flux structure in superconducting lead films near the critical film thickness”, Solid State Commun. **9**, 1183–1186 (1971) (cit. on p. 26).

[51] M. R. Koblischka and R. J. Wijngaarden, “Magneto-optical investigations of superconductors”, Supercond. Sci. Technol. **8**, 199–213 (1995) (cit. on p. 26).

[52] R. J. Wijngaarden, K. Heeck, M. Welling, R. Limburg, M. Pannetier, K. van Zetten, V. L. G. Roorda, and A. R. Voorwinden, “Fast imaging polarimeter for magneto-optical investigations”, Rev. Sci. Instrum. **72**, 2661–2664 (2001) (cit. on p. 29).

[53] D. Gheorghe, “Magneto-optics of superconductors with nanotailored pinning and with ferromagnetic layers”, PhD thesis (Vrije Universiteit Amsterdam, 2010) (cit. on p. 29).

[54] L. Dorosinskii, M. Indenbom, V. Nikitenko, Y. Ossip'yan, A. Polyanskii, and V. Vlasko-Vlasov, "Studies of HTSC crystal magnetization features using indicator magnetooptic films with in-plane anisotropy", Phys. C Supercond. **203**, 149–156 (1992) (cit. on p. 29).

[55] A. Lee, *VirtualDub* (cit. on p. 32).

[56] W. Rasband, *ImageJ*, Bethesda (cit. on p. 37).

[57] D. A. Garanin, "Theory of Deflagration and Fronts of Tunneling in Molecular Magnets", in *Mol. magnets*, edited by J. Bartolomé, F. Luis, and J. F. Fernández, NanoScience and Technology (Springer Berlin Heidelberg, Berlin, Heidelberg, 2014) Chap. 6, pp. 129–159 (cit. on pp. 38, 145).

[58] M. Pannetier, F. Klaassen, R. Wijngaarden, M. Welling, K. Heeck, J. Huijbregtse, B. Dam, and R. Griessen, "Magneto-optical investigation of flux penetration in a superconducting ring", Phys. Rev. B **64**, 144505 (2001) (cit. on p. 41).

[59] L. Helseth, "Model for imaging magnetic fields using a magnetooptic indicator", J. Magn. Magn. Mater. **247**, 230–236 (2002) (cit. on p. 41).

[60] T. Johansen, M. Baziljevich, H. Bratsberg, Y. Galperin, P. Lindelof, Y. Shen, and P. Vase, "Direct observation of the current distribution in thin superconducting strips using magneto-optic imaging", Phys. Rev. B **54**, 16264–16269 (1996) (cit. on p. 41).

[61] D. A. Garanin and S. Shoyeb, "Quantum deflagration and supersonic fronts of tunneling in molecular magnets", Phys. Rev. B **85**, 1–10 (2012) (cit. on pp. 50, 156).

[62] M. Modestov, V. Bychkov, and M. Marklund, "Pulsating regime of magnetic deflagration in crystals of molecular magnets", Phys. Rev. B **83**, 214417 (2011) (cit. on p. 50).

[63] K. Schubert, *Kristallstrukturen zweikomponentiger Phasen*, Berlin, 1964 (cit. on p. 51).

[64] G. Bergerhoff, *Inorganic Crystal Structure Database (ICSD) - FIZ Karlsruhe*, 2015 (cit. on p. 51).

[65] K. Momma and F. Izumi, "VESTA 3 for three-dimensional visualization of crystal, volumetric and morphology data", J. Appl. Crystallogr. **44**, 1272–1276 (2011) (cit. on p. 51).

[66] K. H. J. Buschow and J. F. Fast, "Crystal Structure and Magnetic Properties of Some Rare Earth Germanides", Phys. Status Solidi B **21**, 593–600 (1967) (cit. on pp. 52–53, 66, 94).

[67] P. Villars, *Material Phases Data System (MPDS) - Springer Materials*, 2014 (cit. on p. 53).

[68] K. S. V. L. Narasimhan, H. Steinfink, and E. V. Ganapathy, "The Magnetic Susceptibilities of Some Rare Earth Silicides and Germanides with the D88 Structure", J. Appl. Phys. **40**, 51 (1969) (cit. on p. 53).

[69] A. P. Vokhmyanin and Y. A. Dorofeev, "Magnetic Structure of Er5Ge3 at 4.2 K", Phys. Solid State **45**, 1735–1741 (2003) (cit. on p. 53).

[70] A. V. Morozkin, O. Isnard, P. Henry, and P. Manfrinetti, "Magnetic structure of the Mn5Si3-type Er5Ge3 compound", J. Magn. Magn. Mater. **307**, 124–127 (2006) (cit. on p. 53).

[71] A. V. Morozkin, O. Isnard, P. Henry, and P. Manfrinetti, "The magnetic ordering in the Ho5Si3 and Ho5Ge3 compounds", J. Alloys Compd. **464**, 219–226 (2008) (cit. on p. 53).

[72] A. V. Morozkin, O. Isnard, R. Nirmala, and S. Malik, "Magnetic properties and magnetic structure of the Mn5Si3-type Tb5Si3 compound", J. Alloys Compd. **470**, 20–23 (2009) (cit. on p. 53).

[73] B. Maji, K. G. Suresh, and A. K. Nigam, "Observation of spontaneous magnetization jump and field-induced irreversibility in Nd5Ge3", EPL **91**, 37007 (2010) (cit. on pp. 53, 68, 72, 89, 100, 108, 111, 116).

[74] B. Maji, K. G. Suresh, and A. K. Nigam, "Low temperature cluster glass behavior in Nd5Ge3.", J. Phys. Condens. Matter **23**, 506002 (2011) (cit. on pp. 53, 56, 61, 65, 68, 79, 86–87).

[75] R. Nirmala et al., "Competing magnetic interactions in the intermetallic compounds Pr5Ge3 and Nd5Ge3", J. Appl. Phys. **109**, 07A716 (2011) (cit. on p. 53).

[76] Y. Mudryk, D. Paudyal, V. K. Pecharsky, and K. a. Gschneidner, "Low-temperature crystal structure and magnetic properties of Gd5Ge3", Phys. Rev. B **85**, 014116 (2012) (cit. on p. 53).

[77] P. Kushwaha and R. Rawat, "Low temperature irreversible field induced magnetic transition in Gd5Ge3", Solid State Commun. **152**, 1824–1828 (2012) (cit. on p. 53).

[78] B. Maji, K. G. Suresh, X. Chen, and R. V. Ramanujan, “Magnetic and magnetocaloric properties of ball milled Nd5Ge3”, J. Appl. Phys. **111**, 073905 (2012) (cit. on p. 53).

[79] B. Maji and K. Suresh, “Nonequilibrium magnetic properties in Nd5Ge3”, J. Alloys Compd. **605**, 29–33 (2014) (cit. on p. 53).

[80] M. Kurisu, T. Mitsumata, and I. Oguro, “Dense Kondo compound Ce5Ge3”, Phys. B Condens. Matter **259-261**, 96–98 (1999) (cit. on pp. 53, 94).

[81] M. Doerr et al., “Magnetostructural irreversibilities in R5Ge3 (R=Gd, Nd) intermetallics”, J. Phys. Conf. Ser. **150**, 042025 (2009) (cit. on pp. 53, 109–110).

[82] T. Tsutaoka, Y. Nishiume, and T. Tokunaga, “Magnetic and transport properties of R5Ge3 (R=Gd,Tb) single crystals”, J. Magn. Magn. Mater. **272-276**, E421–E422 (2004) (cit. on pp. 53, 94).

[83] T. Tsutaoka, A. Tanaka, Y. Narumi, M. Iwaki, and K. Kindo, “Irreversible magnetic-field-induced antiferromagnetic to ferromagnetic transition in Nd5Ge3”, Phys. B Condens. Matter **405**, 180–185 (2010) (cit. on pp. 53, 57, 61–62, 66–68, 73–74, 76, 79, 82, 87, 99, 108).

[84] D. Joshi, A. Thamizhavel, and S. K. Dhar, “Magnetic behavior of single-crystalline Pr5Ge3 and Tb5Ge3 compounds”, Phys. Rev. B **79**, 014425 (2009) (cit. on pp. 53, 82).

[85] S. Blundell, *Magnetism in Condensed Matter* (Oxford University Press, 2001) (cit. on pp. 54, 88).

[86] P. Schobinger-Papamantellos and K. Buschow, “Magnetic properties of Nd5Ge3 studied by neutron diffraction and magnetic measurements”, J. Magn. Magn. Mater. **49**, 349–356 (1985) (cit. on pp. 54–56, 61).

[87] A. P. Vokhmyanin, B. Medzhi, A. N. Pirogov, and A. E. Teplykh, “Magnetic structure of the Nd5Ge3 compound”, Phys. Solid State **56**, 34–38 (2014) (cit. on p. 56).

[88] T. Tsutaoka, Y. Andoh, G. Nakamoto, and M. Kurisu, “Neutron diffraction studies on the magnetic field induced irreversible antiferromagnetic to ferromagnetic transition in Nd5Ge3”, Act. Rep. Neutron Scatt. Res. Exp. Reports **18** (2011) (cit. on pp. 56, 111).

[89] E. Levin, V. K. Pecharsky, K. Gschneidner, and G. Miller, "Electrical resistivity, electronic heat capacity, and electronic structure of Gd5Ge4", Phys. Rev. B **64**, 235103 (2001) (cit. on p. 57).

[90] S. B. Roy, M. K. Chattopadhyay, P. Chaddah, J. D. Moore, G. K. Perkins, L. F. Cohen, K. a. Gschneidner, and V. K. Pecharsky, "Evidence of a magnetic glass state in the magnetocaloric material Gd5Ge4", Phys. Rev. B - Condens. Matter Mater. Phys. **74**, 3–6 (2006) (cit. on p. 61).

[91] M. Balanda, "AC Susceptibility Studies of Phase Transitions and Magnetic Relaxation: Conventional, Molecular and Low-Dimensional Magnets", Acta Phys. Pol. A **124**, 964–976 (2013) (cit. on pp. 65–66).

[92] E. V. Sampathkumaran and A. Niazi, "Superparamagnetic-like ac susceptibility behavior in the partially disordered antiferromagnetic compound Ca3CoRhO6", Phys. Rev. B **65**, 180401 (2002) (cit. on p. 66).

[93] J. A. Mydosh, *Spin glasses: an experimental introduction* (Taylor & Francis, London, 1993), p. 280 (cit. on p. 66).

[94] A. Malinowski, V. L. Bezusyy, R. Minikayev, P. Dziawa, Y. Syryanyy, and M. Sawicki, "Spin-glass behavior in Ni-doped La1.85Sr0.15CuO4", Phys. Rev. B **84**, 024409 (2011) (cit. on p. 66).

[95] C. Tien, C. H. Feng, C. S. Wur, and J. J. Lu, "Ce2CuGe3: A nonmagnetic atom-disorder spin glass", Phys. Rev. B **61**, 12151–12158 (2000) (cit. on p. 66).

[96] J. Jensen and A. Mackintosh, *Rare earth magnetism* (Clarendon Press - Oxford, 1991) (cit. on p. 66).

[97] V. Hardy et al., "Observation of spontaneous magnetization jumps in manganites", Phys. Rev. B **68**, 220402 (2003) (cit. on p. 73).

[98] T. Wu and J. Mitchell, "Magnetization steps in manganite films: Time delay of the metamagnetic transition", Phys. Rev. B **69**, 1–4 (2004) (cit. on p. 73).

[99] D. Q. Liao, Y. Sun, R. F. Yang, Q. A. Li, and Z. H. Cheng, "Spontaneous magnetization and resistivity steps in the bilayered manganite (La0.5Nd0.5)1.2Sr1.8Mn2O7", Phys. Rev. B **74**, 2–7 (2006) (cit. on p. 73).

[100] Z. Jian-Jun, L. Yi, Haosibayar, X. Ru, Y. Ren-Fu, L. Qing-An, S. Young, and C. Zhao-Hua, "Spontaneous magnetization and resistivity jumps in bilayered manganite (La0.8Eu0.2)4/3Sr5 /3Mn2O7 single crystals", Chinese Phys. B **17**, 2717–2720 (2008) (cit. on p. 73).

[101] T. Tang, C. Tien, R. S. Huang, and B. Y. Hou, "Steplike magnetization and resistivity transition in the half-doped manganite compound Pr0.75Na0.25MnO3", Solid State Commun. **146**, 133–136 (2008) (cit. on p. 73).

[102] T. Tang, R. S. Huang, and S. Y. Zhang, "Ultra-sharp metamagnetic transition in manganite Pr0.6Na0.4MnO3", J. Magn. Magn. Mater. **321**, 263–266 (2009) (cit. on p. 73).

[103] P. Čermák, *Magnetic properties of Ce compounds studied by specific heat*, tech. rep. (2010), p. 51 (cit. on p. 80).

[104] J. S. Hwang, K. J. Lin, and C. Tien, "Measurement of heat capacity by fitting the whole temperature response of a heat-pulse calorimeter", Rev. Sci. Instrum. **68**, 94 (1997) (cit. on p. 81).

[105] E. Dachs and C. Bertoldi, "Precision and accuracy of the heat-pulse calorimetric technique: low temperature heat capacities of milligram-sized synthetic mineral samples", Eur. J. Mineral. **17**, 251–259 (2005) (cit. on p. 81).

[106] C. Kittel, *Introduction to Solid State Physics*, 8th (Wiley, New York, 2005), p. 703 (cit. on p. 82).

[107] M. Bouvier, P. Lethuillier, and D. Schmitt, "Specific heat in some gadolinium compounds. I. Experimental", Phys. Rev. B **43**, 13137–13144 (1991) (cit. on p. 83).

[108] J. Hoffmann, A. Paskin, K. Tauer, and R. Weiss, "Analysis of ferromagnetic and antiferro-magnetic second-order transitions", J. Phys. Chem. Solids **1**, 45–60 (1956) (cit. on p. 83).

[109] B. Woodfield, M. Wilson, and J. Byers, "Low-Temperature Specific Heat of La1-xSrxMnO3+δ", Phys. Rev. Lett. **78**, 3201–3204 (1997) (cit. on p. 84).

[110] C. He, H. Zheng, J. F. Mitchell, M. L. Foo, R. J. Cava, and C. Leighton, "Low temperature Schottky anomalies in the specific heat of LaCoO3: Defect-stabilized finite spin states", Appl. Phys. Lett. **94**, 102514 (2009) (cit. on p. 86).

[111] N. P. Gorbachuk, "Melting enthalpies and heat capacities of lower germanides of rare-earth metals", Powder Metall. Met. Ceram. **49**, 474–477 (2010) (cit. on p. 86).

[112] R. K. Harris, *Encyclopedia of Nuclear Magnetic Resonance, Vol. 5*, edited by D. M. Granty and R. K. Harris (Wiley, New York, 1996) (cit. on p. 86).

[113] T. Chatterji, G. J. Schneider, L. van Eijck, B. Frick, and D. Bhattacharya, “Direct evidence for the Nd magnetic ordering in NdMnO3 from the hyperfine field splitting of Nd nuclear levels.”, J. Phys. Condens. Matter **21**, 126003 (2009) (cit. on pp. 86–87).

[114] C. Sürgers, G. Fischer, P. Winkel, and H. V. Löhneysen, “Large topological Hall effect in the non-collinear phase of an antiferromagnet.”, en, Nat. Commun. **5**, 3400 (2014) (cit. on p. 97).

[115] V. K. Pecharsky, a. P. Holm, K. a. Gschneidner, and R. Rink, “Massive magnetic-field-induced structural transformation in Gd5Ge4 and the nature of the giant magnetocaloric effect.”, Phys. Rev. Lett. **91**, 197204 (2003) (cit. on p. 111).

[116] C. Webster, O. Kazakova, J. Gallop, P. Josephs-Franks, A. Hernández-Mínguez, and A. Tzalenchuk, “Influence of thermal coupling on spin avalanches in Mn12-Acetate”, Phys. Rev. B **76**, 012403 (2007) (cit. on p. 113).

[117] M. Zou, H. Tang, D. L. Schlagel, T. A. Lograsso, K. A. Gschneidner, and V. K. Pecharsky, “Spontaneous generation of voltage in single-crystal Gd5Si2Ge2 during magnetostructural phase transformations”, J. Appl. Phys. **99**, 08B304 (2006) (cit. on pp. 118, 123).

[118] M. Zou, J. A. Sampaio, V. K. Pecharsky, and K. A. Gschneidner, “Spontaneous generation of voltage in the magnetocaloric compound La(Fe0.88Si0.12)13 and comparison to SmMn2Ge2”, Phys. Rev. B **80**, 172403 (2009) (cit. on pp. 118, 123).

[119] M. F. Reid et al., “Spontaneous generation of voltage in the magnetocaloric compound Tb5Si2.2Ge1.8 and elemental Gd”, J. Alloys Compd. **488**, 550–553 (2009) (cit. on pp. 118, 123).

[120] P. Subedi et al., “Onset of a Propagating Self-Sustained Spin Reversal Front in a Magnetic System”, Phys. Rev. Lett. **110**, 207203 (2013) (cit. on pp. 133, 137, 150).

[121] B. C. Passenheim, “Heat Capacity of RuO2 and IrO2 between 0.54 and 10 K”, J. Chem. Phys. **51**, 320 (1969) (cit. on p. 140).

[122] H. Williams, W. Shockley, and C. Kittel, “Studies of the Propagation Velocity of a Ferromagnetic Domain Boundary”, Phys. Rev. **80**, 1090–1094 (1950) (cit. on p. 141).

[123] S. Zapperi, P. Cizeau, G. Durin, and H. Stanley, “Dynamics of a ferromagnetic domain wall: Avalanches, depinning transition, and the Barkhausen effect”, Phys. Rev. B **58**, 6353–6366 (1998) (cit. on p. 141).

[124] J. E. Jensen, W. A. Tuttle, R. B. Stewart, H. Brechna, and A. Prodell, *Brookhaven National Laboratory selected cryogenic data notebook*, Brookhaven National Laboratory Selected Cryogenic Data Notebook v. 2 (Brookhaven National Laboratory, Associated Universities, Inc., 1980) (cit. on p. 150).

[125] O. Jukimenko, C. M. Dion, M. Marklund, and V. Bychkov, “Multidimensional Instability and Dynamics of Spin Avalanches in Crystals of Nanomagnets”, Phys. Rev. Lett. **113**, 217206 (2014) (cit. on p. 151).

[126] M. Modestov, V. Bychkov, and M. Marklund, “Ultrafast spin avalanches in crystals of nanomagnets in terms of magnetic detonation”, Phys. Rev. Lett. **107**, 1–5 (2011) (cit. on p. 156).

[127] C. M. Dion, O. Jukimenko, M. Modestov, M. Marklund, and V. Bychkov, “Anisotropic properties of spin avalanches in crystals of nanomagnets”, Phys. Rev. B **87**, 014409 (2013) (cit. on pp. 156, 173).

[128] O. Jukimenko, M. Modestov, M. Marklund, and V. Bychkov, “Magnetic detonation structure in crystals of nanomagnets controlled by thermal conduction and volume viscosity”, Phys. Rev. B **91**, 094428 (2015) (cit. on p. 156).

[129] N. H. Balshaw, *Practical Cryogenics: An Introduction to Laboratory Cryogenics* (Oxford Instruments Superconductivity Limited, Eynsham, Oxfordshire, 2001), p. 96 (cit. on p. 158).

[130] F. Pobell, *Matter and Methods at Low Temperatures* (Springer Berlin Heidelberg, Berlin, Heidelberg, 2007) (cit. on p. 159).

[131] J. M. Hernàndez, “Fenómenos cuánticos de espín en sistemas mesoscópicos”, PhD thesis (2001) (cit. on p. 165).